

ISSN 0973-3302

# THE JOURNAL OF ACOUSTICAL SOCIETY OF INDIA

Volume 44

Number 1

January 2017



A Quarterly Publication of the ASI  
<http://www.acousticsindia.org>



# The Journal of Acoustical Society of India

The Refereed Journal of the Acoustical Society of India (JASI)

**CHIEF EDITOR:**

**B. Chakraborty**

CSIR-National Institute of Oceanography

Dona Paula,

Goa-403 004

Tel: +91.832.2450.318

Fax: +91.832.2450.602

E-mail: bishwajit@nio.org

**ASSOCIATE SCIENTIFIC EDITOR:**

**A R Mohanty**

Mechanical Engg. Department

Indian Institute of Technology

Kharagpur-721302, India

Tel. : +91-3222-282944

E-mail : amohantyemech.iitkgp.ernet.in

**Editorial Office:**

**MANAGING EDITOR**

**Mahavir Singh**

**ASSISTANT EDITORS:**

**Yudhisther Kumar**

**Devraj Singh**

**Kirti Soni**

ASI Secretariat,

C/o Acoustics, Ultrasonics & Vibration

Section CSIR-National Physical Laboratory

Dr. KS Krishnan Road

New Delhi 110 012

Tel: +91.11. 4560.8317

Fax: +91.11.4560.9310

E-mail: asisecretariat.india@gmail.com

The **Journal of Acoustical Society of India** is a refereed journal of the Acoustical Society of India (ASI). The ASI is a non-profit national society founded in 31st July, 1971. The primary objective of the society is to advance the science of acoustics by creating an organization that is responsive to the needs of scientists and engineers concerned with acoustics problems all around the world.

Manuscripts of articles, technical notes and letter to the editor should be submitted to the Chief Editor. Copies of articles on specific topics listed above should also be submitted to the respective Associate Scientific Editor. Manuscripts are refereed by at least two referees and are reviewed by Publication Committee (all editors) before acceptance. On acceptance, revised articles with the text and figures scanned as separate files on a diskette should be submitted to the Editor by express mail. Manuscripts of articles must be prepared in strict accordance with the author instructions.

All information concerning subscription, new books, journals, conferences, etc. should be submitted to Chief Editor:

*B. Chakraborty, CSIR - National Institute of Oceanography, Dona Paula, Goa-403 004,  
Tel: +91.832.2450.318, Fax: +91.832.2450.602, e-mail: bishwajit@nio.org*

Annual subscription price including mail postage is Rs. 2500/= for institutions, companies and libraries and Rs. 2500/= for individuals who are not ASI members. The Journal of Acoustical Society of India will be sent to ASI members free of any extra charge. Requests for specimen copies and claims for missing issues as well as address changes should be sent to the Editorial Office:

*ASI Secretariat, C/o Acoustics, Ultrasonics & Vibration Section, CSIR-National Physical Laboratory, Dr. KS Krishnan Road,  
New Delhi 110 012, Tel: +91.11.4560.8317, Fax: +91.11.4560.9310, e-mail: asisecretariat.india@gmail.com*

The journal and all articles and illustrations published herein are protected by copyright. No part of this journal may be translated, reproduced, stored in a retrieval system, or transmitted, in any form or by any means, electronic, mechanical, photocopying, microfilming, recording or otherwise, without written permission of the publisher.

Copyright © 2017, Acoustical Society of India

ISSN 0973-3302

Printed at Alpha Printers, WZ-35/C, Naraina, Near Ring Road, New Delhi-110028 Tel.: 9810804196. JASI is sent to ASI members free of charge.

**B. CHAKRABORTY**

Chief Editor

**MAHAVIR SINGH**

Managing Editor

**A R MOHANTY**

Associate Scientific Editor

**Yudhishter Kumar Yadav**

**Devraj Singh**

**Kirti Soni**

Assistant Editors

## EDITORIAL BOARD

**M L Munjal**

IISc Bangalore, India

**S Narayanan**

IIT Chennai, India

**V R SINGH**

PDM EI New Delhi-NCR, India

**R J M Craik**

HWU Edinburg, UK

**Trevor R T Nightingale**

NRC Ottawa, Canada

**N Tandon**

IIT Delhi, India

**J H Rindel**

Odeon A/S, Denmark

**E S R Rajagopal**

IISc Bangalore, India

**G V Anand**

IISc Bangalore, India

**S S Agrawal**

KIIT Gurgaon, India

**Yukio Kagawa**

NU Chiba, Japan

**D D Ebenezer**

NPOL Kochi, India

**Sonoko Kuwano**

OU Osaka, Japan

**Mahavir Singh**

CSIR-NPL, New Delhi, India

**A R Mohanty**

IIT Kharagpur, India

**Manell E Zakharia**

ENSAM Paris, France

**Arun Kumar**

IIT Delhi, India

**Ajesh K. Abraham**

IISH Mysore, India

**S V Ranganayakulu**

GNI Hyderabad, India



# The Journal of Acoustical Society of India

A quarterly publication of the Acoustical Society of India

Volume 44, Number 1, January 2017

## ARTICLES

**Mid-to-High Frequency (6-10 kHz) Measurements of Acoustic Bottom Backscattering**

*Sreeram Radhakrishnan* ..... 1

**Effect of multipath propagation on replica correlation processing of linear frequency modulated signals**

*R.P. Raju and P.V. Nair* ..... 9

**Optimum band for passive broadband sonar in surface duct environments**

*S. Neethu, S. Satheesh Kumar and P.A. Maheswaran* ..... 15

**Real-time enhancement of climatological temperature profile using *in-situ* profile**

*P. Anand* ..... 23

**Hydrostatic response of 1-3 Piezocomposite large-area Hydrophones**

*R. Ramesh, S.V. Periera, K. Sreelatha, T.K. Vinod Kumar, B. Jayakumar and C. Durga Prasad* ..... 29

**Transmission line and finite element modelling of a high frequency, underwater acoustic transducer**

*R. Ramesh, Pushpa Abraham, E. R. Ratheesh and Manoj N. Unni* ..... 36

**Development of acoustic absorber panels for underwater stealth applications**

*V. G. Jayakumari, Rahna K. Shamsudeen, R. Rajeswari and T. Mukundan* ..... 45

**Studies on influence of curing agents on carbon black and nanoclay reinforced chloroprene rubber for acoustic sensor applications**

*P. Annadurai, P. Jayesh, T. Mukundan, Rani Joseph and T. Santhanakrishnan* ..... 53

## INFORMATION

Information for Authors

Inside back cover



## FOREWORD

SONARs form an important application of acoustics in the underwater domain. As acoustic waves are practically the only form of energy which can propagate long distances underwater without severe attenuation, SONARs provide the sole means of navigation, communication and detection in the underwater domain. Ever since submarines emerged as determinants of success in Naval warfare, development of more and more powerful and sophisticated SONAR technologies have received the highest priority from the Navies the world over. Thus no efforts were spared by governments in investing resources and manpower in developing ever more sophisticated SONAR systems. This has resulted in intensive R&D efforts in this area and tremendous pace of introduction of ever newer technologies and systems.

In India too, our leadership from both the Scientific community as well as the Naval side have been fully aware of the importance of this technology. It is a tribute to their vision that they thought it fit to initiate indigenous R&D efforts in this area as early as 1950's. SONAR systems are highly multi-disciplinary in nature. The development and testing of SONAR systems also call for specialized test and evaluation facilities. These competencies and facilities were patiently acquired and built up within the country over these years. These fledgling efforts have today flowered and borne fruit and India has emerged as one of the few countries in the world capable of developing sophisticated SONAR systems for Naval ships, submarines and aircraft.

Therefore, it was no surprise that when JASI decided to come out with a special issue on SONARs during 2016, it received a very enthusiastic response from the R&D community from within India. Nine papers were accepted in the special issue. Since there were more papers which could not be accommodated in that issue, a decision was taken to come out with a second special issue on the same topic. There are eight papers in this second edition, which makes it seventeen papers in toto. It is noted that the papers cover a wide range of areas related to SONAR technologies and are of high quality.

I thank all the authors for their contributions in both these special issues. The SONAR community is indebted to JASI for proposing these special issues. In particular, I thank Dr. Bishwajit Chakraborty, Prof. S. K. Bhattacharyya, Prof. Rajendar Bahl and Dr. D.D. Ebenezer for their sustained interest and efforts in making these special issues a great success.

Before I sign off, I would like to bring to the notice of all readers of JASI that the DRDO is organizing an International Conference on SONARs (ICONS-18) during 22-24 Feb. 2018 at Kochi. The three-day conference will cover all aspects of SONAR technologies and underwater acoustics. I invite all prospective authors to visit [www.icons2018.org](http://www.icons2018.org), contribute papers, and participate actively to make this conference a grand success.

**S. Kedarnath Shenoy**

*Director*

Naval Physical and Oceanographic Laboratory  
Defence Research and Development Organisation  
Ministry of Defence, Kochi, Kerala-682021

# EDITORIAL

## Guest Editor's Introduction to the Second special issue on Sonar

This second special issue on Sonar is a continuation of the previously published October 2016 issue on Sonar. This special issue comprised of eight articles from the researchers of the NPOL, DRDO. Four papers on the various active acoustics issues are based on the field experiments conducted in the Arabian Sea, and remaining papers cover active and passive sensor/transducer as well as underwater stealth application.

In a first paper, *Sreeram Radhakrishnan* had presented bottom backscattering data and related analysis of mid-to-high acoustic signal frequencies (6-10 kHz) as a function of grazing angle (14-80 degrees) measured from a shallow water location in the Arabian Sea off the west coast of India. *Raju* and *Nair* had conducted an experiment at a shallow shelf area where depth varies within the 45-60 m. The experiment reveals, the energy spreading loss (ESL) is proportional to the pulse-width for chirp sonar within a specific bandwidth. The transmission Loss mosaics for sound radiated by an objects is computed using the suitable propagation algorithm as presented by *Neethu et al.* in an another experiment. *Anand* had developed a method to employ climate temperature profile at a remote point and compared the difference between it and the measured profile. The method is tested in the South-Eastern Arabian Sea during the different seasons. *Ramesh et al.* presented the effect of high hydrostatic pressures up to 30 bar on the receiving sensitivity of 1-3 piezocomposite planar hydrophones. The measurements were made in an anechoic- high pressure-hydrophone calibrating facility. Again, *Ramesh et al.* employed finite element modelling (FEM) for active acoustic high-frequency transducer design applications. *Jayakumari et al.* had dealt with the acoustic absorber panel design parameters for underwater stealth application using FEM. *Annadurai et al.* had investigated the influence of curing agents on nanoclay and carbon black/nanoclay reinforced chloroprene rubber compounds.

We express our sincere gratitude to Shri S. Kedarnath Shenoy, Director, Naval Physical Oceanographic Laboratory, DRDO for his encouragement to bring out this special issue.

**Dr. D. D. Ebenezer**

Naval Physical Oceanographic Laboratory, DRDO, Kochi

**Prof. S. K. Bhattacharyya**

IIT Madras, Chennai

**Dr. Bishwajit Chakraborty**

CSIR-National Institution of Oceanography, Dona Paula, Goa

# Mid-to-High Frequency (6-10 kHz) Measurements of Acoustic Bottom Backscattering

Sreeram Radhakrishnan

Naval Physical and Oceanographic Laboratory, Thrikkakara, Kochi, India  
sreeramr@gmail.com

[Received: 22-09-2016; Revised: 15-04-2017; Accepted: 10-05-2017]

## ABSTRACT

Results and analysis of mid-to-high frequency (6-10 kHz) acoustic bottom backscattering measurements as a function of grazing angle (14-80 degrees) made at a shallow water location in the Arabian Sea off the west coast of India are presented. Measured results are compared with those obtained from bottom scattering models to identify the contributions of interface roughness and sediment volume scattering. Measured results show that backscattering strength increases with increase in frequency and there is only a weak dependence of backscattering strength on grazing angle from 14-25 degrees. However, when grazing angle increases from 25 to 55 degrees, the scattering strength increases by 5-10 dB. Data analysis results combined with interpretive modeling analysis show that the interface roughness scattering is dominant and the bottom mainly consists of hard consolidated sediments.

## 1. INTRODUCTION

When a sound signal is transmitted underwater, it is scattered by the rough sea surface, sediment interface and volume inhomogeneities in the water column. The component of incident energy returned by the sea bottom back to the source is referred to as bottom backscattering and it leads to reverberation in active sonar. Reverberation from the bottom may limit the performance of sonar systems and hence, it is important to know the scattering characteristics of various seafloor sediment types. Sea bottom properties are also required for predictions of mine burial and the detection ranges of sea mines. For sediments composed of silt and clay, the bottom returns are dominated by backscatter from inhomogeneities within the sediment volume whereas for fine sands, both surface roughness and volume inhomogeneities contribute to backscattering. For coarser sediment types, only the surface roughness contributes to backscattering (Jackson and Richardson, 2007). Many studies have been carried out to correlate high frequency (> 10 kHz) bottom reverberation with in-situ sediment properties in shallow waters (Kuo, 1964; Jackson and Briggs, 1992). Haris *et al.* (2011) conducted seafloor sediment characterization studies employing high-frequency multi-beam echo-sounding system at 95 kHz and dual-frequency single-beam system at 33 and 210 kHz in the central part of the western continental shelf of India off Goa. They compared bottom backscattering strength measured across the three frequencies with composite roughness scattering model (Jackson *et al.*, 1986) and found the 95 kHz multi-beam data to be more suitable for sediment characterization in terms of mean grain size and seafloor roughness and sediment volume parameters. La and Choi (2010) present bottom backscattering measurements at 8 kHz for grazing angles ranging from 6-31 degrees made at a shallow water site (~16 m depth) with a silty bottom on the south coast of Korea. From measurements, they estimated

backscattering strengths between -42 and -30 dB and concluded that sediment volume scattering is dominant over scattering from bottom interface roughness at 8 kHz frequency for a silty bottom. These studies show the influence of reverberation on sediment type and how it generally varies with grazing angles and frequency. In this paper, the properties of bottom backscattering are investigated in the mid-to-high frequency range at a shallow water location in the southern part of the western continental shelf of India off Kerala. Bottom backscattering measurements at 6, 8 and 10 kHz frequencies as a function of grazing angle (14-80 degrees) are presented and compared to the predictions obtained from a theoretical backscattering model.

## 2. EXPERIMENTAL DESCRIPTION AND OBSERVATIONS

Monostatic bottom backscattering measurements were made in October 2013 at a shallow water location in the Arabian Sea. Reverberation data was collected in silent ship regime onboard INS *Sagardhwani* anchored in a water depth of 62 m at frequencies ranging from 6 to 10 kHz. Analysis of sediment grab samples collected at the site reveal that the area with water depth ranging from 60 to 80 m is covered with sand. Sandy seafloor is predominant in the Western Continental Margin of India in water depths of 50 -100 m due to the effect of sea level rise (Nair, 1975). The Western Continental Shelf of India features a suite of prominent submarine terraces which are extensive flat surfaces with an average width of about 2 to 4 km. These terraces are prominent between 50 and 150 m water depth (Wagle *et al.*, 1994). For sand, the estimated compressional wave speed varies from 1626 to 1828 m/s. The sound speed profile in the water column was measured with Conductivity-Temperature-Depth (CTD) casts. An M18-C6 spherical transducer from Geospectrum Transducers Inc., Nova Scotia, Canada was deployed at a depth of 50 m onboard INS *Sagardhwani* and used for all the transmissions. At 11.5 kHz, the transmit pattern for the spherical transducer is omnidirectional in the vertical and horizontal directions. The transmitted signals were received using a hydrophone placed at a depth of 53 m to receive signals backscattered from the bottom without any interaction from the sea surface by using a window in the time domain. Depth sensors were attached to monitor source and receiver depths.

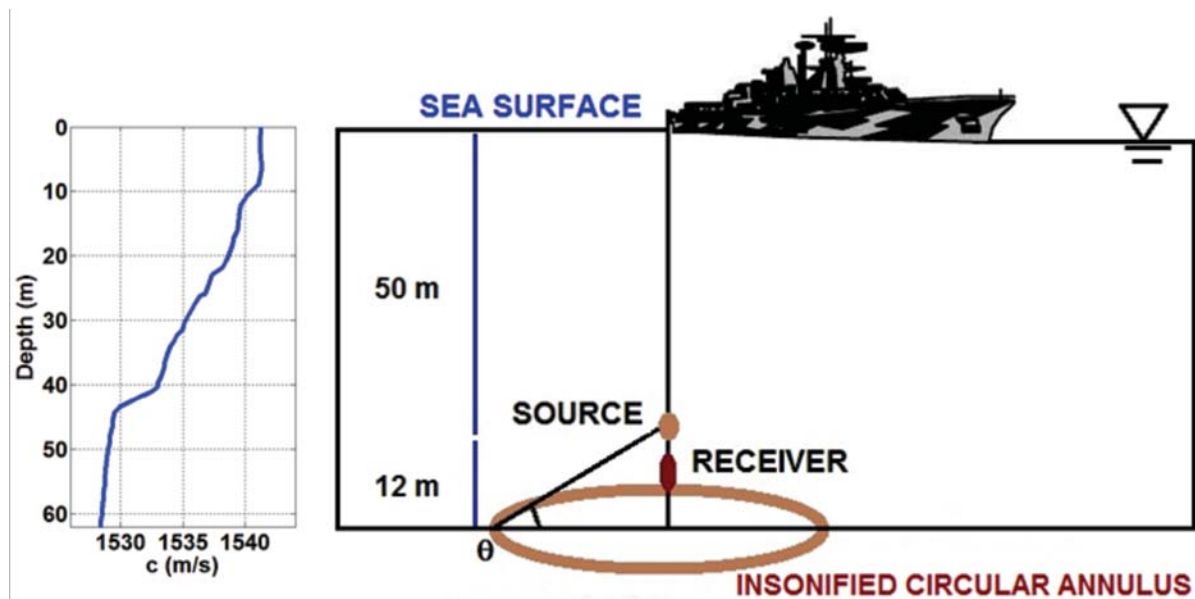


Fig.1. LEFT: Sound speed profile measured by CTD cast. RIGHT: Geometry of the reverberation experiment showing the source, receiver, and insonified circular annulus on the bottom. Source depth is 50m, receiver depth is 53 m, and the water depth is 62m.



The sound speed profile in the water column and a schematic representation of the reverberation experiment geometry are shown in Fig. 1. The signals backscattered from the bottom were received at varying grazing angles before the first fathometric return. CW pulses of length 2 ms were transmitted every 0.5 s at frequencies of 6, 7, 8, 9 and 10 kHz. Each set of received signals was sampled at 49 kHz and band-pass filtered with 1 kHz bandwidth for noise removal. The sound speed profile was uniform for depth greater than 40 m (~1528 m/s) where the measurements were carried out.

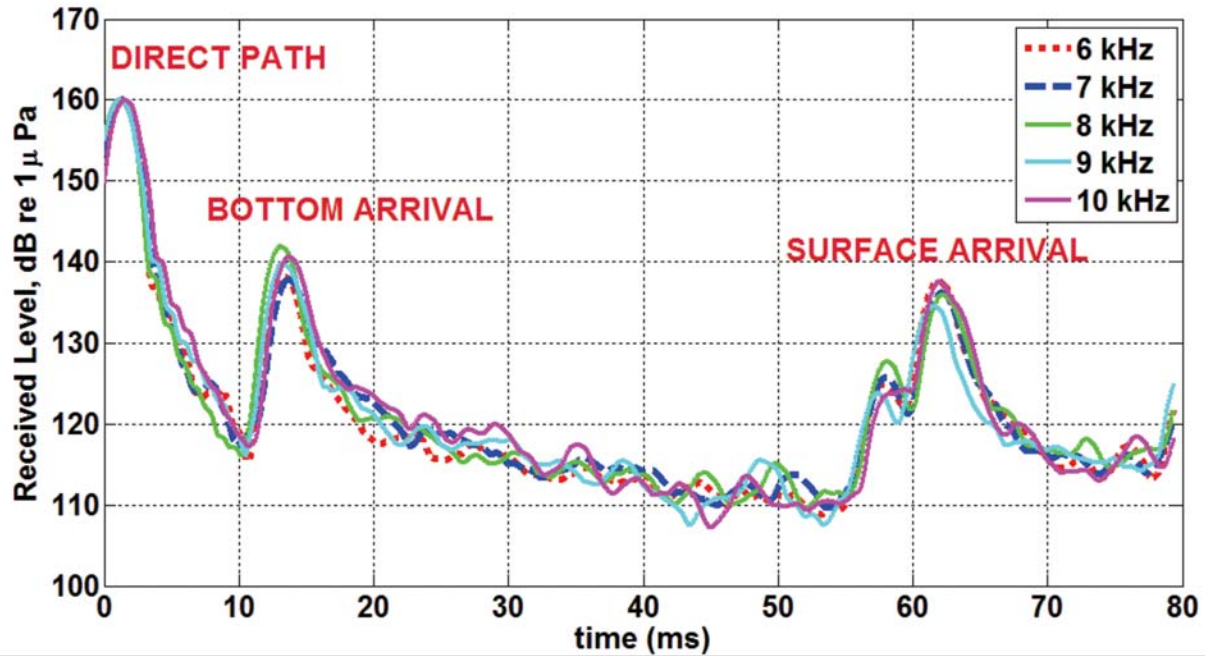


Fig. 2. Averaged intensity of received level at 6-10 kHz frequencies for the configuration shown in Fig. 1. Bottom and surface reflected arrivals are well separated. Direct path received level of the 2 ms CW pulse is normalized to 160 dB re 1  $\mu$ Pa.

Fig. 2 shows the reverberation time series received at the omni-directional hydrophone at 6, 7, 8, 9 and 10 kHz. The data presented here represents an azimuthally averaged intensity level reaching the hydrophone from the insonified circular annulus. In this paper, the reverberation data at 6, 8 and 10 kHz are processed to estimate the bottom backscattering strength. Measurements of ambient noise were carried out in the silent ship regime onboard INS *Sagardhwani* to estimate the background noise floor in preparation for reverberation time series data collection. A 72 dB noise floor was observed at 6 kHz and the reverberation levels were much higher relative to ambient noise during the experiment.

### 3. MEASURED BACKSCATTERING STRENGTH

The sonar equation for estimating the bottom backscattering strength as a function of grazing angle is given by

$$BS(\theta) = RL - 2TL - 10 \log A \quad (1)$$

where  $BS(\theta)$  is the bottom scattering strength in dB re 1  $m^2$  over the insonified area ( $A$ ) at a grazing angle  $\theta$ ,  $RL$  is the received level in dB re 1  $\mu$ Pa,  $SL$  is the source level, and  $TL$  is the one-way transmission loss in dB from the source to the bottom patch corresponding to the grazing angle  $\theta$ .  $TL$  is predicted by estimating

the spherical spreading loss, which is  $20 \log_{10} \left( \frac{c_w \tau}{2} \right)$  where  $c_w$  and  $\tau$  are the compressional wave speed in

water and the two-way travel time to the insonified patch, respectively. Absorption loss is considered to be negligible because the absorption coefficient obtained using the formula suggested by Francois and Garrison (1982) is  $\sim 0.5 \times 10^{-3}$  dB/m for 10 kHz. The insonified area is assumed to be a circular annulus and determined by the beam patterns of the source and receiver (Chapman and Harris, 1962) (Fig. 1).

The bottom backscattering corresponds to the slant range interval of  $c_w \tau / 2$  and the insonified area

$$A = \frac{1}{2} \cos^2 \theta c_w^2 \tau \quad (2)$$

where  $\tau$  is the pulse length of the source signal. However, since the hydrophones are omnidirectional, the data sets are expected to yield only a mean value (averaged over the azimuth) for the backscattering strength. The source level and the receiving hydrophone sensitivity (6-10 kHz band) were measured with error less than  $\pm 1$  dB. The sound speed profile was very stable over the course of the acoustic measurements and hence, the errors arising from the spreading term are less than  $\pm 1$  dB.

#### 4. BOTTOM BACKSCATTERING STRENGTH MODELLING

The bottom backscattering strength, BS is a function of the grazing angle. It is the scattering cross-section in dB and is expressed as

$$BS(\theta) = 10 \log_{10} [\sigma_r(\theta) + \sigma_v(\theta)] \quad (3)$$

where  $\sigma_r(\theta)$  is the backscattering cross-section per unit solid angle per unit area due to interface roughness and  $\sigma_v(\theta)$  is the backscattering cross-section per unit solid angle per unit area due to sediment volume inhomogeneities from below the interface. Typically, the bottom backscattering strength can be estimated empirically using Lambert's law (LL) given by

$$BS_{LL} = 10 \log_{10}(\sin^2 \theta) + 10 \log_{10}(\mu) \quad (4)$$

where  $\mu$  is the bottom scattering cross section associated with the insonified area. For comparing with the measured backscattering strengths,  $10 \log_{10}(\mu) = -27$  dB as reported by Mackenzie (1961) is used. Here the model developed by Gragg *et al.* (2001) is implemented to compute backscattering strength due to interface roughness where acoustic scattering by a random rough interface is modeled based on local small slope theory. Scattering from sediment volume inhomogeneities is computed by a model used by Mourad and Jackson (1989). The present model uses the eight physical parameters as input.

**Table 1.** Definition of parameters used as model inputs

Symbol	Definition
$M_z$	Mean grain size $M_z = -\log_2(d/d_0)$ where $d$ is the grain diameter in millimetres, and $d_0$ is the reference length, equal to 1 mm
$\rho_2/\rho_1$	Ratio of sediment mass density to water mass density
$v_2$	Ratio of compressional wave speed in sediment to sound speed in water, $c_p/c_w$
$c_s/c_w$	Ratio of shear wave speed in sediment to sound speed in water
$\delta$	Loss parameter: Ratio of imaginary wave number to real wave number for the sediment, $\delta = v_2 c_w (\alpha/f) \log_e(10)/40\pi$ where $(\alpha/f)$ is compressional attenuation in sediment expressed in dB/m/kHz and $f$ is frequency in kHz
$\sigma_2$	Ratio of sediment volume scattering cross section to sediment attenuation coefficient
$\gamma_2$	Exponent of bottom relief spectrum
$w_2$	Strength of bottom relief spectrum with units of (length) <sup>4</sup>

Definitions and values of these parameters describing bottom interface roughness and volume scattering are listed in Table 1.

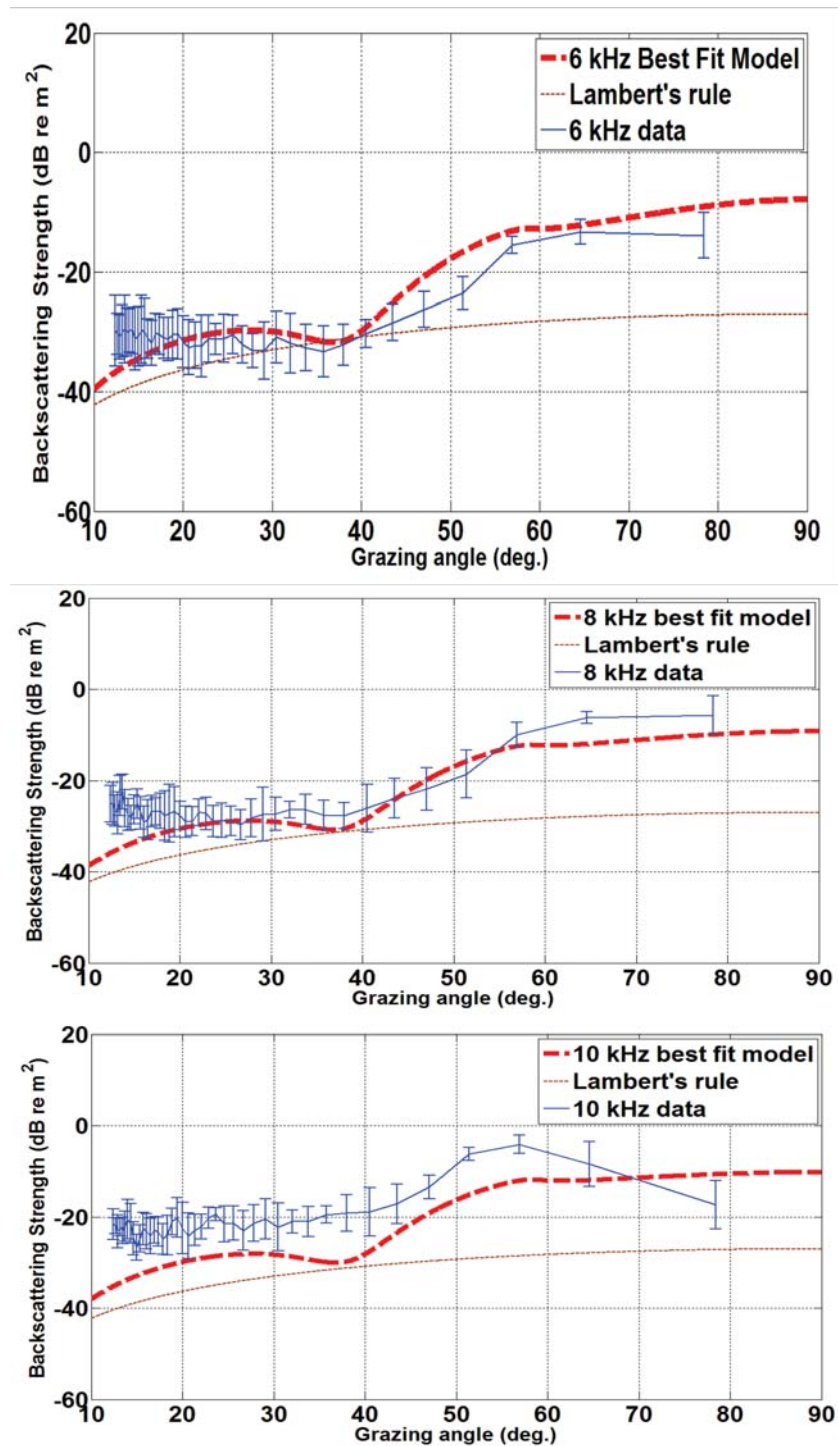


Fig. 3. The measured BBS and the best-fit model at 6, 8, and 10 kHz. Lambert's rule curve (dashed curve) with  $10 \log_{10}(\mu) = -27$  dB is also shown for reference.

## 5. DATA-MODEL COMPARISON

As per measurement geometry, the surface arrivals are expected at a grazing angle of 14 degrees which is evident from the high backscatter with fluctuations around that angle. The reverberation data for grazing angles less than 14 degrees contain the effect of sea surface also. Therefore, in this analysis, data for grazing angles more than 14 degrees is utilized which represents exclusively the effect of the sea bottom.

The measured bottom backscattering strength data and the best-fit model at 6, 8 and 10 kHz are presented Fig. 3. The Lambert's law curve for  $10 \log_{10}(\mu) = -27$  dB is also plotted for reference. The plot of measured data shows mean  $\pm$  one standard deviation which represents an averaged bottom backscattering strength estimate of 15 individual pings transmitted at each of the frequencies. The best-fit model is obtained by fitting the datasets at 6, 8, and 10 kHz to the theoretical model in the least square sense. Different types of sediments and their corresponding bottom interface roughness and volume scattering parameters were used to model BBS. The best-fit corresponds to the model with the least value of mean squared error between the measured and modelled BBS for a given type of the sediment. The bottom interface roughness and volume scattering parameters of the best-fit model are listed in Table 2.

**Table 2.** Best-fit Bottom Interface Roughness and Sediment Volume Scattering parameters

Sediment	$M_z$	$\rho_2/\rho_1$	$c_p/c_w$	$c_s/c_w$	$\delta$		$\sigma_2$	$\gamma_2$	$w_2$
					comp	shear			
Consolidated Sediment	1.5	2.0	1.9 - 0.01i	0.5 - 0.05i	0.043	0.10	0.002	3.3	0.002

At 6 kHz, the measured BBS agrees well in slope and level with model predictions for grazing angles ranging from 15-40 degrees and 55-80 degrees (Fig. 3). The measured backscattering strengths are about 5 dB higher than the best-fit model curve in the grazing angle range of 40-55 degrees. The measured data shows that the compressional critical angle is close to 58 degrees. It can be inferred from the grazing angle dependence of the measured backscattering strengths that the shear wave velocity and attenuation need to be considered for modeling especially, for grazing angles below critical. This is expected for hard consolidated sediments which give rise to shear waves. For the best-fit model, the compressional velocity and attenuation values used for modeling are 2903 m/s and 0.1 dB/m/kHz respectively. The shear wave velocity and attenuation values are 764 m/s and 7.2 dB/m/kHz.

In the best-fit model, the contribution from sediment volume scattering component towards total bottom backscattering strengths at 6-10 kHz is much lower than that of interface roughness scattering which is expected for consolidated sediments. At these frequencies, the depth of acoustic penetration into the seabed is minimal and scattering is effectively a surficial mechanism. The roughness interface scattering is found to be the dominant scattering process as observed from data-model comparisons.

At 8 kHz, the best-fit model agrees well with the measured data for grazing angles ranging from 20 to 55 degrees. However, the model predictions are lower by about 4-8 dB for grazing angles greater than 60 degrees. At 10 kHz, the best-fit model results are lower than the measured data by about 5- 10 dB for all grazing angles. The oscillating features represented by the measured data at 10 kHz, which may be attributed to layering or due to the presence of ripples, lagoons or terraces in the seabed are not fully captured by the theoretical interface roughness model. At this frequency, the peak backscattering value is observed at 55 degrees. The backscattering strength falls off gradually as grazing angle approaches 90 degrees.

## 6. CONCLUSIONS

The measured data shows that the compressional critical angle is close to 58 degrees which corresponds to the sediment type of hard consolidated sediment bottoms. For a hard consolidated sediment bottom, the acoustic interaction is mainly surficial as the depth of penetration is limited in the frequency range of 6-10 kHz. Under such conditions, the interface roughness scattering is expected to be the dominant scattering mechanism. The data is found to be frequency dependent and showed oscillating features which is representative of a layered bottom where the depth of interaction depends on the frequency of transmitted signal. Microtopographical roughness due to a rippled bottom may also result in oscillating values of bottom backscattering strength.

The measured data was compared with modeled backscattering strength based on the theoretical models for interface roughness and volume scattering. The best-fit model is obtained by fitting the datasets at 6, 8 and 10 kHz to the theoretical model in the least square sense. The compressional velocity and attenuation values of the best-fit model are 2903 m/s and 0.1 dB/m/kHz respectively. The corresponding shear wave velocity and attenuation values are 764 m/s and 7.2 dB/m/kHz.

At 6 kHz, measured bottom backscattering strength agrees well in slope and level with model predictions for grazing angles ranging from 15-40 degrees and 55-80 degrees. At 8 kHz, the best-fit model agrees well with the measured data for grazing angles ranging from 20 to 55 degrees. At 6 and 8 kHz, the best-fit model gives good estimates of bottom backscattering strength for a hard consolidated bottom for grazing angles greater than 20 degrees. At lower grazing angles, the depth of penetration increases and the effects of layering become important. The model fails to account for the effect of layering in the sediment bottom.

The model estimates at 10 kHz are about 5-10 dB lower than the measured data. At 10 kHz, it is evident from data-model comparisons that there is a considerable amount of uncertainty associated with the measurements of bottom backscattering strengths. As interface roughness is the dominant scattering process, it is likely that the bottom roughness parameters (strength and exponent of bottom relief spectrum) used for modeling are not accurate and contribute to uncertain backscattering strength estimates.

Actual measurements of bottom relief at the test location were not made during the conduct of the experiment which further adds to the uncertainty in modeling. For improved modeling, analysis needs to be carried out by varying the strength and exponent of bottom relief spectrum. Future work will focus on validating the modeled results using an additional set of measurements carried out at the same location. Also, measurements will also be made to obtain data at lower grazing angles which is not addressed in the present analysis.

## 7. ACKNOWLEDGEMENTS

Author is thankful to Shri. Kedarnath S. Shenoy, Director, NPOL for providing the facilities and encouragement to do the work. Author also appreciates the support and co-operation extended by fellow scientists and the crew of INS *Sagardhwani* that helped in collecting high quality data.

## 8. REFERENCES

- [1] R.P. Chapman and J.H. Harris, 1962. Surface backscattering strengths measured with explosive sound sources. *J. Acoustical Soc. America*. **34**, 405-418.
- [2] R.E. Francois and G.R. Garrison, 1982. Sound absorption based on ocean measurements: Part II: Boric acid contribution and equation for total absorption. *J. Acoustical Soc. America*. **72**, 1879-1890.
- [3] R.F. Gragg, D. Wurmser and R.C. Gauss, 2001. Small-slope scattering from rough elastic ocean floors: General theory and computational algorithm. *J. Acoustical Soc. America*. **110**, 2878-2901.
- [4] K. Haris, B. Chakraborty, C. De, R.G. Prabhudesai and W. Fernandes, 2011. Model-based seafloor characterization employing multi-beam angular backscatter data - A comparative study with dual-

- frequency single beam. *J. Acoustical Soc. America*. **130**, 3623-3632.
- [5] D.R. Jackson and K.B. Briggs, 1992. High frequency bottom backscattering: roughness versus volume scattering. *J. Acoustical Soc. America*. **92**, 962-977.
- [6] D.R. Jackson and M.D. Richardson, 2007. High-Frequency Seafloor Acoustics. Springer-Verlag, New York. Chap., **12 and 13**, 321-376.
- [7] D.R. Jackson, D.P. Winebrenner and A. Ishimaru, 1986. Application of the composite roughness model to high frequency bottom backscattering. *J. Acoustical Soc. America*. **79**, 1410-1422.
- [8] E.Y. Kuo, 1964. Wave scattering and transmission at irregular surfaces. *J. Acoustical Soc. America*. **36**, 2135-2142.
- [9] H.La and J.W. Choi, 2010. 8-kHz bottom backscattering measurements at low grazing angles in shallow water. *J. Acoustical Soc. America*. **127**, EL160-165.
- [10] K.V. Mackenzie, 1961. Bottom reverberation for 530- and 1030-cps sound in deep water. *J. Acoustical Soc. America*. **33**, 1498-1504.
- [11] P.D. Mourad and D.R. Jackson, 1989. High frequency sonar equation models for bottom backscatter and forward loss. in Proceedings of OCEANS '89 (*IEEE, New York*), 1168-1175.
- [12] R.R. Nair, 1974. Holocene sea levels on the western continental shelf of India. *Proc. Ind. Acad. Sci.*, **79**, 197-203.
- [13] B.G. Wagle, K.H. Vora, S.M. Karisiddaiah, M. Veerayya and F. Almeida, 1994. Holocene submarine terraces on the western continental shelf of India; Implications for sea-level changes. *Marine Geology*. **117**, 207-225.

# Effect of multipath propagation on replica correlation processing of linear frequency modulated signals

R.P. Raju and P.V. Nair

Naval Physical and Oceanographic Laboratory, Kochi-682021, India

e-mail: rpraju@npol.drdo.in

[Received: 15.09.2016; Revised: 14.02.2017; Accepted: 29.06.2017]

## ABSTRACT

Active SONARs use Linear Frequency Modulated (LFM) pulse, also known as chirp, of different time-bandwidth (TW) product for detecting underwater targets. Generally, Replica Correlation (RC) is the detection technique used in case of LFM pulses. The shallow water acoustic channel involves multiple paths of propagation that causes time spreading of the transmitted LFM pulse and a reduction in peak energy of RC output which is also termed as Energy Spreading Loss (ESL). The ESL term is part of the degradation factor in the active sonar equation. A one-way acoustic experiment was conducted, at a shallow water site of 45 to 60 m depth, off the East coast of India, to determine the ESL of LFM pulses of different TW product, for a particular source-receiver geometry. It is found that the ESL is proportional to the pulse-width for a LFM pulse of specific bandwidth. The value of ESL is found to be as high as 10.5 dB, in case of a LFM pulse of 600 Hz bandwidth centred at 7.5 kHz.

## 1. INTRODUCTION

An active sonar is used for detecting, estimating range and bearing, and classifying underwater targets. Detection is inhibited by various physical processes such as spreading, scattering and attenuation, that occur during propagation of the acoustic wave through the medium. Active sonars employ different waveforms such as Continuous Wave (CW), Linear Frequency Modulated (LFM) pulse and Hyperbolic Frequency Modulated (HFM) pulse. In shallow water environment or reverberation-limited conditions, active sonars usually employ LFM pulses<sup>1</sup>. LFM/Chirp pulses of different time-bandwidth (TW) products centred at frequencies ranging from 2 to 15 kHz are employed to detect targets in shallow water environment.

A LFM pulse is expressed as :

$$s(t) = A \sin \left\{ 2\pi \left[ f_0 t + 0.5 \left( \frac{w}{T} \right) t^2 \right] \right\} \quad (1)$$

where  $f_0$  is the lower frequency limit of the frequency bandwidth,  $w$  and  $T$  is the pulse width.

The energy level of the transmitted pulse<sup>2</sup>, in dB relative to  $(1 \mu\text{Pa})^2\text{Hz}^{-1}$ , is expressed as :

$$E_t = 10 \log_{10} \left[ \frac{\left( \int p^2(t) dt \right)}{p_{ref}^2} \right] \quad (2)$$

where,  $p$  is the amplitude of the pressure in the far-field and extrapolated to 1 m from the source and  $p_{ref}$  is  $1 \mu Pa$ . The transmitted pulse of energy level,  $E_t$  undergoes loss as it propagates through the medium and the energy level corresponding to the time stretched received pulse  $r(t)$  is given by

$$E_r = 10 \log_{10} \left[ \frac{\left( \int p_r^2(t) dt \right)}{p_{ref}^2} \right] \quad (3)$$

where  $p_r$  is the amplitude of the pressure of the received pulse and  $p_{ref}$  is  $1 \mu Pa$ .

A matched filtering detection process is used by active sonars in association with LFM pulses, which is also termed as replica correlation (RC). The process of RC is mathematically represented as cross correlation of two time-series<sup>3</sup>,

$$R(\tau) = \int_{-\infty}^{\infty} s(t) r(t - \tau) dt \quad (4)$$

It is basically a measure of similarity between the two time series. If one of the time series is shifted in time by  $t'$  then the peak of the cross correlation will be shifted by  $t'$ . The main assumption in simple RC processing is that there is no distortion of LFM pulse after propagation through the medium and interaction with the target. This is not true for any ocean environment, and less so for the shallow water environment. The typical shallow water acoustic channel is characterised by multipath propagation. The multipath propagation leads to time-stretching of transmitted pulses<sup>4</sup>. Energy Spreading Loss (ESL) is a measure of the time spreading in a multipath environment that leads to a reduction in the output peak of the RC processor.

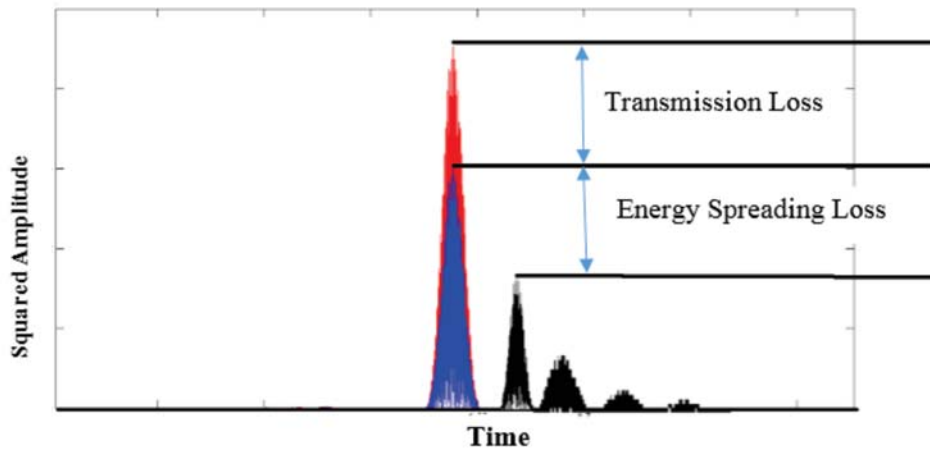


Fig. 1. Schematic Representation of RC output [Red -  $s$  and  $s$ , Blue -  $s$  and  $s_a$ , Black -  $s$  and  $r$ ]

In RC detection processing of received signal, the expectation is that received pulse will be similar to the transmitted pulse and will produce a peak, whereas the noise will not lead to a peak in the output.

An attenuated LFM pulse,  $s_a$  with same energy level as in the received pulse will have an amplitude  $p_a$  given by

$$p_a(t) = \sqrt{\frac{E_r}{E_t}} p(t) \quad (5)$$

The replica correlation of  $s$  (with amplitude corresponding to  $E_t$ ) and attenuated LFM pulse with amplitude  $p_a$  is plotted in figure 1 (Blue). This output represents the ideal RC output, if the transmitted pulse had undergone transmission loss only. The premise used in ideal RC processing is increasingly lost



with medium-induced distortion. Also, the validity of the narrowband approximation for RC processing is lost if<sup>5</sup>,  $T_w^2/f_c \gg 1$ . The replica correlation of  $s$  (with amplitude corresponding to  $E_t$ ) and time stretched received pulse,  $r$  is plotted in figure 1 (Black). The time spreading of the received pulse is seen as time spread in RC output. The RC output of transmitted LFM pulse,  $s$  with itself is plotted in figure 1 (Red). The difference (in dB) in peaks between Red curve and ideal RC output (Blue) is the transmission loss. The peak of the ideal RC output (Blue) is higher than the actual RC output (Black) and the difference between the peaks, in decibel, is the ESL. The ESL is higher if there is no direct path of acoustic propagation between source and the target. The difference (in dB) in peaks between Red curve and actual RC output (Black) is the total loss, which is not accounted for in the active SONAR equation.

The transmission loss is one of the medium-dependent parameters in active Sonar equation. The mono-static active sonar equation is given in terms of Figure of merit (FOM) as<sup>6</sup>

$$FOM = \frac{1}{2}[SL - (NL - DI) - DT + TS] \tag{6}$$

where,  $SL$  is the source level,  $NL$  is the ambient noise level,  $DI$  is the directivity index,  $DT$  is the detection threshold and  $TS$  is the Target Strength. All the terms of (6) are in decibel. Equation (6) is valid for noise limited conditions of target detection. FOM represents the maximum allowable one-way transmission loss for a sonar to detect a target of a given  $TS$ . The degradation in the received pulse in terms of amplitude is accounted for by  $TL$  or FOM. The distortion in the shape and spectrum of LFM pulse in a multipath channel can be accounted for by including a ESL term in the active sonar equation. Hence, the active sonar equation is re-written with ESL as the degradation term as,

$$FOM_a = \frac{1}{2}[SL - (NL - DI) - (DT + 2ESL) + TS] \tag{7}$$

Equation (7) indicates clearly that increase in ESL will lead to decrease in FOM. The decrease in FOM leads to changes in Expected Sonar Range for a given sonar and ocean conditions. In this paper, the Energy Spreading Loss (ESL) of LFM pulse is experimentally determined. Simulation studies on ESL have been carried by Tanaka (1996)<sup>7</sup>. But, these simulation studies on ESL consider CW pulses only. The methodology used by Smith (1998)<sup>8</sup> has been extended to experimentally determine ESL of LFM pulses in this paper.

## 2. EXPERIMENTAL SETUP AND DATA ANALYSIS

An underwater acoustic experiment was conducted off the East coast of India, onboard INS Sagardhwani, at a shallow water site with water depth of 45 to 60 m. The experimental setup (Figure 2) for the study of

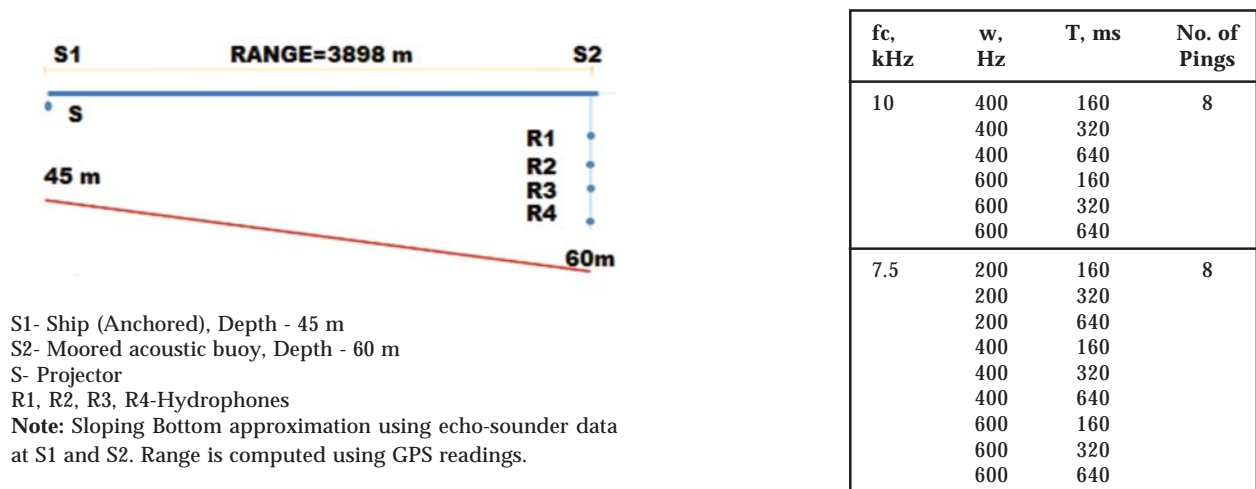


Fig. 2. Experimental set up.

Table 1: Transmission sequence.

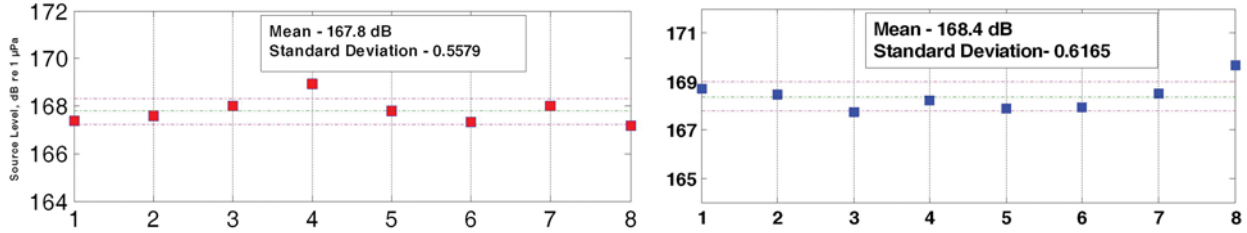


Fig. 3. Measured Source Level of transmitted LFM pulses (SL vs. Ping Number)  
 (a)  $f_c=10$  kHz,  $w=600$  Hz,  $T=160$  ms (b)  $f_c=7.5$  kHz,  $w=600$  Hz,  $T=160$  ms

The received signals are contaminated by noise and other effects. The desired signal is extracted using a band pass filter for 'respective' bandwidths using *sptool* in Matlab<sup>9</sup>. The Energy spreading loss (ESL) at two hydrophones R2 and R3 is computed for each transmission and is plotted as a function of,  $Tw^2/f_c$  (Figure 4 and 5). As shown in equation 7, the ESL is a processing dependent loss term, over and above the TL.

### 3. RESULTS AND DISCUSSION

The active sonar equation<sup>3</sup>, which includes degradation in various terms of the equation as operational degradation factor (DFO) and processing degradation factor (DFP) is given as,

$$FOM = \frac{1}{2}[SL - (NL - DI) - DT + TS - (DF_o + DF_p)] \tag{8}$$

In the absence of measured values, the value of the total degradation ( $DF_o + DF_p$ ) is assumed to be 8 dB for active sonar employing RC detection processing<sup>10</sup>.

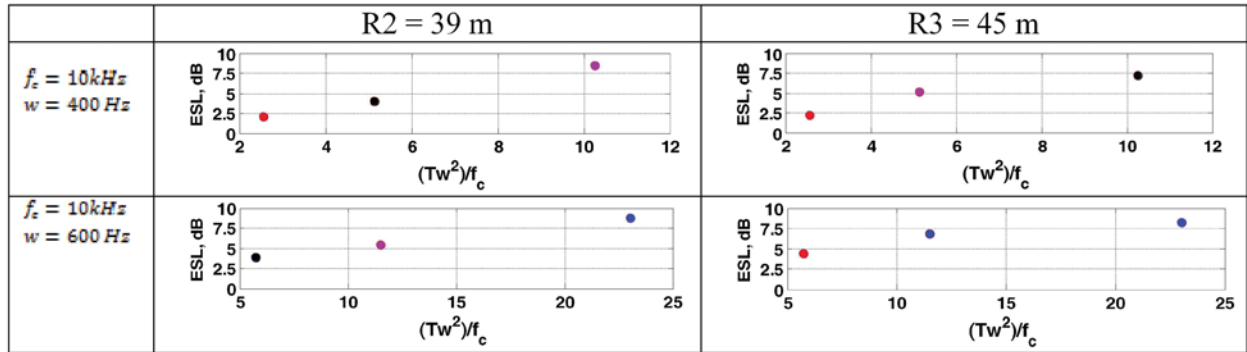


Fig. 4. ESL Plots for 10 kHz LFM pulses of different TWproducts

The degradation due to RC processing using sub-optimum replica (transmitted pulse) manifests as ESL. As seen in figure 4 and 5, ESL value itself is above 5-7 dB in case of LFM pulses with pulse length of 320 ms. The ESL increases as the pulse width of the transmitted LFM pulse increases for a given a bandwidth. This property is seen across all the TW product LFM pulses. The value of ESL varies from 2 to 3.5 dB for a 160 ms LFM pulse centred at 7.5 kHz. The value of ESL is 8.5 dB for 640 ms LFM pulse of bandwidth 600 Hz centred at 10 kHz. The maximum ESL value of 10.5 dB is for 640 ms LFM pulse of bandwidth 600 Hz centred at 7.5 kHz. The increase in ESL with increasing  $Tw^2/f_c$ , leads to decrease in FOM. The experimentally determined ESL at two depths of 39 m and 49 m for this specific shallow water channel is tabulated in table 2.

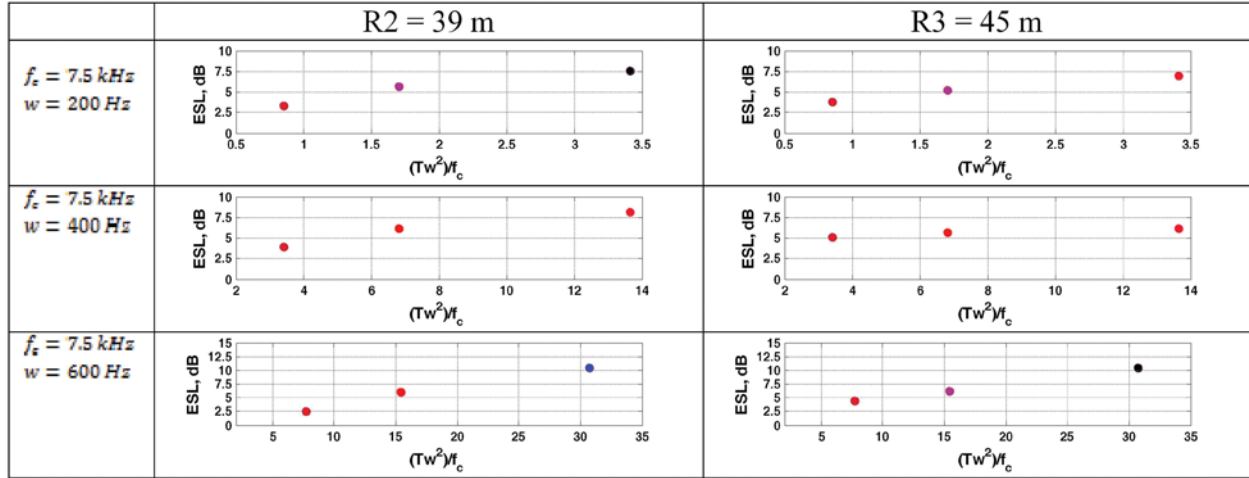


Fig. 5. ESL Plots for 7.5 kHz LFM pulses of different TW products.

fc, kHz	w, Hz	T, ms	ESL, dB	
			R2	R3
10	400	160	2.0	3.3
	400	320	4.0	5.2
	400	640	8.5	7.3
	600	160	3.9	4.4
	600	320	5.5	7.0
	600	640	8.5	8.2
	7.5	200	160	3.3

fc, kHz	w, Hz	T, ms	ESL, dB	
			R2	R3
7.5	200	320	5.7	5.2
	200	640	7.5	7.0
	400	160	4.0	5.1
	400	320	6.1	5.7
	400	640	8.1	6.2
	600	160	2.5	4.5
	600	320	6.1	7.3
	600	640	10.5	10.5

Table 2: ESL at R2 and R3

#### 4. CONCLUSION

The degradation in FOM due to RC processing become prominently higher as TW product of LFM pulse increases. Also, the assumed total degradation value<sup>10</sup> of 8 dB under-estimates the decrease in FOM due RC processing. The degradation of FOM due to ESL has to be considered for robust active sonar design and accurate Sonar performance analysis in shallow water environments. The computational technique described above can be integrated in to SONAR system for *in-situ* computation of ESL for the Ocean environment in which it is operating. The periodic update of ESL in SONAR performance prediction tool will provide a tactical edge during Anti-Submarine Warfare operations.

#### 5. ACKNOWLEDGEMENT

The authors would like to thank Shri S Kedarnath Shenoy, Director, for his encouragement to take up research on ocean acoustic model based detection techniques at NPOL. The authors would also like to acknowledge the encouragement provided by Group Head (Ocean Science) and, Division Head (Ocean Acoustics) and all colleagues from Ocean Science group. The authors would also like to place on record the contribution of the Marine Acoustic Research Ship - *INS Sagardhwani* in conduct of this experiment

## 6. REFERENCES

- [1] Q. Li, 2012. Digital Sonar design in underwater acoustics: Principles and Applications. Springer.
- [2] R.J. Urick, 1983. Principles of Underwater Sound. McGraw Hill Book Company.
- [3] W.S. Burdic, 1991. Underwater acoustic system analysis. Second Edition, Prentice Hall.
- [4] A.V. Vavilin, A.R. Kozel'skii, V.G. Petnikov, V.M. Reznikov and E.A. Rivelis. 1987. Characteristics of dispersion distortions of pulse signals in acoustic waveguides. *Soviet Physics Acoustics*. **33**(5), 481-483.
- [5] J.P. Hermand and W.I. Roderick, 1993. Acoustic Model-Based Matched Filter Processing for Fading Time-Dispersive Ocean Channels: Theory and Experiment. *IEEE Journal of Ocean Engineering*. **18**(4), 447-465.
- [6] A.D. Waite, 2002. Sonar for practicing engineers. Third Edition, John Wiley and Sons.
- [7] A. Tanaka, 1996. An analysis of energy spreading loss associated with tactical active sonar performance in a shallow water environment. Master's Thesis, Naval Postgraduate School, Monterey, CA.
- [8] P.W. Smith, 1998. Model analysis of energy spreading loss off the Carolina coast for tactical active sonars. Master's Thesis, Naval Postgraduate School, Monterey, CA.
- [9] Signal Processing Toolbox, MATLAB®. The Mathworks, Inc.
- [10] R.L. Dawe, 1997. Detection Threshold modeling explained. DSTO-TR-0586.

# Optimum band for passive broadband sonar in surface duct environments

S. Neethu, S. Satheesh Kumar and P.A. Maheswaran

*Naval Physical and Oceanographic Laboratory*

*Kochi-682021, India*

*e-mail: neethu.s@npol.drdo.in*

[Received: 23.09.2016; Revised: 15.04.2017; Accepted: 10.05.2017]

## ABSTRACT

The waters in the oceans are often horizontally stratified with a mixed layer at the top that forms a surface acoustic duct. In sonar applications, it is of primary interest to detect objects that are below the layer and a long distance away. The optimum frequency band in which the detector should operate is determined by the frequency-dependent radiation, the Transmission Loss mosaic, and the location and characteristics of the receiving system. In this paper, the Transmission Loss mosaics for sound radiated by objects is computed using the SCOOTER algorithm package for sound speed profiles that are typically found off the Indian coast. Sound radiation by sources at various depths within and below the layer is studied and used to recommend optimum frequency bands for the detectors that are within or below the layer

## 1. INTRODUCTION

The most effective method for detection of underwater targets makes use of acoustic energy. Sonar (Sound Navigation And Ranging) uses sound to detect and localise underwater targets. Sound undergoes various physical phenomena such as spreading, reflection, refraction, and scattering that depend upon the environmental conditions. Thus the performance of sonar is highly dependent on the environmental conditions and needs to be modelled. The sound speed profile that is the variation of speed of sound with depth is fundamental to all models. The speed of sound depends mainly on temperature, salinity and hydrostatic pressure (a function of depth). A typical deep sea sound speed profile can be divided into four layers (i) surface duct layer where there is a slight increase in sound speed with depth due to increase in pressure whereas the temperature is constant due to mixing of water by the action of wind (ii) seasonal thermocline where the sound speed decreases due to decrease in temperature and is dependent on seasonal variation (iii) main thermocline, where the sound speed decreases with depth due to decrease in temperature and is not affected by seasonal variation and (iv) deep isothermal layer where the sound speed increases with depth due to increase in hydrostatic pressure while the temperature remains constant [1]. If there is a minimum in the sound speed profile between the main thermocline and the deep isothermal layer, the depth at which it occurs is called the SOFAR (SOund Fixing And Ranging) channel axis.

Sound propagates to larger distances in wave guided environments. Surface duct and SOFAR channels are examples of such wave guides. In our environments (around India), the sound speed profiles typically show a negative gradient even at deeper depths and SOFAR channel occurs at depths greater than 1000 m.

Operating sonars at such deeper locations are practically not feasible and hence long range propagation using SOFAR channels are impossible in our environments. Thus surface ducts are the only long range supporting waveguides that can be exploited in our environment.

Sound bends towards regions of lower sound speed when it undergoes refraction. If a source is inside a surface duct, the acoustic energy radiated from it gets trapped in the duct through refraction and surface reflection and propagates to longer ranges. But this is not true for all frequency components of the radiated signal. As with the case of all wave guided propagation, here also there is a low frequency cut-off. Cut-off frequency is defined as the minimum frequency, for a given layer depth, required to trap at least one mode in the surface duct. An approximate formula for cut-off frequency that is arrived at by using simplifying assumptions regarding the sound speed and mode function is

$$f = \frac{23000}{H^3 g} \quad (1)$$

where  $H$  is the duct thickness and  $g$  is the average sound speed gradient inside the duct [2]. The depth of the surface duct is the depth below the surface at which the sound speed reaches its first local maximum.

Acoustic energy emitted by a broadband source at frequencies well-below the cut-off frequency is not affected by the presence of the duct and does not propagate to longer ranges. However, energy at frequencies well-above the cut-off frequency is ducted and propagates to longer ranges.

When the source is below the layer, almost the entire acoustic energy refracts down and horizontal propagation of acoustic energy is limited. Thus irrespective of whether the source is in the layer or below the layer, detection of distant targets below the layer is very challenging. Exploring the possibility of an optimum band and an optimum depth of operation for passive sonar to get maximum detection range for below-layer targets is given utmost importance in this paper.

Several authors discuss optimum frequency of propagation or optimum sonar operating frequencies. Zhou *et al.* [3] focus on optimum frequency for acoustic propagation in shallow water. Their work concentrates on the effect of non-linear frequency dependence of sea bottom attenuation on optimum frequency. Jensen *et al.* [4] discuss the dependence of optimum frequency on sound speed profile and water depth in shallow water environments. Stewart *et al.* [5] discuss the method of determination of optimum frequency for active sonars by maximizing the echo-to-noise ratio. Matika *et al.* [6] focus on the optimization of frequency range for detection of acoustic signals based on the research on sea noise and noise of vessels. There are various papers on Matched Field Processing (MFP) and model based matched filtering [7], but they require three-dimensional sound speed information. However, this is rarely available and these processors have limitations in ocean acoustic applications.

Passive sonar receives and processes the sound radiated from targets. Two types of processing can be done on the received signals - narrow band processing for identifying the tonals and broadband processing for a broad frequency range. The present work started with the idea of exploiting the frequency dependent response of the surface duct and to arrive at an optimum band for passive broadband processing for a target in-layer or below the layer. The optimum band depends on the radiated noise level, Transmission Loss, and directivity index or array gain of the receiving sonar across the receiving frequency band. Among these, the deciding parameter is the Transmission Loss. The objective of present work is to find such an optimum band, if it exists, based on the Transmission Loss estimate.

## 2. METHODOLOGY

The surface duct shows seasonal and diurnal variations. In Indian waters, there can be no layer at times and at other times it can be as deep as 120 m. Three different representative surface-duct environments are chosen for the present study : (1) a 30 m surface duct profile taken from the climatology of off-Mumbai region, (2) a 50 m surface duct profile taken from the climatology of off-Kochi region and (3) an 80 m surface duct profile collected from off-Kochi region

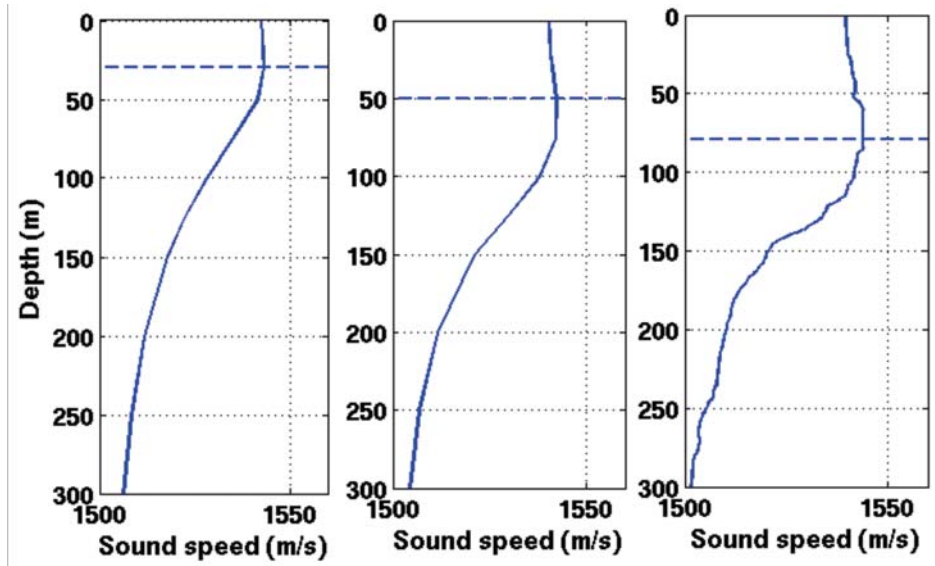


Fig. 1. Sound speed profiles considered for the present study. The dotted lines indicate layer depth.

In all the cases a 1000 m deep, range-independent water column environment is considered. The sound speed profiles up to 300 m of water column depth for the three environments are shown in Figure 1. The cut-off frequencies of the above three environments are 965 Hz, 335 Hz and 150 Hz respectively. The sea state is assumed to be 2. A very soft sediment half space is assumed in order to reduce the effect of bottom. Study is carried out using simulation of frequency dependent Transmission Loss for two different source depths: 20 m and 100 m.

In this study, three different situations are considered: (i) The source and the receiver are in the layer (ii) The source and the receiver are below the layer (iii) The source is in the layer and the receiver is below the layer. Due to reciprocity, the TL in the third situation is the same as that when the source and receiver positions are interchanged.

It is sufficient to do the analysis in a frequency band that starts at about one third of the cut-off frequency of the profile under consideration and ends at three times the cut-off frequency. Frequencies outside this band are not considered as the propagation of acoustic energy at lower frequencies is not affected by duct and that at higher frequencies is mostly confined to the region in which the source is located (in the layer or below the layer). However, for convenience, all the results are presented in the 50 to 3000 Hz band.

### 3. RESULTS AND DISCUSSIONS

#### 3.1 Transition band

The optimum band for processing is inferred from the computed Transmission Loss. There are different approaches for modelling Transmission Loss in underwater environments. Parabolic and ray based approaches are approximation to the wave model. BELLHOP [8], a ray based model, is not considered for our study as it fails to model Transmission Loss for low frequencies (less than or near to cut-off frequency) in shallow duct environments. Several parabolic equation based models are available, but these forward marching models are not computationally efficient choices for modelling long range propagation of the order of 50 km in range independent environments. KRAKEN and SCOOTER [8] are wave theory based models in which the former is a normal mode model. It is computationally efficient compared to SCOOTER in environments where water trapped modes are dominant (modes that have phase speed less than compressional sound speed of the sediment). Since our environment is assumed to be a water column over

an absorptive sediment half-space, this is not chosen. Hence the Transmission Loss mosaics for particular sonar-target geometry are computed in the frequency range of 50 - 3000 Hz by using SCOOTER. In FORTRAN-based SCOOTER, the acoustic field is computed by using wavenumber integration in the radial direction and finite elements along the depth. Transmission Loss curves for the Environment 1, with both the source and receiver at a depth of 20 m (both in-layer) for ranges 10 km, 20 km, 30 km, 40 km and 50 km across the frequency range are shown in Figure 2(a). The cut-off frequency for this environment is 965 Hz and it is indicated by a dotted line in the Figure. The Transmission Loss values at frequencies below cut-off frequency are much greater than that at frequencies above cut-off frequency. The decrease in Transmission Loss is not abrupt but happens over a range of frequencies which is roughly 800 - 1700 Hz in this case. When the range increases, the slope of the frequency-dependent TL is steeper in the neighbourhood of the cut-off frequency. Transmission Loss curves for a below-layer receiver at 40 m depth and for ranges 6 km, 8 km and 10 km are shown in Figure 2(b). There is a nominal minimum for the Transmission Loss curves around the cut-off frequency in the range of 800 - 1700 Hz which is the transition range for an in-layer receiver.

Transmission Loss curves for the Environment 2 with both the source and receiver at a depth of 20 m (both in-layer) for ranges 10 km, 20 km, 30 km, 40 km and 50 km across the frequency range are shown in Figure 3(a). Here the cut off frequency is 335 Hz. Significant reduction in Transmission Loss values is observed for frequencies above cut-off frequency and it is more prominent for longer ranges. The transition range in this case is around 200 - 400 Hz. Transmission Loss curves for source depth of 20 m and receiver depth of 75 m (below-layer) for ranges 6 km, 8 km and 10 km across the frequency band are shown in Figure 3(b). A prominent minimum of the Transmission Loss curves can be observed in the transition range. The Transmission Loss oscillates for higher frequencies (approximately more than 1 kHz in this case) due to interference of modes that are trapped in the surface duct. Transmission Loss curves for in-layer (20 m) and below-layer receivers (100 m) for Environment 3 that has a cut-off frequency of 150 Hz, when the source is at 20 m are presented in Figures 4(a) and 4(b). Here also similar results are obtained. Significant reduction in Transmission Loss values is observed for higher frequencies and the transition range is 150 - 300 Hz for an in-layer receiver. For below-layer receiver, Transmission Loss minimum can be noticed in the range 150 - 300 Hz. The Transmission Loss curves for all the three profiles across the frequency range for both source and receiver in-layer (20 m) and at range 25 km are shown in Figure 5(a). Respective cut-off frequencies are also indicated using dotted lines. The reduction in Transmission Loss values is very prominent for Environments 2 and 3 whereas in the case of Environment 1, even though there is a reduction in Transmission Loss values above cut-off frequency, it is about 20 dB higher than that in the other two cases. Figure 5(b) is also a comparison of Transmission Loss values for the three profiles, but for a below-layer receiver at a depth of 100 m and range 10 km. In this figure, clear minimum is noticed for Environments 2 and 3 while there is only a nominal minimum for Environment 1 in the transition range of frequencies.

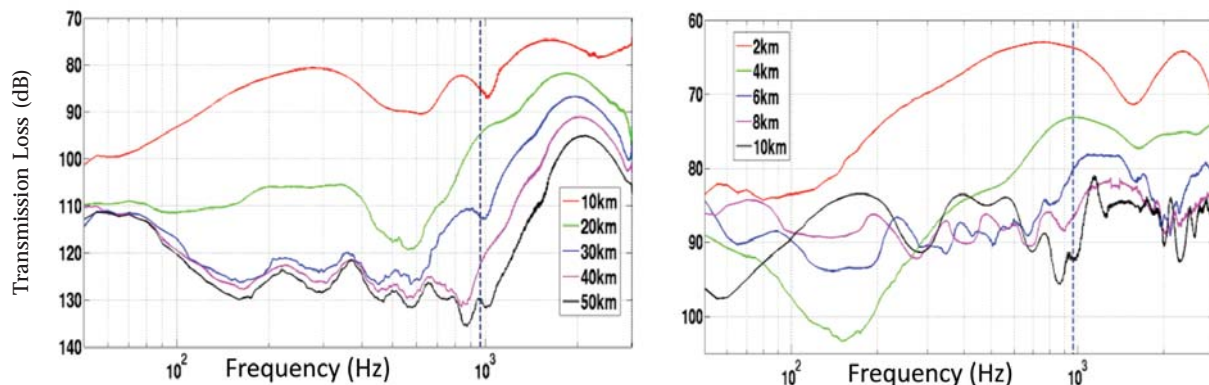


Fig. 2. Transmission Loss in Environment 1 for a source at 20 m. The receiver is at (a) 20 m (in-layer) and (b) 40 m (below-layer).



Optimum band for passive broadband sonar in surface duct environments

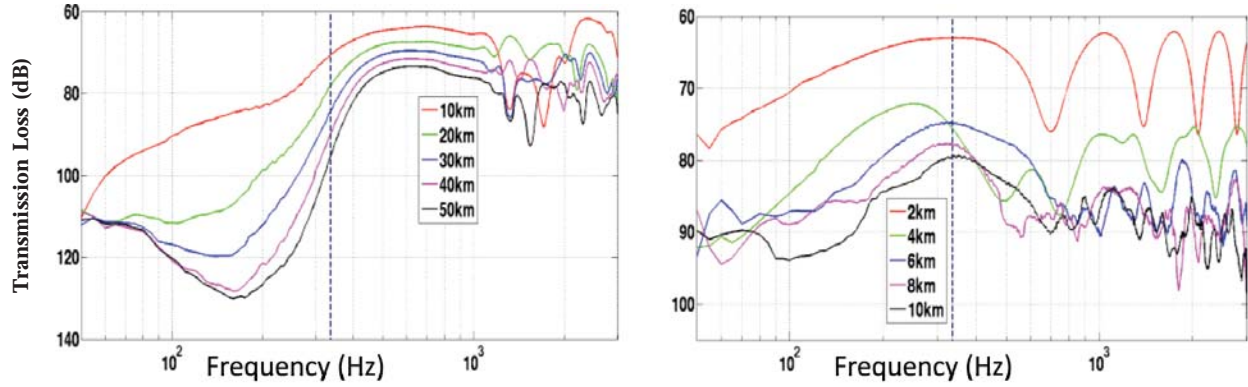


Fig. 3. Transmission Loss in Environment 2 for a source depth of 20 m. The receiver is at (a) 20 m (in-layer) and (b) 75 m (below-layer).

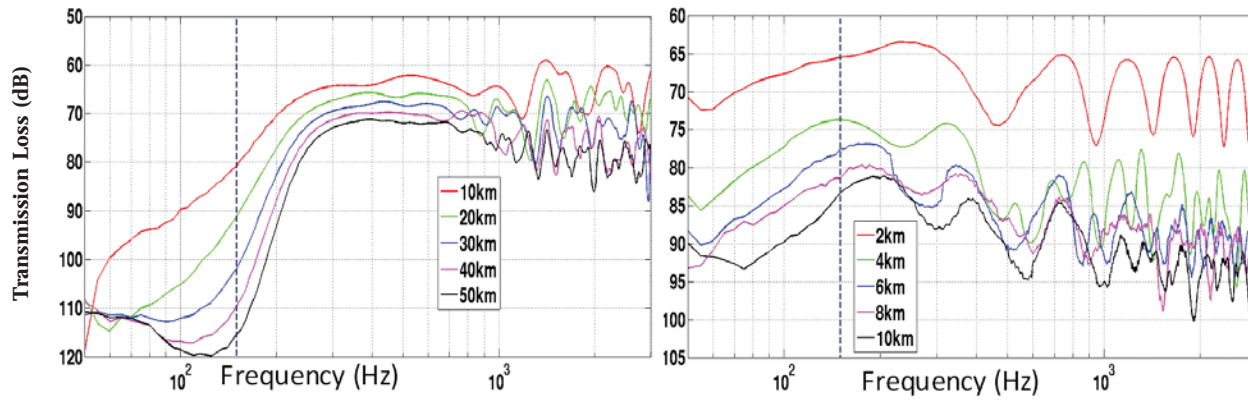


Fig. 4. Transmission Loss in Environment 3 for a source depth of 20 m. The receiver is at (a) 20 m (in-layer) and (b) 100 m (below-layer).

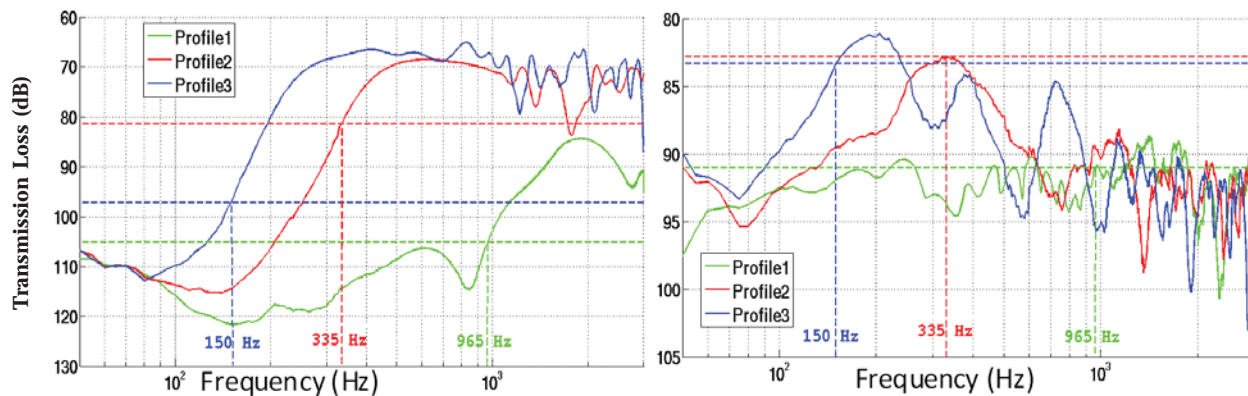


Fig. 5. Transmission Loss curves across the frequency band 50 – 3000 Hz for all the three environments for receiver depths of (a) 20 m (in-layer) & range 25 km and (b) 100 m (below-layer) & range 10 km. The source is at a depth of 20 m.

This study clearly brings out the presence of a transition frequency band that is approximately one octave wide through which the ducting of energy gradually progresses. Cut-off frequency can lie anywhere in the transition range since it is only an approximate value. It is also noticed that the transition is steeper for longer ranges.

### 3.2 Source in surface layer and receiver below the layer

It is also observed that there is a reduction in Transmission Loss values for frequencies in the transition band, when the receiver is just below the surface duct. This is due to diffraction of acoustic energy out of the duct which is significant for frequencies in the transition band. This is illustrated in Figure 6. Transmission Loss mosaics for three different frequencies 100 Hz, 335 Hz (cut-off frequency) and 750 Hz for Environment 2 (layer depth 50 m) are shown in the figure. The dotted line indicates a below-layer depth of 75 m. It is seen from the figure that for frequencies below cut-off frequency, most of the acoustic energy goes down and long range detection is not possible for both in-layer and below-layer depths. For frequencies near cut-off frequency some part of the energy gets diffracted from the surface duct and hence a reduction in Transmission Loss values is observed for below-layer depths. For frequencies above cut-off frequency, most of the energy is concentrated in the surface duct and here also long range detection is not possible when the receiver is below the layer.

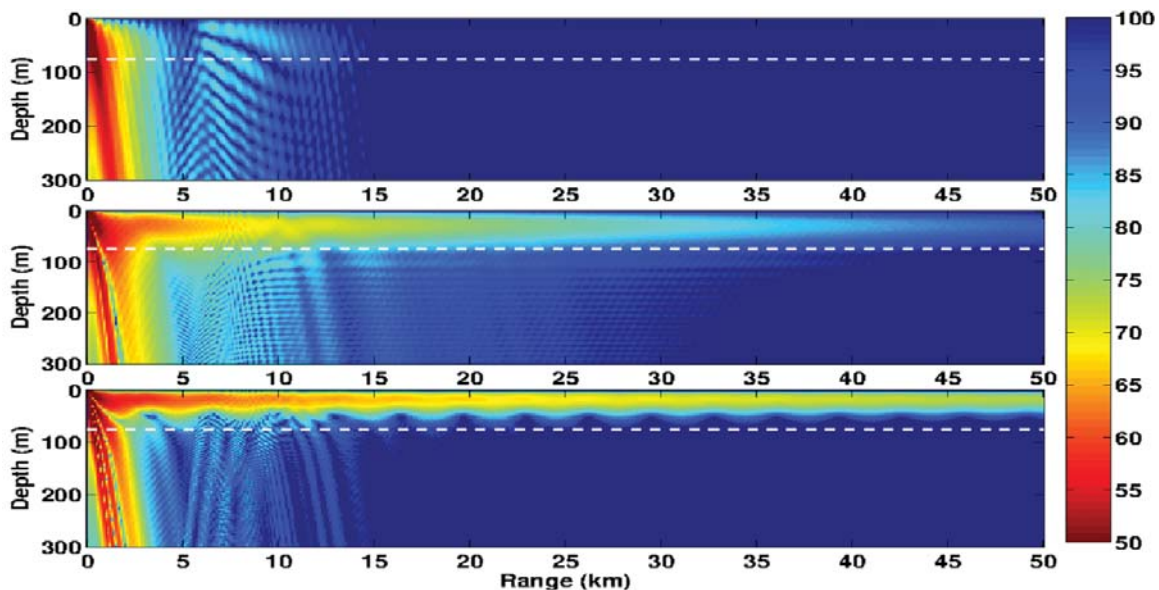


Fig. 6. Transmission Loss mosaics for a source at 20 m in the case of Environment 2 for three different frequencies 100 Hz, 335 Hz and 750 Hz (below, equal to and above cut-off frequency).

### 3.3 Source and receiver below the layer

Transmission Loss mosaics for three different frequencies 100 Hz, 335 Hz (cut-off frequency) and 750 Hz for the Environment 2 are shown in Figure 7. Both source and receiver are at a depth of 100 m and is indicated by the dotted line in the Figure. It is seen that irrespective of the frequencies, major portion of the acoustic energy refracts down and long range horizontal propagation is not possible. The interference pattern occurring in the range 5-11 km is due to bottom bounce. Neglecting the effect of bottom bounce, it is seen that the horizontal reach of the acoustic energy is about 5 km in all the three cases and detection ranges more than 5 km is not possible in this Environment when both the source and receiver are below the layer.

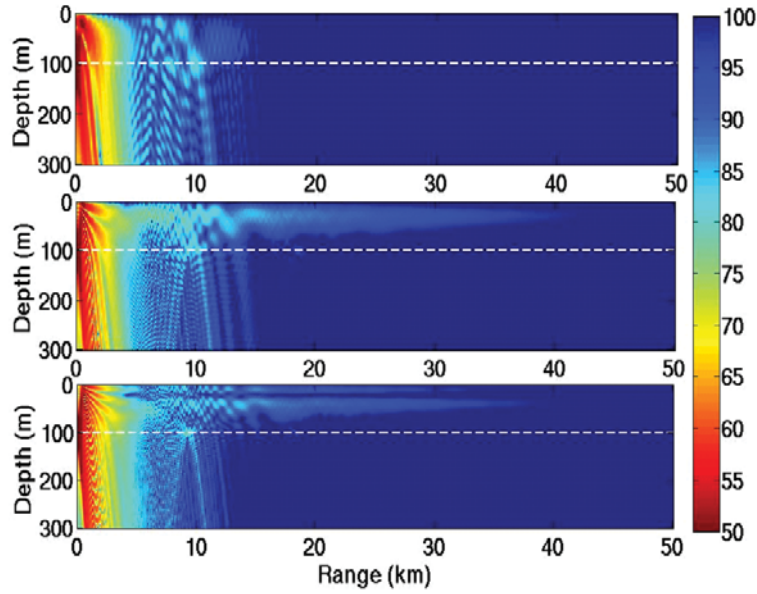


Fig. 7. Transmission Loss mosaics for source and receiver at 100 m in Environment 2 for three different frequencies 100 Hz, 335 Hz and 750 Hz (below, equal to and above cut-off frequency).

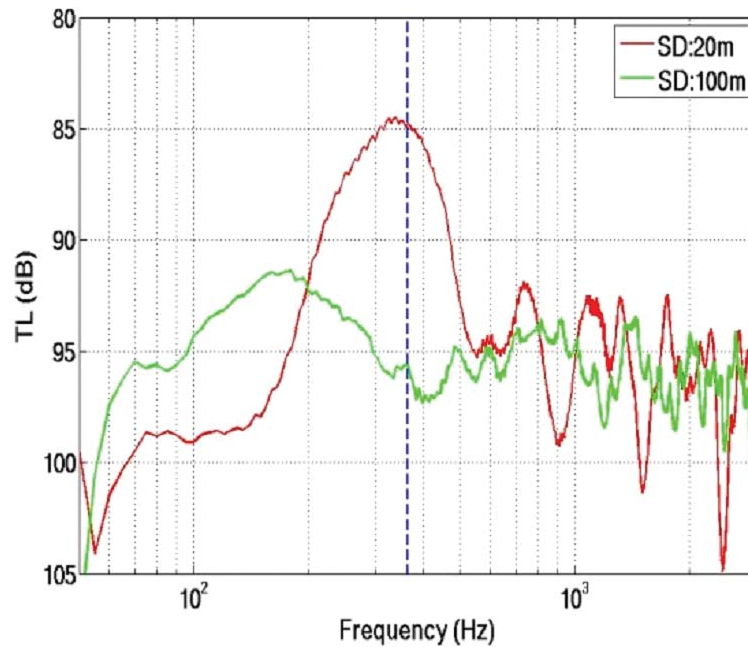


Fig. 8. Transmission Loss curves for range 12 km and depth 100 m for two source depths - 20 m and 100 m in the case of Environment 2

Transmission Loss curves for a receiver range of 12 km (where interference effect is not present) and depth of 100 m for two source depths, 20 m and 100 m, are shown in Figure 8. It is noticed that for source depth of 20 m, there is a significant reduction in Transmission Loss values in the transition band whereas no such reduction is noticed when the source is at 100 m. This indicates that in-layer source depths are advantageous than below layer depths when the receiver is below the layer.

### 3.4 Optimum band for broadband processing

The Transmission Loss results presented above give a clear indication that there is an optimum band for passive broadband processing in a surface duct environment. The optimum band for in-layer receiver lies in the higher side of the cut-off frequency or just after the transition band and detection ranges can be more while processing in the optimum band with source in the layer. For a below-layer receiver, the optimum band lies in the transition band and here too the source needs to be positioned at in-layer depths.

## 4. CONCLUSION

The study based on the modelled Transmission Loss for three different shallow duct environments shows that, in a layered environment, there exists an optimum band for broadband processing that can give maximum detection range. This study brought out the presence of a transition band, the band of frequencies through which ducting of energy progresses. This transition band is one octave wide about the cut-off frequency. The diffraction of acoustic energy (that is, leakage of ducted acoustic energy) peaks in the transition band. This makes the transition band as the optimum band of operation for targets just below the layer while operating sonar in-layer. When sonar is also below the layer, detection of a below-layer target is restricted to few kilometres range in our region, neglecting bottom bounce detection. Thus detection of below layer target through passive broadband processing is found to be effective while operating sonar at in-layer depths. For an in-layer target, maximum detection range is possible while operating sonar in-layer and the optimum band lies in the higher side of cut-off frequency (or more clearly, right side of the transition band).

## 5. REFERENCES

- [1] F.B. Jensen, W.A. Kuperman, M.B. Porter and H. Schmidt, 2001. "Computational Ocean Acoustics", Second Edition, Springer, Chapter 1.
- [2] A.C. Kibblewhite and R.N. Denham, 1965. "Experiment on Propagation in Surface Sound Channel," *Journal of Acoustical Society of America*.
- [3] Ji-xun Zhou, Xue-zhen Zhang and Peter H. Rogers, 1987. "Effect of frequency dependence of sea-bottom attenuation on the optimum frequency for acoustic propagation in shallow water," *Journal of Acoustical Society of America*, **82**(1), 287-292.
- [4] F.B. Jensen and W.A. Kuperman, 1983. "Optimum frequency of propagation in shallow water environments," *Journal of Acoustical Society of America*, **73**(3), 813-19.
- [5] J.L. Stewart, E.C. Westerfield and M.K. Brandon, 1961. "Optimum frequencies for active sonar detection," *Journal of Acoustical Society of America*, **33**, 1216-1222.
- [6] D. Matika, Z. Vukic and D. Pavlekovic, 2000. "Optimization of the frequency range for detection of acoustic signals in the Adriatic Sea," *IEEE OCEANS 2000*, 1037-1042.
- [7] H.P. Bucker, 1976. "Use of calculated sound fields and matched field detection to locate sound sources in shallow water," *Journal of Acoustical Society of America*, **59**, 368-373.
- [8] M.B. Porter, 2010. "Acoustic Toolbox," <http://oalib.hlsresearch.com>.

# Real-time enhancement of climatological temperature profile using *in-situ* profile

P. Anand

Naval Physical and Oceanographic Laboratory, Kochi-21  
e-mail: anandp@npol.drdo.in

[Received: 29.09.2016; Revised: 01.07.2017; Accepted: 16.07.2017]

## ABSTRACT

Accurate temperature and salinity profiles are important inputs required for Anti-Submarine-warfare operations at sea. Estimates of the oceanic conditions required for simulating acoustic propagation can be obtained either from climatology or *in-situ* data. But, climatologies are generally available in coarse grids and may not always represent true conditions. The best source of reliable local information is *in-situ* observations. However, the oceanic conditions at a remote location may not be readily available during an operation. Hence, there arises a need to estimate the condition at distant points. A method is implemented to enhance climatological temperature profile at a remote point by estimating the difference between it and the actual profile. The method is tested in Indian waters using the data collected in the South-Eastern Arabian Sea for different seasons viz. Pre-monsoon (April) and Summer monsoon (July). The enhanced-profile is found to be in better agreement with the *in-situ* data than climatology.

## 1. INTRODUCTION

Accurate ocean thermal structure information is essential for anti-submarine warfare (ASW) operations. Estimates of ocean conditions that are used to generate sound velocity profiles and acoustic range predictions can be obtained either from in-situ measurements, climatology, or ocean models. Climatology is a long term average of temperature profiles at grid points that are 15 nautical miles apart. The best possible source of information for any ASW application at sea is the in-situ measurement. These present or true temperature profiles at points of interest that are used to estimate the sonar range. However, it is not practical to simultaneously measure the in-situ profiles at several grid points. Pollak (1984) presents a method to estimate the present profiles using climatological data and one in-situ measurement. In this paper, this method is used to predict the profiles at several grid points on a track in the Arabian Sea. These estimated profiles are then compared with the profiles measured. This type of estimations are used in the Expanded Ocean Thermal Structure analysis (EOTS) (Holl *et al.*, 1979) which is run daily at Fleet Numerical Oceanography Center (FNOC), USA. Various other methods of extrapolation are also used. Simple methods such as used by Druyan (1972) involve assigning values to grid points by weighting the observation inversely proportional to the square of the distance from the grid point. Other more sophisticated methods require the use of a "trial value" at any arbitrary location (Kruger, 1969). In these applications, the deviation of the trial value from the observation is multiplied by a weighting factor before adding to the trial value (climatology) at the extra polated position. These types of analyses differ according to the scheme used in determining the weighting factor.

Naval ships at sea may not have a large number of observations available to generate a regular network of representative values for its operational area. Thus, utilizing a single observation to estimate oceanic conditions at distant locations is a desirable approach. The simple method of enhancing climatology described is really a special case of optimal interpolation where only one observation is used.

## 2. DATA AND METHOD

### 2.1 Data

The data used in this study is along a single track off Kochi (10°N) collected on-board INS Sagardhwani for different seasons using Conductivity-Temperature-Depth Profiler (CTD). The climatology profile is sourced from World Ocean Database (2009). As the study region (Fig. 1) shows higher variability of the oceanic properties in the shallow-water region (depth < 200 m) than in the deep-water region (depth > 200 m), study is carried out separately for the two regions. The shallow and deep water stations where measurements are done at 5 and 15 nautical mile intervals, respectively. Climatological data is available at grid points that are 15 nautical miles apart. The climatology profile used in simple enhancement is taken from the grid point that is closest to the station at which the in-situ measurement is done. In both the regions, the centre profile is taken as the base for enhancement and stations on both sides are used for validation.

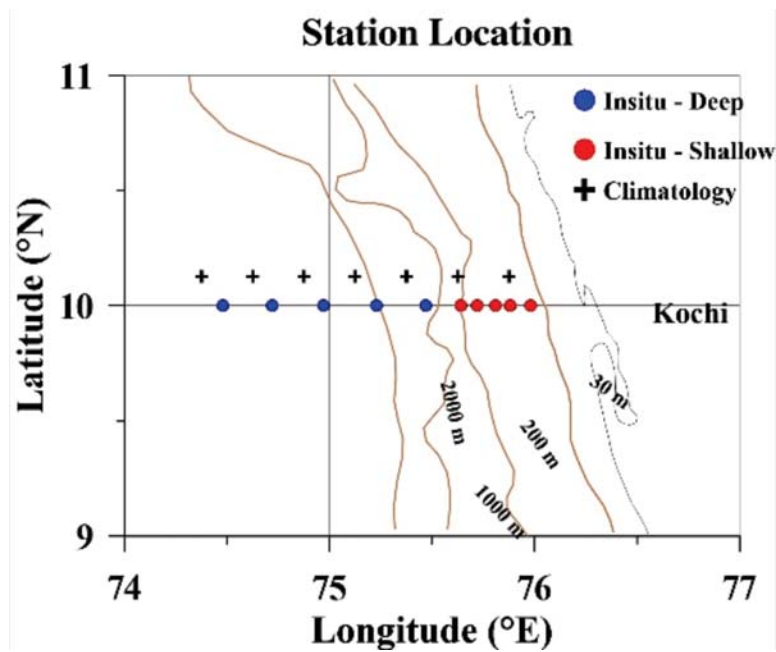


Fig. 1. Study Region

### 2.2 Simple enhancement

A single observation,  $T_m(r)$ , at position  $r$  can be used to enhance the climatology,  $C(x)$  at some other location,  $x$ , by the following formula:

$$C_e(x) = C(x) + [T_m(r) - C(r)] \quad (1)$$

where  $C_e$  is the enhanced climatology

The accuracy of ocean thermal structure estimates obtained using simple enhancement depends a great deal on the homogeneity of the oceanic region under consideration. Equation (1) provides a convenient

means of enhancing climatology using an observed anomaly. These statistical results give only a crude indication of the horizontal space scales for which simple enhancement may be useful in ASW applications, *i.e.*, several hundred kilometres or more. Large errors would be expected when extrapolating an observation across the boundary of such an anomaly to obtain an enhanced temperature profile. The real skill may become more apparent in depicting a "representative" temperature profile for a given region. This may be more appropriate for ASW applications. It is of significance that active sonar systems with typical ranges of 30-40 km make an implicit assumption that the ocean is homogeneous over these ranges. Thus, range-independent acoustic models usually use a sound velocity profile at a single point. Due to internal waves and other small scale fluctuations, an observation of a temperature profile at a single point may not be representative. Here, the point can be made that the usefulness of simple enhancement will depend on the type of application for which it will be used.

CTD data from the centre station is used to provide "locally observed" temperature profile. The anomaly of this temperature profile with the climatology profile for the same region is then calculated. With this deviation known for the one station, the enhanced profiles for the adjacent stations are computed using Eq. (1). The results are evaluated for the adjacent two points, East and West of it. The test was done for two different seasons *viz.* Pre-monsoon (April) and Summer monsoon (July). The study was conducted for both offshore (Depth > 200m) and shallow (Depth < 200m) stations separately. The results are discussed below.

### 3. RESULTS AND DISCUSSION

#### 3.1 Pre-monsoon Season

During the period of April where the sea surface is warm and winds are weak, the difference between the climatology and *in-situ* surface temperatures are, in general, very small. But, in the thermocline, the changes are evident. The method was tested for deep as well as shallow stations. Fig. 2(a) shows the comparison of the profiles *viz.* climatology of the location, *in-situ* collected data and enhanced profile. Fig. 2(b) shows the anomaly of the *in-situ* with climatology and enhanced.

In the case of deep stations, from Fig. 2(a), it is evident that the enhanced profile is closer to the *in-situ* measured profile. The error is less than 1°C in the upper 100 m whereas it increases with increase in depth. In the thermocline region the error is slightly higher (>1°C and <1.5°C). But at all levels the enhanced profile is much more realistic than climatology. In the thermocline region it can be seen that the enhanced profile is more than 1°C closer to the *in-situ* profile (Fig. 2(b)). Below 200 m, as the depth increases, the error

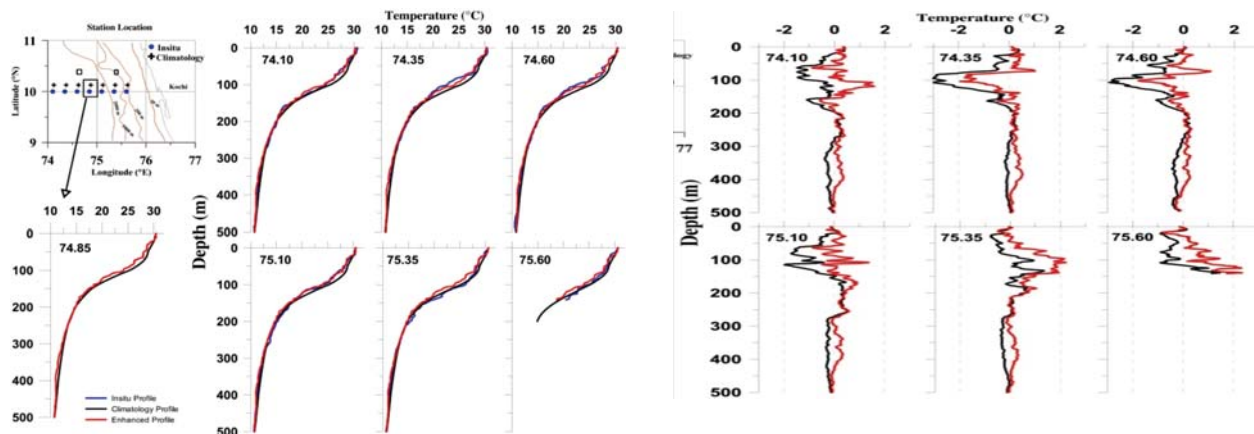


Fig. 2(a). Comparison of the *s viz.* Climatology, *in-situ* data and enhanced profile for the deep stations.

Fig. 2(b). anomaly of the *in-situ* with climatology (dashed black line) and enhanced (solid red line)

decreases in both climatology and enhanced profile. It is also noticed that, the anomaly increases as we move away from the chosen 'local point'.

In case of shallow stations, the results are very much different. In the four stations taken for testing, two of the stations which are on the offshore side of the 'local point' seem to be departing from the in-situ data in a much larger way than that of climatology (Fig. 3(a)). The enhanced profiles for the other two stations which are towards the coast are observed to be more realistic than that of climatology. The error is very less ( $< 2^{\circ}\text{C}$ ) in the upper 20m. Below 20m depth, the error seems to be slightly high ( $> 0.25^{\circ}\text{C}$  and  $< 0.5^{\circ}\text{C}$ ) (Fig. 3(b)).

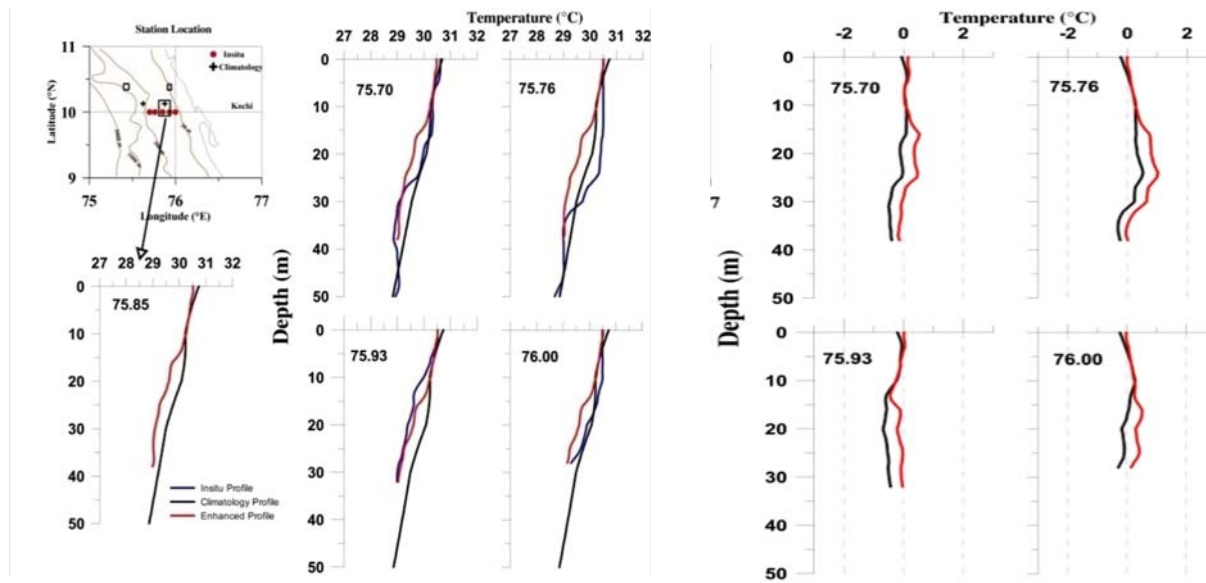


Fig. 3(a). Comparison of the *s viz.* Climatology, *in-situ* data and enhanced profile for the shallow stations.

Fig. 3(b). anomaly of the *in-situ* with climatology and enhanced.

### 3.2 Monsoon Season

In the case of monsoon season, where the sea is quite active and mixing is high, it is difficult to obtain good agreement between the in-situ profile and one based on statistics. There is a significant difference between the in-situ profile and that based on climatology even at a depth of 40m. A difference of  $2^{\circ}\text{C}$  is noticed at the central location where the profile is chosen for enhancement

In the case of deep stations, it is noticed that, in most of the stations, the enhancement of the profiles seems to be better than the climatology. Even though there is a good match between the profiles, Isothermal Layer Depth (ILD) computed from the enhanced profile is found to be very less in the stations which are distant from the central point (Fig 4(a)). The ILD at the adjacent stations from the 'local point' is found to be matching well. An inference from the error plot is that, in both the cases, the profiles show a departure of more than  $2^{\circ}\text{C}$  in the thermocline region, but for all other depths, it is less than  $1^{\circ}$  or even less than  $0.5^{\circ}$  (Fig 4(b))

In the case of shallow stations, it is noticed that, in most of the stations, the enhanced profile is more accurate than that based only on climatology. The climatology at each location is far departed from the *in-situ* profile. In all the cases, the enhanced profiles are well matching with the in-situ observations (Fig 5(a)). The error plot shows that, except in one case, the profiles show a departure of less than  $1^{\circ}\text{C}$  even when the climatology showed large departures (Fig 5(b))



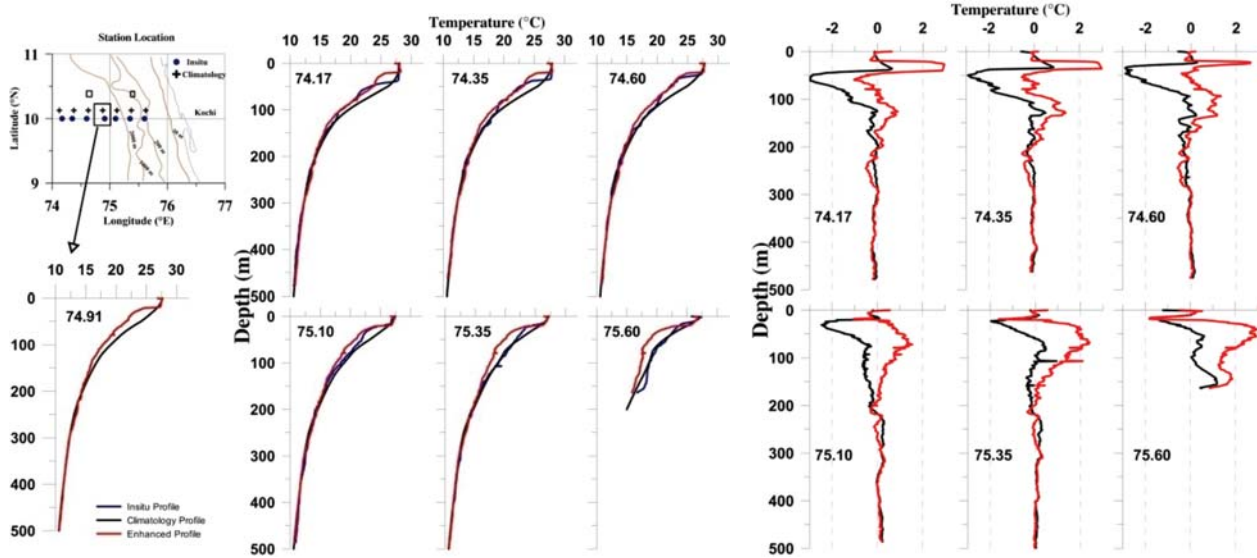


Fig. 4(a). Comparison of the *s viz.* Climatology, *in-situ* data and enhanced profile for the deep stations.  
 Fig. 4(b). anomaly of the *in-situ* with climatology and enhanced.

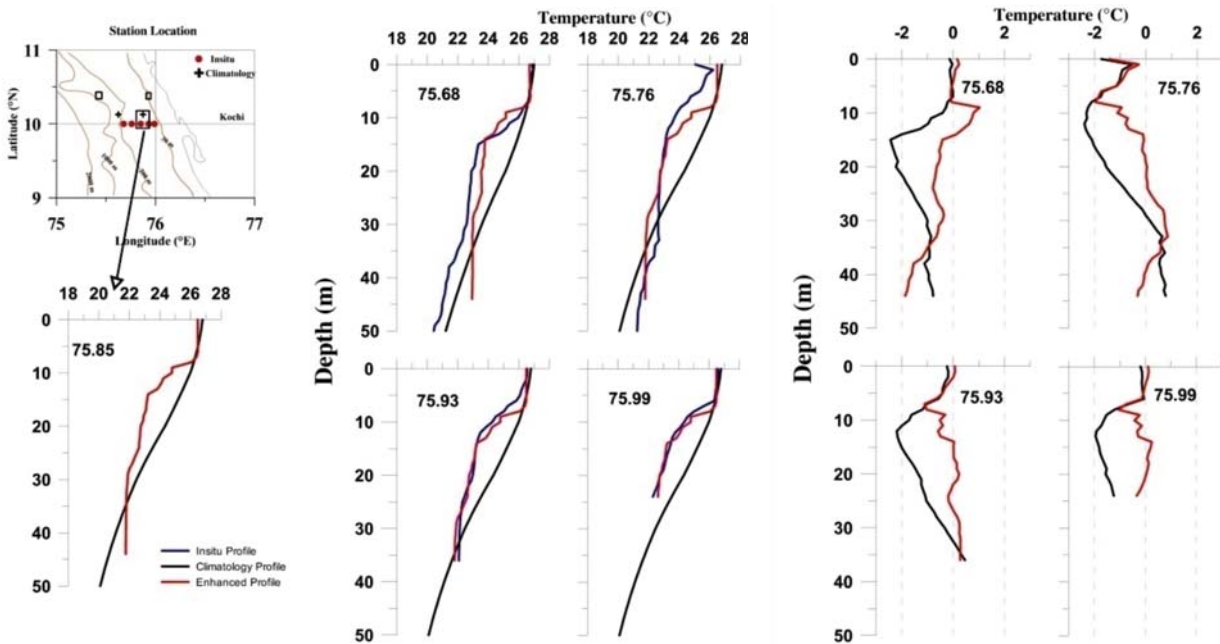


Fig. 5(a). Comparison of the *s viz.* Climatology, *in-situ* data and enhanced profile for the deep stations.  
 Fig. 5(b). anomaly of the *in-situ* with climatology and enhanced.

#### 4. SUMMARY AND CONCLUSION

A method using simple enhancement is done in the region off Kochi for two seasons to estimate the profile for a remote location. This is for predicting the oceanic conditions at a remote location which is not available otherwise. Using this method, the climatology profile of the remote location enhanced matches to the

*in-situ* profile. The enhancement has been tested for two different seasons (Pre-monsoon and Summer monsoon) and separately for deep and shallow stations. The results show that, this method is advisable for the deep waters in both the seasons in which it is tested. In the shallow region, where the maximum variability occurs, accuracy of this method is slightly less. More studies are to be conducted for other seasons to test the efficacy of this method. This method could provide the user with an improved ASW capability

## 5. ACKNOWLEDGEMENT

Authors are thankful to Shri. SK Shenoy, OS, Director, NPOL and Dr. KV Sanilkumar, Sc G for the encouragement and motivation to carry out this study.

## 6. REFERENCES

- [1] R.M. Clancy and K.D. Pollak, 1983. "A Real-Time Synoptic Ocean Thermal Analysis/Forecast System," *Progress in Oceanography*, **12**, 383-424.
- [2] L.M. Druyan, 1972. "Objective Analysis of Sea-Level Winds and Pressure Derived from Simulated Observations of a Satellite Radar-Radiometer and Actual Conventional Data," *Journal of Applied Meteorology*, **11**(3), 413-428.
- [3] M.M. Holl, M.J. Cuming and B.R. Mendenhall, 1979. The Expanded Ocean Thermal Structure Analysis System: A Development Based on the Fields by Information Blending Methodology, Technical Report M-2 41, Meteorology International Incorporated, Monterey, California 93940, 216.
- [4] H.B. Kruger, 1969. General and Special Approaches to the Problem of Objective Analysis of Meteorological Variables, *Quarterly Journal Royal Meteorological Society*, **95**, 22-39.
- [5] Kenneth D. Pollak, 1984. Real-time enhancement of a climatology or forecast of ocean thermal structure using observed ocean temperatures. Master's Thesis, Naval Postgraduate School, California.

# Hydrostatic response of 1-3 Piezocomposite large-area Hydrophones

R. Ramesh<sup>1\*</sup>, S.V. Periera<sup>1</sup>, K. Sreelatha<sup>1</sup>, T.K. Vinod Kumar<sup>1</sup>,  
B. Jayakumar<sup>1</sup> and C. Durga Prasad<sup>2</sup>

<sup>1</sup>Naval Physical & Oceanographic Laboratory, Kochi-682 021

<sup>2</sup>Naval Materials Research Laboratory, Ambernath-421 506

\*e-mail: ramesh\_rmani@hotmail.com

[Received: 25.01.2017; Revised: 15.07.2017; Accepted: 26.07.2017]

## ABSTRACT

Large-area hydrophones have the advantage of high Signal-to-Noise Ratio (SNR) which enables long-range detection in a passive sonar system. When such systems are used in a submarine, high hydrostatic pressure acts on the hydrophones. The acoustic characteristics of hydrophones, usually measured under ambient pressure and temperature conditions, may not remain the same under high pressures. Therefore, it is important to study this effect before using the hydrophones in actual applications. This paper presents the effect of high hydrostatic pressures up to 30 bar on the receiving sensitivity of 1-3 piezocomposite planar hydrophones, measured in an anechoic, high pressure, hydrophone calibrating facility. The free-field receiving sensitivity is found to increase with hydrostatic pressure by about 5 dB in the frequency band 0.5 to 5 kHz. This characteristic property of 1-3 piezocomposite hydrophones is an advantage over piezoceramic-based hydrophones for high depth applications.

## 1. INTRODUCTION

Piezocomposites are potential materials for developing electro-acoustic transducers [1-4]. They are two-phase materials comprised of piezoelectric and polymer components. Their high hydrostatic piezoelectric coefficients, high coupling coefficients, low acoustic impedance and tailor-made properties render them very useful for wide-band underwater acoustic and ultrasonic imaging applications. Although several connectivity patterns do exist, piezocomposites with 1-3 connectivity have become increasingly popular [1] owing to the simplicity in structural configurations and compatibility to large-scale manufacturing process [3].

1-3 piezocomposites transducers are commonly used as projectors as well as hydrophones in various high frequency underwater acoustic systems that operate typically in the frequency region from 10 kHz to 1 MHz [5]. In active systems such as ultrasonic medical imaging and high resolution underwater acoustic imaging sonar systems, the piezocomposites are operated predominantly at the thickness-mode resonance, where the response is maximum. The uni-modal operation makes use of 33-mode vibrations of piezoelectric material and generates stronger signals in the medium because, piezoelectric 33-coefficients are much higher than the 31- or 32-coefficients. On the other hand, piezoelectric transducers used in pure passive acoustic systems are operated far below the first fundamental mode resonance. At low frequencies, the response is

controlled by the combined effect of thickness-mode and lateral-mode coefficients. It is termed as hydrostatic response.

The hydrostatic mode of operation is predominant in receiver systems where hydrophones are operated in non-resonant modes and the lateral dimensions of hydrophones are much larger than the thickness. Therefore, the hydrostatic material coefficients are to be used instead of pure mode coefficients.

Piezoelectric voltage ( $g$ ) and charge ( $d$ ) coefficients of piezocomposite active materials in the hydrostatic mode are of interest in broadband, large area hydrophones. The hydrostatic voltage coefficient is defined as,  $g_h = g_{33} + g_{32} + g_{31}$  [1,2]. For laterally isotropic  $\infty$  mm crystal class piezoceramic material,  $g_{32} = g_{31} \approx -g_{33}/2$  and therefore,  $g_h$  is negligibly small. Similarly, the hydrostatic charge coefficient  $d_h$  is small as well, resulting in very small hydrostatic figure of merit,  $g_h d_h$ . Since 1-3 piezocomposites have strong lateral decoupling due to the presence of compliant polymer matrix, their FoM in the hydrostatic mode of operation is much higher than that of dense piezoceramic materials [1].

Large area hydrophones have become popular in recent times and find extensive application in conformal arrays and flank arrays of submarines. Hydrophones covering large surface area have some inherent advantages over finite sized hydrophones. Incident signals that are coherent get added and noises that are incoherent get averaged out over a large area, resulting in high Signal-to-Noise Ratio (SNR). This enhances the capability of receiver systems to detect very weak signals such as ambient noise at Sea State 0.

Such large area hydrophones can be constructed using 1-3 piezocomposites. Further, the large area hydrophones designed for high depth applications are subjected to hydrostatic pressures. The characteristics of hydrophones usually measured at ambient temperature and pressure conditions may no longer be valid under high pressure conditions. In this context, it is important to measure the response of 1-3 piezocomposite hydrophones under high hydrostatic pressures.

Planar hydrophones are constructed using 1-3 piezocomposite active materials. Their acoustic characteristics are measured initially under ambient conditions. Then the hydrophones are subjected to high hydrostatic pressure upto 30 bar in an anechoic high pressure calibration chamber and the receiving sensitivities are measured in the frequency band 0.5 to 5 kHz. The results of the experimental studies are presented in this paper.

## 2. 1-3 PIEZOCOMPOSITE HYDROPHONES

Planar hydrophones are constructed from 1-3 piezocomposite slabs. The piezocomposite specimens are synthesised by dice-and-fill technique [1]. The active component is of type PZT5H and the passive component is Araldite resin CY203 and hardener HY956 of Ciba. The ceramic volume fraction in the composite is about 30%. The width, length and thickness of the piezocomposite specimens are 50 mm, 50 mm and 6 mm, respectively. The major surfaces of the specimens are applied with silver epoxy electrodes and they are

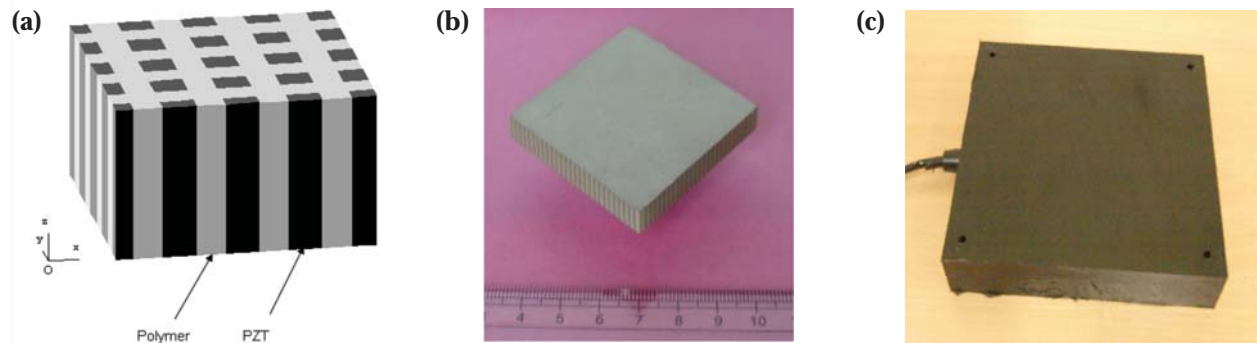


Fig. 1. 1-3 piezocomposite (a) Structure, (b) Bare plate and (c) Planar hydrophone.

poled along the thickness direction at high dc electric field in a temperature-controlled oil bath. Planar hydrophones are constructed using 1-3 piezocomposite slabs. Stiffening plates made up of GRP boards are attached on the top and bottom surfaces and electrical leads are soldered to them. This assembly is fixed on the backing layer using epoxy adhesives. The hydrophones are made water-worthy by encapsulating with polyurethane. Fig. 1 shows the 3D model, and photographs of the 1-3 piezocomposite active layer and the moulded planar hydrophone.

### 3. MEASUREMENT SYSTEM FOR HYDROSTATIC RESPONSE

The electrical characteristics of piezocomposite hydrophones are evaluated in air and underwater prior to subjecting them to acoustic measurements, in order to ensure that the hydrophones are assembled properly and free from defects. The electrical admittance spectra of hydrophones are measured using an impedance analyser, in the frequency range from 100 Hz to 30 kHz.

The acoustic characteristics of hydrophones under ambient conditions are measured under free-field conditions in an open tank. The characteristics under different hydrostatic pressures are measured in a closed anechoic chamber, under free-field condition. Fig. 2 shows the schematic diagram of the anechoic pressure chamber and the block diagram of the measurement setup. The pressure chamber is made up of steel and the inner surface is fitted with anechoic wedges, in order to minimise the strength of echoes from the boundaries by absorbing the radiations. This is essential to ensure nearly free-field conditions in the chamber. The chamber is filled with water and is pressurised using a sophisticated system that generates, monitors and controls the pressure. The pressure can be varied from 0 bar to 75 bar in a well-controlled manner. The system is capable of varying the temperature from  $-4^{\circ}\text{C}$  to  $40^{\circ}\text{C}$ . The system has provision to set the rate of increase and decrease of pressure and temperature by setting the required ramp-rate through the control software. After attaining and stabilising the required environmental conditions, acoustic measurements are carried out.

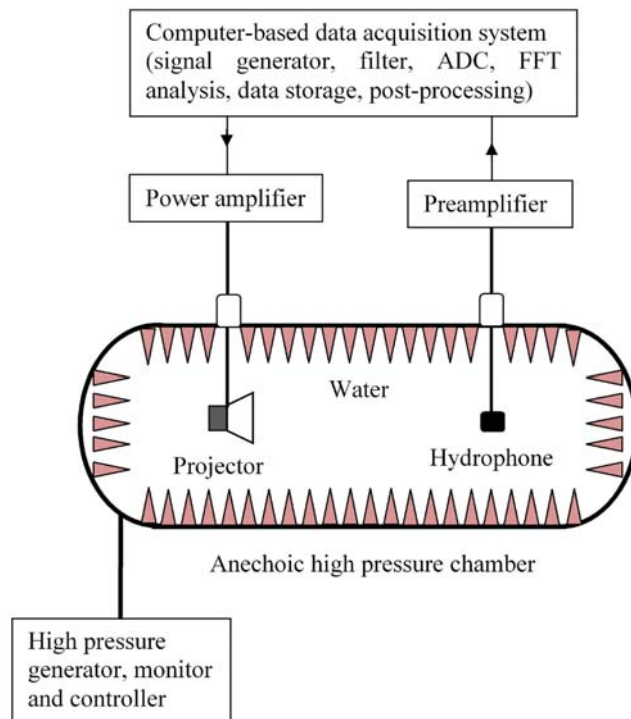


Fig. 2. Schematic diagram of the anechoic high pressure chamber used for studying hydrostatic response of the piezocomposite hydrophones.

The acoustic response, namely, the receiving sensitivity of hydrophones is measured by comparison calibration method [6]. The block diagram of the measurement system is shown in Fig. 2. The projector and the hydrophones are positioned along the axis of the chamber through the hatches provided on the top. The separation between the projector and the hydrophone is set according to the far-field criterion. Acoustic signals of required shape and frequency are generated, amplified using a power amplifier and transmitted through the projector. Output signals from the standard hydrophone and the test hydrophone are successively measured by substituting one for another at the same location. The hydrophone output signals are pre-amplified using a B&K preamplifier, and filtered, digitised and processed by the computerised data acquisition system. The receiving sensitivity of the test hydrophone ( $M_t$ ) is determined using the relation,

$$M_t = \frac{V_t}{P} = \frac{V_t}{V_s} M_s \quad (1)$$

where,  $V_t$  and  $V_s$  are the output voltage amplitudes of the test and standard hydrophones, respectively,  $P$  is the incident pressure amplitude and  $M_s$  is the receiving sensitivity of the standard hydrophone. The unit of receiving sensitivity is V/Pa and it is usually presented in dB scale with a reference of 1V/ $\mu$ Pa. The free-field receiving sensitivities of hydrophones are measured at various hydrostatic pressures in the anechoic pressure chamber shown in Fig. 2.

#### 4. RESULTS AND DISCUSSION

Electrical admittance characteristics of the hydrophones are measured prior to acoustic measurements in order to study the resonance patterns. Fig. 3 shows the electrical admittance spectra of a 1-3 piezocomposite planar hydrophone measured in water. The real and imaginary parts of admittance, namely, conductance ( $G$ ) and susceptance ( $B$ ), respectively, are plotted as a function of frequency. The first fundamental resonance occurs at about 25 kHz and therefore, the usable frequency band with nearly constant response is expected up to about 12 kHz. However, the acoustic measurements are restricted to 5 kHz

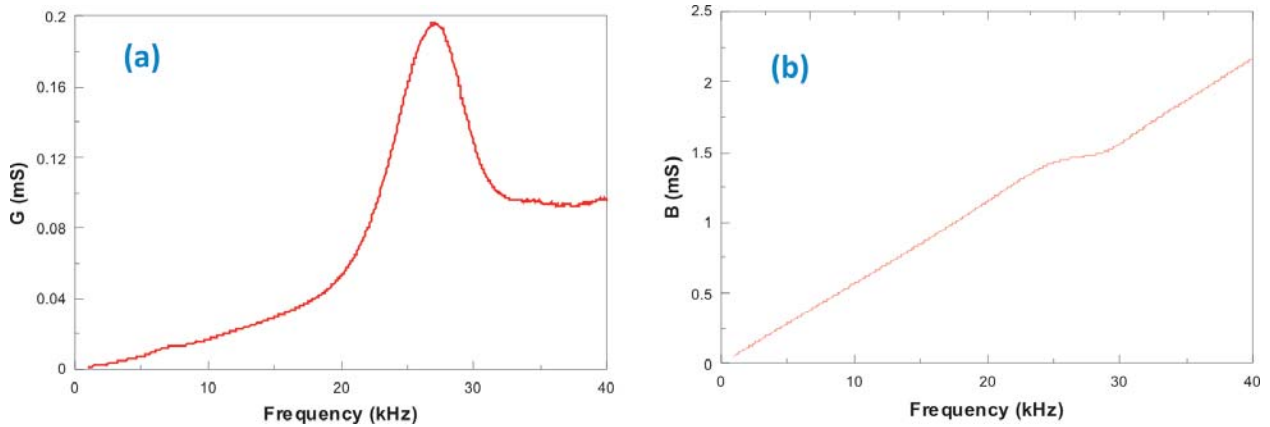


Fig. 3. Electrical admittance spectra of 1-3 piezocomposite hydrophone in water.  
(a) Conductance,  $G$  and (b) Susceptance,  $B$

The hydrostatic pressure dependent characteristics of two configurations of 1-3 piezocomposite hydrophones are studied. The two types of hydrophones have similar design and constructed with two different backing materials. They are designated as first and second types. Free-field voltage sensitivities are measured as a function of hydrostatic pressure at ambient temperature. Figs. 4 & 5 show the sensitivity plots of these hydrophones for frequencies up to 5 kHz and hydrostatic pressure ranging from 0 to 30 bar (*i.e.* 0 to 300 m water depth). The sensitivity at ambient condition remains fairly constant over the band and

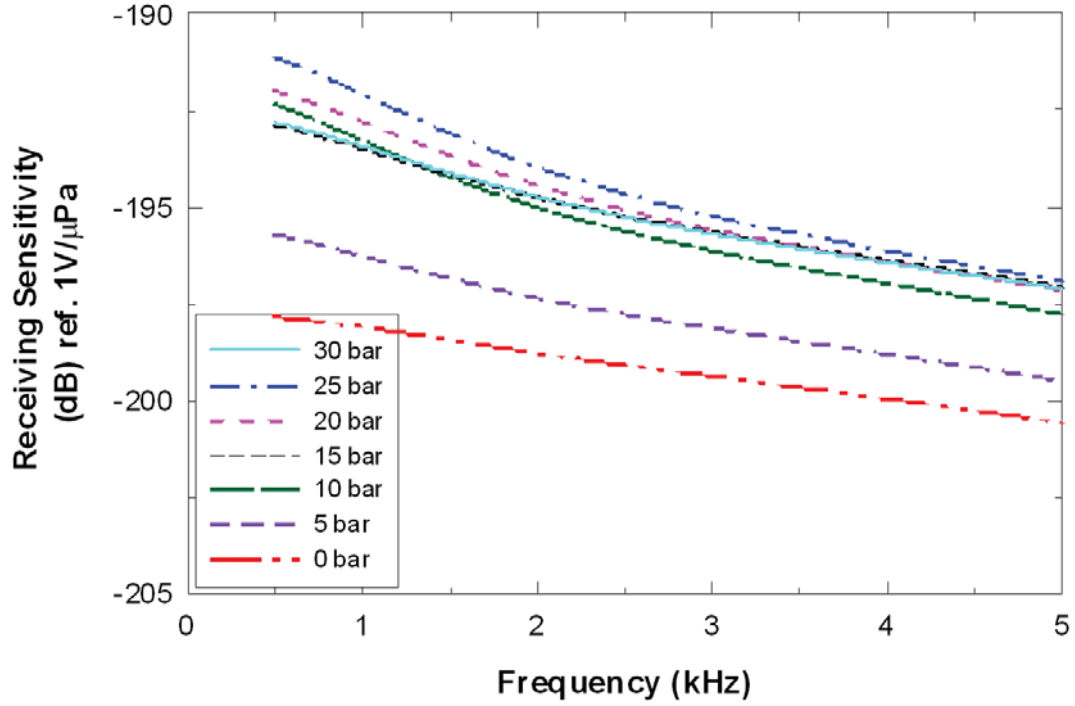


Fig. 4. Hydrostatic pressure-dependent receiving sensitivity of 1-3 piezocomposite hydrophone of first type

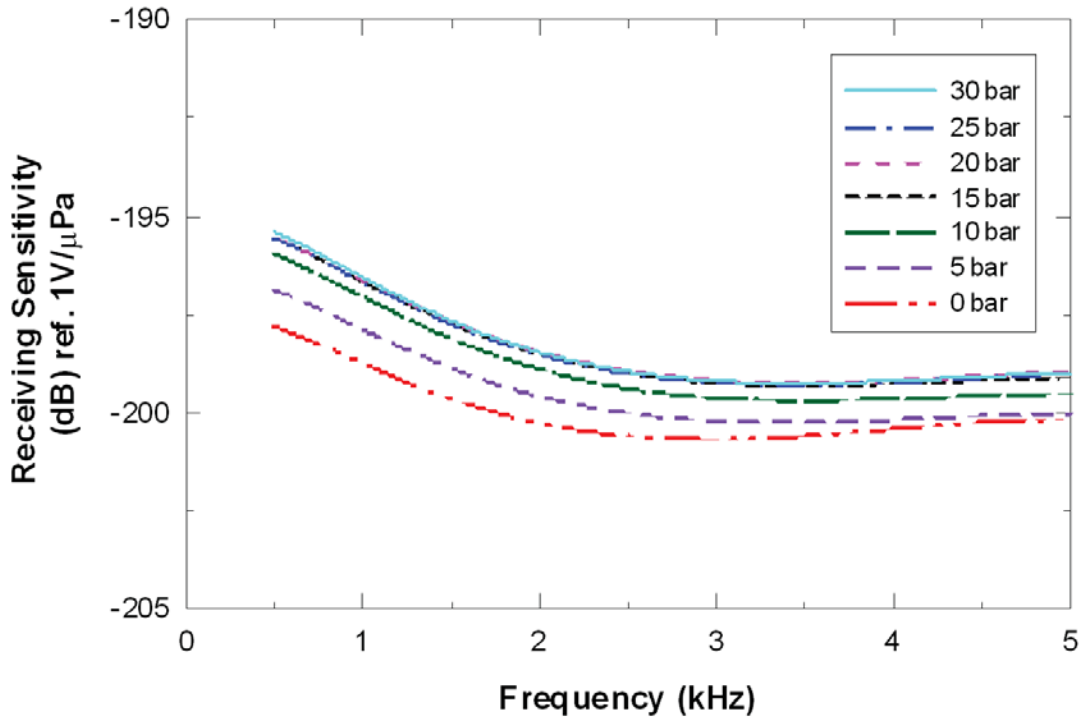


Fig. 5. Hydrostatic pressure- dependent receiving sensitivity of 1-3 piezocomposite hydrophone of second type.

a variation of about 2 dB is observed for both the hydrophones. The overall frequency response is shifted upwards as the hydrostatic pressure acting on the hydrophone is increased.

Fig. 6 shows the variations in receiving sensitivity as a function of hydrostatic pressure at different frequencies for the first type of hydrophone. The sensitivity increases when the pressure is increased from 0 bar to about 20 bar and remains almost constant beyond this point. Under hydrostatic pressure, the receiving sensitivity of a planar hydrophone is directly proportional to the piezoelectric hydrostatic voltage coefficient  $gh$  [2]. Presence of compliant polymer matrix in the 1-3 piezocomposite effectively reduces the lateral mode  $g$  coefficient, namely,  $g_{31}$  and the longitudinal mode coefficient  $g_{33}$  predominantly contributes to  $gh$  and hence to sensitivity.

An increase in sensitivity of about 2 dB with hydrostatic pressure has been reported in literature for 1-3 piezocomposite SonoPanel [3]. On the other hand, negligible change in sensitivity with pressure upto 100 bar is reported for hydrophones made up of porous piezoceramics and damage due to delamination is reported for PVDF hydrophones [7]. However, in the present study the 1-3 piezocomposite hydrophones have not undergone any damage due to high hydrostatic pressure and they have regained their original properties when the pressure is released.

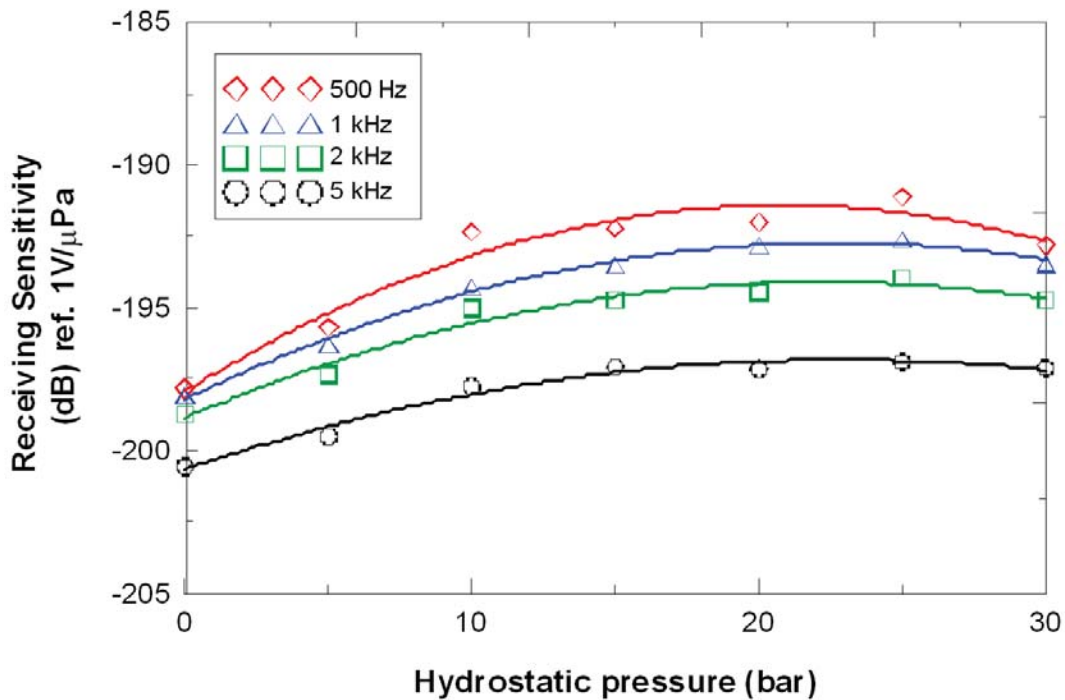


Fig. 6. Variations in receiving sensitivity with hydrostatic pressure at different frequencies, for the first type of hydrophone. Markers are the measured data and solid lines are the best fits.

## 5. CONCLUSIONS

Large area planar hydrophones are constructed using 1-3 piezocomposites. Two types of hydrophones are assembled with two different backing materials. Both the hydrophones show fairly constant receiving sensitivity over the frequency band 0.5 to 5 kHz. The hydrophones are subjected to high hydrostatic pressures up to 30 bar in an anechoic, high pressure, hydrophone calibrating facility. The free-field receiving sensitivity of 1-3 piezocomposite hydrophones is found to increase with hydrostatic pressure and approaches saturation values at very high pressure levels. The present study indicates that the 1-3 piezocomposite hydrophones



are suitable for submarine-based underwater acoustic systems in which high hydrostatic pressure acts on the hydrophone during operation

## 6. ACKNOWLEDGEMENT

The authors thank Smt. K.P. Krishnaveni and Shri R. Sooraj for help in high pressure measurements, Dr.Reji John for providing a backing material, Dr. D. Thomas and Shri. M.R. Subash Chandrabose for support, Dr. D.D. Ebenezer for technical discussion and Director for providing facilities, support and permission to publish this paper.

## 7. REFERENCES

- [1] R.E. Newnham, L.J. Bowen, K.A. Klicker and L.E. Cross, 1980. Composite piezoelectric transducers, *Materials in Engg.*, **2**, 93-106.
- [2] W.A. Smith, 1993. Modeling 1-3 composite piezoelectrics: Hydrostatic response, *IEEE Trans. Ultrason. Ferroelec. Freq. Control*, **40**, 41-48.
- [3] T.R. Howarth and R.Y. Ting, 2000. Piezoacoustic evaluation of 1-3 piezocomposite Sono Panel materials, *IEEE T. Ultrason. Ferroelec. Freq. Control*, **47(4)**, 886-894.
- [4] R. Ramesh, C. Durga Prasad, T.K. Vinod Kumar, L.A. Gavane and R.M.R. Vishnubhatla, 2006. Experimental and finite element modelling studies on single-layer and multi-layer 1-3 Piezocomposite transducers, *Ultrasonics*, **44**, 341-349.
- [5] Product catalogue, Materials System Inc., USA, ([www.matsysinc.com](http://www.matsysinc.com))
- [6] R.J. Bobber, 1988, Underwater electroacoustic measurements, Peninsula Publishing, Los Altos
- [7] C. Audoly and M. Richard, 1994. Large area hydrophones for sonar receiving antennas - comparison of different piezoelectric materials, *Proc. IEEE Ultrason. Symp.*, 561-564.

# Transmission line and finite element modelling of a high frequency, underwater acoustic transducer

R. Ramesh, Pushpa Abraham, E. R. Ratheesh and Manoj N. Unni

*Naval Physical & Oceanographic Laboratory, Kochi 682 021*

*e-mail: ramesh\_rmani@hotmail.com*

[Received: 01.02.2017; Revised: 15.07.2017; Accepted: 26.07.2017]

## ABSTRACT

A high frequency, underwater, electroacoustic transducer is modelled using a distributed-parameter electrical equivalent-circuit model. Each component of the transducer is modelled as an electrical transmission line and subsequently cascaded to represent the complete transducer. The transmission line model results are compared with Finite Element Model results. A transducer is then fabricated and evaluated in a water tank in the 210-250 kHz frequency band. The transmitting voltage response predicted by the models are found to agree well with the measured results thus validating the models.

## 1. INTRODUCTION

High frequency transducers that operate typically in the frequency region from about a few hundred kHz to a few MHz find extensive applications in underwater ultrasonic systems. For example, high frequency transducers are used in echo sounders for detecting the water depth during ship navigation and in proximity warning alarm for avoiding undesirable collision with other objects in the vicinity. Arrays are used in sea bed mapping and underwater acoustic imaging systems. Operating frequencies of about a few hundred hertz provide reasonable high resolution and long range capabilities.

Piezoceramic drivers used in such transducers operate in the thickness-moderesonance where the efficiency and the amplitude of response have peaks. Further, the bandwidth of the transducer is an important design parameter, particularly for acoustic imaging and communication systems. The bandwidth is greatly improved by adding a suitable quarter wavelength matching layer in the front. Control of radiation pattern is another important factor and is accomplished by using suitable backing layer on the rear. Appropriate combination of the active and passive layers with required dimensions and acoustic impedances is carefully chosen to obtain the design goals. It is important to validate and optimise the design using theoretical studies before actually constructing the transducers. A high frequency transducer is modelled using two methods, namely, equivalent circuit modelling and finite element modelling.

Equivalent circuit modelling technique is commonly used to model electro-acoustic transducers where the well-developed electrical network theory is utilised to solve analogous acoustic problems<sup>[1-3]</sup>. Lumped parameter models can predict the performance of transducers reasonably well in a frequency band around resonance<sup>[4]</sup>. At high frequencies, the dimensions of the transducers are comparable to the acoustic wavelengths and therefore the transducer analysis requires more accurate distributed parameter modelling. In distributed parameter modelling, every component of the transducer is treated as a transmission line and all the components are suitably combined to model the complete transducer<sup>[5,6]</sup>. Two types of

transmission line models are available, namely, Mason model and *KLM* model and both the models give same results<sup>[7]</sup>. Mason equivalent circuit is used in the present work.

Another powerful method of modelling transducers is the Finite Element Modelling (*FEM*). The software package ATILA is widely used in piezoelectric transducer modelling<sup>[8]</sup>. The design of the transducer is verified by defining the geometry and material properties of the components, and executing the programme in the required frequency band. The output performance parameters are estimated in the modelling studies. It is fast and convenient method of modelling, however, the accuracy of results depends strongly on the accuracy of input material parameters of the components.

This paper deals with the transmission line model of a high frequency transducer. The equivalent circuit model is verified by FEM studies. A high frequency transducer is constructed and its transmitting response is measured experimentally and is used to validate the model results.

## 2. TRANSMISSION LINE MODEL

Fig. 1 shows the constructional details of a typical high frequency transducer. It is analysed using transmission line model, by splitting it into various functional components such as PZT driver, backing layer and matching layer. Let,  $Z_{aco}^P$ ,  $Z_{aco}^B$  and  $Z_{aco}^M$  are the acoustic impedances of these three layers, respectively. The ends are terminated with radiation impedances of the fluid media, for example,  $Z_r^{air}$  for air behind the backing layer and  $Z_r^{water}$  for water in front of the matching layer. The cross sectional area,  $A$ , of each layer is assumed to be equal. The characteristics of the individual layers are determined by describing them as *T-network* formed by three impedance branches<sup>[1,6,7]</sup>.

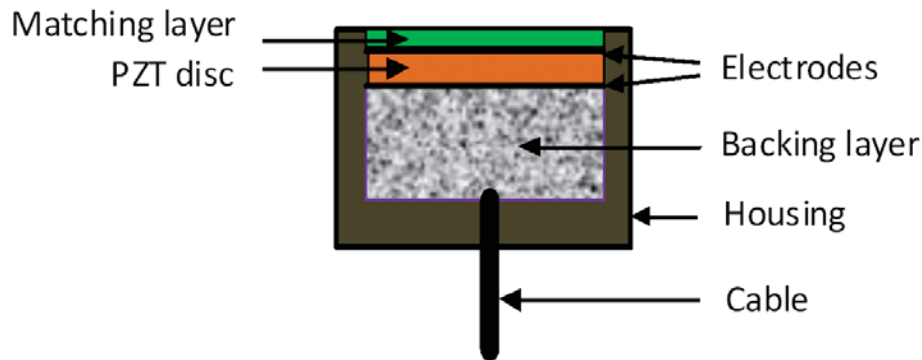


Fig. 1. Schematic diagram of a high frequency transducer

### 2.1 Model formulation

The high frequency transducer shown in Fig. 1 is represented by cascading the corresponding T-networks of backing layer, piezoceramic layer and matching layer. The combined transmission line model that includes the active and passive layers is shown in Fig. 2. The impedances  $Z_a^i$  and  $Z_b^i$  characterising the individual layers are identified by the superscripts, *B*, *P* and *M* corresponding to backing, piezoelectric and matching layers, respectively. The rear face of the backing layer and the radiating face of the matching layer are terminated with the radiation impedances of air  $Z_r^{air}$  and  $Z_r^{water}$  water, respectively.

Impedance of the backing layer that appears at the acoustic port 1 of piezoceramic disc is determined from the *T-Network* of the backing layer. The acoustic port on one side is air-loaded and its radiation impedance  $Z_r^{air}$  is negligible compared with all other impedances in the circuit. Therefore, the impedance  $Z_1$  at port 1 is written as,

$$Z_1 = Z_a^B + \frac{Z_a^B Z_b^B}{Z_a^B Z_b^B} \quad (1)$$

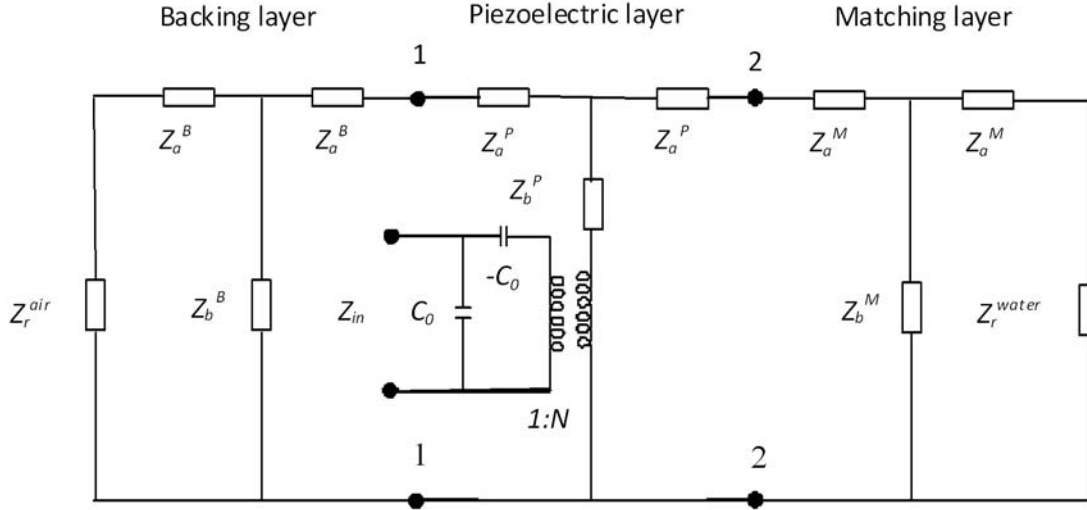


Fig. 2. Transmission line model of a high frequency transducer constructed by cascading the *T-Network* of backing, piezoceramic and matching layers.

Similarly, the impedance of matching layer that appears at the acoustic port 2 of piezoceramic disc is determined from the corresponding *T-Network* of the matching layer. Front face of the transducer is terminated with the radiation impedance of water ( $Z_r^{water}$ ). Therefore, the impedance  $Z_2$  that appears at port 2 is written as,

$$Z_2 = Z_a^M + \frac{Z_b^M (Z_a^M + Z_r^{water})}{Z_b^M + Z_a^M + Z_r^{water}} \quad (2)$$

The impedances  $Z_1$  and  $Z_2$  given in Eqs.(1) and (2) are included as load impedances on the acoustic ports, in the *T-network* of the piezoceramic layer

### 2.2 T-network of passive layers

The transmission line of passive layers such as, matching layer and backing layer, is described as a two-port *T-network* as shown in Fig. 2. The ends are terminated with corresponding radiation impedances. The *T-network* of each passive layer is formed by two impedances  $Z_a^i$  and  $Z_b^i$ ,  $i = B, M$ , as given by,

$$Z_a^i = jZ_{aco}^i \tan \frac{k^i t}{2} \quad (3)$$

$$Z_b^i = jZ_{aco}^i \operatorname{cosec} k^i t \quad (4)$$

where,  $Z_{aco}^i = \rho^i v^i A$  is the characteristic impedance,  $\rho^i$  is the density,  $v^i$  is the sound speed,  $t$  is the thickness and  $k^i$  is the wave number given by  $\omega/v^i$ . The superscript  $i$  on the material parameters refers to the  $i^{th}$  passive layer, namely, backing or matching layers as applicable. Passive layers are completely characterised by using this model.

### 2.3 T-network of piezoceramic layer

The transmission line model of the piezoelectric driver is represented by a 3-port network consisting of two acoustic ports and an electrical port inter-connected through the electromechanical transformer of turns ratio  $N$ , as shown in Fig. 2. The two acoustic ports are terminated with acoustic impedances  $Z_1$  and  $Z_2$  determined by the velocities and forces  $u_i$  and  $F_i$ ,  $i = 1, 2$  respectively, acting on the ends and given by

Eqs.(1) and (2). The  $T$ -network of the piezoceramic layer is formed by two impedances  $Z_a^P$  and  $Z_b^P$  as given by<sup>[1,7]</sup>,

$$Z_a^P = jZ_{aco}^P \tan \frac{k^P t}{2} \quad (5)$$

$$Z_b^P = jZ_{aco}^P \operatorname{cosec} (k^P t) \quad (6)$$

where  $Z_{aco}^P = \rho^P v^P A$  is the characteristic impedance,  $\rho^P$  is the density,  $v^P$  is the sound speed,  $t$  is the thickness and  $k^P$  is the wave number given by  $\omega/v_p$ . The superscript  $P$  on the material parameters refers to the piezoceramic layer.

The electrical port consists of two branches of the electrical impedances ( $Z_0$ ) due to dielectric capacitance ( $C_0$ ) of the piezoceramic layer. The electrical parameters are transformed into acoustic parameters and vice versa through the electromechanical turns ratio ( $N$ ) written as

$$N = \frac{nd_{33}A_r}{ts_{33}^E} \quad (7)$$

where,  $n$  is the number of piezoceramic rings,  $d_{33}$  is the longitudinal mode piezoelectric charge coefficient,  $A_r$  is the cross sectional area of the transducer and  $s_{33}^E$  is the short-circuit elastic compliance coefficient.

The  $T$ -network of the piezoceramic layer shown in Fig. 2 is simplified by transforming all the mechanical parameters in terms of equivalent electrical parameters. The mechanical impedance of the circuit ( $Z_m$ ) is determined from various impedances using the relation,

$$Z_M = Z_b^P + \frac{(Z_a^P)^2 + Z_a^P(Z_1 + Z_2) + Z_1Z_2}{2Z_a^P + Z_1 + Z_2} \quad (8)$$

The mechanical term  $Z_m$  is transformed into electrical term ( $Z_M$ ) using the relation,

$$Z_M = \frac{Z_m}{N^2} \quad (9)$$

The net electrical impedance ( $Z_{in}$ ) of the circuit as measured at the input terminals of the piezoceramic layer is obtained from the relation,

$$Z_{in} = \frac{-(Z_0)^2 + N^2 + Z_0Z_m}{Z_m} \quad (10)$$

## 2.4 Voltage Transfer function

The input voltage applied across the electrical port gets modified by various impedance branches shown in Fig.2 and the portion of it appearing across the radiation impedance gets converted into useful acoustic output of the transducer. The ratio of the output voltage to the input voltage of the network is defined as its *Voltage Transfer function (VTF)*. The output voltage represents the acoustic pressure manifested by the radiation impedance at the surface of the transducer. The voltage transfer function of the transmission line model shown in Fig. 2 is derived as,

$$VTF = \frac{V_{out}}{V_m} = \frac{Z_2Z_pZ_m}{(Z_2 + Z_a^P)(Z_p + Z_b^P)(Z_m - Z_0)} \quad (11)$$

where,  $Z_m$  is the net mechanical impedance of ports 1 and 2 as given by Eq.(8) and  $Z_p$  is the impedance of the two parallel branches of the simplified circuit given by,

$$Z_p = \frac{(Z_a^P)^2 + Z_a^P(Z_1 + Z_2) + Z_1Z_2}{2Z_a^P + Z_1 + Z_2} \quad (12)$$

The impedances of the backing layer ( $Z_1$ ) and matching layer ( $Z_2$ ) are determined from Eqs. (1) and (2) by applying appropriate boundary conditions.

## 2.5 Transmitting Voltage Response

The Transmitting Voltage Response (*TVR*) of the transmission line transducer is determined from the corresponding voltage transfer function of the network given by Eq.(11). The voltage ( $V_{in}$ ) applied between the input terminals of the transducer gets transformed into force ( $F$ ) across the radiation impedance ( $Z_r^{water}$ ) of the radiating face. In equivalent electrical analogy, the force generated is written in terms of the output voltage ( $V_{out}$ ) through the electromechanical turns ratio ( $N$ ) as given by,

$$F = NV_{out} \quad (13)$$

or 
$$V_{out} = \frac{PA}{N} \quad (14)$$

where,  $P$  is the pressure and  $A$  is the surface area of the radiating face. Dividing Eq. (14) by  $V_{in}$ , we get the voltage transfer function (*VTF*) of the network,

$$VTF = \frac{V_{out}}{V_{in}} = \frac{PA}{V_{in}N} \quad (15)$$

The ratio  $P/V_{in}$  is the Transmitting Voltage Response (*TVR*) and is written as,

$$TVR = VTF \frac{N}{A} = \frac{Z_2 Z_p Z_m N}{(Z_2 + Z_a^p)(Z_p + Z_b^p)(Z_m - Z_0)A} \quad (16)$$

Various impedances appearing in Eq. (16) are functions of frequency and therefore, it gives rise to frequency-dependent *TVR*.

## 2.6 Numerical details

The high frequency transducer shown in Fig. 1 is modelled using transmission-line model described in this paper. The functional components of the transducer, namely, piezoceramic disc, matching layer and backing layer are modelled as corresponding *T*-network and are cascaded to represent the complete transducer as shown in the equivalent circuit in Fig. 2. Applicable boundary conditions are (i) water on the front face of the matching layer, providing radiation loading and (ii) air behind the backing layer, providing mechanical short-circuit condition. The input data to the model are the diameter, thickness and material coefficients of various components of the transducer and are given in Table 1. The same properties are used as input to the finite element model as well. The output parameters of interest are the electrical impedance and the Transmitting Voltage Response (*TVR*) and they are determined from Eq.(10) and Eq.(16), respectively.

## 3. FINITE ELEMENT MODEL

The equivalent circuit model presented in the previous section is compared with the finite element modelling. A high frequency transducer described in Fig. 1 is modelled using the FEM code ATILA [8]. The transducer is axi-symmetric and half of the transducer is modelled. The thickness of backing, piezoceramic and matching layers are 10 mm, 10 mm and 3.5 mm, respectively. The diameter of all the layers are taken as 38 mm and axially-polarised PZT4 disc is used as the active material. Electrodes are defined on the flat surfaces and 1V electric potential is applied between them. The transducer is surrounded by water medium of radius 50 mm. Non-reflective radiation boundary condition is assigned on the outer surface, which simulates infinite extent of the water medium that is required to ensure acoustic free-field condition. Structured mesh with 8-noded QUAD elements is used for the analysis. Harmonic analysis is carried out in the frequency range (210-250) kHz. Fig. 3 shows the finite element mesh of the transducer. Dimensions and material coefficients of various layers, namely, backing, piezoceramic and matching layers used in the model studies are given in Table 1 where  $\rho$  is the density,  $S_{i,j}$  are the applicable elastic compliance coefficients,  $d_{i,j}$  are the piezoelectric charge coefficients,  $\epsilon_{i,j}^s$  are the dielectric constants at constant strain,  $\epsilon_0$  is the dielectric constant of free space,  $E'$  and  $E''$  are the real and imaginary parts of Young's modulus, respectively, and  $\sigma$  is the Poisson's ratio of the corresponding materials.

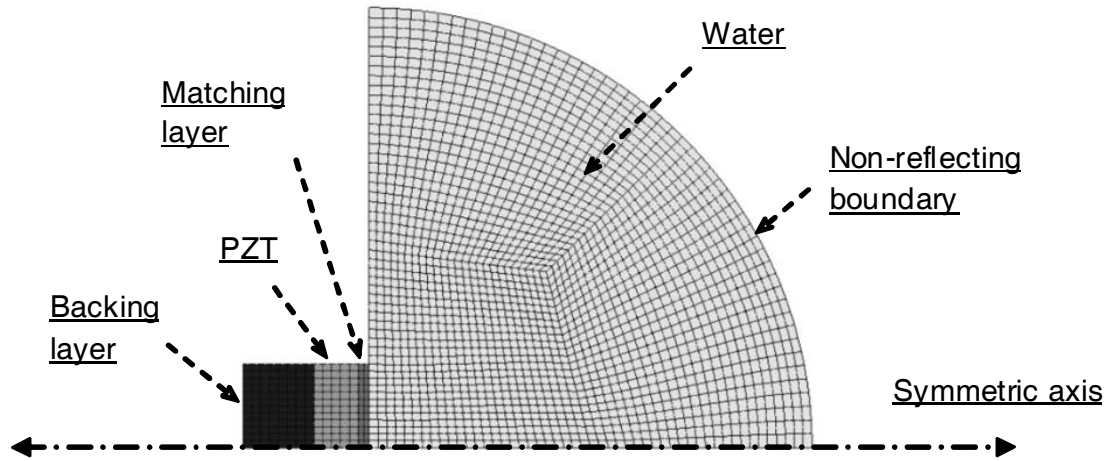


Fig. 3. Finite element model of the high frequency transducer.

**Table 1. Dimensions and material coefficients of transducer components, used in the transmission-line and finite element modelling studies.**

Component	Material Properties	Size
Piezoelectric Disc (PZT 4)	$\rho = 7750 \text{ kg/m}^3$ $S_{11}^E = 11.5 \times 10^{-12} \text{ m}^2/\text{N}$ $S_{12}^E = -4.69 \times 10^{-12} \text{ m}^2/\text{N}$ $S_{13}^E = -4.799 \times 10^{-12} \text{ m}^2/\text{N}$ $S_{33}^E = 15.5 \times 10^{-12} \text{ m}^2/\text{N}$ $S_{44}^E = 3.9 \times 10^{-12} \text{ m}^2/\text{N}$ $S_{66}^E = 3.039 \times 10^{-11} \text{ m}^2/\text{N}$ $d_{31} = -123 \times 10^{-12} \text{ m/V}$ $d_{33} = 289 \times 10^{-12} \text{ m/V}$ $d_{15} = 496 \times 10^{-12} \text{ m/V}$ $\epsilon_{33}^s/\epsilon_0 = 730$ $\epsilon_{11}^s/\epsilon_0 = 635$	Diameter : 38 mm Thickness : 10 mm
Matching Layer (Perspex)	$E' = 4 \times 10^9 \text{ Pa}$ , $E'' = 0.4 \times 10^9 \text{ Pa}$ $\sigma = 0.4$ , $\rho = 1800 \text{ kg/m}^3$	Diameter : 38 mm Thickness : 3 mm
Backing Layer (Syntactic foam)	$E' = 4 \times 10^9 \text{ Pa}$ , $E'' = 0.4 \times 10^9 \text{ Pa}$ $\sigma = 0.35$ , $\rho = 700 \text{ kg/m}^3$	Diameter : 38 mm Thickness : 10 mm

#### 4. EXPERIMENTAL DETAILS

The results obtained in the equivalent circuit model and finite element model are validated by experiments. A high frequency transducer as described in the model studies is designed and fabricated. It operates in the thickness-mode resonance of the piezoceramic disc. The piezoelectric disc is attached with backing and matching layers and is encased into a transducer housing. The assembled transducer is evaluated in an underwater acoustic measurement facility in the frequency range (210-250) kHz. The photograph of the transducer constructed for this purpose is shown in Fig. 4a.

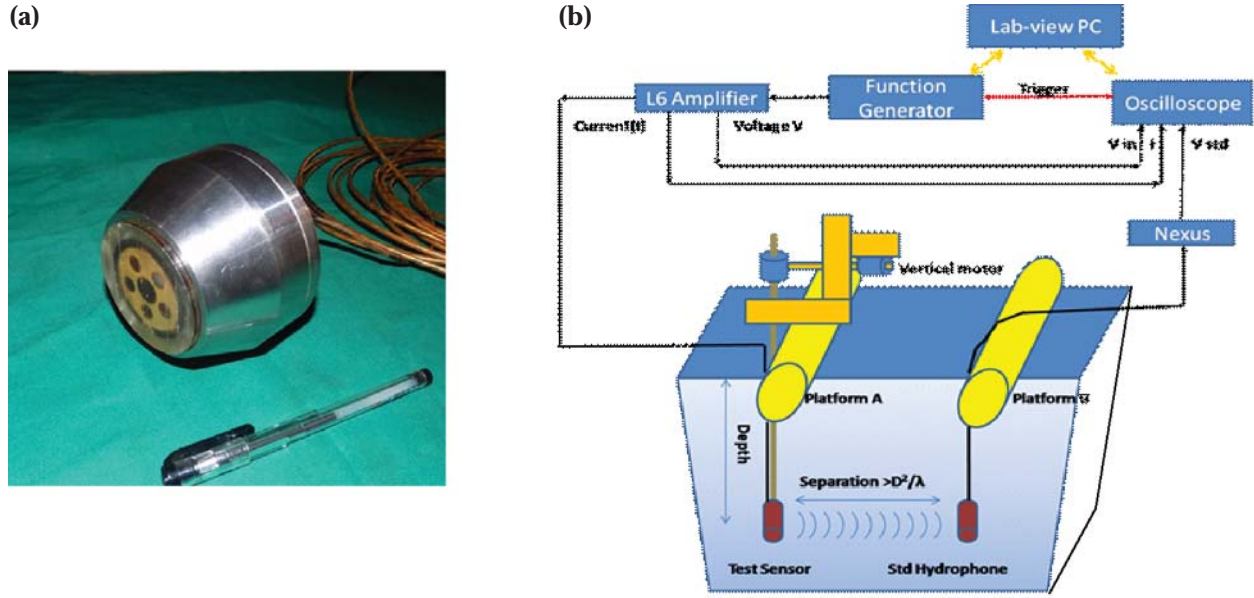


Fig. 4.(a). Photograph of the assembled transducer and (b) experimental setup used to measure acoustic characteristics of the transducer

Acoustic characteristics of the transducer are measured using the tone-burst method in a water tank under free-field condition. Fig. 4b shows the experimental set up, which is a LabView-based automatic data acquisition system. Input signal of required characteristics is generated, amplified and transmitted through the test transducer. A standard hydrophone positioned in the far-field, along the common acoustic axis of both the transducers, receives the signal. The transmitting voltage response is determined in the frequency range 210-250 kHz using the amplitudes of transmitted and received signal, and the receiving sensitivity of the standard hydrophone.

## 5. RESULTS AND DISCUSSION

The transmission line model and the finite element model presented in this paper are validated by experimental studies, by comparing the model results with the measured results. Equivalent circuit analysis

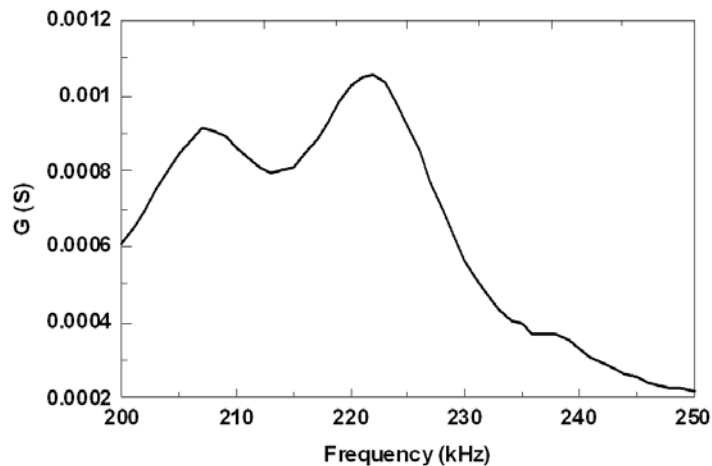


Fig. 5. Electrical conductance spectrum of the transducer as predicted by the Transmission-Line (TL) model.



is carried out using transmission line model. The main components of the transducer, namely, piezoceramic disc, matching layer and backing layer are modelled as corresponding  $T$ -network and are cascaded to represent the assembled transducer as shown in Fig. 2. The resonance behaviour of the transducer is studied by predicting the electrical admittance spectrum. Fig. 5 shows variation of electrical conductance ( $G$ ) with frequency. It is seen from the figure that the transducer resonates at about 220 kHz.

The acoustic characteristics of the transducer, namely, the Transmitting Voltage Response ( $TVR$ ) is determined using Eq. (16) and also using  $FEM$  studies. The dimensions and material coefficients of various components of the transducer as given in Table 1 are used in Transmission-line model and  $FEM$  studies. Both the model results are compared with the experimental data and presented in Fig. 6. As seen in the figure, the  $TVR$  plots predicted by the transmission line model and the finite element model agree well with that measured experimentally over the band 210-250 kHz, validating both the models. Minor variations observed in the measured data are attributed to spurious resonances of the housing structure.

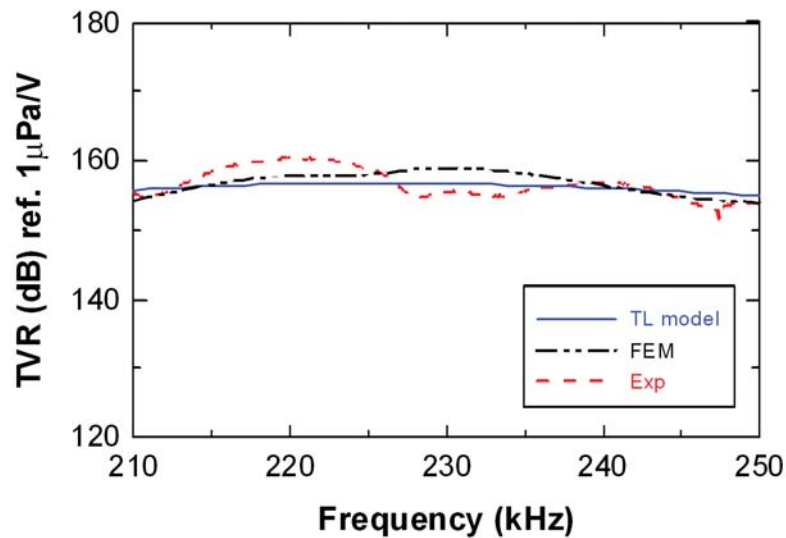


Fig. 6. Transmitting voltage response of the transducer as predicted by the Transmission-Line (TL) model and Finite Element Model (FEM), and compared with the experimental data.

## 6. CONCLUSIONS

A high frequency transducer is modelled using electrical equivalent circuit analysis and Finite Element Modelling technique. In the equivalent circuit analysis, the components of the high frequency transducer are modelled as transmission lines and the individual  $T$ -networks of the components are cascaded to represent the complete transducer. Appropriate boundary conditions are imposed in the model in order to truly simulate the actual transducer. Details of transmission line model and finite element model are presented. A transducer is fabricated with same configuration as the models. Transmitting voltage response plots as predicted by the theoretical studies agree well with the measured data. This validates the equivalent circuit model and the finite element model. This type of transducers is useful for applications such as echo ranging, depth profiling and proximity warning systems.

## 7. ACKNOWLEDGEMENT

The authors thank Dr. D. Thomas and Shri. M.R. Subash Chandra bose for support, and Dr. D.D. Ebenezer for technical discussion and critical comments on the paper, and Director for providing facilities and permission to publish this paper.

## 8. REFERENCES

- [1] D.A. Berlincourt, D.R. Curran and H. Jaffe, 1964. Piezoelectric and piezomagnetic materials and their functions in transducers, Ed. W.P. Mason, *Physical Acoustics: Principles and Methods*, Academic Press, New York, Vol. **1A**, Chap. 3.
- [2] R. Krimholtz, D.A. Leedom and G.L. Mathaei, 1970. New equivalent circuits for elementary piezoelectric transducers, *Electron. Lett.*, **6**, 398-399.
- [3] A. Ballatto, 2001. Modeling piezoelectric and piezomagnetic devices and structures via equivalent networks, *IEEE Trans. Ultrason. Ferroelec. Freq. Control*, **48**(5), 1189-1239.
- [4] R. Ramesh and D.D. Ebenezer, 2008. Equivalent circuit for broadband underwater transducers, *IEEE Trans. Ultrason. Ferroelec. Freq. Control*, **55**, 2079-2083.
- [5] S.Y. Lin, 2004. "Effect of electric load impedances on the performance of sandwich piezoelectric transducers," *IEEE Trans. Ultrason. Ferroelec. Freq. Control*, **5**, 1280-1286.
- [6] D.D. Ebenezer and Nirmala Ravi, 1992. An equivalent circuit approach to determine the in-situ radiation impedance of underwater electroacoustic projectors, *J. Acoust. Soc. India*, **XXI**, 110-115.
- [7] S. Sherritt, S.P. Leary, B.P. Dolgin and Y. Bar-Cohen, 1999. Comparison of the Mason and KLM equivalent circuits for piezoelectric resonators in the thickness mode, *Proc. IEEE Ultrason., Symp.*, **2**, 921-926.
- [8] ATILA - FEM software for elastic, piezoelectric, magnetostrictive and electrostrictive structures radiating in a fluid, (2006), ISEN Recherche, Lille, France.

# Development of acoustic absorber panels for underwater stealth applications

V. G. Jayakumari, Rahna K. Shamsudeen, R. Rajeswari and T. Mukundan  
*Naval Physical and Oceanographic Laboratory, Kochi 682021, India*  
*e-mail: jaya\_gnair@yahoo.co.in*

[Received: 22.02.2017; Revised: 01.08.2017; Accepted: 21.08.2017]

## ABSTRACT

Viscoelastic polyurethane elastomer and its variations containing different geometric inclusions of various shapes were used to design high performance acoustic absorber tiles that can be effective in selected regions of frequency. Using DMA, the dynamic mechanical properties were determined in the low frequency region. Time temperature superposition (TTS) was performed to generate the material properties in the high frequency range (1 to 25 kHz). Acoustic behavior of these materials was modeled using COMSOL which is a commercial FEM code. The modeling results were compared with the analytical results as well as experimental results measured using a water-filled pulse tube facility.

## 1. INTRODUCTION

In the major prevailing techniques used for detecting the presence of a submarine, or any such object, acoustic wave reflection from solid structures is used. To evade such surveillance systems, the outer surface of the submarine hulls is coated with sound absorbing linings [1,2]. These linings are to be of very small thickness, low in weight, and smooth from outside to reduce the drag force from the sea. They should be easily mountable on the submarine hull, and at the same time should retain their mechanical integrity under all sea conditions, all depths and all speeds of the platforms. It is important to develop damping materials suitable for these applications. In many situations, damping obtained with a single material may not be sufficient; rather a combination of different layers of materials may be required [3,4]. Modeling can afford theoretical optimization of performance with respect to material configurations, thickness of different graded layers and effect of size and concentration of various fillers. Analytical modeling of multilayers and prediction of their properties as well as FEM modeling using a suitable software for complicated geometries are feasible [5, 6].

Perforated layers of rubbers were used as acoustic absorbers for many years. The role of voids in damping material can be explained by mode conversion mechanism. *i.e.*, mode conversion of longitudinal deformation to shear deformation is readily achieved at the boundaries of a soft (air filled) cavity in a solid. This is because in polymeric materials shear waves typically travel with very low speeds and are rapidly attenuated. To attenuate the incident sound energy, the shear deformation energy is converted to heat by molecular relaxation, most prominently happening in porous viscoelastic polymer, in which the shear modulus at interface is much lower than the bulk modulus. The cavities may be microscopic (dimension much smaller than the wavelength of sound), or macroscopic with dimensions comparable to at least the shortest sound wavelength (usually the shear wavelength) in the host material, in the frequency range of interest. The

advantage of macroscopic cavities is that large sound absorption can be obtained with a relatively thin coating. An Alberich lining is a direct example of implementation of simple cylindrical holes. A wide variety of cylindrical holes with varying diameters were implemented in a single layer to account for the different resonant frequencies and thus broader absorption range. Conical, modifications of conical shapes are also being tried nowadays for better performances[7-9].

This work was carried out with an objective to arrive at a design that can act as good acoustic absorber over a broad range, or over selected frequencies. Geometries that can give optimum performance of echo reduction with minimum thickness was arrived at with the help of COMSOL FEM modelling. Several variations were studied out of which we could arrive at lot of interesting results that can act as a guide for the design of high performance acoustic absorber panels for underwater applications.

## 2. EXPERIMENTAL

### 2.1 Sample Preparation

The raw materials for polyurethane from Industrial Marketing Company, Pune was used as matrix material for absorber fabrication. The materials were mixed thoroughly and degassed for about two minutes to remove trapped air bubbles. The degassed material was then poured into a preheated mold (at 50°C). The mould was placed in an oven at 60°C for 24 hours and then de-molding was done. An acoustically transparent composition (PU 1) and a composition (PU 2) with higher damping were made by varying the composition of the raw materials. Samples for DMA analysis (20 × 5 × 2 mm) and pulse tube measurements (49 mm dia, 25 mm thickness) were made. For pulse tube specimens, the mould was provided with cylindrical, conical and modified conical protrusions to give the required cavities in the molded specimen. The dimensions of the cylindrical inclusion is 22 mm height and 10 mm dia and for conical inclusion dimension is 22 mm height and 10 mm base dia. A schematic of the modified cone is shown in Fig. 1(a). Fig.1 (b) shows photographs of the samples casted. Thickness of PU matrix between center to center distances of holes was kept 0.5mm in all cases. The samples are designated as PU - CYL, PU - CON and PU - MODCON for PU samples containing cylindrical, conical and modified conical inclusions

### 2.2 Experimental evaluation.

The dynamic mechanical properties of the samples were evaluated using Q 800 DMA (TA Instruments). The test mode, the specimen geometry and dimensions, and the measured stiffness allow calculation of various moduli, viz., complex modulus ( $E^*$ ), storage modulus ( $E'$ ) and loss modulus ( $E''$ ) of the material.

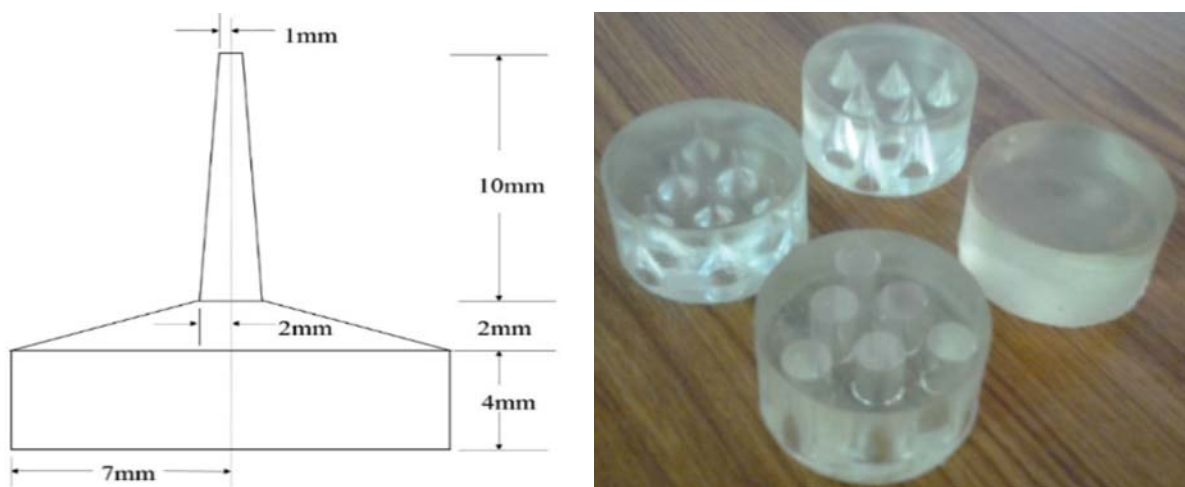


Fig. 1(a). Dimensions optimized for modified conical inclusion, (b) Samples for pulse tube evaluation

The loss tangent,  $\tan \delta$ , which is the ratio of  $E''$  to  $E'$ , is also obtained. The samples were scanned from  $-40^\circ\text{C}$  to  $+50^\circ\text{C}$ . The tests were carried out at frequencies of 0.5, 1, 2, 5, 10, 20 and 50 Hz with a  $5^\circ\text{C}$  step in the temperature range. The isotherms obtained were shifted with respect to a reference temperature of  $30^\circ\text{C}$  with the help of time - temperature superposition (TTS) software (TA Instruments) to produce master curves of dynamic storage modulus ( $E'$ ) and loss factor ( $\tan \delta$ ) in the frequency range of 1 to 25 kHz. TTS was done using the William - Landel - Ferry (WLF) equations [10, 11]. It is well known that linear viscoelastic behavior of amorphous polymers and elastomers obeys the TTS principle. This principle states that characteristic viscoelastic functions measured at different temperatures may be superimposed by parallel shifts along time or frequency axis. This helps to broaden the choice of frequency range using data obtained from experiments at various temperatures over a limited frequency range. The WLF equation is typically used to describe the time - temperature behaviour of polymers in the glass transition region (temperature at which transition from glassy to rubbery stage occurs; denoted as  $T_g$ ). In the transition zone ( $T_g$  to  $T_g + 50^\circ\text{C}$ ), the WLF superposition principle generally applies to many polymers. The WLF equation is

$$\log a_T = \frac{-C_1(T - T_r)}{C_2 + (T - T_r)} \quad (1)$$

where  $a_T$  is the shift factor,  $T_r$  is the reference temperature,  $C_1$  and  $C_2$  are constants and their values at  $T_g$  are;  $C_1 = 17.4$  and  $C_2 = 51.6$ . Once all the individual data points were shifted, a complete master curve for modulus and damping properties was obtained over an extended range of frequencies.

Acoustic properties of the samples were measured using a water-filled pulse tube of 50 mm bore diameter and 1.48 m length in 3 to 15 kHz frequency range [6]. A plane wave of known pressure amplitude propagates along the axis of the pulse tube and meets the specimen at normal incidence. The incident wave is partially reflected at the interface, partially absorbed by the material and partially transmitted through the thickness of the material, as described schematically in Fig. 2(a). The fractions of the incident acoustic signal that are transmitted and reflected are represented as Transmission coefficient (TC) and Reflection coefficient (RC) as defined by

$$\text{TC} = 10 \log (I_t/I_i) = 20 \log (P_t/P_i) \quad (2)$$

and

$$\text{RC} = 10 \log (I_r/I_i) = 20 \log (P_r/P_i) \quad (3)$$

where,  $I_t$ ,  $I_r$  and  $I_i$  are the intensities of the transmitted, reflected and incident waves, and  $P_t$ ,  $P_r$  and  $P_i$  are the corresponding pressure amplitudes, respectively. Echo reduction (ER) is the same as RC with the sign reversed.

The experimental setup for measurement of acoustic property using pulse tube included a transmitter section consisting of an impulse generator (HP 3314 A, Hewlett Packard, California) and a power amplifier L2 (Instruments Inc., California) along with a low pass band filter (B & K 2650, Brüel and Kjaer, Denmark) to prevent excitation of higher order modes in the tube. This excited a transducer that is made up of two lead zirconate rings sandwiched between two metal masses. The transducer is fitted at the bottom of the tube, and it generates a sound pulse that travels along the axis of the tube. A half sine wave was used to excite the transducer. A dynamic signal analyzer (HP 3562 A) was used for recording and for fast Fourier transform of received impulse signals and subsequent analysis. The samples for RC measurements were pasted on the steel back plate of diameter the same as that of the sample, and 10 mm thickness, and was inserted into the tube from the top. The water layer on the top of the sample was removed carefully. The transducer was operated in the trans-receiver mode so that the same was used for generating the acoustic signal and also for receiving the reflected signal. After recording the reflected signal, the sample was removed, and the reflection from the water-air interface was measured. The ratio of these two measurements is the RC of the test sample as given in Eq. (3).

### 2.3 Analytical modeling

A MATLAB code has been generated to estimate Echo Reduction of a viscoelastic sample using transfer matrix (TM) method. This is a method used to analyze propagation of waves through a stratified medium which can also be extended to layers with holes as geometric inclusions. If the field is known at the beginning of a layer, the field at the end of the layer can be derived from simple matrix operations. A stack of layers can then be represented as a system matrix which is the product of individual matrices. The final step of the method involves converting the system matrix back into reflection and transmission coefficients. The analytical method to derive the transfer matrix starting from the basic equations connecting the state variables of normal stress, shear stress, tangential velocity and normal velocity was used [5,12]. The input parameters were density in  $\text{g/cm}^3$  (1.03 for PU1, 1.07 for PU 2, 0.001 for air inside geometric inclusions and 1.0 for water), storage moduli,  $\tan \delta$ (DMA superposed values) and Poisson's ratio(0.49). Based on these values transfer matrix for each layer is constituted. In a simple case represented here acoustic propagation is through water, PU1/PU2, Steel and air. It is well-known that the transfer matrix of one layer can be multiplied by transfer matrix of the second material to generate the resultant transfer matrix of a multi-layer structure. Mathematically, for multi-layer configuration with n number of layers, the generalized expression can be defined as:

$$TM_{1-n} = TM_1 TM_2 \dots\dots\dots TM_n \quad (4)$$

The reflection coefficient can be evaluated using the expression

$$RC = \frac{\{T_{11}Z_{02} + T_{14} - Z_{01}(T_{41}Z_{02} + T_{44})\}}{\{T_{11}Z_{02} + T_{14} + Z_{01}(T_{41}Z_{02} + T_{44})\}} \quad (5)$$

where,  $Z_{01} = \rho_1 c_1$  and  $Z_{02} = \rho_2 c_2$  and  $\rho_1, c_1, \rho_2$  and  $c_2$  are density and sound speed in the incident medium (water) and transmission medium (air/water), respectively and  $T_{11}, T_{14}$  etc. refers to elements of the transfer matrix and are calculated using the input material properties. For the limiting case of normal excitation (as in our requirement), Echo Reduction (ER) has been computed using the following expression.

$$ER = 20 \log (|1/RC|) \quad (6)$$

### 2.4 FEM modelling

The finite element modeling package COMSOL was used for studying the transmission and reflection characteristics of acoustic materials. The physics interface used was acoustics-structure interaction that combines the pressure acoustics, frequency domain and solid mechanics interfaces to connect the acoustic pressure in a fluid domain with the structural deformation in the solid domain. Special interface conditions define the fluid loads on the solid domain and the structural acceleration's effect on the fluid. A plate that extends infinitely in the lateral dimensions but has finite thickness can be studied by modeling a small portion of the material and applying periodic boundary conditions on the lateral sides. Acoustic plane waves of known amplitude and frequency are assumed to propagate in the positive z-direction from the fluid medium. Mesh size is to be set according to the shortest wavelength expected during the event. Physics controlled meshing system with fine option in COMSOL was used to generate mesh according to the physics governing each component and maximum element size is  $1/5^{\text{th}}$  of wavelength. All four sides are given roller condition to restrict radial deformation and thus simulate infinite condition. The schematic diagram of the acoustic material in the form of tiles considered in the present modeling study is as shown in Fig. 2(a). The boundary pressure probes M1, M2 and M3 were introduced to extract incident, reflected and transmitted sound pressures[13]. These values were used for calculation of RC as given in eq. (3) and from the same echo reduction was obtained. Air filled inclusions of various geometries such as cylindrical, conical and a modified conical shapes were incorporated in the tile and modeled as shown in Fig. 2(b) - Fig. 2(d)

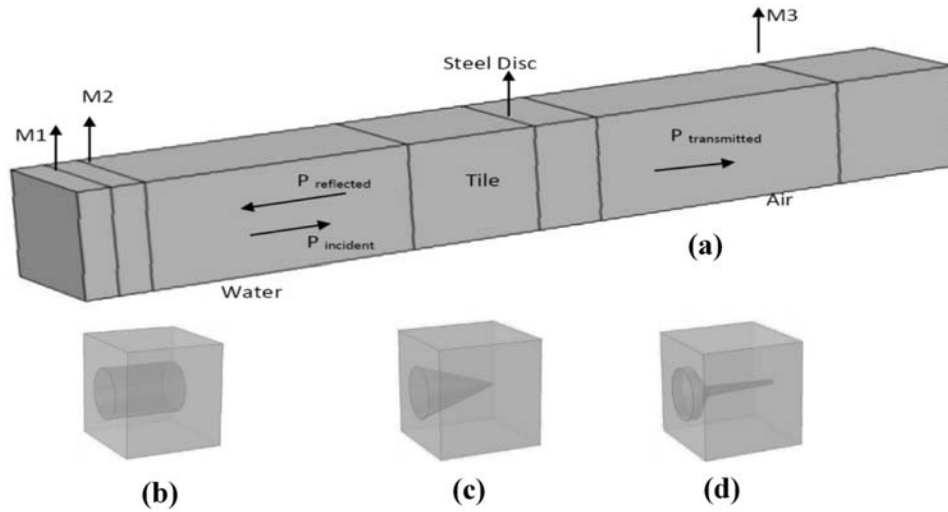


Fig. 2(a). Schematic of the acoustic wave propagation, (b) Tile portion with cylindrical (c) conical (d) modified conical geometries used for FEM modelling, showing boundary pressure probes M1, M2 and M3

### 3. RESULTS AND DISCUSSION

#### 3.1 DMA analysis

Fig. 3(a) and Fig. 3(b) show TTS predicted values of storage modulus  $E'$  and  $\tan \delta$  for PU1 and PU2, respectively at frequencies up to 25 kHz. Storage modulus represents the stored energy and  $\tan \delta$  gives the damping efficiency as dissipated heat in a viscoelastic material. PU 2 shows lower storage modulus and higher  $\tan \delta$  compared to PU1 and therefore it is a more damping composition. These results were used for modeling studies.

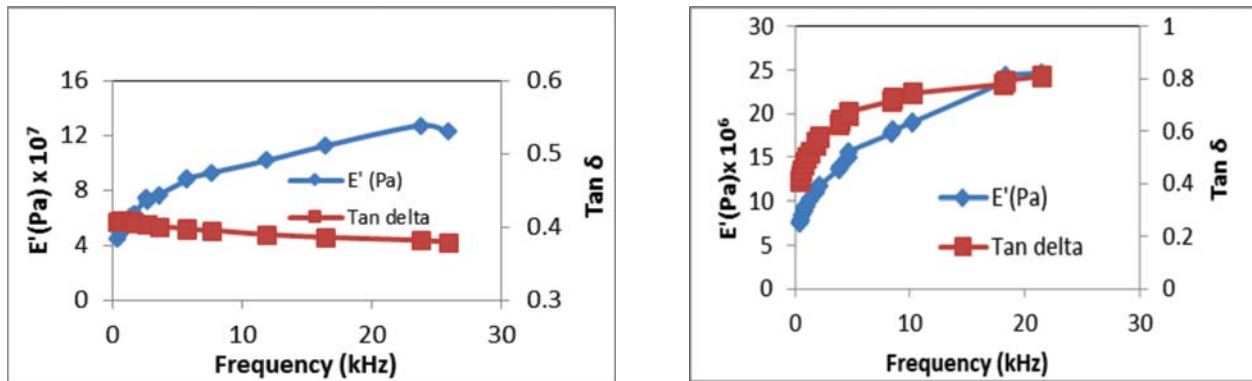


Fig. 3. TTS data for (a) PU1 and (b) PU 2

#### 3.2 Modeling and validation

As a first step, an evaluation of COMSOL for FEM modeling of acoustic materials was carried out for PU 1 and PU 2 samples (25 mm thick) using analytical modeling and the results were also compared with experimental evaluation using pulse tube set up. Fig. 4(a) and Fig. 4(b) show that the results are matching

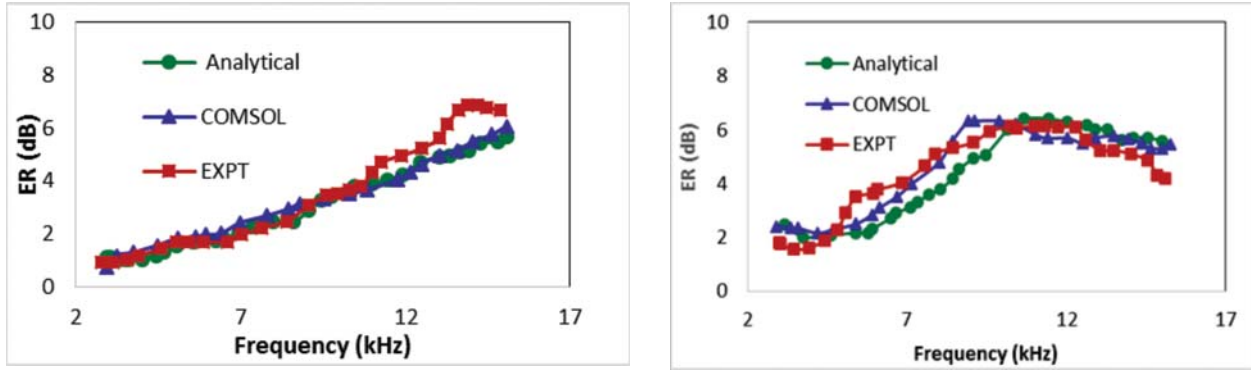


Fig. 4. Validation of COMSOL results using analytical and experimental techniques for (a) PU1, (b) PU2 with no inclusions

very well for PU 1 as well as PU 2. Analytical modeling was done using transfer matrix method described earlier.

Fig. 5(a) shows the effect of thickness on ER. The higher damping composition PU 2 was selected for these studies. It was observed that as the thickness increases the maximum damping peak shifts to lower frequency side as expected. In order to optimize dimensions of inclusions to get optimum performance, parametric sweep method available in COMSOL was used to find the dimension that gives the best performance. This technique was applied for each geometric inclusion, thus varying all the individual dimensions possible within the limit of thickness. Fig. 5 (b) shows results for one of the dimensions (20 mm thick) chosen for each type of inclusion that gave best performance. Conical and modified conical geometries are more effective for a broader range of frequencies than cylindrical inclusions. Maximum attenuation is obtained for frequencies where resonance occurs for the air inside geometric inclusions [14]. Attenuation is due to mode conversion and associated molecular relaxation processes explained earlier. After the resonance peak, viscoelastic effect of polymer matrix is the predominant factor for attenuation which is higher at frequencies where damping factor  $\tan \delta$  is high. Therefore PU 2 that has maximum material effect compared to samples with air inclusions gives better result than PU 2 - CYL and PU 2 - CON at higher frequencies. At lower frequencies resonance effect is predominant. PU 2 - MODCON showed a different behavior expected due to different shape for the geometry and that has got more material content also compared to cylindrical and conical inclusions.

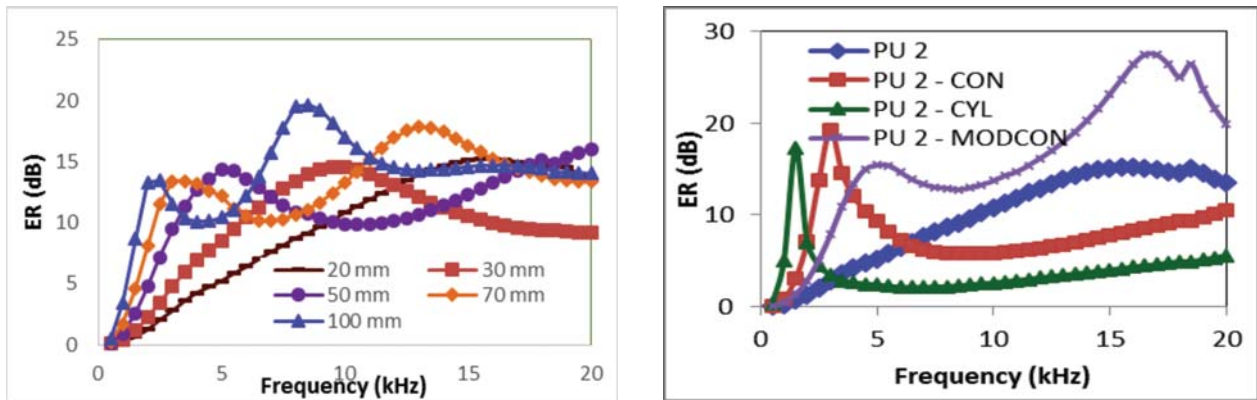


Fig. 5(a) Effect of thickness on ER, (b) Effect of variation in geometric inclusions



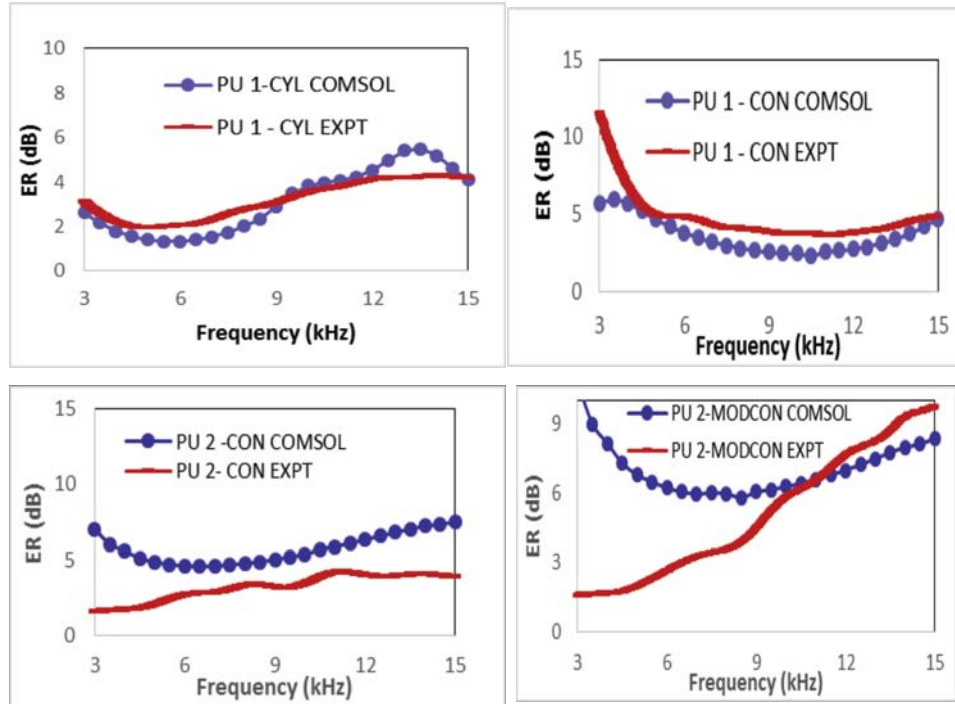


Fig. 6. Comparison of modeling and experimental results for (a) PU1 with cylindrical inclusions (b) PU1 with conical inclusions (c) PU2 with conical inclusions (d) PU2 with modified conical inclusions

Further, validation of modeling results were carried out by comparing with acoustic evaluation results of samples with the same geometries in pulse tube set up. Results for PU1 with cylindrical and conical inclusions and PU 2 with conical and modified conical inclusions are shown in Fig. 6(a) - Fig. 6(d). All the samples are 25 mm thick. The results show very good match in most of the cases. The comparison was done in 3 to 15 kHz frequency region only due to the limitations of the experimental set up. In some cases a deviation between modeling and experimental results were observed at some frequencies when compared to results given in Fig. 4 for PU1 and PU 2, that are polyurethanes with no geometric inclusions. The difference obtained for samples with geometric inclusions can be due to some coupling of resonances due to air inclusions which needs further investigation. But, overall, these studies can act as a guide to selection of materials, thickness, shape and size of inclusions for application at selected frequencies.

#### 4. CONCLUSIONS

FEM Modeling was used to predict the effect of thickness of absorber layer, effect of variations in viscoelastic properties and effect of resonant geometric inclusions on echo reduction performance. It was observed that COMSOL acoustic modelling software can be effectively used for the design of high performance absorbers effective in various frequency regions as required. Two compositions based on polyurethanes and with geometric inclusions of three different shapes were developed and experimentally evaluated their acoustic performance. These materials can be cast in any desired size and thickness for their application as absorber panels for underwater stealth applications.

#### 5. ACKNOWLEDGEMENTS

The authors thank Director, NPOL for granting permission to publish this work, Transducer Group, NPOL for providing the acoustic measurement support and Dr. S. N. Panigrahi, IIT, Bhubaneswar for modeling support.

## 6. REFERENCES

- [1] R.D. Corsaro and L.H. Sperling, 1990. Eds., Sound and Vibration Damping with Polymers, ACS, Washington DC.
- [2] H. Meng, J. Wen, H. Zhao, Lv Linmei and X. Wen, 2012. Analysis of absorption performance of anechoic layers with steel back plating, *J. Acoustical Soc. America*, **132**(1), 69-75.
- [3] T. Wang, S. Chen, Q. wang and X. Pei, 2010. Damping analysis of polyurethane/epoxy graft interpenetrating polymer network composites filled with short carbon fiber and micro hollow glass bead, *Materials and Design*, **31**, 3810-3815.
- [4] B. Philip, J. K.Abraham, V. K.Varadan, V.Natarajan and V. G.Jayakumari, 2004. Passive underwater acoustic damping materials with Rho-C rubber - carbon fiber and molecular sieves, *Smart Mater. Struct.*, **13**, N99-N104.
- [5] G.S. Sharma, A. Skvortsov, I. MacGillIvray and N. Kessissoglou, 2016. Sound transmission through periodically voided soft elastic medium submerged in water, Wave motion, DOI: <http://dx.doi.org/10.1016/j.wavemoti.2016.10.006>
- [6] V.G. Jayakumari, Rahna K. Shamsudeen, R. Ramesh and T. Mukundan, 2011. Modeling and validation of polyurethane based passive underwater acoustic absorbers., *J. Acoustical Soc. America*, **130**(2), 724-730.
- [7] S.M. Ivansson, 2008. Numerical design of Alberich anechoic coatings with superellipsoidal cavities of mixed sizes, *J. Acoustical Soc. America.*, **124**, 1974-1984.
- [8] T. Meng, 2014. Simplified model for predicting acoustic performance of an underwater sound absorption coating, *Journal of Vibration and Control*, **20**, 339-354.
- [9] G.C. Gaunard, 1977. One dimensional model for acoustic absorption in a viscoelastic medium containing short cylindrical cavities, *J. Acoustical Soc. America*. **62**, 298-307.
- [10] M.L. Williams, R.F. Landel and J.D. Ferry, 1955. The temperature dependence of relaxation mechanisms in amorphous and other glass forming liquids, *J. Acoustical Soc. America*, **77**, 3701-3707.
- [11] J.D. Ferry, 1980. Viscoelastic properties of polymers, Wiley, New York, pp. 287-290.
- [12] J.S. Sastry and M.L. Munjal, 1995. A transfer matrix approach for evaluation of the response of a multi-layer infinite plate to a two-dimensional pressure excitation, *Journal of Sound and Vibration*, **182**, 109-128.
- [13] A.F. Sybert and D.F. Ross, 1976. Experimental determination of acoustic properties using a two-microphone random-excitation technique. *J. Acoustical Soc. America*, **61**, 1362-1370.
- [14] [https://en.wikipedia.org/wiki/Acoustic\\_resonance](https://en.wikipedia.org/wiki/Acoustic_resonance)

# Studies on influence of curing agents on carbon black and nanoclay reinforced chloroprene rubber for acoustic sensor applications

P. Annadurai<sup>1\*</sup>, P. Jayesh<sup>1</sup>, T. Mukundan<sup>1</sup>, Rani Joseph<sup>2</sup> and T. Santhanakrishnan<sup>1</sup>

<sup>1</sup>Naval Physical and Oceanographic Laboratory, Kochi 682021, Kerala, India.

<sup>2</sup>Department of Polymer Science and Rubber Technology, CUSAT, Kochi 682022, Kerala.

\*e-mail: annanpol@yahoo.com

[Received: 08.06.2017; Revised: 15.07.2017; Accepted: 27.07.2017]

## ABSTRACT

Rubber compounds are widely used for encapsulation of underwater acoustic sensors. The curing agents play a major role in determining the mechanical and water resistant properties of these rubber compounds. Therefore, the judicious selection of curing agents is very much vital. The present paper investigates the influence of curing agents on nanoclay and carbon black/nanoclay reinforced chloroprene rubber compounds to select the best possible composition. The rubber composite filled with dual phase fillers and lead oxide curative shows higher tensile, tear, improved water resistance and ageing characteristics in comparison to the ZnO/MgO curative system.

## 1. INTRODUCTION

Electro-acoustic transducers are widely used for communication and detection of targets in underwater scenario. Polychloroprene or Chloroprene rubber (CR) is one of the prominent synthetic rubbers extensively used in the area of underwater sensor technologies [1]. Chloroprene rubber is most attractive due to inherent characteristics of balance of properties like easy processability, flame retardency, superior strength and bondability with dissimilar substrates [2, 3]. A combination of these properties is very essential for development of encapsulant materials used for underwater sensor application. The primary function of encapsulation material is to shield the acoustic sensors from physical damage and water ingress and also work as an electrical insulator [4]. The mechanical, electrical and dynamic properties of the final rubber products are influenced by various factors such as the nature of rubbers, types of fillers, curing system and temperature [5]. Earlier studies [6, 7] have shown that use of Carbon black (CB)/Nanoclay (NC) hybrid filler in rubber matrix resulted in considerable improvement of technical properties compared to conventional micro composites which are made using only conventional fillers. Chloroprene rubber is generally vulcanized using metallic oxides curing systems [8, 9]. A combination of magnesium oxide (MgO) and zinc oxide (ZnO) is a common curative and generally results in a good balance of processing safety and cure rate. One of the key concerns when using CR is its higher percentage of water absorption under continuous exposure to sea environments and related changes in properties. For improved water resistance, a red lead (Pb3O4) is commonly employed in curing CR [10]. Conventional rubber composite filled with CB and curing agents are in practice. However the effect of curing agents on NC and CB/NC reinforced chloroprene rubber for underwater rubber encapsulation has not been reported much in the literature. In this study, influence of curing agents on NC and CB/NC reinforced chloroprene rubber compounds are examined in order to

evaluate the best possible composition for under water acoustic encapsulant. In this paper, studies on the effect of two types of curing agents on the cure behaviour, rubber filler interaction, mechanical and electrical properties, and changes in these properties after salt water ageing are carried out to identify the better composite for use as an encapsulant of underwater sensors.

## 2. EXPERIMENTAL

### 2.1 Materials and Instrument Techniques

The elastomer used is chloroprene rubber (Neoprene W grade of Dupont Dow Elastomers, USA) supplied by M/s. Pollmann India Limited, Mumbai. Zinc oxide (Sp. gravity - 5.5, Zinc oxide content - 98%) was supplied by M/s Meta Zinc Ltd., Mumbai. Active Magnesium oxide (AR grade of sp. gravity 3.2) was supplied by S D Fine Chemicals, Mumbai. Nanoclay (Cloisite15A) was purchased from the Southern Clay, USA. Fast extrusion furnace black (FEF) was procured from Philips Carbon Black, India. All other compounding ingredients such as Polymerized 2,2,4 trimethyl 1,2-dihydroquinoline (Vulcanox HS), N-(1,3-Dimethylbutyl)-N-phenyl-p-phenylenediamine (Vulcanox 4020), red lead (Pb3O4), ethylene thiourea (NA-22) and Benzothiasoledisulphide (MBTS) etc., were obtained from local rubber chemical suppliers.

The cure characteristics and rubber filler interaction of the different rubber compositions are studied by Rubber Process Analyser (RPA 3000), M/s. Montech, Germany. Tensile and tear strength properties are carried out by a Universal Testing Machine (Zwick 1476). X ray diffraction (XRD) studies are performed to see the dispersion of filler in a polymers matrix on a Philips X-ray diffractometer (40 kV, 40 mA) in the range of  $2\theta = 2.0$  to 10 degree. The  $d$  spacing is calculated using the Bragg's Law formula  $2d \sin \theta = n\lambda$ ; where  $n$  is the order of Bragg's diffraction,  $\lambda$  is the wavelength of X-ray,  $d$  is the interplanar distance, and  $\theta$  is the angle of incidence of X-ray. The dynamic mechanical property of the composites is studied by using a dynamic mechanical analyzer (DMA Q 800).

### 2.2 Preparation of Compound Formulation

The compound formulations for both zinc oxide and lead oxide are prepared in a laboratory size two roll mill and are given in Table 1. Mixing of compound for gum samples is done as per the order in single stage mixing but for nanoclay filled compound, master batch containing CR and nanoclay is prepared first and then other ingredients are mixed as per the formulation given in Table 1. The gum sample (Gum) does not contain any filler whereas sample NC contains nanoclay and sample NB3 contains both nanoclay and carbon black.

**Table 1. Compound formulation**

Ingredients	Gum/Z	NC/Z	NB3/Z	Gum/Pb	NC/Pb	NB3/Pb
Neoprene W	100	100	100	100	100	100
Nanoclay	-	5	5	-	5	5
MgO	4	4	4	-	-	-
Stearic acid	1	1	1	1	1	1
Vulcanox HS	1	1	1	1	1	1
Vulcanox 4020	1	1	1	1	1	1
FEF	-	-	15	-	-	15
Pb3O4	-	-	-	6	6	6
ZnO	5	5	5	-	-	-
NA 22	0.6	0.6	0.6	0.6	0.6	0.6
MBTS	-	-	-	1.5	1.5	1.5
Total	112.6	117.6	132.6	111.1	116.1	131.1

### 3. RESULTS AND DISCUSSIONS

#### 3.1 Cure Characteristics

The cure characteristics of the different rubber compounds listed in Table 1 from Gum/Z to NB3/Pb are studied at 150°C as per respective cure time obtained from rheogram and are given in Table 2.

Table 2. Cure Characteristics of Rubber Compounds

Sample Designation	Minimum torque (dNm)	Maximum torque (dNm)	Scorch time ts2 (min)	Optimum cure time t90 (min)
Gum/Z	0.48	4.20	5.63	19.22
NC/Z	0.56	4.59	7.03	26.59
NB3/Z	0.73	7.56	4.67	19.87
Gum/Pb	0.53	4.64	5.14	17.71
NC/Pb	0.55	4.93	6.76	16.53
NB3/Pb	0.89	7.71	4.40	15.95

The results show that cure reaction is fast with comparable scorch safety for red lead system compared to zinc oxide. For nanoclay and dual filler filled rubber compound, the cure times for red lead cured sample are 16 and 15 min, respectively whereas the cure times are 19 and 26 min, respectively for zinc oxide.

#### 3.2 Strain Sweep Studies

The strain sweep measurements on vulcanized samples are conducted using RPA 3000 to study the rubber-filler interaction and the results are shown in Fig. 1. The storage modulus  $G'$  which represents the stored energy and hence the elastic portion is measured. The effect of strain amplitude on the storage modulus  $G'$  is called Payne effect. The testing temperature is 100°C and the shear strain is varied from 0.5% to 90% keeping the frequency of measurements at 1.0 Hz. Results show that the difference in storage modulus measured at 1% and 90% of strain is 132 kPa for NB3/Pb sample and 194 kPa for NB3/Z. The sample NB3/Pb shows lower value of storage modulus (*i.e.* low Payne effect) due to better polymer filler interaction compared to sample NB3/Z.

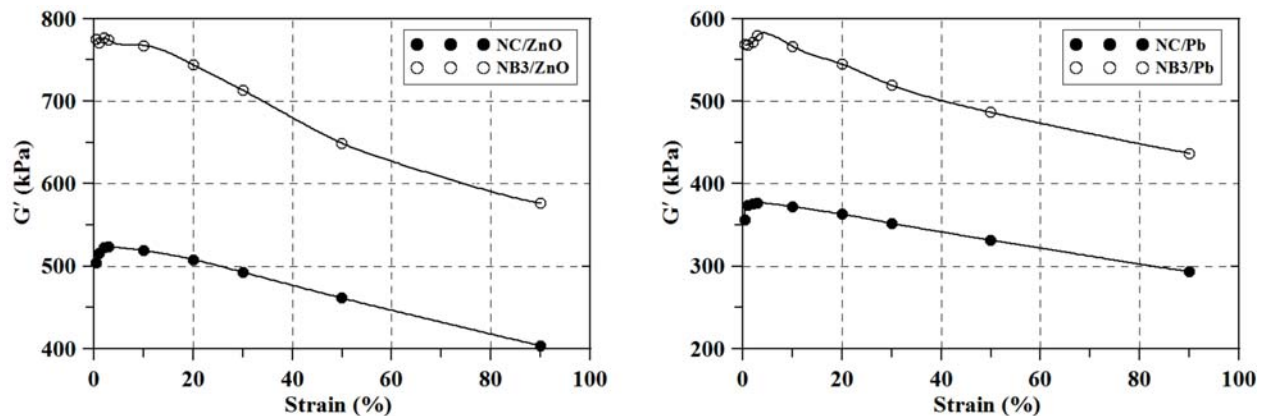


Fig. 1. Strain sweep for composites cured with Zinc and Lead Oxides

### 3.3 Physico-mechanical Properties

The effects of zinc oxide and red lead on the physico-mechanical properties are studied as per ASTM standards and the results obtained from an average value of the five test specimens are given in Table 3.

**Table 3. Physico-mechanical properties of compounds**

Properties	Test standard	SAMPLE DESCRIPTION					
		Gum/Z	NC/Z	NB3/Z	Gum/Pb	NC/Pb	NB3/Pb
Hardness, Shore	AASTM D 2240	38	41	51	37	42	50
Salt water absorption, % at 40 °C for 24 hrs (after 1 week)	ASTM D 471	0.68 (1.81)	0.65 (1.75)	0.60 (1.65)	0.31 (0.66)	0.29 (0.60)	0.26 (0.28)
Tensile strength (MPa)	ASTM D 412	8.60	11.35	19.21	8.31	11.19	18.66
M 300% (MPa)	ASTM D 412	1.58	2.70	4.96	1.52	2.09	4.24
Elongation at Break, %	ASTM D 412	1081	1061	849	1085	1061	901
Tear strength (N/cm)	ASTM D 624	192	263	455	183	254	412
Volume Resistivity @1000V, Ω cm	ASTM D 257	4.80 × 10 <sup>10</sup>	5.08 × 10 <sup>10</sup>	6.23 × 10 <sup>10</sup>	6.99 × 10 <sup>10</sup>	5.16 × 10 <sup>11</sup>	5.12 × 10 <sup>11</sup>

From Table 3, it is observed that there is no significant difference in the tensile and tear strength properties. The compound with zinc oxide shows marginally higher modulus, tensile strength and comparable electrical resistivity characteristics. Though, comparable mechanical and electrical properties are obtained for both curative filled systems, the water absorption of compound with lead oxide curing system is lower than the compound with zinc oxide based cure system. The effect of compound and curing system on tensile strength before and after ageing at 40°C for 7 days is studied and the results are shown in Fig. 2. Similar to lower water absorption, retention of tensile strength property after saltwater ageing is higher for compound with lead oxide cure system.

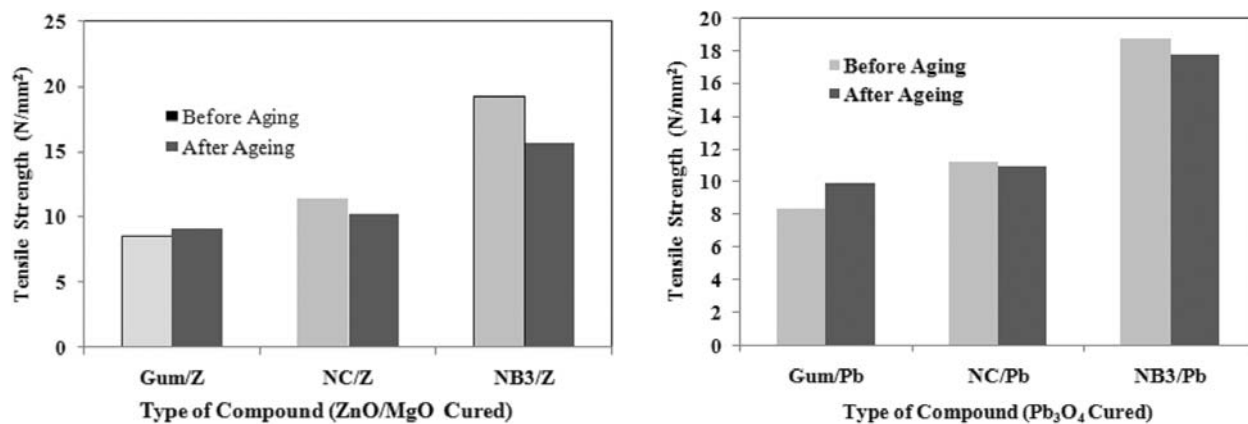


**Fig. 2. Effect of compound and curing agent on tensile strength**

The maximum retention of properties on ageing is observed for the compound cured by lead oxide system. This can be explained on the basis of formation of by-product during curing reaction. The by-product PbCl<sub>2</sub> is more hydrophobic compared to the formation of MgCl<sub>2</sub> and absorbs less water in saltwater environment compared to zinc oxide curing.

### 3.4 Morphology by XRD

The XRD results on organo-clay powder (nanoclay), nanoclay filled CR composites (NC/Z and NC/Pb) and optimised compound containing both nanoclay and carbon black (NB3/Z and NB3/Pb) are shown in Figs. 3-5.

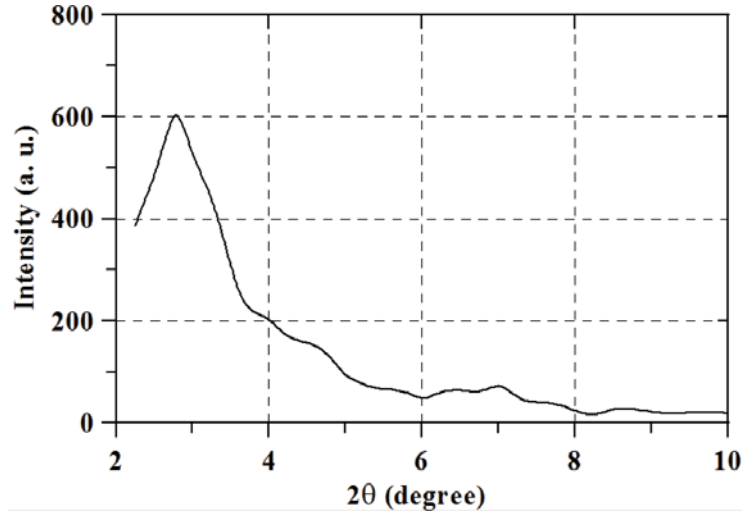


Fig. 3. XRD Graphs for nanoclay

The nanoclay powder shows intensity peak at  $2\theta = 2.9^\circ$  and  $7^\circ$ . These two main peaks are attributed to the presence of different length of the alkyl chain and the amount of intercalant in the clay platelets.

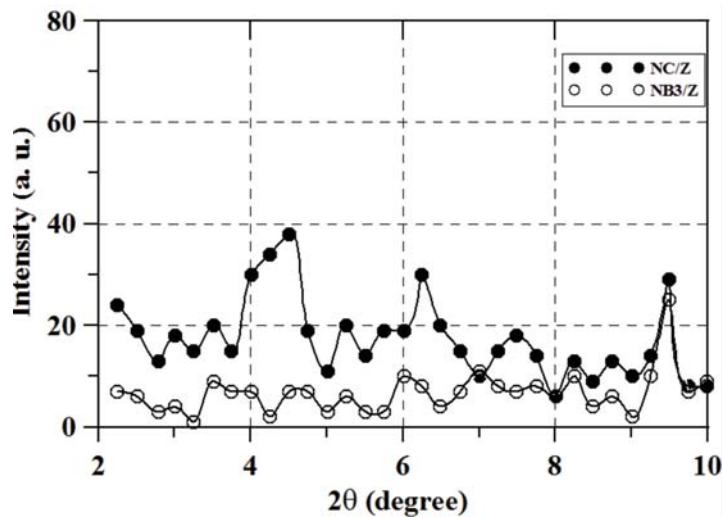


Fig. 4. XRD Graphs for nanoclay and hybrid filler composites cured by ZnO

But addition of nanoclay and carbon black with curing agents into the rubber matrix lowers the intensity of the peak due to carbon black effect on intercalation of CR macromolecules through the clay platelets. The intensity of the peak reduced for the composites cured by lead oxides compared to composites cured by ZnO system. This can be explained due to faster activity of lead oxide, which facilitates interaction of fillers and increases the gallery gap of nanoclay for improved intercalation.

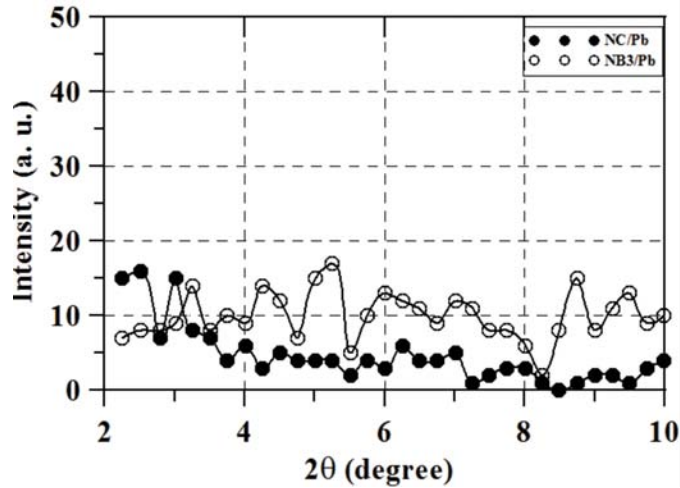


Fig. 5. XRD Graphs for nanoclay and hybrid filler composites cured by  $Pb_3O_4$

### 3.5 Dynamic Mechanical Properties

The dynamic temperature sweep tests are conducted within a temperature range of  $-60^\circ C$  to  $+50^\circ C$  at a heating rate of  $5^\circ C/min$  keeping fixed frequency as 1 Hz and strain at 0.25%. The results are shown in Figs. 6 and 7.

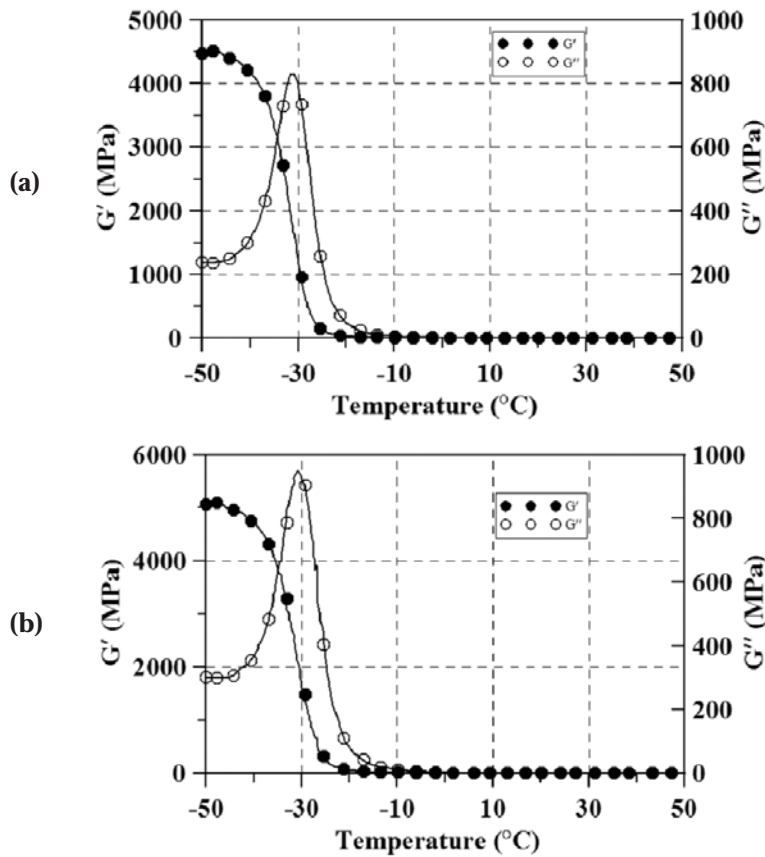


Fig. 6. Dynamic modulus of compound with curing system (a) NB3ZnO and (b) NB3PbO



The results indicate that both cured systems show comparable storage and loss modulus. The loss modulus measures the energy dissipated as heat representing the viscous portion of the compound. The low value of tan delta was obtained for the composite cured with lead oxide than that of zinc oxide. The composites of having lower damping constant (tan delta) values are also considered to be acoustically transparent material

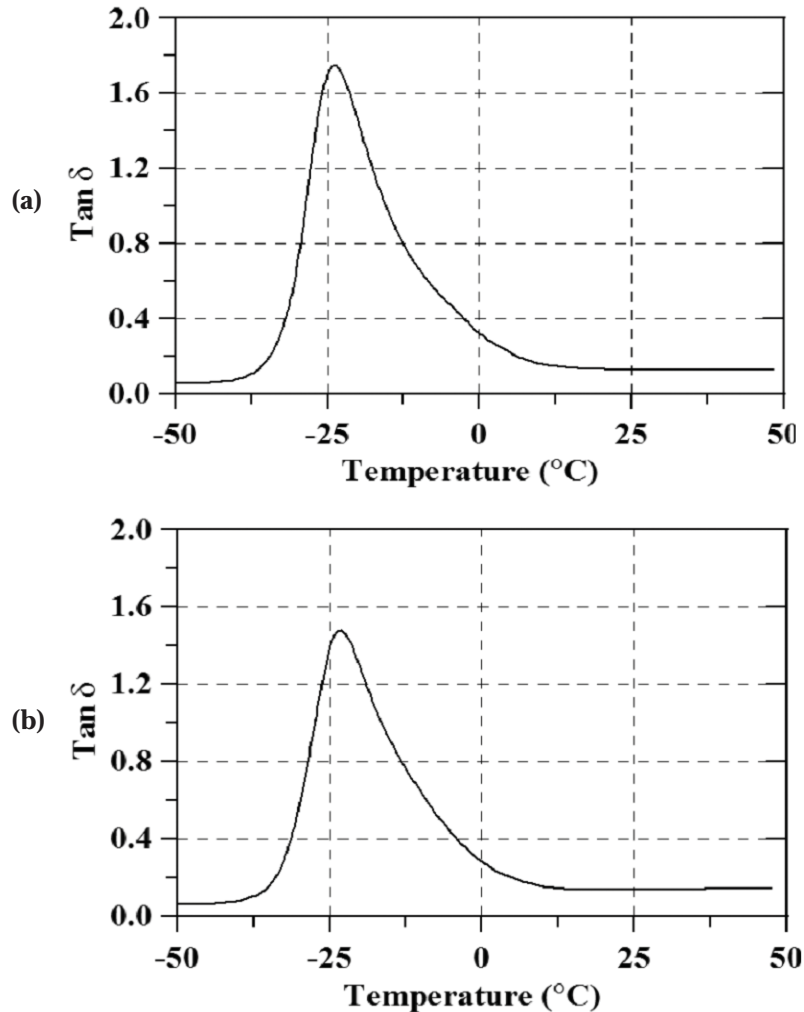


Fig. 7. Damping constant of compound with curing system (a) NB3ZnO and (b) NB3PbO

#### 4. CONCLUSION

In this work, the effect of curing agents on nanoclay and dual fillers reinforced chloroprene (CR) rubber are investigated. The results show that cure reaction is fast and improved polymer filler interaction is obtained for sample NB3/Pb compared to NB3/Z. Compound cured with lead oxide show lower water absorption and maximum retention of strength properties on ageing although compound cured with zinc oxide systems shows comparable electrical and mechanical properties. DMA studies confirmed that lead oxide cure gives slightly better storage modulus and lower damping constant, which is important for encapsulation materials. It is concluded that carbon black and nanoclay in right proportion and cured by lead oxide cure system gives best balance of properties in CR based rubber compound and therefore, this compound is suggested for use as encapsulant materials for underwater acoustic sensor applications.

## 5. ACKNOWLEDGEMENT

Authors are thankful to the Director, NPOL for granting permission to publish this work.

## 6. REFERENCES

- [1] R.N. Capps, F J Weber and T.M Thompson, 1981. *Hand book of Sonar passive materials*, Memmo. Report. 4311, NRL, Washington DC.
- [2] G.E. Jones, D.S. Tracey and A.L. Tisler, 2001. *Rubber Technology Compounding and Testing for Performance*, John S. Dick, Ed.; Hanser Publishers, Munich.
- [3] C.M. Blow, 1981. *Rubber Technology and Manufacture*, Butterworths.
- [4] A.W. Cox, 1974. *Sonar and Underwater Sound*, Lexington Books, Lexington, MA.
- [5] V.B. Pillai and J.N. Das, 1992. Influence of carbon black filler types on dynamic mechanical properties of certain underwater polychloroprene rubber vulcanizates, *Plastics, Rubber and Composites Processing and Applications*, **18**(3), 155-60.
- [6] P. Annadurai, T. Mukundan, Rani Joseph and T. Santhanakrishnan, 2013. Influence of carbon black in polychloroprene organoclay nanocomposite with improved mechanical, electrical and morphology characteristics, *Intl. Journal of Plastics, Rubber and Composites*, **42**(9), 379-384.
- [7] P. Annadurai, S. Kumar, T. Mukundan, Rani Joseph, P. Sarkar and S. Chattopadhyay, 2014. Effect of two stage mixing & dispersion agent on morphology and dynamic mechanical properties of CR/CB/ Nanoclay compositions for underwater acoustic application, *Intl. conference on Polymers and Allied Materials*, IIT, Patna, 30-34.
- [8] J.A. Brydson, 1978. *Rubber Chemistry*, Applied Science Publishers Ltd, London.
- [9] R.S. Graff, 1987. *Rubber Technology*, Edited. Maurice Morton, Van Nostrand Reinhold, New York.
- [10] H. Ismail and H.C. Leong, 2001. Curing characteristics and mechanical properties of natural rubber/ chloroprene rubber and epoxidised natural rubber/ chloroprene rubber blends, *Polymer Testing* **20**, 509-516.

# INFORMATION FOR AUTHORS

## ARTICLES

The Journal of Acoustical Society of India (JASI) is a refereed publication published quarterly by the Acoustical Society of India (ASI). JASI includes refereed articles, technical notes, letters-to-the-editor, book review and announcements of general interest to readers.

Articles may be theoretical or experimental in nature. But those which combine theoretical and experimental approaches to solve acoustics problems are particularly welcome. Technical notes, letters-to-the-editor and announcements may also be submitted. Articles must not have been published previously in other engineering or scientific journals. Articles in the following are particularly encouraged: applied acoustics, acoustical materials, active noise & vibration control, bioacoustics, communication acoustics including speech, computational acoustics, electro-acoustics and audio engineering, environmental acoustics, musical acoustics, non-linear acoustics, noise, physical acoustics, physiological and psychological acoustics, quieter technologies, room and building acoustics, structural acoustics and vibration, ultrasonics, underwater acoustics.

Authors whose articles are accepted for publication must transfer copyright of their articles to the ASI. This transfer involves publication only and does not in any way alter the author's traditional right regarding his/her articles.

## PREPARATION OF MANUSCRIPTS

All manuscripts are refereed by at least two referees and are reviewed by the Publication Committee (all editors) before acceptance. Manuscripts of articles and technical notes should be submitted for review electronically to the Chief Editor by e-mail or by express mail on a disc. JASI maintains a high standard in the reviewing process and only accept papers of high quality. On acceptance, revised articles of all authors should be submitted to the Chief Editor by e-mail or by express mail.

Text of the manuscript should be double-spaced on A4 size paper, subdivided by main headings-typed in upper and lower case flush centre, with one line of space above and below and sub-headings within a section-typed in upper and lower case understood, flush left, followed by a period. Sub-sub headings should be italic. Articles should be written so that readers in different fields of acoustics can understand them easily. Manuscripts are only published if not normally exceeding twenty double-spaced text pages. If figures and illustrations are included then normally they should be restricted to no more than twelve-fifteen.

The first page of manuscripts should include on separate lines, the title of article, the names, of authors, affiliations and mailing addresses of authors in upper and lower case. Do not include the author's title, position or degrees. Give an adequate post office address including pin or other postal code and the name of the city. An abstract of not more than 200 words should be included with each article. References should be numbered consecutively throughout the article with the number appearing as a superscript at the end of the sentence unless such placement causes ambiguity. The references should be grouped together, double spaced at the end of the article on a separate page. Footnotes are discouraged. Abbreviations and special terms must be defined if used.

## EQUATIONS

Mathematical expressions should be typewritten as completely as possible. Equation should be numbered consecutively throughout the body of the article at the right hand margin in parentheses. Use letters and numbers for any equations in an appendix: Appendix A: (A1, (A2), etc. Equation numbers in the running text should be enclosed in parentheses, i.e., Eq. (1), Eqs. (1a) and (2a). Figures should be referred to as Fig. 1, Fig. 2, etc. Reference to table is in full: Table 1, Table 2, etc. Metric units should be used: the preferred from of metric unit is the System International (SI).

## REFERENCES

The order and style of information differs slightly between periodical and book references and between published and unpublished references, depending on the available publication entries. A few examples are shown below.

### Periodicals:

- [1] S.R. Pride and M.W. Haartsen, 1996. Electro seismic wave properties, *J. Acoust. Soc. Am.*, **100** (3), 1301-1315.
- [2] S.-H. Kim and I. Lee, 1996. Aeroelastic analysis of a flexible airfoil with free play non-linearity, *J. Sound Vib.*, **193** (4), 823-846.

### Books:

- [1] E.S. Skudrzyk, 1968. *Simple and Complex Vibratory Systems*, the Pennsylvania State University Press, London.
- [2] E.H. Dowell, 1975. *Aeroelasticity of plates and shells*, Nordhoff, Leyden.

### Others:

- [1] J.N. Yang and A. Akbarpour, 1987. Technical Report NCEER-87-0007, Instantaneous Optimal Control Law For Tall Buildings Under Seismic Excitations.

## SUBMISSIONS

All materials from authors should be submitted in electronic form to the JASI Chief Editor: B. Chakraborty, CSIR - National Institute of Oceanography, Dona Paula, Goa-403 004, Tel: +91.832.2450.318, Fax: +91.832.2450.602, (e-mail: bishwajit@nio.org) For the item to be published in a given issue of a journal, the manuscript must reach the Chief Editor at least twelve week before the publication date.

## SUBMISSION OF ACCEPTED MANUSCRIPT

On acceptance, revised articles should be submitted in electronic form to the JASI Chief Editor (bishwajit@nio.org)

ISSN 0973-3302

# THE JOURNAL OF ACOUSTICAL SOCIETY OF INDIA

Volume 44

Number 2

April 2017



A Quarterly Publication of the ASI  
<http://www.acousticsindia.org>



# The Journal of Acoustical Society of India

The Refereed Journal of the Acoustical Society of India (JASI)

**CHIEF EDITOR:**

**B. Chakraborty**

CSIR-National Institute of Oceanography

Dona Paula,

Goa-403 004

Tel: +91.832.2450.318

Fax: +91.832.2450.602

E-mail: bishwajit@nio.org

**ASSOCIATE SCIENTIFIC EDITOR:**

**A R Mohanty**

Mechanical Engg. Department

Indian Institute of Technology

Kharagpur-721302, India

Tel. : +91-3222-282944

E-mail : amohantyemech.iitkgp.ernet.in

**Editorial Office:**

**MANAGING EDITOR**

**Mahavir Singh**

**ASSISTANT EDITORS:**

**Yudhisther Kumar**

**Devraj Singh**

**Kirti Soni**

ASI Secretariat,

C/o Acoustics, Ultrasonics & Vibration

Section CSIR-National Physical Laboratory

Dr. KS Krishnan Road

New Delhi 110 012

Tel: +91.11. 4560.8317

Fax: +91.11.4560.9310

E-mail: asisecretariat.india@gmail.com

The **Journal of Acoustical Society of India** is a refereed journal of the Acoustical Society of India (ASI). The ASI is a non-profit national society founded in 31st July, 1971. The primary objective of the society is to advance the science of acoustics by creating an organization that is responsive to the needs of scientists and engineers concerned with acoustics problems all around the world.

Manuscripts of articles, technical notes and letter to the editor should be submitted to the Chief Editor. Copies of articles on specific topics listed above should also be submitted to the respective Associate Scientific Editor. Manuscripts are refereed by at least two referees and are reviewed by Publication Committee (all editors) before acceptance. On acceptance, revised articles with the text and figures scanned as separate files on a diskette should be submitted to the Editor by express mail. Manuscripts of articles must be prepared in strict accordance with the author instructions.

All information concerning subscription, new books, journals, conferences, etc. should be submitted to Chief Editor:

*B. Chakraborty, CSIR - National Institute of Oceanography, Dona Paula, Goa-403 004,  
Tel: +91.832.2450.318, Fax: +91.832.2450.602, e-mail: bishwajit@nio.org*

Annual subscription price including mail postage is Rs. 2500/= for institutions, companies and libraries and Rs. 2500/= for individuals who are not ASI members. The Journal of Acoustical Society of India will be sent to ASI members free of any extra charge. Requests for specimen copies and claims for missing issues as well as address changes should be sent to the Editorial Office:

*ASI Secretariat, C/o Acoustics, Ultrasonics & Vibration Section, CSIR-National Physical Laboratory, Dr. KS Krishnan Road,  
New Delhi 110 012, Tel: +91.11.4560.8317, Fax: +91.11.4560.9310, e-mail: asisecretariat.india@gmail.com*

The journal and all articles and illustrations published herein are protected by copyright. No part of this journal may be translated, reproduced, stored in a retrieval system, or transmitted, in any form or by any means, electronic, mechanical, photocopying, microfilming, recording or otherwise, without written permission of the publisher.

Copyright © 2017, Acoustical Society of India

ISSN 0973-3302

Printed at Alpha Printers, WZ-35/C, Naraina, Near Ring Road, New Delhi-110028 Tel.: 9810804196. JASI is sent to ASI members free of charge.

**B. CHAKRABORTY**  
Chief Editor  
**MAHAVIR SINGH**  
Managing Editor  
**A R MOHANTY**  
Associate Scientific Editor



# The Journal of Acoustical Society of India

A quarterly publication of the Acoustical Society of India

Volume 44, Number 2, April 2017

## ARTICLES

**Yudhishter Kumar Yadav**  
**Devraj Singh**  
**Kirti Soni**  
Assistant Editors

## EDITORIAL BOARD

**M L Munjal**  
IISc Bangalore, India  
**S Narayanan**  
IIT Chennai, India  
**V R SINGH**  
PDM EI New Delhi-NCR, India  
**R J M Craik**  
HWU Edinburg, UK  
**Trevor R T Nightingale**  
NRC Ottawa, Canada  
**N Tandon**  
IIT Delhi, India  
**J H Rindel**  
Odeon A/S, Denmark  
**E S R Rajagopal**  
IISc Bangalore, India  
**G V Anand**  
IISc Bangalore, India  
**S S Agrawal**  
KIIT Gurgaon, India  
**Yukio Kagawa**  
NU Chiba, Japan  
**D D Ebenezer**  
NPOL Kochi, India  
**Sonoko Kuwano**  
OU Osaka, Japan  
**Mahavir Singh**  
CSIR-NPL, New Delhi, India  
**A R Mohanty**  
IIT Kharagpur, India  
**Manell E Zakharia**  
ENSAM Paris, France  
**Arun Kumar**  
IIT Delhi, India  
**Ajesh K. Abraham**  
IISH Mysore, India  
**S V Ranganayakulu**  
GNI Hyderabad, India

- Flow-acoustic lumped element analysis of the side-inlet and axial-outlet combination muffler**  
*Vikas Kumar and M. L. Munjal* ..... 61
- Application of free layer damping treatment for vibration and noise attenuation**  
*V. Ramakrishna, P.V.S. Ganesh Kumar, V. Rama Mohana Rao, D.A. Rao, T.V. Ratnam and K. Seetha Ramaiah* ..... 71
- Analysis of physiographic provinces - marginal highs in the continental slope of India using multibeam and sub-bottom backscatter profiles**  
*Milind Naik, Govind Ranade and Rajesh B Lohani* ..... 78
- Studies of Ultrasonic and acoustic parameters of complexes derived from Copper (II) surfactant of Mustard oil with N and S atoms containing ligands in Non- aqueous media (benzene) at 303.15 K**  
*Pragya Tank, Rashmi Sharma and Arun Kumar Sharma* ..... 87
- Influence of air pollutants to mixing height in different seasons by multiple regressions model in urban region Delhi, India**  
*Kirti Soni\*, Mahavir Singh and Y.K. Yadav* ..... 100
- Evaluation of disc and shell horns sound quality characteristics**  
*Tapan. K. Mahanta and B. Venkatesham* ..... 112

## INFORMATION

Information for Authors

Inside back cover



# Flow-acoustic lumped element analysis of the side-inlet and axial-outlet combination muffler

Vikas Kumar<sup>1</sup> and M. L. Munjal<sup>2</sup>

<sup>1</sup>*Mahindra & Mahindra Ltd., Mahindra Research Valley, Chengalpattu - 603 204*

<sup>2</sup>*Facility for Research in Technical Acoustics (FRITA),*

*Department of Mechanical Engineering, Indian Institute of Science, Bangalore - 560 012*

*e-mail: munjal@iisc.ac.in*

[Received: 31-09-2016; Accepted: 16-01-2017]

## ABSTRACT

The side-inlet type of muffler configuration forces the mean flow as well as acoustic waves to change their direction and hence cannot be analyzed by means of the 1-D plane wave analysis. Internal lining of the muffler makes the modeling still more challenging for sufficiently low frequencies, of the range of the first few firing frequencies of a typical engine showing peaks in the un-muffled sound pressure level. The distributed elements can be approximated as the 0-D or lumped elements in order to obtain a  $2 \times 2$  transfer matrix relating the state variables of the segment involving change of direction of the acoustic waves. For the remaining part of the muffler in which acoustic wave does not change its direction, the usual 1-D plane wave analysis can be used. Lumped flow-resistance network theory is used to evaluate the mean flow distribution throughout the muffler configuration. The transmission loss predicted by using the lumped element analysis has been compared with that of the partial 1-D plane wave analysis and the 3-D finite element analysis (FEA). The comparison shows that the lumped element analysis is able to capture the low frequency performance which is crucial for the design of mufflers for adequate insertion loss for the diesel generators sets.

## 1. INTRODUCTION

The exhaust mufflers used in the DG (Diesel Generator) sets are mounted horizontally on the canopy (acoustic enclosure) because of the logistic reasons and hence demand the side-inlet type of configurations. The outlet-pipe may be installed as side-inlet or axial-outlet. Typically, for a DG set the required insertion loss is at least 25 dBA, for which cross-flow perforated elements are used as essential constituents of the exhaust muffler. The cross-flow perforated element offers high back-pressure as compared to other perforated elements[1]. Therefore, the mean flow velocity in the exhaust/tail pipe is kept low. This results in comparatively large mufflers.

The exhaust gases enter the inlet of the exhaust muffler passing through the exhaust manifold. The side-inlet configuration forces the mean flow as well as the acoustic waves to change its direction while passing through the perforation of the inlet-pipe of the exhaust muffler as shown in Fig. 1. This change in direction of the acoustic waves rules out the usual 1-D plane wave method of analysis. However, 3-D Finite Element Analysis (FEA) can be used to analyze these side-inlet configurations but would be very cumbersome and time consuming if one were to use it for design optimization.



Generally, the lowest natural frequency of the exhaust muffler lies around 50-100 Hz, which is the frequency range in which insertion loss would have a sharp dip and the firing frequency of the engine would lie, representing a peak in unmuffled sound pressure level [1]. Thus it is customary to design a muffler for adequate insertion loss at its firing frequency.

At such low frequencies, the distributed acoustic elements can well be approximated as lumped acoustic elements. The wave number  $k = \omega/c$  would be small enough such that  $\sin kl$  can be approximated as  $kl$  and  $\cos kl$  can be approximated as 1, where  $l$  is the typical length of the exhaust pipe, intermediate pipe(s) and the tail pipe.

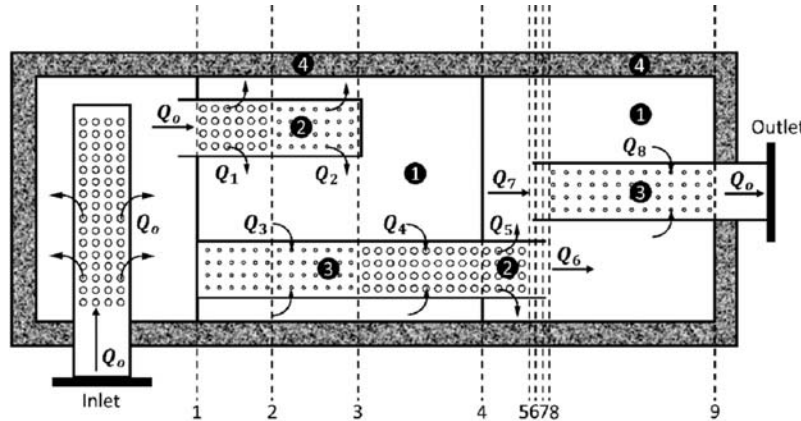


Fig. 1. Schematic diagram of a side-inlet and axial-outlet muffler.

The performance of the side-inlet exhaust muffler configuration has been evaluated using the lumped element analysis and the results thus obtained are compared against that of 1-D plane wave analysis and the 3-D FEA. For the 1-D plane wave analysis, the first chamber of the muffler shown in Fig. 1 has been modelled using the lumped element theory which gives a  $2 \times 2$  matrix relating the inlet state variables (acoustic pressure and acoustic mass velocity) to the state variables at the inlet of the inside pipe-1. The remaining part of the muffler is then analysed using the usual 1-D plane wave method employing the ITM (Integrated Transfer Matrix) approach[2] which results in another  $2 \times 2$  matrix relating the state variables at the inlet of the inside pipe-1 to the state variables at the outlet-pipe of the exhaust muffler. Thus, multiplying these two  $2 \times 2$  matrices, the overall transfer matrix can be obtained for the whole muffler and then the acoustic performance can be predicted using the existing tools as described in Ref.[1]. For the analysis, the viscous effects of the exhaust gasses have been neglected. The end covers and the shell of the muffler are lined with an absorptive layer, as shown in Fig. 1. To evaluate the flow distribution throughout the muffler and back-pressure, the lumped flow-resistance network theory has been used[3].

## 2. DESCRIPTION OF THE MUFFLER CONFIGURATION

The muffler configuration with side-inlet and axial-outlet as shown in Fig. 1 is mounted horizontally on the DG set.

Specifications of the engine on which the muffler configuration is used are listed in Table 1.

Table 1. Engine specifications

Sl. No.	Parameter	Value
1	Number of Cylinders	2
2	Gas Flow (kg/s)	0.0273
3	Exhaust Gas Temperature (°C)	582
4	Gas Velocity at Inlet of Silencer (m/s)	19.6
5	Engine Speed (RPM)	1500

### 3. MEAN FLOW DISTRIBUTION AND BACK-PRESSURE CALCULATION

As shown in Fig. 1, the total mean flow  $Q_0$  enters through the inlet-pipe of the muffler. The flow passes through the perforations of the inlet-pipe and enters the first cavity. From the cavity, the flow enters the inside pipe-1 which has two different types of continuous perforations, thus the flow divides into two parts ( $Q_1$  and  $Q_2$ ) and passes through the perforations and reaches the second cavity. The inside pipe-2 also has two different continuous perforations and the flow divides accordingly into  $Q_3$  and  $Q_4$ . The flow from the inside pipe-2 reaches the third cavity by two different paths. One is the straight opening of the pipe into the third cavity and other part through the extended perforations of the inside pipe-2. The flow combines in the third cavity and divides again into two parts one flows through the perforations of the outlet-pipe and other part goes through the opening of the outlet pipe. The flow-resistance network diagram of the muffler of Fig. 1 is shown in Fig. 2.

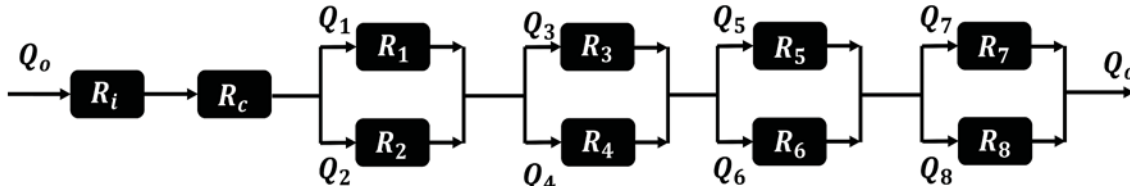


Fig. 2. Flow-resistance network diagram of the muffler configuration of Fig. 1.

In Fig. 2,  $R_1, R_2, R_3, R_4, R_5$  and  $R_8$  are flow-resistances faced by the flow component  $Q_1$  between section 1-2,  $Q_2$  between section 2-3,  $Q_3$  between section 1-3,  $Q_4$  between section 3-4,  $Q_5$  between section 4-5, and  $Q_8$  between section 8-9, respectively.  $R_i$  is the cross flow-resistance of the inlet-pipe, and  $R_c, R_6$  and  $R_7$  are flow-resistances due to sudden contraction at the entrance of inside pipe-1, sudden expansion at the exit of the inside pipe-2, and sudden contraction at the entrance of the outlet pipe, respectively.

The flow-resistance due to perforated section has been calculated using[1, 3, 4],

$$R_{\text{perforate}} = \frac{\rho_0}{2(C_D S_p)^2} \quad (1)$$

where  $\rho_0$  is the density of the medium,  $C_D (= 0.8)$  is the coefficient of discharge and  $S_p$  is the perforated open area. The flow-resistance due to sudden contraction or expansion has been evaluated using[1, 3, 4],

$$R_{\text{entry/exit}} = \epsilon \frac{\rho_0}{2A^2} \quad (2)$$

where  $A$  is the area of cross-section the narrower pipe, and loss coefficient  $\epsilon = 1$  for the outflow (exit) and  $\epsilon = 1/2$  for the inflow (entry). For the circuit shown in Fig. 2, applying Kirchhoff's first law and second law, we have:

$$Q_1 + Q_2 = Q_0, \quad Q_3 + Q_4 = Q_0, \quad Q_5 + Q_6 = Q_0, \quad Q_7 + Q_8 = Q_0. \quad (3a-d)$$

$$R_1 Q_1 |Q_1| - R_2 Q_2 |Q_2| = 0, \quad R_3 Q_3 |Q_3| - R_4 Q_4 |Q_4| = 0 \quad (4a-b)$$

$$R_5 Q_5 |Q_5| - R_6 Q_6 |Q_6| = 0, \quad R_7 Q_7 |Q_7| - R_8 Q_8 |Q_8| = 0 \quad (5a-b)$$

The above system of equations can be solved in terms of  $Q_0$ . For the given muffler, using  $Q_0 = 0.655 \text{ m}^3$ , the total back-pressure is found out to be,

$$\Delta P = 0.522 \text{ kPa} \quad (6)$$

### 4 LUMPED ACOUSTIC ELEMENT MODEL

The lumped acoustic element model of the muffler configuration in Fig. 1 is shown in Fig. 3, where  $Z_{13}, Z_{11}, Z_{10}, Z_8, Z_7, Z_6, Z_5, Z_3$  and  $Z_1$  are the lumped perforate impedances of inlet-pipe, pipe-1 (section 1-2), pipe-

1 (section 2-3), pipe-2 (section 1-3), pipe-2 (section 3-4), pipe-2 (section 4-5), pipe-2 (section 6-7), outlet-pipe (section 6-7) and outlet-pipe (section 7-8), respectively, and are evaluated as follows.

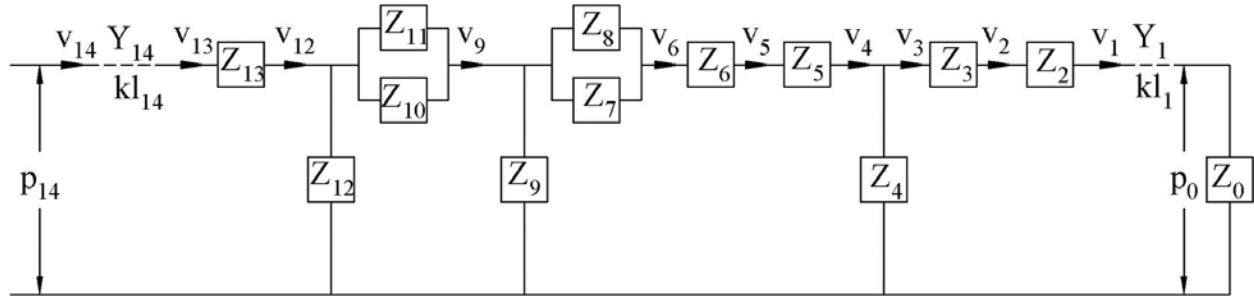


Fig. 3. Lumped acoustic element model of the muffler shown in Fig. 1. (elements 1 and 14 are modelled as distributed elements).

The lumped impedance is defined as the ratio of the acoustic pressure difference to the acoustic mass velocity whereas the non-dimensional acoustic impedance  $\zeta$  is defined as the ratio of the acoustic pressure difference to the product of  $u\rho_0c_0$ , where  $u$  is the radial acoustic velocity,  $\rho_0$  is the density of the medium, and  $c_0$  is the velocity of sound. The lumped perforate impedance can be expressed in terms of the non-dimensional acoustic impedance as[1],

$$Z_p = \zeta \frac{c_0}{S} \quad (7)$$

where  $S$  is the overall surface area of the perforate over the length of the perforate. Thus Eq. 7 can be used to evaluate the lumped perforate impedances.

Impedances  $Z_{12}$ ,  $Z_9$  and  $Z_4$  are the lumped compliance of the first, second and third cavity, respectively. The cavities can be modeled as lumped capacitance of the cavity with air ( $Z_a$ ) (excluding the lining), lumped impedance of the perforated protective plate ( $Z_p$ ) and that of the absorptive lining in the cavity ( $Z_l$ ). The lumped impedance of the cavity is given by,

$$\frac{1}{Z_{cavity}} = \frac{1}{Z_a} + \frac{1}{(Z_p + Z_l)} \quad (8)$$

where  $Z_a$ ,  $Z_p$  and  $Z_l$  are given by[1]

$$Z_p = \zeta \frac{c_0}{S}, \quad Z_a = -j \frac{c_0^2}{\omega V_a} \text{ and } Z_l = -j \frac{c_0^2}{V_w} \left( \frac{k_w}{k_0} \right) \left( \frac{Y_0}{Y_w} \right) \quad (9a-c)$$

here subscript 'a' refers to air side and 'w' refers to the lining side,  $k$ [5, 6] is the wave number,  $Y$ [5, 6] is the characteristics impedance of the medium given as  $Y = \rho c$ ,  $V$  is the volume. Using Eqs. (8) and (9), one can evaluate all the lumped impedances shown in Fig. 3.

The parallel impedances can be replaced by their equivalent impedance and then multiplying out all the constituent transfer matrices one can obtain the overall transfer matrix of the muffler configuration as follows.

The transfer matrix of the lumped in-line element of impedance  $Z$  is given by[1]:

$$[T] = \begin{bmatrix} 1 & Z \\ 0 & 1 \end{bmatrix} \quad (10)$$

whereas the transfer matrix of the lumped shunt element of impedance  $Z$  is given by[1]:

$$[T] = \begin{bmatrix} 1 & 0 \\ 1/Z & 1 \end{bmatrix} \quad (11)$$

The equivalent impedance of two impedances  $Z_1$  and  $Z_2$  in series or parallel are given as[1]:

$$Z_{series} = Z_1 + Z_2, \quad Z_{parallel} = \frac{Z_1 Z_2}{Z_1 + Z_2} \quad (12a-b)$$

Using Eqs. (10), (11) and (12a, 12b), the overall transfer matrix of the muffler is given by,

$$\begin{aligned} \begin{bmatrix} p_{14} \\ v_{14} \end{bmatrix} &= \begin{bmatrix} \cos(kl_{14}) & jY_{14} \sin(kl_{14}) \\ \frac{j \sin(kl_{14})}{Y_{14}} & \cos(kl_{14}) \end{bmatrix} \begin{bmatrix} 1 & Z_{13} \\ 0 & 1 \end{bmatrix} \begin{bmatrix} 1 & 0 \\ \frac{1}{Z_{12}} & 1 \end{bmatrix} \begin{bmatrix} 1 & Z_{11,10} \\ 0 & 1 \end{bmatrix} \begin{bmatrix} 1 & 0 \\ \frac{1}{Z_9} & 1 \end{bmatrix} \\ & \begin{bmatrix} 1 & Z_{8,5} \\ 0 & 1 \end{bmatrix} \begin{bmatrix} 1 & 0 \\ \frac{1}{Z_4} & 1 \end{bmatrix} \begin{bmatrix} 1 & Z_{3,2} \\ 0 & 1 \end{bmatrix} \begin{bmatrix} \cos(kl_1) & jY_9 \sin(kl_1) \\ \frac{j \sin(kl_1)}{Y_1} & \cos(kl_1) \end{bmatrix} \begin{bmatrix} p_0 \\ v_0 \end{bmatrix} \end{aligned} \quad (13)$$

Multiplying out the intermediate matrices we get an overall  $2 \times 2$  transfer matrix,

$$\begin{bmatrix} p_{14} \\ v_{14} \end{bmatrix} = \begin{bmatrix} T_{11} & T_{12} \\ T_{21} & T_{22} \end{bmatrix} \begin{bmatrix} p_0 \\ v_0 \end{bmatrix} \quad (14)$$

Finally, transmission loss can be calculated using[1]:

$$TL = 20 \log \left[ \left( \frac{Y_d}{Y_u} \right)^{\frac{1}{2}} \frac{1}{2} \left| T_{11} + \frac{T_{12}}{Y_d} + T_{21} Y_u + T_{22} \frac{Y_u}{Y_d} \right| \right] \quad (15)$$

where  $Y_d$  and  $Y_u$  are characteristic impedance of the upstream and downstream pipes. Insertion loss (IL) is defined as the difference between the acoustic powers radiated without muffler and with muffler. The expression for the insertion loss IL is given by[1]:

$$IL = 20 \log \left[ \left( \frac{\rho_{0,2} R_{0,1}}{\rho_{0,1} R_{0,2}} \right)^{\frac{1}{2}} \left| \frac{Z_{n+1}}{Z_{n+1} + Z_{0,1}} \right| |VR_{n+1}| \right] \quad (16)$$

where subscripts '1' and '2' denote systems without and with muffler respectively,  $Z_{0,1}$  is the radiation impedance,  $R$  is the real part of the corresponding radiation impedance with and without muffler,  $VR_{n+1} = v_{n+1}/v_0$  is the velocity ratio, and  $Z_{n+1} = (0.707 - j0.707) Y_0$  is the source impedance.

## 5 1-D PLANE WAVE ANALYSIS

The required  $2 \times 2$  transfer matrix between the inlet of the muffler and the inlet face of the inside-pipe 1 is obtained by modeling the inlet pipe and the first cavity as a lumped acoustic element. From the inlet face of the inside-pipe 1 upto the outlet, one can use the ITM (Integrated Transfer Matrix) approach to obtain the  $2 \times 2$  transfer matrix[1, 2]. Thus, multiplying out these two matrices, the overall transfer matrix of the muffler can be evaluated.

For the first cavity and the inlet pipe, using the lumped acoustic element model we have transfer matrix  $[T_1]$  that relates the state variable at the inlet pipe to the state variable at the inlet of the inside-pipe 1.

The second cavity is divided into 4 sections and the third cavity into 6 sections as shown in Fig. 1. For the second cavity using the ITM approach [2], the intermediate transfer matrices for different sections are listed in Table 2.

**Table 2.** Transfer matrix relations between section 1-4 shown in Fig. 1

Segment	Comment	Transfer Matrix
1-2	4 interacting ducts with absorptive layer	$[T_{1-2}] = [APE_{1,2,3,4,1-2}]_{8 \times 8}$
2-3	4 interacting ducts with absorptive layer	$[T_{2-3}] = [APE_{1,2,3,4,2-3}]_{8 \times 8}$
3-4	3 Interacting ducts with absorptive layer	$[T_{4-5}] = [APE_{1,3,4,3-4}]_{6 \times 6}$

where the notation  $APE_{i,j,k,l,m,n}$ , indicates that elements  $i, j, k$  and  $l$  are interacting with each other within the length of section  $m - n$ . The boundary conditions are :

$$v_{1,1} = v_{3,1} = v_{4,1} = v_{2,3} = v_{1,4} = v_{4,4} = 0 \quad (17)$$

Using the above transfer matrices and the boundary conditions and rearranging one can have:

$$[T_A]_{20 \times 20} \begin{bmatrix} [S_{1,1}] \\ \vdots \\ \vdots \\ [S_{4,4}] \end{bmatrix}_{20 \times 1} = \begin{bmatrix} [0] \\ \vdots \\ [S_{3,4}] \\ [0] \end{bmatrix}_{20 \times 1} \quad (18)$$

Inverting the matrix  $[T_A]$ , a  $2 \times 2$  transfer matrix can be obtained such that:

$$\begin{bmatrix} p_{2,1} \\ v_{2,1} \end{bmatrix} = [T_2]_{2 \times 2} \begin{bmatrix} p_{3,4} \\ v_{3,4} \end{bmatrix} \quad (19)$$

For the third cavity, using the ITM approach, the transfer matrices obtained are listed in Table 3:

**Table 3.** Transfer matrix relations between section 4-9 shown in Fig. 1

Segment	Comment	Transfer Matrix
4-5	3 interacting ducts with absorptive layer	$[T_{4-5}] = [APE_{1,2,4,4-5}]_{6 \times 6}$
6-7	Rigid walled pipe - 1	$[T_{6-7(1)}] = [P_{1,6-7}]_{2 \times 2}$
6-7	Rigid walled pipe - 2	$[T_{6-7(2)}] = [P_{2,6-7}]_{2 \times 2}$
6-7	Rigid walled pipe - 3	$[T_{6-7(3)}] = [P_{3,6-7}]_{2 \times 2}$
6-7	Rigid walled pipe - 4	$[T_{6-7(4)}] = [P_{4,6-7}]_{2 \times 2}$
8-9	3 interacting ducts with absorptive layer	$[T_{8-9}] = [APE_{1,3,4,8-9}]_{6 \times 6}$

The boundary conditions for the section 4-9 shown in Fig. 1 are as follows:

$$v_{1,4} = 0, v_{4,4} = 0, v_{2,5} = v_{2,6}, v_{4,5} = v_{4,6}, v_{4,7} = v_{4,8}, v_{3,7} = v_{3,8} \quad (20a-f)$$

$$p_{2,5} = p_{2,6}, p_{4,5} = p_{4,6}, p_{4,7} = p_{4,8}, p_{3,7} = p_{3,8} \quad (21a-d)$$

$$p_{1,5} = p_{1,6} = p_{3,6}, v_{1,5} = v_{1,6} + v_{3,6}, p_{2,7} = p_{1,7} = p_{1,8}, v_{1,8} = v_{2,7} + v_{1,7} \quad (22a-d)$$

$$\frac{p_{1,6}}{v_{1,6}} = -jY_{1w} \cot(k_w l) \frac{\rho_w}{\rho_0} \text{ and } \frac{p_{4,6}}{v_{4,6}} = -jY_{4w} \cot(k_w l) \quad (23a-b)$$

Using the above boundary conditions and the transfer matrices described in Table 3, and rearranging yields,

$$[T_B]_{38 \times 38} \begin{bmatrix} [S_{1,4}] \\ \vdots \\ \vdots \\ [S_{4,9}] \end{bmatrix}_{38 \times 1} = \begin{bmatrix} [0] \\ \vdots \\ [S_{3,9}] \\ [0] \end{bmatrix}_{38 \times 1} \quad (24)$$

Inverting the  $[T_B]$  matrix, a  $2 \times 2$  transfer matrix is obtained such that:

$$\begin{bmatrix} p_{2,4} \\ v_{2,4} \end{bmatrix} = [T_3]_{2 \times 2} \begin{bmatrix} p_{3,9} \\ v_{3,9} \end{bmatrix} \quad (25)$$

Thus the overall transfer matrix  $[T]$  of the muffler is given by

$$[T] = [T_1][T_2][T_3] \quad (26)$$

Finally, the transmission loss can be calculated using Eq. (15).

## 6 3-D FINITE ELEMENT ANALYSIS

To validate the results (transmission loss) evaluated by using the lumped acoustic element model, the 3-D finite element analysis results are used. A commercial software LMS Virtual. Lab 13.2 of SIEMENS[7] is used for the analysis of the muffler configurations shown in Fig. 1. The entire acoustic domain has been modelled and discretized/meshed using the 4-node tetra-mesh elements. In matrix form, the variational formulation of the governing equations of acoustics yields[1],

$$([M] - k_0^2 [p] + j\rho_0 \omega [c]) \{p_n\} = -j\rho_0 \omega [F] \quad (27)$$

where  $[M]$ ,  $[p]$  and  $[c]$  are the inertia, stiffness and damping matrices, respectively.  $\{F\}$  is the forcing vector and  $\{p_n\}$  represents the nodal pressure vector. The analysis is carried out for stationary medium but the effect of the grazing flow as well as bias flow on the perforate impedance are duly considered[4]. The perforated plate is modeled as two continuous surfaces, inner and outer surface, of the pipe connected through transfer admittance relation given by[7].

$$\begin{bmatrix} v_1 \\ v_2 \end{bmatrix} = \begin{bmatrix} \alpha_1 & \alpha_2 \\ \alpha_4 & \alpha_5 \end{bmatrix} \begin{bmatrix} p_1 \\ p_2 \end{bmatrix} + \begin{bmatrix} \alpha_3 \\ \alpha_6 \end{bmatrix} \quad (28)$$

where subscripts '1' and '2' on  $v$  (acoustic velocity) and  $p$  (acoustic pressure) represent the two surfaces of the perforate.  $\alpha_1$ ,  $\alpha_2$ ,  $\alpha_4$  and  $\alpha_5$  are complex admittance coefficients and  $\alpha_3$  and  $\alpha_6$  are complex source coefficients. The complex admittance coefficients can be determined in terms of the perforate impedance[7] and the complex source coefficients are zero for all the current muffler configurations. For the 1-D plane wave and 3-D FEM analysis, the perforate impedance as described in Ref.[4] has been used. The boundary conditions used are:

- Panel velocity boundary condition at the inlet face,  $v = -1$  m/s. Negative sign indicates that the direction of the velocity is into the acoustic domain.
- Absorbent panel property at the outlet face is assigned to get anechoic termination for which the acoustic impedance is  $\rho_0 c_0$ .

Solving the system of equations iteratively at each frequency provides the complex acoustic pressure  $\{p_n\}$  distribution within the acoustic domain, and subsequently the complex acoustic velocity distribution. Exporting these data available at the inlet-face and the outlet-face, transmission loss can be calculated by[7, 1].

$$TL = 20 \log_{10} \left| \frac{p_i + Y_i v_i}{2 Y_0 v_0} \right| \quad (29)$$

where subscript 'i' and 'o' represent the inlet and outlet, respectively.

## 7 RESULTS AND DISCUSSION

The transmission loss of the configuration of Fig. 1 evaluated using Eq. (15) by employing the lumped element analysis is compared and validated against that of the 1-D plane wave analysis and the 3-D FEM (using LMS Virtual Lab[7]) as shown in Fig. 4[8].

From Fig. 4, it can be observed that the agreement is reasonable up to 250 Hz, which is good enough for the design of muffler for insertion loss. It also confirms that at low frequencies, the performance predicted by the lumped element method is in good agreement with the 1-D plane wave analysis as well as the 3-D FEM.

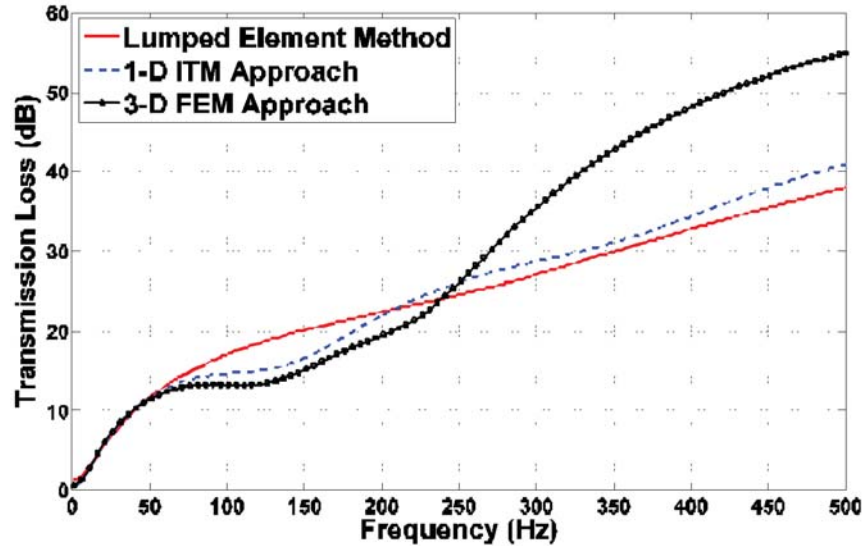


Fig. 4. Comparison of transmission loss evaluated using different methods for the muffler configuration shown in Fig. 1.

Finally, insertion loss of the muffler of Fig. 1 evaluated using the lumped element method is shown in Fig. 5.

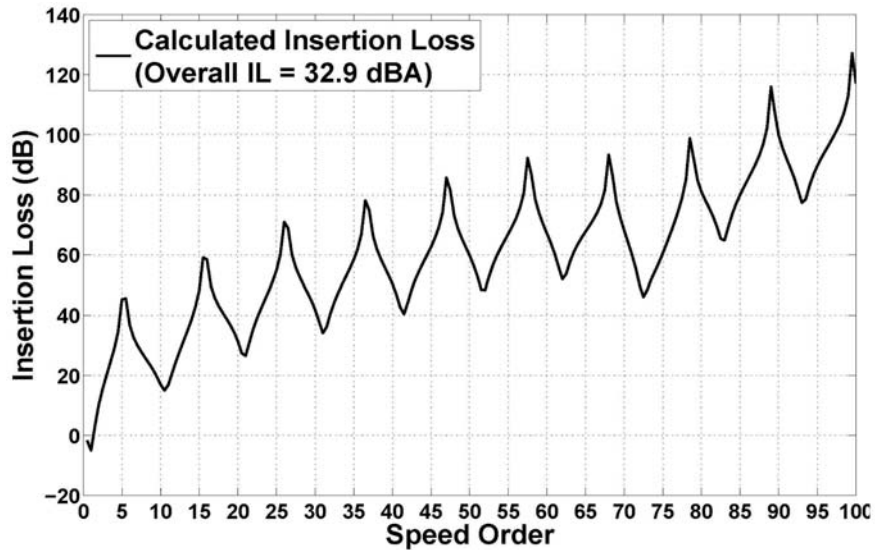


Fig. 5. Insertion loss of the muffler of Fig. 1 evaluated using the lumped element method.

Here, speed order of a given frequency is defined as:

$$SO \equiv \frac{\text{frequency in Hz}}{\text{engine speed in revolutions per second}} = \frac{f}{RPM/60} = \frac{f}{1500/60} = \frac{f}{25}$$

Conversely,

$$f = 25 \times SO$$

The periodic peaks and troughs are due to the standing wave pattern in the long reference pipe. The troughs due to the reference pipe of length  $l$  occur at[1]

$$f_m = m \frac{c}{2l} = m \times \frac{586}{2 \times 1.15} = 255 \text{ m}, \quad m = 1, 2, 3, \dots$$

For two consecutive troughs,

$$\Delta f = 255 \text{ Hz}$$

and

$$\Delta SO = \frac{\Delta f}{25} = \frac{255}{25} = 10.2$$

This may be seen to check with the gap between two consecutive troughs in Fig. 5. The monotonously increasing average values of IL is due to the

- (a) absorptive lining inside the shell and the end plates of the combination muffler, and
- (b) aeroacoustic resistance due to the bias flow and grazing flow at the perforates and area discontinuities.

The overall IL, defined as the difference between the total unmuffled exhaust SPL and the muffled SPL, would depend not only on the IL curve of Fig. 5, but also the measured spectrum of the unmuffled exhaust SPL at the tail pipe end[1]. For the particular DG set used in this investigation (see Table 1 for specifications), the overall IL works out to be 32.9 dBA as indicated above in Fig. 5. However, this value may be in considerable error because the lumped-element analysis holds strictly for the low frequencies (upto 250 Hz, corresponding to speed orders of less than 10, as per Fig. 4), and presumes a constant velocity source (source impedance tending to infinity).

## 8 CONCLUSION

The exhaust noise of an internal combustion engine predominates at the firing frequency and its first few harmonics. At such low frequencies, the lumped-element analysis recommends itself as a much faster alternative. In this paper, lumped-element transfer matrices have been derived for the multiply-connected perforated elements as well as acoustically lined cavity. The resulting TL Spectrum is validated against the 1-D (plane wave) analysis as well as the 3-D FEM. Finally, overall insertion loss of a side-inlet combination muffler is computed. The flow-resistance network is used for calculation of the meanflow distribution and back pressure. The resulting MATLAB code can now be used for optimization of the muffler configuration for the required IL as well as back-pressure.

## 9 ACKNOWLEDGEMENT

The authors benefited substantially from their technical discussions with Mr. Krishna Mohan Kumar, a doctoral student in the Facility for Research in Technical Acoustics (FRITA).

## 10 REFERENCES

- [1] M.L. Munjal, *Acoustics of Ducts and Mufflers - Second Ed.*, John Wiley & Sons, Chichester, UK (2014).
- [2] N.K. Vijayasree and M.L. Munjal, On an Integrated Transfer Matrix Method for Multiply Connected Mufflers, *Journal of Sound and Vibration*, **331**, ( 2012) 1926-1938.



- [3] M.L. Munjal, N.K. Vijayasree and P. Chaitanya, Flow Resistance Network Analysis of the Back-Pressure of Automotive Mufflers, *Indian Journal of Engineering & Materials Sciences*, **39**(2), (2013) 339-349.
- [4] T. Elnady, M. Abom and S. ALLAM, 2010. Modeling Perforates in Mufflers Using Two-Ports, *Journal of Vibration and Acoustics*, **132**(6), 061010.
- [5] M.E. Delany and B.N. Bazley, 1970. Acoustical characteristics of fibrous absorbent materials, *Applied Acoustics*, **3**, 106-116.
- [6] F.P. Mechel, 1976. Extension of Low Frequencies of the Formulae of Delany and Bazley for Absorbing Materials, *Acoustica*, **35**, 210-213.
- [7] LMS Virtual. Lab 12-SL1, 2012. *Technical Documentation*, LMS International I, Belgium.
- [8] Vikas Kumar, 2016. Analysis and Design of the Side-Inlet Combination Mufflers for DG Sets, ME Dissertation, Indian Institute of Science, Bangalore.

# Application of free layer damping treatment for vibration and noise attenuation

**V. Ramakrishna, P.V.S. Ganesh Kumar, V. Rama Mohana Rao,  
D.A. Rao, T.V. Ratnam and K. Seetha Ramaiah**  
*Naval Science and Technological Laboratory, Visakhapatnam, India*  
*e-mail: ramakrishna.v@nstl.drdo.in*

[Received: 20-02-2017; Revised: 26-05-2017; Accepted: 29-05-2017]

## ABSTRACT

This paper presents studies on application of mastic on a floating barge for vibration and noise attenuation. Mastic is putty like viscous paste. The study involves design of damping parameters based on barge geometry, application of mastic as per design on the barge, setting up experiment in a water tank and effectiveness of mastic by way of vibration and underwater noise measurements. Data obtained from measurements was analyzed for frequency Spectrum of interest. The results indicate significant attenuation of both vibration and underwater noise due to mastic application

## 1. INTRODUCTION

Generally vibrations in the underwater and surface vehicles occur primarily due to onboard machinery like Diesel Engines, Gas turbines, pumps, compressors etc. These vibrations are transmitted to hull and then as underwater radiated noise into sea. This leads to the vulnerability of the vessel as noise is detectable by sonars. Hence, vibration control onboard marine vehicle is of paramount importance. Vibrations can be controlled by either passive or active means. Damping of structural vibration by passive means is most common and efficient because of the simplicity in application and maintenance[1]. The passive damping is employed normally in two ways, namely Free Layer Damping (FLD) and Constrained Layer Damping (CLD)[2]. The technique is based on application of a visco-elastic material on the structure, either without or with a stiff constraining layer[3]. Visco-elastic materials provide necessary properties for damping and hence, these are mostly used for this purpose.

In FLD, polymer coating of required thickness is applied on vibrating surface, which provides damping by way of flex-extensional deformations. FLD is applied either as a polymer sheet with adhesive or as mastic. Basically mastic is a two component compound. It is solvent free putty like compound based on thermosetting polymer material. On mixing of the components in proper proportions, the mastic would cure to the extent of 90-95% by chemical reaction in 24 hours and will be cured completely (hard dried) in 48 hours. Required thickness can be built up by one coat. More coats may be used for better surface finish.

The dynamic behaviour of free layer damping beams with thick visco-elastic layer is analyzed to reproduce the mechanical behavior of free layer damping beams with thick visco-elastic layer [4]. Prior to carrying out studies reported in this paper, beam samples were experimentally tested for evaluating effectiveness of mastic. This paper presents the experimental study carried out on noise and vibration attenuation due to mastic applied on a floating barge.

## 2. FLD TREATMENT - DESIGN APPROACH

A typical FLD arrangement is shown in Fig. 1. The substrate of thickness  $H_1$  is covered with a Visco-elastic material of thickness  $H_2$  with the help of rigid and strong adhesive. The visco-elastic material is self-adhering after curing process. If glue is used, it must have higher dynamic modulus than the visco-elastic material so as to transfer most of the stress to the visco-elastic material that ensures the loss would be maximized. The substrate undergoes flex extensional motion under vibration. As a result, the visco-elastic material also experiences the tensile and compression forces and the flex extensional losses will take place in the visco-elastic material.

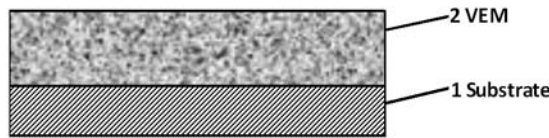


Fig. 1. FLD performance-Nomogram [5]

Further, from Nomogram, it can be observed that:

- (i) For higher damping, both elastic modulus and loss factor of the Visco-elastic material must be high.
- (ii) There is not much increase in system loss factor beyond a certain thickness ratio.

Thickness ( $H_2$ ) of mastic treatment for the present case was arrived at based on this nomogram.

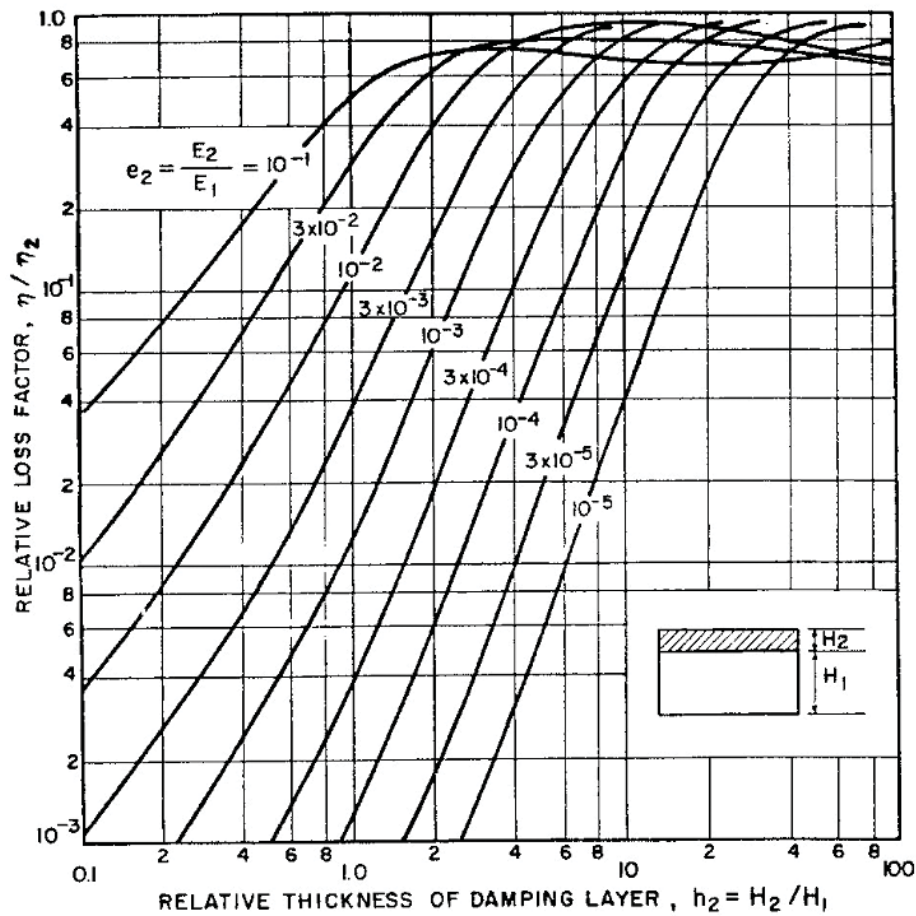


Fig. 2. Typical FLD configuration

### 3. EXPERIMENTAL SET UP

A fabricated MS Barge was utilized for experimental study of mastic. The dimensions of the barge are 3.0 x 2.2 x 0.6 m. Barge deck bottom plate has thickness of 6 mm. Barge bottom (inside) was applied with mastic of determined thickness. An air compressor was installed on the barge as source of vibration. The barge mounted with air compressor was floated in a water tank as shown in Fig. 3.



Fig. 3. The floating barge in water tank

Vibration transducers (accelerometers) were mounted at inside bottom of the barge structure (Barge centre) and Compressor corner and Motor Corner of the barge structure. A schematic plan of these locations is shown in Fig. 4.

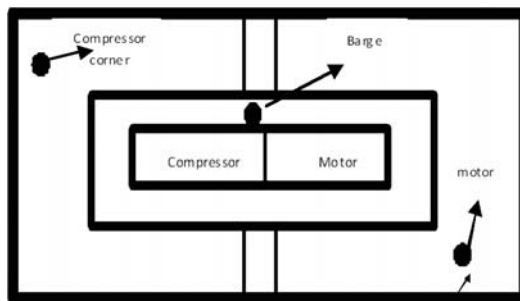


Fig. 4. Vibration monitoring points on barge

For measuring underwater noise, hydrophone was lowered in water below barge at 2m and 4m depths as shown in Fig. 5.

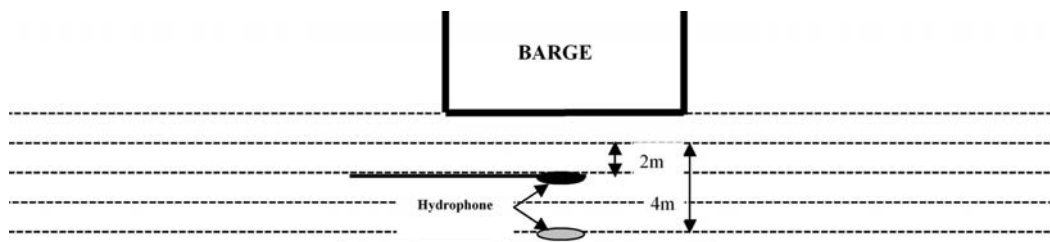


Fig. 5. Hydrophone locations for Under water noise measurements

Vibration and underwater noise data was collected for following two regimes:

- (i) Before application of mastic on the barge.
- (ii) After application of mastic on the barge.

A photograph of section of barge without mastic is shown in Fig. 6. Photographs of section of barge with mastic on deck are shown in Fig. 7.



Fig. 6. Barge without Mastic

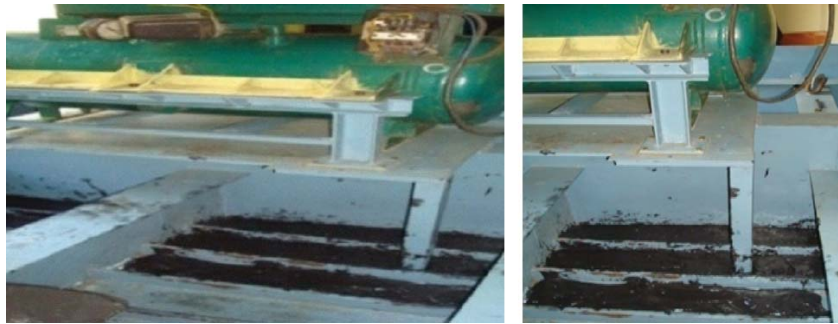


Fig. 7. Barge with mastic

#### 4 DATA MEASUREMENT AND ANALYSIS

The vibration signature was acquired and analyzed by the instrumentation setup as shown in Fig. 8.

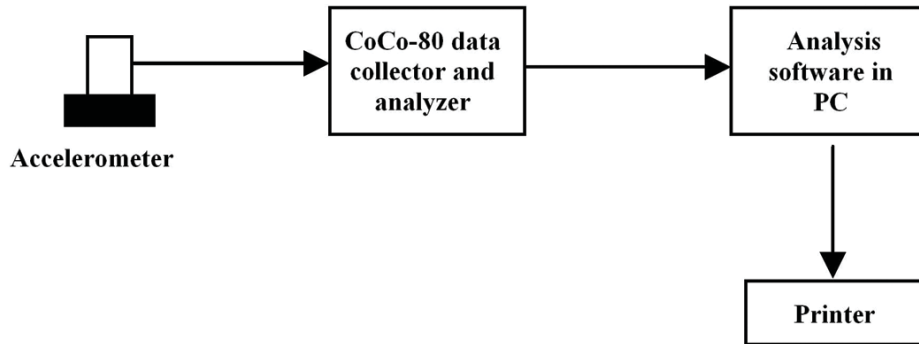


Fig. 8. Vibration measurement and analysis setup

Accelerometers (Type B & K 4526 of Sensitivity  $9.936 \text{ mv/ms}^{-2}$ ) were firmly fixed at the identified locations for measuring the vibration data. These outputs were fed to a COCO- 80 data collector (Make: M/S. Crystal Instruments, USA) and analyzer through coaxial cables. FFT analysis was then carried out on recorded data using Engineering Data Management (Post Processing) software. FFT analysis was performed in 1/3 Octave bands in the frequency range up to 10 kHz.

Underwater noise signature was acquired and analyzed by the instrumentation setup as shown in Fig. 9.

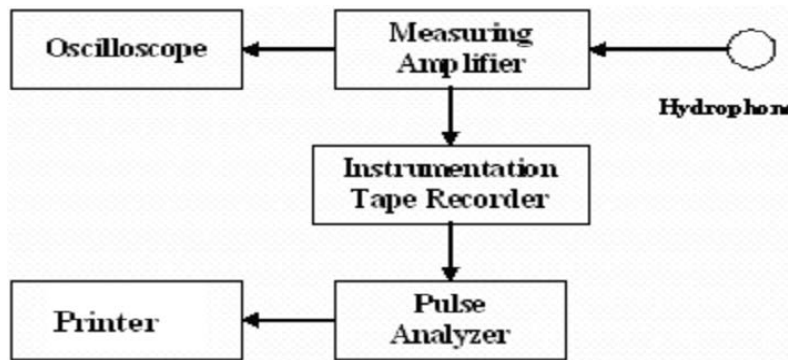


Fig. 9. Underwater Noise measurement and analysis setup

Hydrophone (Type ITC 1042 of sensitivity OCV-200 dB//1V/ $\mu$ Pa) was lowered at specified depths underwater below barge. The electrical output of the hydrophone was connected to the measuring amplifier (Type B&K 2636) through BNC connector. The amplified signal from the amplifier was fed to the input of the instrumented data recorder through BNC connector for recording the radiated noise signal for analysis.. The signal from the data recorder was fed to the PULSE multi analyzer (B&K Type 3560C) and analysis was done in 1/3-octave bands in the frequency range 10 Hz to 10 kHz.

Comparative plots of vibration and underwater noise data without and with mastic are shown in Fig. 10 and 11 respectively.

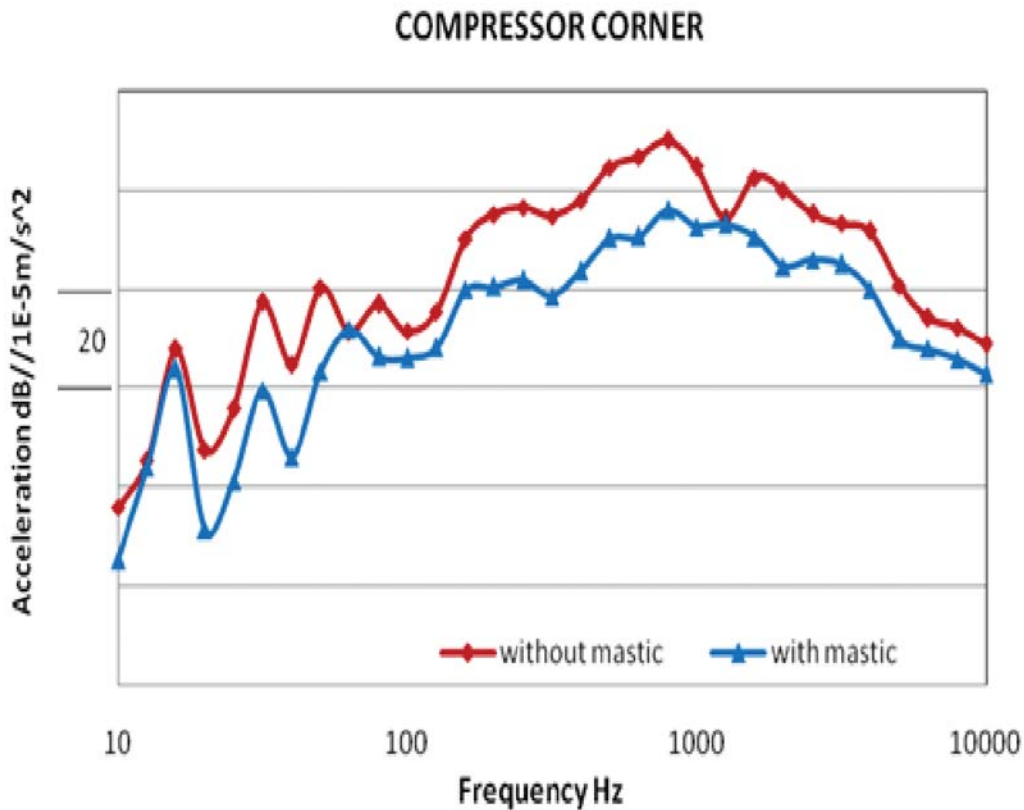


Fig. 10. Vibration levels without and with Mastic

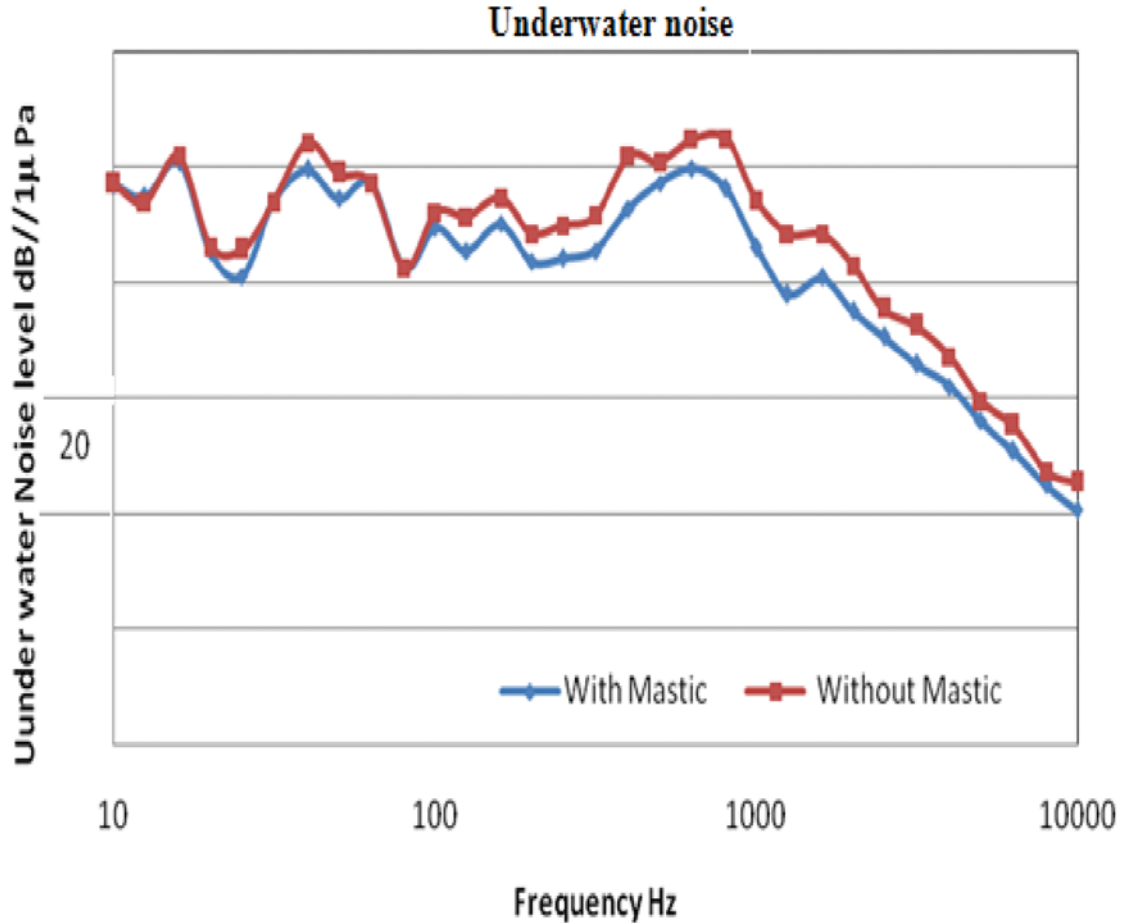


Fig. 11. Underwater noise levels without and with mastic

It can be seen from Fig. 10 and 11 that vibration reduction up to a maximum of 20 A dB and underwater noise reduction by up to a maximum of 10 dB is obtained with application of mastic. Overall Vibration and underwater noise reduction is shown in Table 1.

Table 1. Overall vibration and under water noise levels.

Condition	Vibration (AdB//1e-5m/s <sup>2</sup> )	Noise (dB//1uPa)
Without Mastic	115	130
With Mastic	105	124
Reduction	10	6

It may be seen that overall vibration and noise reduction are about 10 AdB and 6 dB respectively. It also may be observed that attenuation is mainly seen in 1/3 octaves from 125 Hz to 2500 Hz.

## 5 CONCLUSION

- (i) About 44 % of vibration attenuation and 50 % of underwater noise attenuation is achieved by application of mastic for thickness ratio of 2 and weight ratio of 1.
- (ii) Strain energy approach will be used for identifying optimal distribution of mastic in order to reduce mastic weight penalty in future study.

## 6 ACKNOWLEDGEMENT

The authors wish to express their sincere gratitude to Dr O.R.Nanda Gopan, Director, NSTL Visakhapatnam for Permitting to publish this paper. The authors wish to express sincere gratitude to Sri Ch. Sankara Rao, Sc'G' NSTL, Visakhapatnam for encouragement to publish this paper. The authors also wish to express gratitude to polymer division, NMRL, Ambernath for providing the mastic material for this experimental study. The authors also wish to express gratitude to Vibration Studies Division and Acoustic Test Center, NSTL, Visakhapatnam.

## 7 REFERENCES

- [1] Denys J. Mead, 2000. *Passive Vibration Control*, John Wiley and Sons.
- [2] SH Crandall, 1970. "The Role of Damping in Vibration Theory", *Journal of Sound and Vibration*, **11**(1), 3-18.
- [3] A.D. Nashif, DIG Jones and J.P. Henderson, 1985. *Vibration Damping*, Wiley Interscience, New York.
- [4] Fernando Cortés and María Jesús Elejabarrieta, 2008. "Structural Vibration of Flexural Beams with Thick Unconstrained Layer Damping", *International Journal of Solids and Structures*, **45**, 5805-5813.
- [5] Istvan L. Ver and Leo L. Beranek, 2006. *Noise and Vibration Control Engineering*, John wiley & sons, Inc.



# Analysis of physiographic provinces - marginal highs in the continental slope of India using multibeam and sub-bottom backscatter profiles

Milind Naik<sup>1,2</sup>, Govind Ranade<sup>1</sup> and Rajesh B Lohani<sup>2</sup>

<sup>1</sup>CSIR- National Institute of Oceanography, Dona Paula, Goa-403 004

<sup>2</sup>Goa College of Engineering, Farmagudi, Ponda, Goa-403 401

e-mail: nmilind@nio.org

[Received: 06-05-2017; Revised: 15-05-2017; Accepted: 16-05-2017]

## ABSTRACT

A quantitative seabed classification is carried out by analysing the echo-peak data of the normal incidence beam of the multibeam and sub-bottom profiler from marginal highs of the western Continental Margins of India (WCMI). Rice Probability Density Function (PDF) of the echo peak profiles reveals micro-topographic seafloor roughness parameters at 30 and 3.5 kHz frequencies. No correlation is observed between the estimated coherence parameters of two different frequency ranges. A good correlation is seen among the energy parameter of the fourteen profiles of the multibeam and sub-bottom profiler.

## 1. INTRODUCTION

Multibeam echo sounders are increasingly being used for large-scale seabed mapping[1]. Such instruments generate high-resolution bathymetric maps due to narrow beam angles. In addition, by analysing the backscatter signals, the multibeam system is also being used for seabed studies[2-3]. The analysis of multibeam, angular backscatter signals for seabed characterization is a rapidly developing science[4-5]. However, the interpretation of angular backscatter data for roughness classification requires complex numerical computations. By contrast, multibeam echo-peak signals from different directions have the advantage of requiring minimal numerical manipulations before yielding useful information for seabed classification[6-8]. The Rice and Extremal probability density functions (PDFs), in particular, employ minimal numerical manipulations and are hence suitable for real-time seabed classification. In multibeam systems, the depth is determined from the echo peaks within the received pulse (in real-time bottom tracking). It should thus be possible to design a real-time bottom classifier using multibeam angular echo-peak data if a model with minimal numerical computations is available. However, in this chapter, we focus on the use of a sub-bottom profiler to estimate geo-acoustic parameters. The motivation of this work lies in the fact that geo-acoustic parameters are generally difficult to obtain, therefore the measurement on the *in-situ* samples is important. In this work, we also aim to evaluate the potential of sub-bottom profilers, to provide bottom parameters estimate hopefully in near real-time for each sediment layer along a track. In this chapter, a method is presented by which echo-peak data from normal incidence beam of the Kongsberg EM302 multibeam system are analysed. A quantitative seabed classification is carried out by analysing the echo-peak data of the normal incidence beam of the multibeam and sub-bottom profiler from marginal highs of the western Continental Margins of India (WCMI)[9].

## 2. MATERIALS AND METHODS

### 2.1 Multi Beam Data Acquisition

During the cruise SSK-068 of the RV Sindhu Sankalp (conducted by CSIR-NIO, Goa, India), a multibeam bottom backscatter study is carried out in the areas of the WCMI where sediment samples are also recovered. The EM 302 multibeam echo sounder was used that operates on a normal operating frequency of 30 kHz with beam angle of  $1^\circ \times 1^\circ$ . The swath width is typically 5.5 times the water depth depending upon the type of bottom. The multibeam bathymetry profiles of fourteen locations utilized in the study area is shown in Fig. 1.

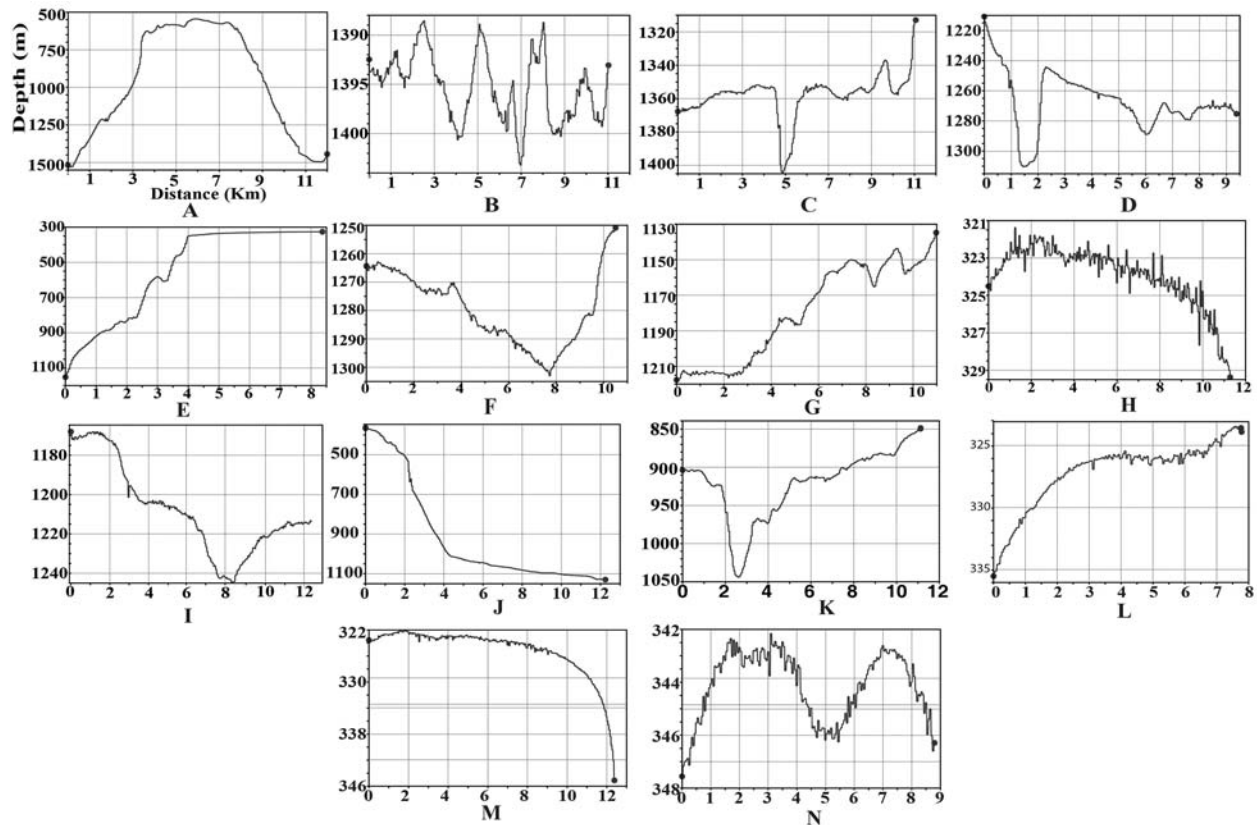


Fig. 1. Multibeam Bathymetric sections A-N in the survey area

### 2.2 Sub Bottom Profiler

The Geopluse sub-bottom profiler, developed by Geoacoustics presently marketed by Kongsberg Maritime (Kongsberg, UK) is installed onboard CSIR-NIO oceanographic vessel RV Sindhu Sankalp. The system operates with  $4 \times 4$  array used for signal transmission and reception. The frequency band of the system is 2.7 kHz. Although the system can be tuned at different frequencies we have used the system at 3.5 kHz resulting in transmit beam of  $30^\circ$ . The sub-bottom profiles were identified and extracted from fourteen locations in the study area as shown in Fig. 2.

### 2.3 Study Area

The study area is situated within  $14^\circ 20' N$  ;  $072^\circ 20' E$  and  $15^\circ 20' N$  ;  $073^\circ 10' E$ . off the central west coast of India, at water depths between 250 and 2050 m (Fig. 3). Here, the continental shelf is about 100 km wide and the shelf break lies between 100 and 125 m water depth. Farther seaward, the present study area is characterized by distinct physiographic provinces- namely, a shelf margin basin, a marginal high, the

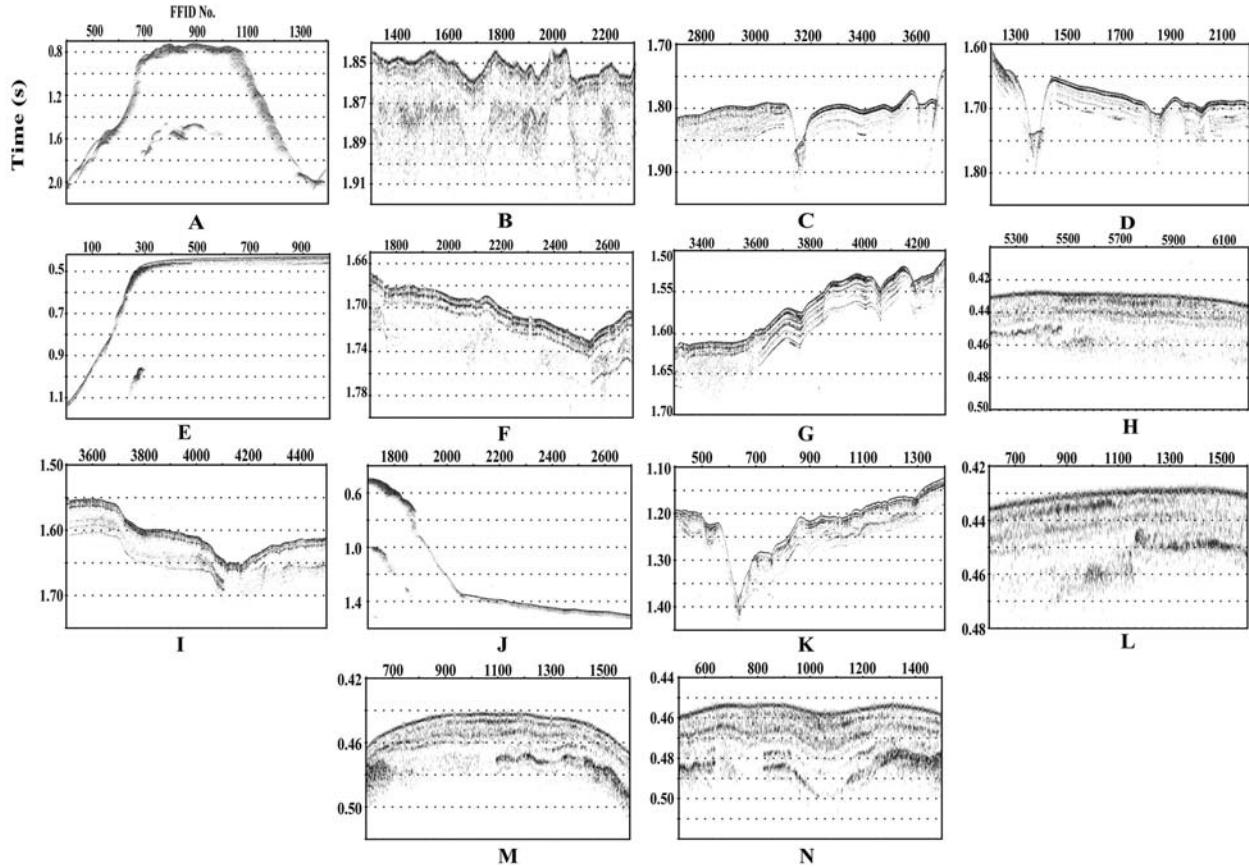


Fig. 2. SBP sections A-N in the survey area

continental slope and the Arabian Basin. Bathymetric data indicate that the upper slope (up to 500 m) is smoother and steeper than the lower slope. However, the mid-lower slope region is strewn with prominent flat-topped marginal highs landward of which is a basin. These marginal highs, lying at shallower depths (325 m), stand several hundred meters above the adjacent seafloor, are 35-40 km long and 10-15 km wide, strike roughly NNW-SSE, more or less parallel to the present shelf edge. Fourteen multibeam bathymetric and backscatter profiles are chosen for the present investigation, where sub-bottom profiles are shown in Fig. 2. Of these profiles, A is located on a 'high' having minimum or no place of sediment retention. Similarly profile B indicates uneven (rugged) topography, and profile C & D possess parabolic reflectors indicating presence of pockmark. Location E shows steep slope, and a small channel is seen at location F. Hummocky topography is seen in profile G. Sub-bottom thickness > 30m is observed in location H. Terrace like seafloor in location I. Mild slope is observed in profile J, presence of hyperbolic reflectors and V-shape profile suggests presence of pockmark in location K. Higher stratified layers of the Sub-bottom Profiles (SBP) L, M & N on 'highs' suggest organic carbonate preservation on 'highs' having sediment thickness of > 60m.

### 3 THEORY

#### 3.1 Rice echo peak PDF

Seafloor surface roughness parameters using normal incidence beams for the multibeam and sub-bottom profiler peak data are investigated in the fourteen areas marked A to N in the survey area. The rice PDF of the echo-peak amplitude  $E$  from the seabed is described as[7]:

$$P(E) = [2E(1 + \gamma) / \langle E^2 \rangle] * \exp \{- [(1 + \gamma) E^2 + \gamma \langle E^2 \rangle] / + E^2\} I_0(q) \quad (1)$$

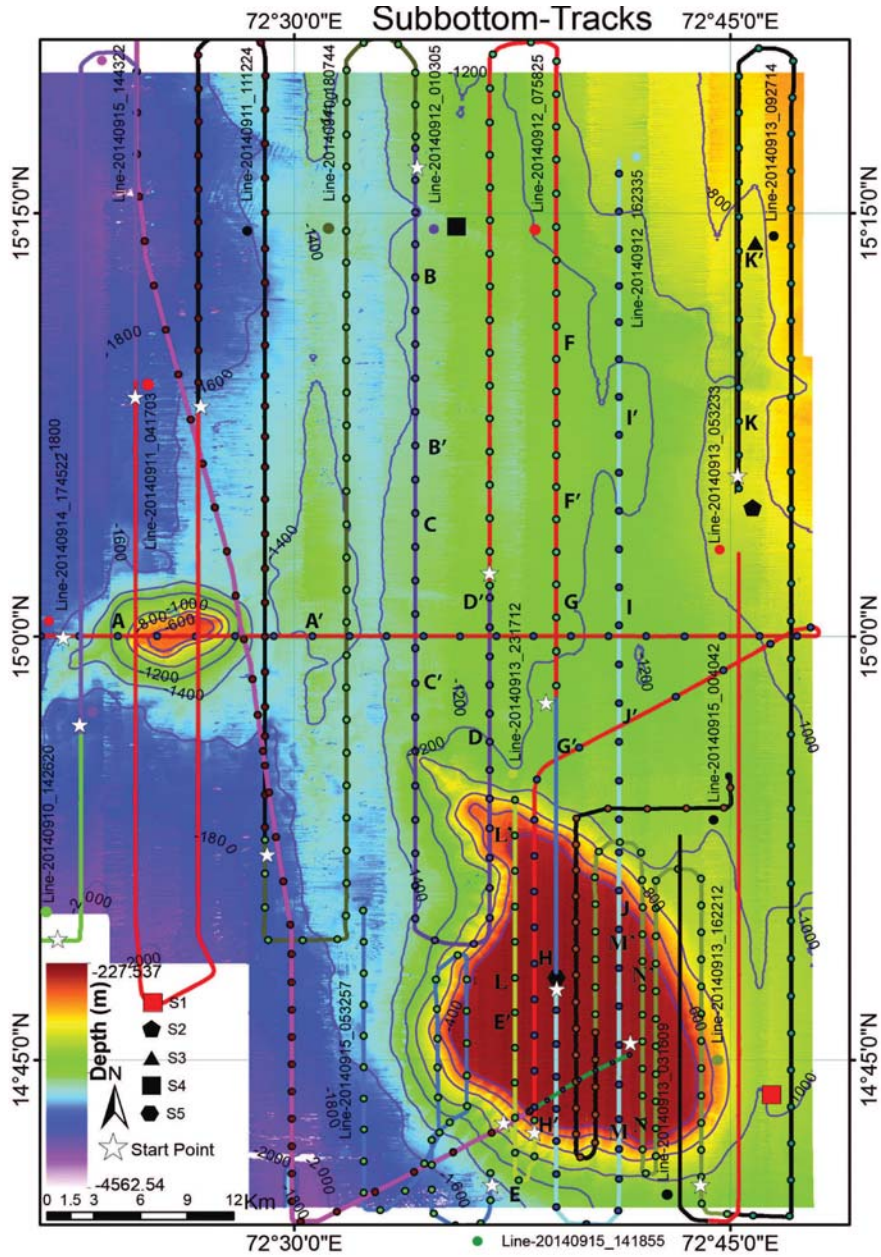


Fig. 3. Bathymetry map with sections A-N marked in the survey area

The term  $q$  in the modified Bessel function  $I_0(q)$  can be expressed as

$$q = 2E [\gamma(1 + \gamma)]^{0.5} / \langle E^2 \rangle^{0.5} \quad (2)$$

where  $\gamma$  is a measure of the relative roughness or smoothness of the bottom, and the expected squared value of the echo peak is denoted by  $\langle E^2 \rangle$ . The Rice PDF is expressed with respect to  $\gamma$ , and appropriate selection of  $\gamma$  is used to fit Rice PDF on the normalised histograms of the normal incidence echo peaks. The area wise echo-pick values are normalised with respect to rms peak value before histograms are drawn. The normalisation of the peak values with rms peak amplitude values of each beam helps to obtain comparable distributions. For the normal incidence beams, a moment method is applied to determine the  $\gamma$

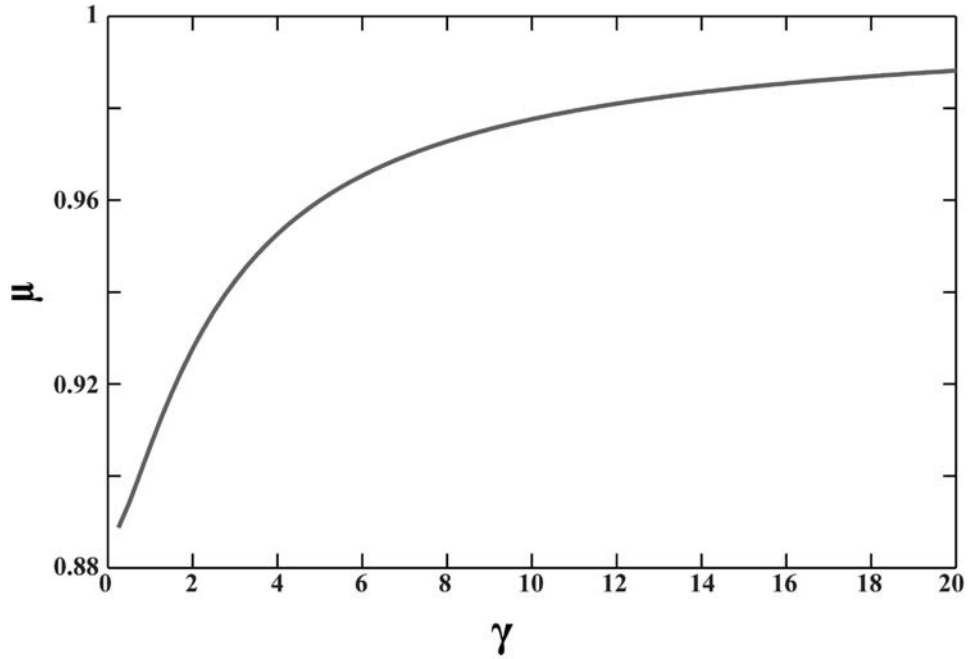


Fig. 4. Mu versus Gama

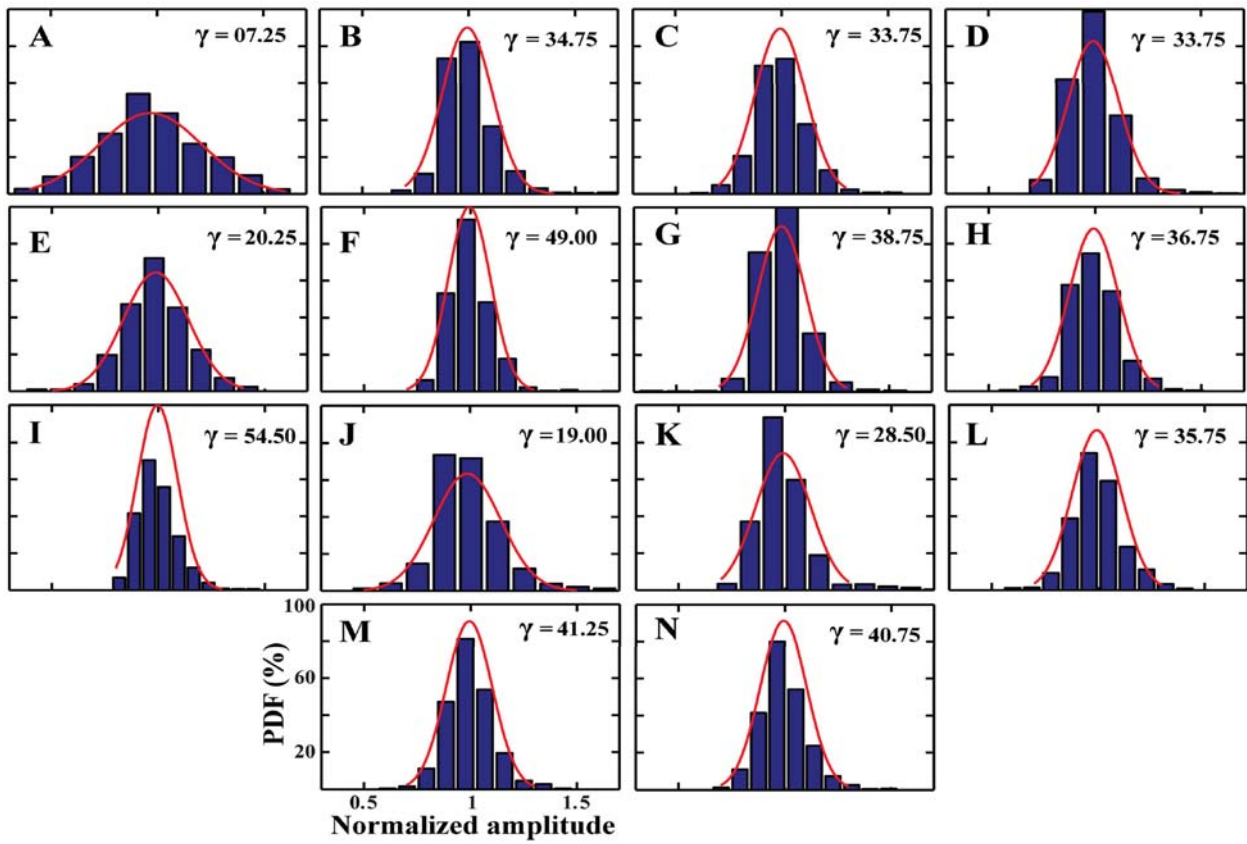


Fig. 5. PDF curves and histograms for all the MBES locations in the survey area

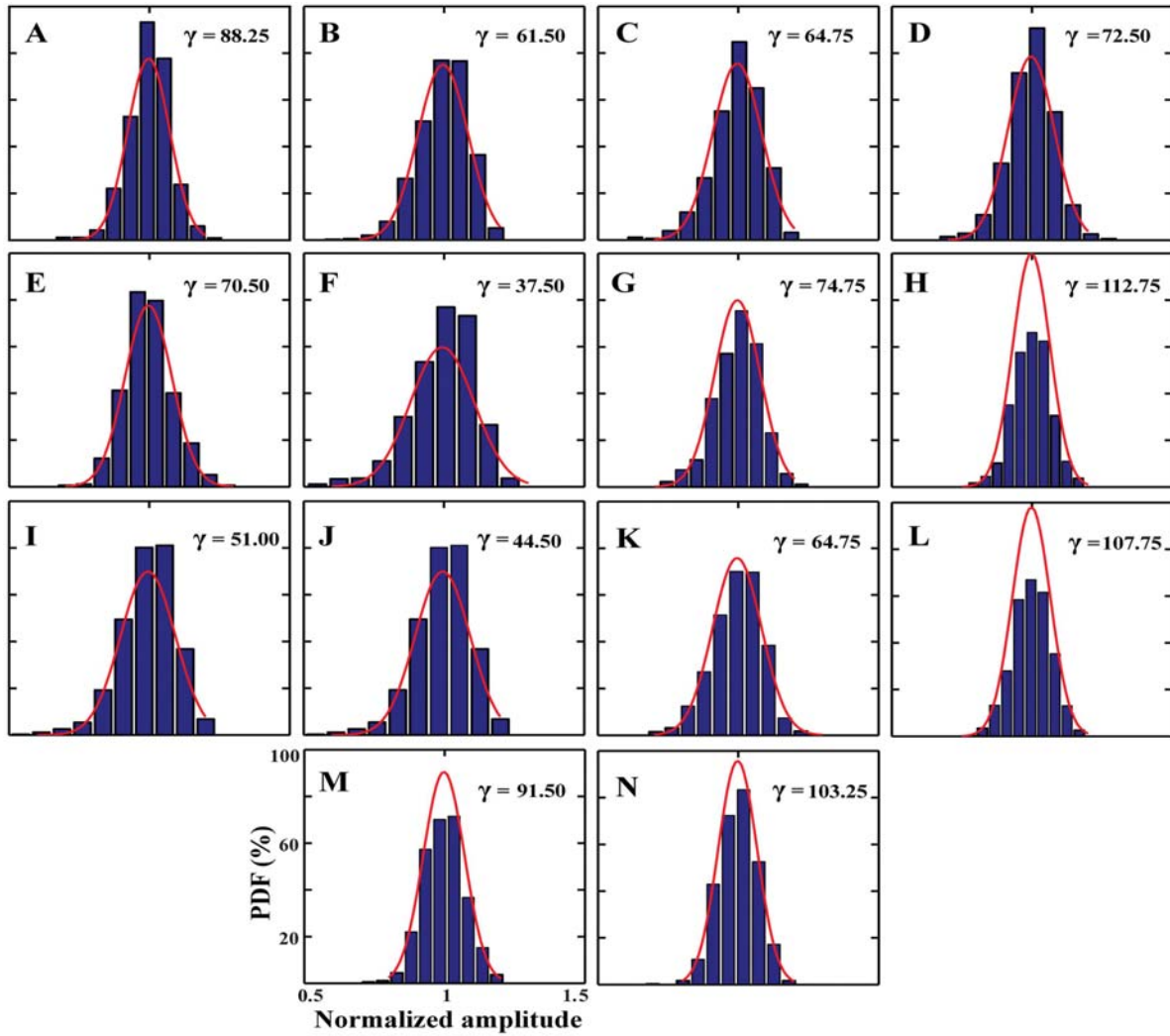


Fig. 6. PDF curves and histograms for all the SBP locations in the survey area

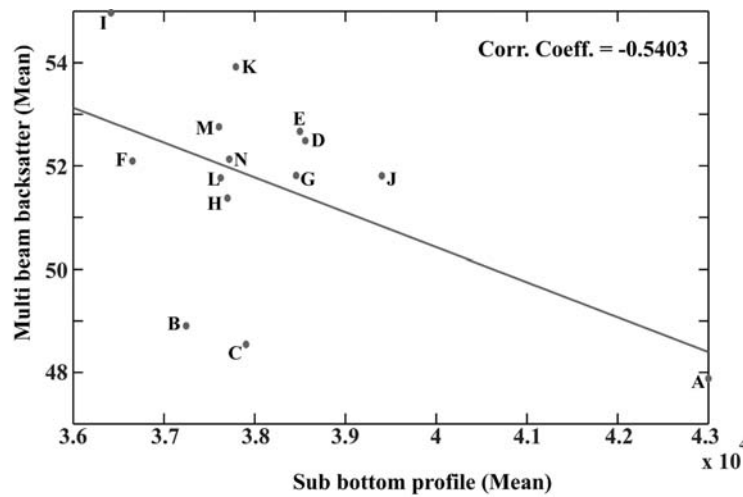


Fig. 7. Scatter plot between the multibeam backscatter mean energy vs SBP backscatter mean energy

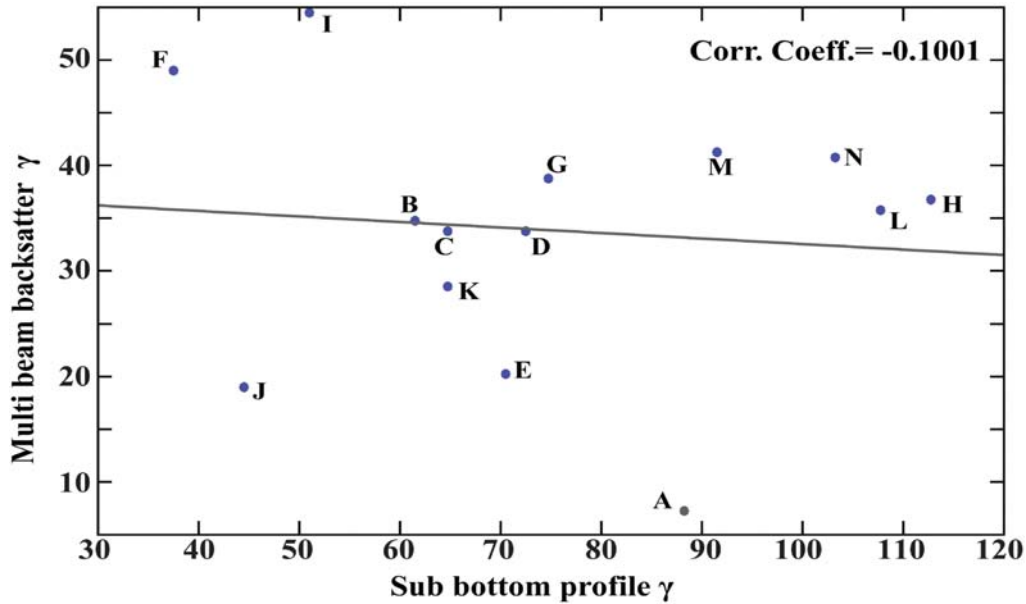


Fig. 8. Scatter plot between the multibeam backscatter gama vs. SBP profiler gama

values for the different areas. The first moment ( $\mu$ ) of the Rice PDF eq.(1) is expressed in terms of  $\gamma$  and  $y'(E/\sqrt{\langle E^2 \rangle})$  by the equation [10]:

$$\mu = \langle y' \rangle = \{ \Gamma(3/2) / (1 + \gamma) 0.5 \} * \exp(-\gamma/2) [(1 + \gamma) I_0(\gamma/2) + \gamma I_1(\gamma/2)] \quad (3)$$

Here,  $\mu$  varies between  $\pi/2$  (Rayleigh PDF,  $\gamma=0$ ) and 1.0 (Gaussian PDF). The  $\mu$  values are determined based on the ratio between the mean and rms values of the area peak data. These values are compared with theoretical mean ( $y'$  using eq. 2) to obtain  $\gamma$ . Relation between  $\mu$  v/s  $\gamma$  is as shown in Fig 4. The histograms represent the experimental echo peaks, whereas the curves describe the theoretical PDFs as illustrated in Fig. 5 & 6 for MB and SBP profiles respectively. In Fig. 7 and 8 we draw the plots between the estimation  $\gamma$  of the various profiles from the fourteen locations. Extremely poor correlation coefficients of 10% are observed. Similarly good correlation coefficients between the mean values of the profiles are observed to 54%.

#### 4 RESULTS AND DISCUSSIONS

In this project we proposed a technique to quantify the seafloor backscatter data employing echo peak normal incidence beams of the MB and SBP profiles. As previously mentioned, the implementation of the present technique is simple which needs minimum numerical computation. Here, we have encountered four seafloor types as seen in the SBP profiles (Fig 2) out of fourteen profiles acquired from the WCMI. The seafloors consist of: (i) hummocky seafloor (B, F, G and I), (ii) slope (A, G and E), (iii) pockmarks (C, D and K) and (vi) highs having stratified layers (H, L, M, and N).

##### 4.1 Echo-peak analyses

The histograms of Fig. 5 and 6 represent the experimental echo peaks while the curves describing the theoretical PDFs. The PDFs are Gaussian in nature for all the profiles obtained using MB and SBP profiles. The estimated  $\gamma$  parameters indicate dominant coherence seafloor type for both the profiles. Due to the difference in operating frequency and beam width the parameters are differ. A poor correlation (10%) is seen among the estimated  $\gamma$  of the MB and SBP profiles of the 14 locations (Fig. 7). The poor correlation is due to the characteristic difference among the fourteen seafloor types. Interestingly, the scatter plot of the mean amplitude values of the MB and SBP backscatter data show fairly good correlation (54.4%). According

**Table 1.** Estimated seafloor micro-topographic roughness parameter from marginal highs in the WCMI

Profiles	Location in DD.DDDD		$\sigma^2lc$	$\sigma$ in m	$\gamma$ (From MB Back-scatter)	$\sigma^2lc$	$\sigma$ in m	$\gamma$ (From SBP Back-scatter)	$\sigma^2lc$	$\sigma$ in m	Sediment Type	Remarks		
	Start Point Latitude (N) Longitude (E)	End Point Latitude (N) Longitude (E)												
A	14.9999	72.3766	15.0002	72.4882	7.25	1.14E-05	0.0192194	0.0134404	88.25	6.28E-09	0.003630624291275	0.002538952882703	-	Hights (no place of sediment retention)
B	15.2098	72.5693	15.1102	72.5694	34.75	2.37E-06	0.0135672	0.0094878	61.50	9.01E-09	0.003934001789234	0.002751109556375	Sand-silt-clay	Uneven ( Rugged ) topography
C	15.0703	72.5693	14.9703	72.5694	33.75	2.44E-06	0.0136555	0.0095495	64.75	8.56E-09	0.003889238975555	0.002719806214109	-	Suspected pockmark
D	14.9376	72.6119	15.0224	72.6121	33.75	2.44E-06	0.0136555	0.0095495	72.50	7.65E-09	0.003792747324892	0.00265232807951	-	Suspected pockmark
E	14.6925	72.6613	14.7683	72.6641	20.25	4.06E-06	0.0152971	0.0106975	70.50	7.86E-09	0.003816398038348	0.002668867396798	-	Steep slope
F	15.1736	72.6501	15.0787	72.6503	49.00	1.68E-06	0.0125697	0.0087902	37.50	1.48E-08	0.00439114350631	0.003070795975916	-	Small channel
G	14.9218	72.650203	15.021	72.6503	38.75	2.12E-06	0.0132427	0.0092608	74.75	7.42E-09	0.003767075399231	0.002634375296619	-	Hummocky topography
H	14.7283	72.6501	14.8299	72.6503	36.75	2.24E-06	0.0133996	0.0093705	112.75	5.00E-09	0.003438242121359	0.002404416994189	Sand-silt	Hights with a reflectors < 30m
I	15.0396	72.686	15.1521	72.6862	54.50	1.51E-06	0.0122761	0.0085849	51.00	1.09E-08	0.004101118493046	0.002867976905583	-	Terrace like Sea-floor
J	14.8382	72.6859	14.9489	72.6862	19.00	4.33E-06	0.0155152	0.01085	44.50	8.56E-09	0.004227271405613	0.002956197628888	-	Mild slope
K	15.1267	72.7548	15.2273	72.755	28.50	2.89E-06	0.0141784	0.0099152	64.75	5.14E-09	0.003889238975555	0.002719806214109	Sand-silt/ Silty-sand	Hyperbole- possibly pockmark
L	14.7368	72.6613	14.8154	72.6616	35.75	2.30E-06	0.013482	0.0094281	107.75	6.06E-09	0.003473074284721	0.002428775675915	Sand-silt	Hights with reflector with variable depth
M	14.7146	72.686	14.8267	72.6862	41.25	1.99E-06	0.01306	0.009133	91.50	5.37E-09	0.003601562886722	0.002518629783714	Sand-silt	Hights with Stratified layers
N	14.8002	72.6996	14.7206	72.6999	40.75	2.02E-06	0.0130954	0.0091578	103.25	5.37E-09	0.003506155973905	0.002451910223414	Sand-silt	Hights with undulated stratified layers



to Stanton and Clay[8], the product term  $\sigma^2 I_c$  contains the essential information to understand the fluctuations from the seafloor. This parameter can be determined from the fluctuation data and then be used for seafloor classification. The  $\sigma^2 I_c$  values of the areas are given in Table 1. The highest value is obtained for area A for MB data. Besides this, remaining values are comparable. Similarly,  $\sigma^2 I_c$  for SBP profiles are lower:

$$\gamma^{-1} = (300/\pi) b^2 K^4 \eta \sigma^{4.5} \quad (4)$$

According to Clay and Leong[10], in above equation  $\eta$  varies between 1 and 5. These two values of  $\sigma$  provide the limits for the ripple correlation lengths varying along two different axes in the horizontal plane. Similarly, the two computed values of sigma for  $\eta = 1$  or 5 reveal possible limits of the rms roughness ( $\sigma$ ) in the study areas. The rms roughness amplitude ( $\sigma$ ) is calculated using eq. (4), based on the assumption that the bottom consists of ripples. We have made this assumption in the absence of photographic evidence for such micro-roughness. The computed rms roughness heights of three different areas are presented in Table 1. For estimated  $\gamma$  values the  $\sigma^2 I_c$  are tabulated for MB and SBP profile data. Comparable seafloor micro-roughness parameters are determined. However, the parameters are different due to the varying sonar conditions of the MB and SBP.

## 5 CONCLUSION

This work also demonstrates hands on example related to the sonar data interpretation of the systems installed scientific research vessel to carry out seafloor studies. The exercise carried out here is essentially useful to carry out estimation of seafloor roughness. The seafloor is an interface between the hydrosphere and lithosphere and such analyses to estimate seafloor roughness parameter using multibeam and sub-bottom profiler becomes handy for the oceanographer to understand the seafloor.

## 6 REFERENCES

- [1] C de Moustier, 1988. State of the art in the Swath Bathymetric Survey system. *Int Hydrogr Rev*, **65**, 25-54.
- [2] C de Moustier, 1986. Beyond bathymetry: Mapping acoustic backscattering from the deep sea oor with Sea Beam. *J Acous. Soc Am*, **79**, 316-331.
- [3] B. Chakraborty, H.W. Schenke, V. Kodagali and R. Hagen, 2001. Analyses of Multibeam-Hydrosweep echo peaks for seabed characterization *Geo-Marine letters*: **20**, 174-181.
- [4] D.R. Jackson, D.P. Winebreuner and A. Ishimaru, 1986. Application of the composite roughness model to high frequency bottom backscattering. *J Acous Soc Am*, **79**, 1410-1422.
- [5] D.R. Jackson and K.B. Briggs, 1992. High frequency bottom backscattering: Roughness versus sediment volume backscattering. *J Acous Soc Am*, **92**, 962-977.
- [6] K.K. Talukdar and Robert Tyce, 1992. Relation of Sea Beam Echo Peak Statistics to the Character of Bottom Topography. *Geo-Marine Letters*. **12**, 200-207.
- [7] T.K. Stanton, 1984. Sonar estimates of sea oor micro-roughness. *J Acous Soc Am*, **75**, 809-818.
- [8] T.K. Stanton and C.S. Clay, 1986. Sonar echo statistics as a remote-sensing tool: volume and seafloor. *IEEE J Oceanogr Eng OE*, **11**, 79-95.
- [9] B.R. Rao and M. Veerayya, 2000. "Influence of marginal highs on the accumulation of organic carbon along the continental slope off western India" *Deep-Sea Research II*, **47**, 303-327
- [10] C.S. Clay and W.K. Leong, 1974. Acoustic estimates of topography and roughness spectrum of the sea floor southwest of Iberian Peninsula. In: Hampton L (ed) *Physics of sound in marine sediment*. Plenum Press, New York.

# Studies of Ultrasonic and acoustic parameters of complexes derived from Copper (II) surfactant of Mustard oil with N and S atoms containing ligands in Non- aqueous media (benzene) at 303.15 K

Pragya Tank, Rashmi Sharma and Arun Kumar Sharma

*Department of Chemistry*

*S.P.C. Govt. College Ajmer-305001, Raj India*

*e-mail: sharmaarun423@gmail.com*

[Received: 28-05-2017; Revised: 23-06-2017; Accepted: 05-07-2017]

## ABSTRACT

Ultrasonic speed have been measured in binary system containing complexes derived from Copper surfactant of mustard oil with Urea/Thiourea/2-amino-6-chloro Benzothiazole Ligands in benzene at 303.15 K. From these values, the specific acoustic impedance  $Z$ , adiabatic compressibility  $\beta_{ad}$ , intermolecular free length  $L_f$ , apparent molar compressibility  $\phi_k$ , molar sound velocity  $R$ , primary solvation number  $S_n$  have been calculated. The results have been analyzed in terms of Bachem's and Masson equation. The results have been explained on the basis of solute-solvent interactions. The decrease in  $\beta$  and  $L_f$  with increasing concentration of the complex is indicating that there is sufficient solute - solvent interaction due to which micellar alignment is considerably affected. The orientation of the solvent molecules around the solutes may be due to the influence of electrostatic fields of solutes and results in the increase in the internal pressure and in lowering the compressibility of the solution i.e. the solution becomes harder to compress.

## 1. INTRODUCTION

Ultrasonic wave in recent years, acquired the status of an important probe for the study of structure and properties of matter in basic essence. Properties of solutions are thermodynamically very important as a part of studies of the thermodynamic, acoustic and transport aspects. The compositional dependence of thermodynamic properties has proved to be very useful in understanding the nature and extent of pattern of molecular aggregation resulting from intermolecular interaction between the components. Ultrasonic technique is a powerful means for characterizing the various aspects of physicochemical behavior of the system and also for studying the interaction between the molecules[1-5]. Ultrasonic parameters of solvent and solvent mixtures have also been studied at various temperatures[6-7]. This has been studied for various binary and ternary mixtures with respect to variation in concentration of the liquids and temperatures[8-10]. Ultrasonic velocity measurements have been extensively used to study the molecular interactions in electrolyte solutions and to get significant information on the arrangement of molecules in aqueous electrolyte solutions[11-15]. Ultrasonic investigation of liquid mixture have significant importance in understanding intermolecular interaction between the component molecules as that finds application in several industrial

and technological processes[16-17]. Derived parameters from ultrasonic velocity measurements provide qualitative information regarding the nature and strength of molecular interactions in liquid mixtures[18-20]. The present work deals with the determination of ultrasonic velocity measurements which have been used to obtain information regarding various acoustic parameters and solute-solute interactions of complexes of Copper (II) surfactants of mustard oil with various ligands containing N and S atoms Like Urea/Thiourea/2-amino-6-chloro Benzothiazole in non-aqueous solvent benzene at 303.15 K to access the effect of solvent molecules on the micellar nature of solute molecule. The studies have also been done to understand the nature of the solution and observed that the increase in the internal pressure and in lowering the compressibility of the solution.

## 2 EXPERIMENTAL

All the chemicals used were of LR/AR grade. Copper soap was prepared by refluxing the edible oil i.e. mustard (extracted from kernels and purified) with ethyl alcohol and 2 N KOH solutions for 3-4 hours (Direct Metathesis). The neutralization of excess of KOH present was done by slow addition of 0.5N HCl. Saturated solution of Copper Sulphate was then added to it, for conversion of neutralized potassium soap into their corresponding Copper soap. Copper soap so obtained was then washed with warm water and 10% alcohol at 50°C and recrystallized using hot benzene. Molecular weights of Copper soap were determined from saponification value[21]. The purified Copper soap derived from edible oil was refluxed with ligand (Urea / Thiourea / 2-amino-6-chloro Benzothiazole) in 1:1 ratio using benzene as a solvent for one hour. It was then filtered hot, dried, recrystallized and purified in hot benzene. TLC using silica gel was used to check the purity of the complex. All the three solid complexes obtained are green in Colour and sticky in nature. They are soluble in benzene and other organic solvents but insoluble in water. All the complexes are stable at room temperature, their physical parameters are discussed in Table-1[22]. On the basis of their elemental analysis, 1:1 (Metal: ligand) type of stoichiometry has been suggested. The Copper soap and complexes are abbreviated as follows :

**Table 1.** Analytical and physical data of copper soaps and complexes derived from mustard oil.

Name of soap /Complex	Colour	Melting Point (°C)	Yield (%)	Metal Content (%)		S.V.	S.E.	Average Molecular Weight
				Observed	Calculated			
CM	Green	90	95	11.1760	9.0750	175.80	319.10	699.724
CMU	Dark Green	68	92	8.4600	8.3580	-	-	759.724
CMT	Dark Green	88	90	8.1280	8.1859	-	-	775.724
CMB	Dark Green	95	91	7.1120	7.1814	-	-	884.224

1. Copper - Mustard soap (CM)
2. Copper - Mustard soap - Urea complex (CMU)
3. Copper - Mustard soap - Thiourea complex (CMT)
4. Copper - Mustard soap - Benzothiazole complex (CMB)

The underlying principle of ultrasonic experimental technique used in the measurement of velocity (U) is based on the accurate determination of the wavelength ( $\lambda$ ) of the medium[23]. Ultrasonic waves of known frequency (f) are produce by a quartz plate fixed at the bottom of the cell. Ultrasonic interferometer from Mittal Enterprises, Model M-82 with accuracy of  $\pm 0.03\%$  was used for the measurements of ultrasonic velocities in various solutions at a fixed frequency 2MHz. Water maintained at 303.15 K temperature in a thermostat was passed through the jacket of the cell before the measurement was actually made. Further, the operative part of the measurement involves the slow movement of micrometer till the anode current

meter shows a maximum. A number of maxima readings of anode current are passed on and their number 'n' are counted. The total distance 'd' (1 cm) thus moved by the micrometer gives the value of wavelength ' $\lambda$ ' with the help of the following relation:

$$d = (n\lambda)/2 \quad (1)$$

Once the wavelength is known, the ultrasonic velocity 'U' in the solution can be calculated with the help of the following relation:

$$U = \lambda \times f \quad (2)$$

### 3. RESULTS AND DISCUSSION

#### 3.1 Acoustic parameters and micellar features of Urea complex of Cu (II) - Mustard Soap (CMU)

Of late, ultrasonic investigations have established their versatility to furnish information as to the understanding of solute - solvent interactions. A number of workers have discussed the physicochemical aspects of ultrasonic velocity and related parameters. Ultrasonic measurements have also been used to determine the solvation number

The specific acoustic impedance 'Z', adiabatic compressibility ' $\beta$ ', intermolecular free length ' $L_f$ ', apparent molar compressibility ' $\phi_k$ ', molar sound velocity 'R' and primary solvation number ' $S_n$ ' have been calculated by using the following relationships[22].

$$Z = d \cdot U \quad (3)$$

$$\beta = U^{-2} d^{-1} \quad (4)$$

$$L_f = K \cdot \sqrt{\beta} \quad (5)$$

$$\phi_k = (\beta_0 M/d_0) + [1000 (\beta d_0 - \beta_0 d)/cd_0] \quad (6)$$

$$\phi_v = (M/d_0) + [1000 (d_0 - d)/cd_0] \quad (7)$$

$$R = (\bar{M} / d) \cdot U^{1/3} \quad (8)$$

$$\bar{M} = M_1 X_1 + M_2 X_2 \quad (9)$$

$$S_n = (n_0/n) [1 - \bar{V}\beta/n_0 \bar{V}_0\beta_0] \quad (10)$$

Where  $\beta_0$ ,  $\beta$ ,  $d_0$ ,  $d$ ,  $n_0$ ,  $n$ ,  $\bar{V}_0$  and  $\bar{V}$  are adiabatic compressibility, density, number of moles and molar volume of solvent and complex (solute) solution respectively. K ( $6.31 \times 10^4$ ), c and U respectively are the temperature dependent Jacobson's constant, concentration of the solution and ultrasonic velocity. The expression for molar volume of the solvent  $\bar{V}_0$  and soap solution  $\bar{V}$  may be written as

$$\bar{V} = (M_1 X_1 + M_2 X_2) / d \quad (11)$$

$$\bar{V}_0 = (M_1 X_1 + M_2 X_2) / d_0 \quad (12)$$

In equations (9), (10) and (12) 'M' represents the molecular weight and 'X' the mole fraction of the component. Here the subscript 1 and 2 refer to solute and solvent respectively.

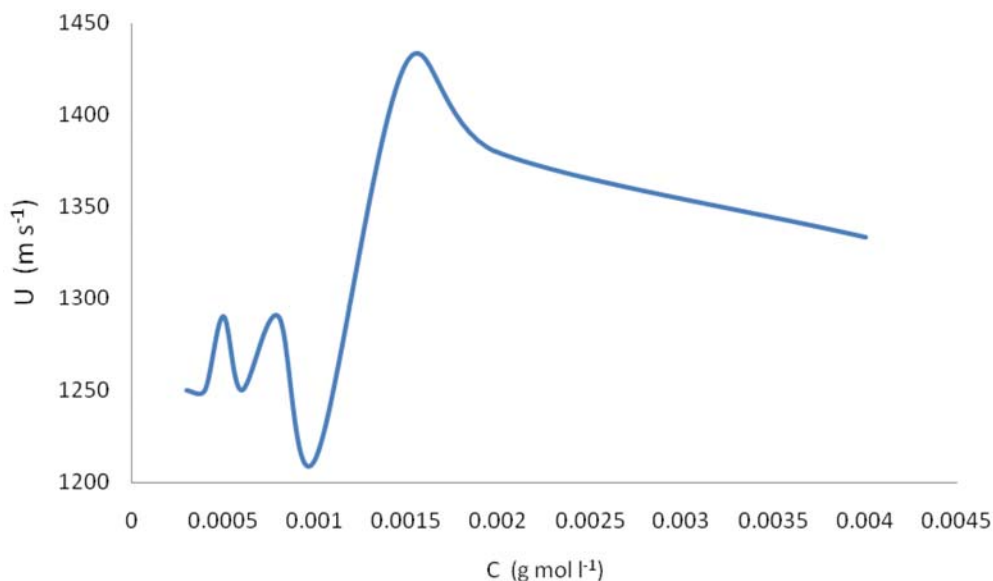
The values of CMC and allied parameters for CMU in benzene are recorded in Table -2 and Table 3 respectively. The perusal of the data suggests that, in general, the values of U, Z,  $\phi_k$ ,  $\phi_v$ , R and  $S_n$  increase with increasing concentration of the solution, where as  $\beta$  and  $L_f$  decrease with the increase in the concentration. The increase in the values of specific acoustic impedance 'Z' with the concentration can be explained on the basis of lyophobic interactions between the solute and solvent molecules, which increases the intermolecular distance leaving relatively wider gaps between the molecules and becoming the main cause of impedance in the propagation of ultrasound waves. Also it is suggested that, the decrease in the intermolecular free length ' $L_f$ ' with the increase in the concentration of the complex indicates that there is significant interaction between solute and solvent molecules and that the structural arrangement is considerably affected[23-24].

**Table 2.** Value of CMC ( $\text{g mole l}^{-1}$ ) obtained for various parametrs for urea, thiourea and benzothiazole complexes of copper (II) - mustard soap solution in benzene.

Graph plotted	CMU	CMT	CMB
$U \text{ v/s } c$	0.0010	0.0008	0.0015
$Z \text{ v/s } c$	0.0010	0.0008	0.0015
$\beta \text{ v/s } c$	0.0010	0.0008	0.0015
$L_f \text{ v/s } c$	0.0010	0.0008	0.0015
$(\beta - \beta_0) / c \text{ v/s } \sqrt{c}$	0.0011	0.0008	0.0015
$\beta_K \text{ v/s } \sqrt{c}$	0.0011	0.0008	0.0015

**Table 3.** Ultrasonic velocity and other acoustic parameters of urea complex of copper (II) mustard soap solutions in benzene.

C ( $\text{g mol l}^{-1}$ )	d ( $\text{g dm}^{-3}$ )	U ( $\text{m s}^{-1}$ )	$Z \times 10^{-5}$ ( $\text{g cm}^{-2} \text{ s}^{-1}$ )	$\beta \times 10^{11}$ ( $\text{cm}^2 \text{ dyn}^{-1}$ )	$L_f$ ( $\text{A}^0$ )	$-\phi_k \times 10^5$	$-\phi_v \times 10^{-4}$	R	$S_n \times 10^{-2}$
0.0003	0.9535	1250	1.1919	6.7122	0.5178	11.7896	32.7411	4092.0983	-262.6908
0.0004	0.9554	1250	1.1942	6.6989	0.5173	8.9247	25.0782	4084.6271	-194.9566
0.0005	0.9575	1290	1.2355	6.2728	0.5006	8.0370	20.5358	4119.5162	-138.4286
0.0006	0.9576	1250	1.1970	6.6831	0.5167	6.0150	17.1253	4076.1976	-128.9373
0.0008	0.9585	1290	1.2367	6.2666	0.5003	5.0415	12.9381	4117.3254	-86.0401
0.0010	0.9592	1212	1.6127	7.0954	0.5324	3.2112	10.4248	4030.2689	-85.5173
0.0015	0.9569	1428	1.3671	5.1205	0.4522	3.4406	6.7440	4270.5917	-30.6435
0.0020	0.9568	1379	1.3198	5.4934	0.4684	2.3918	5.02903	4224.6613	-26.7925
0.0040	0.9568	1333	1.2757	5.8793	0.4846	1.0965	2.4687	4190.0361	-15.4561

**Fig. 1.** Plot of ultrasonic velocity v/s concentration for urea complex of copper (II) - mustard soap solutions in benzene

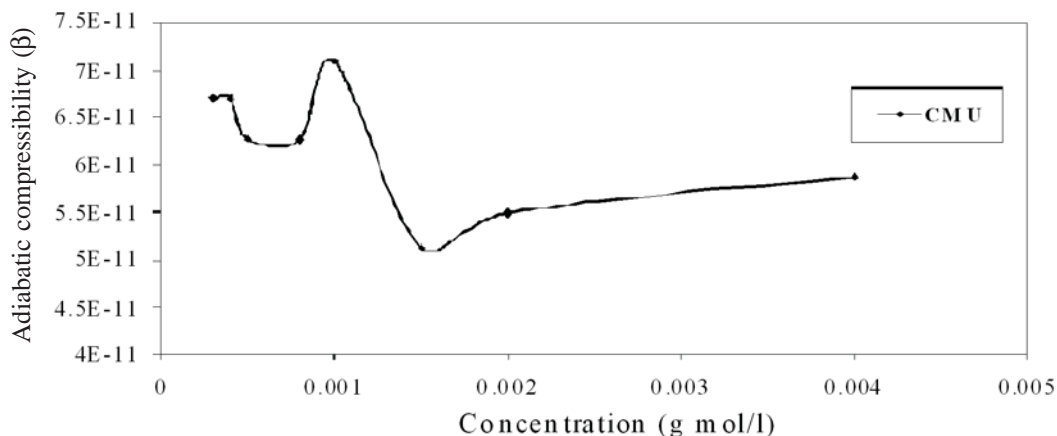


Fig. 2. Plot of adiabatic compressibility v/s concentration for urea complex of copper (II) - mustard soap solutions in benzene

The plots of  $U$  v/s  $c$ ,  $Z$  v/s  $c$ ,  $\beta$  v/s  $c$  and  $L_f$  v/s  $c$  are all characterized by an intersection of two curvatures at a definite concentration (Figure - 1 and 2) corresponding to the CMC of CMU. At CMC, the hydrocarbon chain structure of the complex molecules derived from Mustard oil, allow extensive contact between adjacent chain, possibly accompanied by change in vibrational and rotational degree of freedom of methylene groups of fatty acids of varying composition present in Mustard oil.

The decrease in adiabatic compressibility ' $\beta$ ' and intermolecular free length ' $L_f$ ' of the complex solution with increasing concentration of complex in benzene may be interpreted on the basis of the fact that the non-polar long chains or lyophobic segment of the molecule in the solution are enveloped by a layer of solvent molecules bound and oriented towards lyophobic end. The orientation of the solvent molecules around the solutes may be due to the influence of electrostatic fields of solutes and results in the increase in the internal pressure and in lowering the compressibility of the solution i.e. the solution becomes harder to compress. This indicates that there is sufficient solute - solvent interaction due to which micellar alignment is considerably affected[25-26].

Literature survey also reveals that the decrease in the values of  $\beta$  and  $L_f$  with the increase in the ultrasonic velocity indicates that there is significant interaction between solute - solvent molecules suggesting a consistent change in the lucid micellar orientation in such systems[27].

Various scientists have suggested that the correlation between solvation number  $S_n$  and molar concentration of the solute in the solvent can be understood assuming that solvent molecules in the immediate vicinity of solutes - molecules have modified properties, similar to those of pure solvent under high pressure. Thus solvation about a solute is conceived as a sphere of bound solvent at high pressure and virtually incompressible at the boundary of which compressibility falls to zero[28]. A close perusal of Table -3 leads us to see a persistent rise in solvation property of the solute with increase in concentration. This may be attributed to a greater number of solvent molecules forming solvation shells around the solute.

The adiabatic compressibility ' $\beta$ ' of CMU solutions in benzene is found to obey Bachem's relationship[29].

$$\beta = \beta_0 + A \cdot c + B \cdot c^{3/2} \quad (13)$$

On rearranging, we get

$$(\beta - \beta_0) / c = A + B \sqrt{c} \quad (14)$$

The values of constants 'A' and 'B' have been evaluated from the intercept and slope of the plots  $(\beta - \beta_0) / c$  v/s  $\sqrt{c}$

Unlike other plots of  $U$ ,  $Z$ ,  $\beta$  and  $L_f$  v/s  $c$ , the plot of  $(\beta - \beta_0) / c$  v/s  $\sqrt{c}$  is characterized by intersection of two straight lines at CMC of the complex. Thus the values 'A' and 'B' have been evaluated both below and

above CMC and are designated as  $A_1$ ,  $A_2$  and  $B_1$ ,  $B_2$  respectively. The values of  $A_1$ ,  $A_2$  and  $B_1$ ,  $B_2$  follow the order

$$A_1 < A_2 \text{ and } B_1 > B_2$$

The value of apparent molar compressibility ' $\phi_k$ ' increases continuously with the increasing concentration (Table - 3). The data has also been evaluated in terms of Masson's equation[30].

$$\phi_k = \phi_k^0 + S_k \sqrt{c} \quad (14)$$

Here,  $\phi_k^0$  is the apparent molar compressibility and is a measure of solute - solvent interaction.  $S_k$  is the experimental slope, a measure of solute - solvent interactions. The plot of  $\phi_k$  v/s  $\sqrt{c}$  is characterized by an intersection of two straight lines, thus Masson's equation fits well both below and above CMC. Correspondingly, two values of both  $\phi_k^0$  and  $S_k$  are obtained i.e. below and above CMC, and are designated as  $\phi_{k1}^0$ ,  $\phi_{k2}^0$  and  $S_{k1}$ ,  $S_{k2}$ . It is revealed that negative values of both  $\phi_{k1}^0$  and  $\phi_{k2}^0$  are obtained. The order of the two parameters are observed to be as follows :

$$\phi_{k1}^0 < \phi_{k2}^0 \text{ and } S_{k1} > S_{k2}$$

Literature survey reveals that negative values of  $\phi_k^0$  indicate electrostriction and hydrophobic interaction. The negative values of  $\phi_k^0$  are also attributed to the loss of structural compressibility of solute molecules due to the increased population of hydrophobic non-polar solvent benzene. It shows that structural disruption is much in evidence in solution.

Since  $\phi_{k1}^0 < \phi_{k2}^0$ , thus it may be suggested that solute - solvent interaction is more prominent above CMC as compared to below CMC. It may also be suggested that above CMC, hydrophobic - hydrophobic group interactions between the long alkyl chain fatty acids of CMU, derived from Mustard oil, and non-polar solvent benzene are more dominant as compared to below CMC[31].

### 3.2 Acoustic parameters and micellar features of Thiourea complex of Cu (II) - Mustard Soap (CMT)

At the very outset, it may be mentioned that the acoustic parameters and related equations pertaining to ultrasonic investigations are the same as has been enumerated for CMU solutions in benzene. The values of ultrasonic velocity 'U' and allied parameters of CMT in benzene are recorded in Table-4. It is observed from the data that, in general, the numerical values of U, Z,  $\phi_k$ ,  $\phi_v$ , R and  $S_n$  increases, where  $\beta$  and  $L_f$  decreases with the increase in concentration of the complex solution. Acoustic impedance has a greater significance as a characteristic property of the medium than either density or ultrasonic velocity individually.

**Table 4.** Ultrasonic velocity and other acoustic parameters of thiourea complex of copper (II) mustard soap solutions in benzene.

C (g mol l <sup>-1</sup> )	d (g dm <sup>-3</sup> )	U (m s <sup>-1</sup> )	Z × 10 <sup>-5</sup> (g cm <sup>-2</sup> s <sup>-1</sup> )	β × 10 <sup>11</sup> (cm <sup>2</sup> dyn <sup>-1</sup> )	L <sub>f</sub> (A <sup>0</sup> )	-φ <sub>k</sub> × 10 <sup>5</sup>	-φ <sub>v</sub> × 10 <sup>-4</sup>	R	S <sub>n</sub> × 10 <sup>-2</sup>
0.0003	0.9493	1290	1.2250	6.3269	0.5027	12.9249	31.1392	4153.7642	-241.1744
0.0004	0.9499	1250	1.1873	6.7377	0.5188	8.6798	23.4926	4108.2479	-200.8862
0.0005	0.9512	1379	1.3120	5.5260	0.4698	9.3956	19.0796	4240.0464	-110.4587
0.0006	0.9515	1333	1.2686	5.9119	0.4859	7.1900	15.9368	4191.8327	-105.2537
0.0008	0.9522	1212	1.1542	7.1480	0.5343	3.8547	12.0340	4058.8894	-110.6782
0.0010	0.9509	1290	1.2270	6.3165	0.5023	3.9006	9.4585	4151.3094	-71.6238
0.0015	0.9508	1290	1.2268	6.3170	0.5023	2.5977	6.2705	4154.7083	-47.8309
0.0020	0.9511	1290	1.2272	6.3149	0.5022	1.9496	4.6984	4156.4531	-35.8664
0.0040	0.9511	1290	1.2273	6.3147	0.5022	0.9721	2.3054	4168.6739	-18.0401
0.0060	0.9522	1290	1.2289	6.3076	0.5019	0.6493	1.5279	4176.2777	-12.0389

The decrease in  $\beta$  and  $L_f$  with increasing concentration of the complex, signifies that the complex solution is harder to compress. Thus indicating that there is sufficient solute - solvent interaction due to which micellar alignment is considerably affected. A perusal of Table-4 indicates a continuous increase in the values of solvation number, thus suggesting that greater numbers of solvent molecules are forming solvation shells around the non-polar segment of the molecule.

The plots of  $U$  v/s  $c$ ,  $Z$  v/s  $c$ ,  $\beta$  v/s  $c$  and  $L_f$  v/s  $c$  (Figure - 3 and 4) for CMT solutions in benzene yield two intersecting curvatures at a point corresponding to the CMC of the complex. The values of CMC obtained from these plots are found to be in good agreement with each other.

The adiabatic compressibility ' $\beta$ ' of CMT solutions in benzene is found to obey Bachem's relationship. The value of constants 'A' and 'B' are evaluated both below and above CMC, as the plot of  $(\beta - \beta_0) / c$  v/s  $\sqrt{c}$  is characterized by an intersection of two straight lines at a concentration corresponding to the CMC of the complex. The values of  $A_1, A_2$  and  $B_1, B_2$  follow the order.

$$A_1 < A_2 \text{ and } B_1 > B_2$$

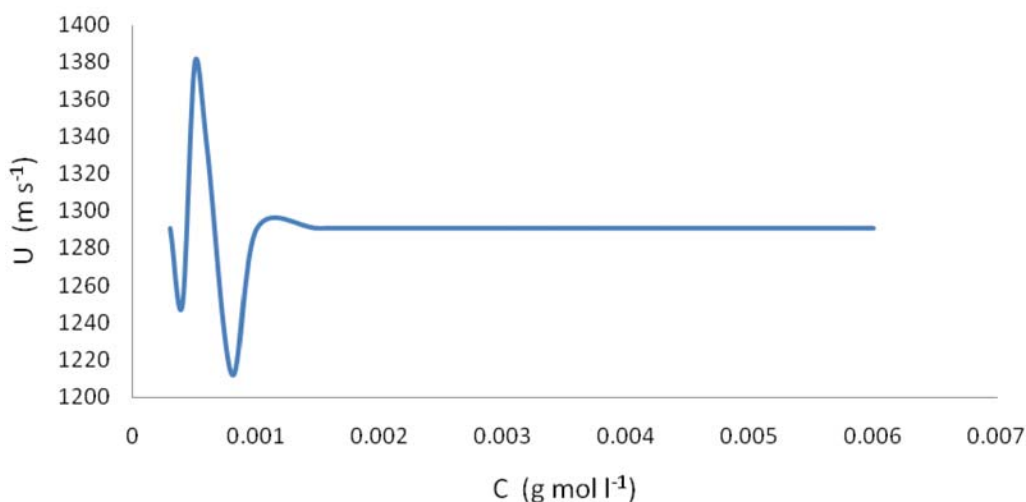


Fig. 3. Plot of ultrasonic velocity v/s concentration for thiourea complex of copper (II) - mustard soap solutions in benzene

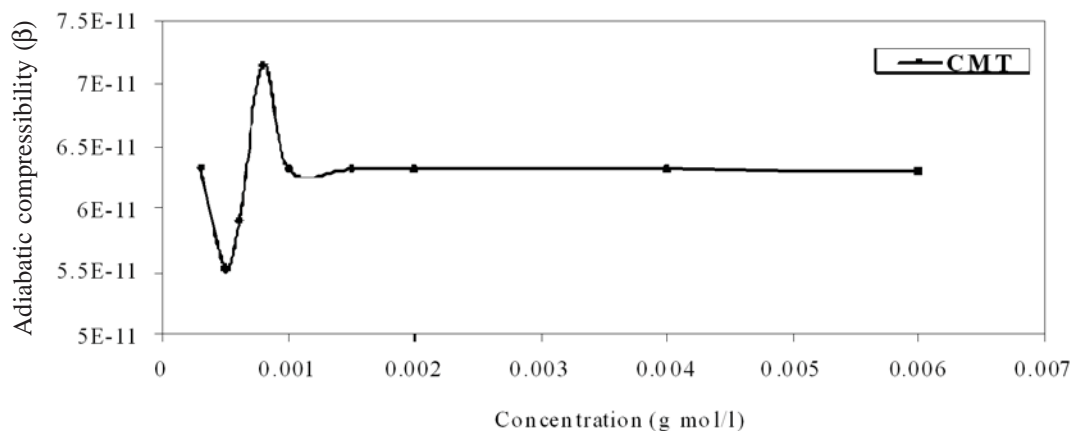


Fig. 4. Plot of adiabatic compressibility v/s concentration for thiourea complex of copper (II) - mustard soap solutions in benzene



The apparent molar compressibility ' $\phi_k$ ' persistently rises with increasing concentration as is observed from Table 4. The acoustic data has also been investigated in terms of Masson equation. The plot of  $\phi_k v/s \sqrt{c}$  for CMT solutions in benzene is characterized by an two intersecting straight lines, which show an abrupt change at a definite concentration corresponding to the CMC of the complex. Since Masson equation fits well both below and above CMC, two values of  $\phi_k^0$  and  $S_k$ , which are designated as  $\phi_{k1}^0$ ,  $\phi_{k2}^0$  and  $S_{k1}$ ,  $S_{k2}$  are evaluated below and above CMC. The orders of these two parameters are obtained in the following order.

$$\phi_{k1}^0 < \phi_{k2}^0 \quad \text{and} \quad S_{k1} > S_{k2}$$

It reveals that both  $\phi_{k1}^0$  and  $\phi_{k2}^0$  are of negative sign convention, which indicates loss of structural compressibility due to electrostriction and hydrophobic interactions. Since  $\phi_{k1}^0 < \phi_{k2}^0$ , it may be suggested that solute - solvent interaction is more prominent above CMC rather than below CMC. The possibility cannot be denied that hydrophobic - hydrophobic group interactions between the long alkyl chain fatty acids of CMT, derived from Mustard oil, and non-polar solvent benzene are more prominent above CMC[32-33].

### 3.3 Acoustic parameters and micellar features of Benzothiazole a complex of Cu (II) - Mustard Soap (CMB)

The acoustic parameters and the related equation pertaining to ultrasonic investigations are the same as has been calculated for CMU and CMT solutions in benzene.

The values of ultrasonic velocity and allied parameters for CMB solutions using pure benzene as a solvent are recorded in Table-5. It is observed that, in general, the numerical values of  $Z$ ,  $\phi_k$ ,  $\phi_v$ ,  $R$  and  $S_n$  increases, where as  $\beta$  and  $L_f$  decreases with the increasing concentration of the complex. The decrease in  $\beta$  and  $L_f$  with increase in the concentration indicates that the complex solution is harder to compress. This suggests the existence of sufficient solute - solvent interaction, which considerably affects the micellar alignment. As observed from the study of Table-5, the values of solvation number continuously increases with the increasing concentration suggesting the formation of solvation shells around the solute molecules by greater number of solvent molecules.

The plots of  $Z v/s c$ ,  $L_f v/s c$  and  $\beta v/s c$  (Figure 5 and 6) for CMB solutions in benzene are plotted and observed to be an intersection of two curvatures at a particular concentration corresponding to the CMC of the complex CMB. The values of CMC obtained from these plots are in good agreement with each other.

The adiabatic compressibility ' $\beta$ ' data for CMB solutions in benzene are found to obey Bachem's relationship. The corresponding values of constants 'A' and 'B' are evaluated both above and below CMC as the plot of  $(\beta - \beta_0)/c v/s \sqrt{c}$  is observed to be an intersection of two straight lines at CMC of the complex. Thus the values  $A_1$ ,  $A_2$  and  $B_1$ ,  $B_2$  are evaluated and observed to be in the following order :

**Table 5.** Ultrasonic velocity and other acoustic parameters of benzothiazole complex of copper (II) mustard soap solutions in benzene.

C (g mol l <sup>-1</sup> )	d (g dm <sup>-3</sup> )	U (m s <sup>-1</sup> )	Z × 10 <sup>-5</sup> (g cm <sup>-2</sup> s <sup>-1</sup> )	$\beta \times 10^{11}$ (cm <sup>2</sup> dyn <sup>-1</sup> )	L <sub>f</sub> (A <sup>0</sup> )	$-\phi_k \times 10^5$	$-\phi_v \times 10^{-4}$	R	S <sub>n</sub> × 10 <sup>-2</sup>
0.0005	0.9467	1212	1.1476	7.1889	0.5359	5.9725	18.0499	4079.0279	-34435.46
0.0006	0.9468	1250	1.1835	6.7593	0.5196	5.6933	15.0365	4121.2616	-25675.04
0.0008	0.9469	1250	1.1836	6.7591	0.5196	4.2690	11.2564	4121.8882	-19296.51
0.0010	0.9470	1250	1.1837	6.7585	0.5195	3.4153	8.9945	4122.2787	-15454.79
0.0015	0.9465	1250	1.1831	6.7620	0.5197	2.2687	5.9249	4126.3183	-10326.59
0.0020	0.9469	1250	1.1837	6.7587	0.5196	1.7040	4.4450	4126.2034	-7740.38
0.0040	0.9471	1250	1.1839	6.7574	0.5195	0.8493	2.1764	4133.1046	-3880.12
0.0060	0.9472	1250	1.1840	6.7570	0.5195	0.5641	1.4182	4140.4746	2594.38

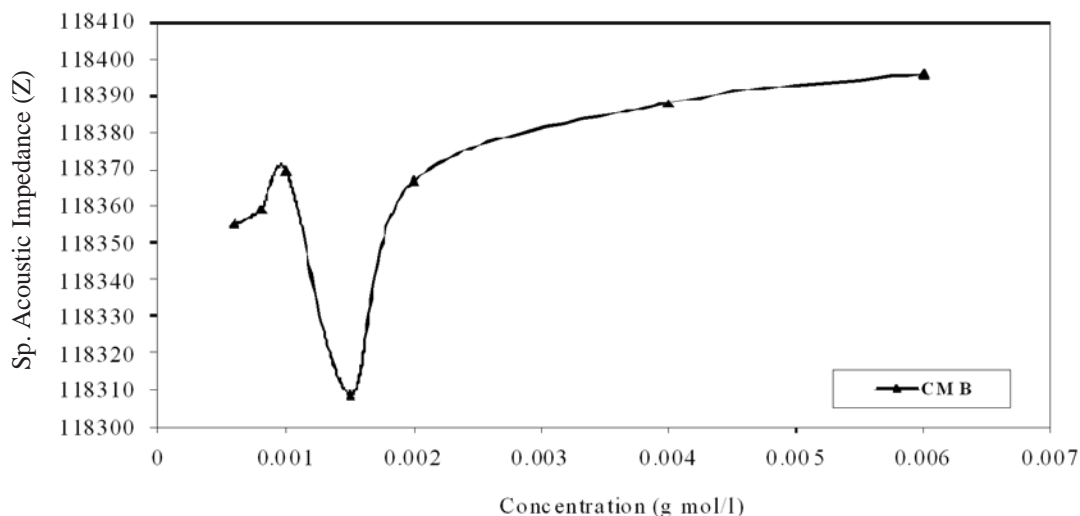


Fig. 5. Plot of specific acoustic impedance v/s concentration for benzothiazole complex of copper (II) - mustard soap solutions in benzene

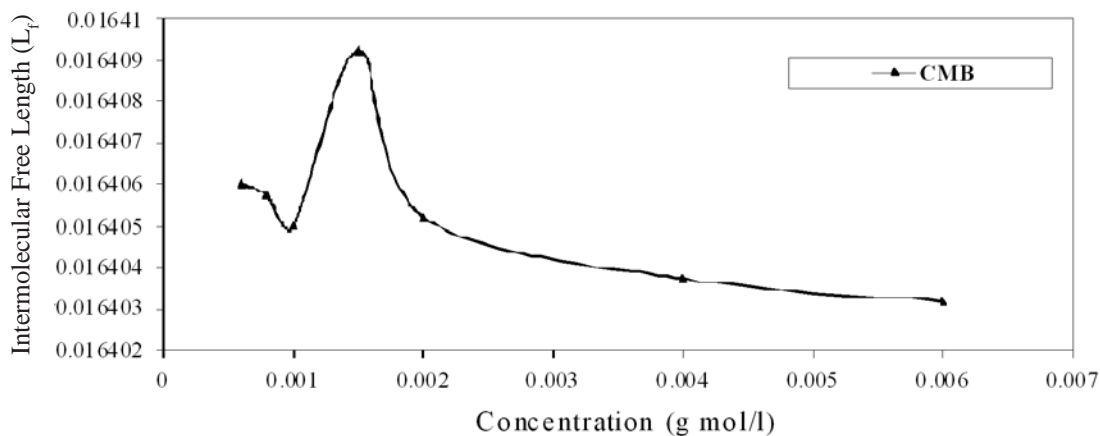


Fig. 6. Plot of intermolecular free length v/s concentration for benzothiazole complex of copper (II) - mustard soap solutions in benzene

$$A_1 < A_2 \text{ and } B_1 > B_2$$

From the acoustic data, the parameter, apparent molar compressibility  $\phi_k$  has also been evaluated. The apparent molar compressibility ' $\phi_k$ ' values are observed to increase continuously with the increasing concentration. The apparent molar compressibility data has been recorded in Table-5. This data has also been analyzed in terms of Masson equation. For CMB solutions in pure benzene, the plot of  $\phi_k$  v/s  $\sqrt{c}$  is characterized by an intersection of two straight lines at the CMC of the complex. As the plot is obtained as an intersection of two straight lines, Masson equation fits well both below and above CMC. Hence two values of both  $\phi_k^0$  and  $S_k$  could be evaluated *i.e.* below and above CMC, and are designated as  $\phi_{k1}^0$ ,  $\phi_{k2}^0$ , and  $S_{k1}$ ,  $S_{k2}$ . The order of these parameters is as follows :

$$\phi_{k1}^0 < \phi_{k2}^0 \text{ and } S_{k1} > S_{k2}$$

A study of Table-6 reveals that  $\phi_{k1}^0$  and  $\phi_{k2}^0$  parameters are of negative sign convention, thus indicating loss of structural compressibility due to electrostriction and hydrophobic interaction as already reported for CMU and CMT systems. Since  $\phi_k^0$  is a measure of solute - solvent interaction, it is reasonable to assume

**Table 6.** Computed parameters for bachem's relationship and masson's equation for all the complexes.

Complex	Bachem's Relation				Masson's Equation			
	$A_1 \times 10^7$	$A_2 \times 10^7$	$B_1$	$B_2$	$\phi_{k1}^0 \times 10^5$	$\phi_{k2}^0 \times 10^5$	$S_{k1}$	$S_{k2}$
CMU	-1.63	-0.34	2.0503	0.1584	-21	-4.7	2.1445	0.1763
CMT	-2.0272	-0.3909	3.2708	0.2679	-24.84	-5.789	3.4874	0.424
CMB	-0.823	-0.3096	2.246	0.4663	-11.16	-4.0526	2.246	0.4452

that greater magnitude of  $\phi_k^0$  suggests greater solute - solvent interaction. As it is observed that  $\phi_{k1}^0 < \phi_{k2}^0$ , it may be suggested that solute - solvent interaction is more prominent above CMC as compared to below CMC. For our referred system CMB, it may be suggested that hydrophobic - hydrophobic group interactions between long alkyl chain fatty acids of CMB, derived from Mustard oil, and non-polar solvent benzene are more prominent above CMC[34].

### 3.4 General profile for our Referred Systems

For all the complexes *i.e.* CMU, CMT and CMB, various acoustic parameters pertaining to ultrasonic investigations have been evaluated. These parameters and other related equations have been enumerated for the complexes using pure benzene as the solvent.

It is observed from the data as recorded in Tables 3, 4 and 5, that numerical values of  $U$ ,  $Z$ ,  $\phi_k$ ,  $\phi_v$ ,  $R$  and  $S_n$ , in general, increase while the values for  $\beta$  and  $L_f$  decrease with increasing concentration for all the complexes. The value of  $U$  remains nearly unchanged for CMB, no significant explanation can be given for this observation. Acoustic impedance has a greater significance as a characteristic property of the medium than either density or ultrasonic velocity individually. The values of  $Z$ , in general, increase with increasing concentration, and the comparative order was found to be

$$CMU > CMT > CMB$$

These results indicate that interaction-strengthening contribution is largest in CMU than those in CMT and CMB. It may be suggested that as  $>C=O$  and  $NH_2$  groups of Urea are capable of making intermolecular hydrogen bonding with other CMU molecules, their interaction strengthening contribution is highest.

For all the complexes, the values of  $\beta$  and  $L_f$  decrease with increasing concentration of the complex. The decreasing values of  $\beta$  and  $L_f$  suggest that the complex becomes harder to compress. As  $L_f$  decreases,  $U$  increases and vice versa showing an inverse behavior. The interdependence of intermolecular free length ' $L_f$ ' and ultrasonic velocity ' $U$ ' have been evolved from a model for sound propagation proposed by Eyring and Kincaid. The decrease in the values of  $\beta$  and  $L_f$  with increase in ultrasonic velocity ' $U$ ' indicates that there is significant interaction between the solute and solvent molecules[35].

For all the complexes, the solvation number ' $S_n$ ' continuously increases with the increase in complex concentration signifying the formation of solvation shells by larger number of solvent molecules around the solute moiety.

For all the complexes, the plots of  $U$  v/s  $c$ ,  $Z$  v/s  $c$ ,  $L_f$  v/s  $c$ ,  $\beta$  v/s  $c$  are characterized as an intersection of two curvatures at a definite concentration corresponding to the CMC of the complex (Figures 1-6). Literature survey reveals that the non-rectilinear behavior of ultrasonic velocity, compressibility and other thermo dynamical parameters of complexes with changing concentration are attributed to the difference in size of solute and solvent molecules and the strength of interactions. The CMC obtained for these parameters are found to be in good agreement with each other for each individual complex. The various parameters in general are in the following comparative order-

$$U : CMU > CMT > CMB$$

$$\beta : CMU < CMT < CMB$$

$$L_f : CMU < CMT < CMB$$

Again for all the three complexes, the adiabatic compressibility ' $\beta$ ' of complex solution in benzene is observed to follow Bachem's relation. The constants 'A' and 'B' are evaluated both below and above CMC for all the complexes. The observations for all the complexes are found to be identical and are in the following order

$$A_1 < A_2 \quad \text{and} \quad B_1 > B_2$$

For all the three complexes, the value of apparent molar compressibility ' $\phi_k$ ' persistently rises with the increasing concentration. The  $\phi_k$  data has been investigated in terms of Masson equation for all the complexes. The plots of  $\phi_k \sqrt{c}$  are obtained as two straight lines intersecting at a concentration corresponding to the CMC of the complex. The parameters  $\phi_k^0$  and  $S_k$  have been evaluated both below and above CMC. For all the complexes, these parameters are found to be in the given order :

$$i \quad \phi_{k1}^0 < \phi_{k2}^0 \quad \text{and} \quad S_{k1} > S_{k2}$$

Since  $\phi_{k1}^0 < \phi_{k2}^0$ , it suggests greater solute - solvent interaction above CMC. Also various scientists have suggested that as more and more - electrons are made available from the basic ligands; the interaction gets stronger and continues increasing as concentration of solute is increased. This explanation supports our observation that  $\phi_{k1}^0 < \phi_{k2}^0$ .

A perusal of Table - 3, 4, 5 and 6 reveals that  $\phi_k$  and  $\phi_k^0$  values are negative, which are indicative of electrostriction and hydrophobic interaction. Thus it may be suggested that above CMC, hydrophobic - hydrophobic group interactions between the long alkyl chain fatty acids of CMU, CMT and CMB, derived from Mustard oil, and non-polar solvent benzene are more dominant as compared to below CMC. Also the negative values of  $\phi_k$  and hence  $\phi_k^0$  indicate the loss of structural compressibility of solute molecules due to the increased population of hydrophobic non-polar solvent benzene.

For each complex the CMC values are found to be in good agreement for all parameters. The comparative order of CMC is as follows :

$$\text{CMB} > \text{CMU} > \text{CMT}$$

## 4 CONCLUSION

The nonlinear variation of ultrasonic velocity and other acoustical parameters with molar concentration of Copper surfactants derived from Mustard oil with non polar pure benzene shows the intermolecular interaction occurs in constituent molecules. The decrease in adiabatic compressibility of the soap solutions with increasing soap concentration may be interpreted on the basis of the fact that the soap molecules are surrounded by a layer of solvent molecules firmly bounded. This results in the increase in the internal pressure and in lowering the compressibility of the solution. This provides useful information about the nature of inter molecular forces existing in the mixture.

## 5 ACKNOWLEDGEMENT

The authors pay their sincere gratitude to UGC, New Delhi for Finance and Principal, S. D. Govt. College, Beawar- 305901 Rajasthan (India) and S.P.C. Govt College Ajmer for providing necessary research facilities to accomplish this study.

## 6 REFERENCES

- [1] R. Sharma, L.C.Heda and S. Sharma, 2015. Photocatalytic Degradation of Copper(II) Palmitates in Non Aqueous Media Using ZnO as Photocatalyst, *Tenside Surf Det.* **52**, 512-516; DOI: 10.3139/113.110404.
- [2] N.R. Pawar and O.P. Chimankar, 2012. Comparative study of ultrasonic absorption and relaxation behavior of polar solute and non-polar solvent, *J. Pure Appl. Ultrason.* **34**, 49-52.
- [3] V. Sivakumar, R.V. Verma, P.G. Rao and G. Swaminathan, 2007. Studies on the use of power ultrasound in solid liquid myrobalan extraction process. *J. Clean Prod.* **15**, 1813-1818; DOI.org/10.1016/j.jclepro.2006.06.006

- [4] N.R. Pawar, 2014. Ph.D thesis Summary on Investigation of Ultrasonic wave absorption in some Bio-liquids, *J. Pure Appl. Ultrason.* **36**, 69-70.
- [5] R. Sharma, L.C. Heda and A. Joram, 2013. Thermogravimetric Analysis of Copper(II) soaps Derived from Azadiractaindica (Neem) and Pongamiapinnata (Karanj) Non-Edible Oils, *Tenside Surf Det.* **50**, 36-38; DOI: 10.3139/113.110230
- [6] V. Kannappan and R. Jayasanthi, 2005. Ultrasonic studies of isomeric butylalcohol in aqueous solutions, *Indian J. Pure Appl. Phys.* **43**, 167-171.
- [7] G. Nath, 2012. Ultrasonic Study of Binary Mixture of Acetone with Bromobenzene and Chlorobenzene at Different Frequencies, *Chem. Sci. Trans.* **1**(3), 516-521; DOI:10.7598/cst2012.171.
- [8] D. Moharatha, M. Talukdar, G.S. Roy and U.N. Dash, 2011. Evaluation of acoustic parameters of halides of alkali metals and Ammonium in aqueous and aqueous Dextran solutions at 298.15K, *Researcher.* **3**, 6-12.
- [9] R. Sharma and S. Khan, 2009. Synthesis, Characterization and Antifungal Activities of Copper(II) Soaps and their Complexes Derived from AzadiractaIndica (Neem) and PongamiaPinnata (Karanj) Oil, *Tenside Surf. Det.* **46**, 145-151; DOI: 10.3139/113.110017.
- [10] R. Palani and S. Balakrishnan, 2010. Acoustical properties of ternary mixtures of 1-alkanols in di-isopropyl ether and 2, 2, 2-trifluoroethanol mixed solvent, *Indian J. Pure Appl. Phys.* **48**, 644-650.
- [11] K. Osamu, J.H. Carl and C.B. George, 1978. Ultrasonic velocities, compressibilities and heat capacities for binary mixtures of benzene, cyclohexane and tetrachloromethane at 298.15K, *J. Chem. Thermodyn.* **10**, 721-730; DOI.org/10.1016/0021-9614(78)90130-1.
- [12] G. Singh and T.S. Banipal, 2008. Partial molar adiabatic compressibilities and viscosities of some amino acids in aqueous glycerol solutions at 298.15K, *Indian J. Chem.*, **47A**, 1355.
- [13] R. Sharma, R. Bhutra and S. Khan, Micellar Behaviour of Copper Surfactants Derived from Fresh (Untreated) Sesame Oil and Used (Treated at High Temperature) Sesame Oil, *Tenside Surf Det.* **47**, 106-112; DOI: 10.3139/113.110059.
- [14] J. Das, K. Dash, S.K. Swain and N.S. Swain, 1999. Ultrasonic investigation in a polar-polar system, methyl-Isobutyl Ketone and aliphatic alcohols, *J. Mol. Liquids.* **81**, 163-179; DOI.org/10.1016/S0167-7322(99)00065-3.
- [15] S.V. Ranganayakulu, C.S. Reddy and D.L. Reddy, 2005. Ultrasonic studies of the binary mixtures of ethyl acetate and cresols-application of Kosower and Dimroth treatments, *Mat. Chem. Phys.* **90**, 213-216; DOI.org/10.1016/j.matchemphys.2004.03.032.
- [16] S.R. Kanhekar, P. Pravina and K.B. Govind, 2010. Thermodynamic properties of electrolytes in aqueous solutions of glycine at different temperatures, *Indian J. Pure Appl. Phys.* **48**, 95-99.
- [17] R. Sharma, P. Tank, M. Saxena, R. Bhutra and K.G. Ojha, 2008. Synthesis and Characterisation of Antifungal Agents Containing Copper(II) Soaps and Derived from Mustard and Soyabean Oil, *Tenside Surf Det.* **45**, 87-92. DOI: 10.3139/113.100366.
- [18] R.J. Fort and W.R. Moore, 1965. Adiabatic compressibilities of binary liquid mixtures, *Trans. Faraday Soc.* **61**, 2102-2111; DOI: 10.1039/TF9656102102.
- [19] P.K. Banipal, A.K. Chakal and T.S. Banipal, 2009. Studies on volumetric properties of some saccharides in aqueous potassium chloride solutions over temperature range (288.15-318.15 K), *J. Chem. Thermodynamic.* **41**, 452-483; DOI.org/10.1016/j.jct.2008.11.009.
- [20] N. Mathur, L.C. Heda, V. K. Mathur and P. Saxena, 2011. Study of CLSI-M44-A Disk Diffusion Method for Determining the Susceptibility of Candida Species against Novel Complexes Derived from Copper Stearate with 2-Amino Benzothiazoles, *Tenside Surf Det.* **48**, 23-27; DOI: 10.3139/113.110099.
- [21] P. Tank, A.K. Sharma and R. Sharma, 2017. Thermal Behaviour and Kinetics of Copper (II) Soaps and Complexes Derived from Mustard and Soyabean Oil, *J. Anal. Pharm. Res.* **4**(2), 1-5; DOI: 10.15406/japlr.2017.04.00102.

- [22] F.D. Gunstone, 1958. "An Introduction to the Chemistry of fats and Fatty acids" Chapman and Hall Ltd, London.
- [23] CRC Handbook of Chemistry and Physics, Ed. D.R.Lide, 76<sup>th</sup> ed., CRC Press, India 1995-1996, 32.
- [24] M. Chauhan, 1992. Ultrasonic measurements on nonaqueous solutions of samarium soaps, *J. Chem. Eng. Data.* **37**(4), 446-450; DOI: 10.1021/je00008a016.
- [25] G. Savaroglu and M. Ozdemir, 2008. Apparent molar volume and apparent molar isentropic compressibility of glycerol in fructose water at different temperature, *J. Mol. Liquids.* **137**, 51-57; DOI.org/10.1016/j.jscs.2014.01.008.
- [26] V.K. Syal, S. Chauhan and R. Gautam, 1998. Ultrasonic velocity measurements of carbohydrates in binary mixtures of DMSO + H<sub>2</sub>O at 25°C, *Ultrasonics.* **36**, 619-621; DOI.org/10.1016/S0041-624X(97)80888-8.
- [27] A. Ali, S. Hyder and A.K. Nain, 1999. Intermolecular and ion solvent interaction of sodium iodide and potassium iodide in dimethyl formamide + I-propanol mixtures at 303K, *J. Pure Appl. Ultrason.*, **21**, 127-131.
- [28] S. Punitha and R. Uvarani, 2014. Physico-chemical studies on some saccharides in aqueous cellulose solutions at different temperatures- Acoustical and FTIR analysis. *J. Saudi Chem. Soc.*, **18**, 657-665; DOI.org/10.1016/j.jscs.2014.01.008.
- [29] C. Bachem, 1936. *Z. Phys.*, **101**, 541.
- [30] D.O. Masson's, 1929. *Phil. Mag.*, **8**, 218.
- [31] V.M. Kagathara, M.R. Sanariya and P.H. Parsania, 2000. Sound velocity and molecular interaction studies on chloroepoxy resins solutions at 30°C, *Eur. Polym. J.*, **36**, 2371-2374; DOI.org/10.1016/S0014-3057(00)00006-9.
- [32] N. Mathur, K.G. Ojha, A. Imran and P. Saxena, 2009. Viscometric Behaviour and Micellization of Complexes of Copper (II) Stearate with N-donor Heterocyclic Dyes, *Tenside Surf. Det.* **46**, 24-30; DOI: 10.3139/113.110004.
- [33] A.K. Dash and R. Paikaray, 2013. Acoustical study on ternary mixture of dimethyl acetamide (DMAC) in diethyl ether and isobutyl methyl ketone at different frequencies, *Phys. Chem. Liq.*, **51**(6), 749-763; DOI.org/10.1080/00319104.2013.795860.
- [34] S. Singh and I. Bahadur, 2014. Density and speed of sound of 1-ethyl-3-methylimidazolium ethylsulphate with acetic or propionic acid at different temperatures, *J. Mol. Liq.*, **199**, 518-523; DOI.org/10.1016/j.molliq.2014.09.055.
- [35] B.V. Jahagirdar, B.R. Arbad., A.A. Walvekar., A.G. Shankarwer and M. Lande, 2000. Studies in partial molar volumes, partial molar compressibilities and viscosity B-coefficients of caffeine in water at four temperatures, *J. mol. liq.*, **85**, 361-373; DOI.org/10.1016/S0167-7322(00)89019-4.

# Influence of air pollutants to mixing height in different seasons by multiple regressions model in urban region Delhi, India

Kirti Soni\*, Mahavir Singh and Y.K. Yadav  
CSIR- National Physical Laboratory, New Delhi-110012, INDIA  
e-mail: 2006.kirti@gmail.com, mahavir.acoustics@gmail.com

[Received: 20-02-2017; Revised: 26-05-2017; Accepted: 29-05-2017]

## ABSTRACT

In this study, the relationship between mixing height(MH)and air pollutants such as SO<sub>2</sub>, NO<sub>2</sub>, and PM<sub>10</sub> was statistically analysed and modelled for the urban region of India during the eight years period from 2006-2014. Statistical analyses have shown a negative and significant correlation between MH and SO<sub>2</sub>, PM<sub>10</sub> while the positive correlation was observed between MH and NO<sub>2</sub>. Finally, regression equations for MH and air pollutants were developed. An inverse relationship has been observed between MH and SO<sub>2</sub> data during all seasons, and positive relationship found between MH and NO<sub>2</sub> during winter, post-monsoon and pre-monsoon season. The almost neutral relation has been found between PM<sub>10</sub> and MH. SO<sub>2</sub> is a major pollutant from industrial emissions whereas NO<sub>x</sub> are the major pollutants emitted by vehicular or mobile sources. As a result, the industrial emissions are predominantly responsible for the decrease in mixing height.

## 1. INTRODUCTION

The atmospheric mixing layer height is the lower part of the atmosphere contiguous to the ground, where constituents released or entrained into it are mixed vertically by convection or mechanical turbulence within a short time scale [1]. The concentration of atmospheric pollutants within the atmospheric boundary layer (ABL) is affected by atmospheric flows and by dispersion [2]. The mixing layer height (MLH) is a very important parameter in atmospheric sciences, as it controls the air volume where the most effective dispersion process takes place [1]. The mixing height is one of the fundamental parameter to characterise its structure and is required in dispersion models. The most important environmental problem India currently faces is air pollution, particularly in the capital city Delhi. The problem is very severe for the city which considered one of the highest polluted cities in the world. The major air pollutant, which could cause potential harm to human health has been included are SO<sub>2</sub>, NO<sub>2</sub>, and particulate matter, etc. Particulate matter is considered one of the main sources of air pollution problems in Delhi. Nitrogen dioxide (NO<sub>2</sub>), in particular, is a critical component in the process that leads to the formation of photochemical smog and tropospheric ozone (O<sub>3</sub>), and thus greatly influences the troposphere's oxidising capacity. The entire northern part of India, especially the Indo-Gangetic Plain, experiences a thick foggy weather during winter with low boundary layer height. The low winds and reduced boundary layer heights result in very low ventilation factors which determine the dispersion of pollutants. During such conditions, pollutants could not be dispersed or mixed with free troposphere [3]. The effect of such conditions is poor visibility and high levels of pollutants in this region.

Numerous short-term and long-term studies have been performed focusing on ambient air quality in India [4-10] and in other countries [11-13]. Besides ambient air quality, a few studies have been performed on the characteristics of boundary layer height i.e. mixing height. Assimakopoulos & Helmis [14] studied Sodar mixing height and air pollution characteristics over a Mediterranean city. Ashrafi *et al.* [15] reported a temporal and seasonal variation of ventilation coefficient. Kumar *et al.* [16] studied the daytime boundary layer behaviour over eastern region and western regions of India. More recently Roy *et al.* [2] studied the Meteorological Parameters and Mixing Height in Gold Mining Area. All the study mentioned above are mainly focus on the temporal and seasonal variation of Sodar mixing height and a limited work has been done on the air pollutant and boundary layer height is i.e. mixing height relationship. Due to the significant importance of mixing height in air pollutant dispersion and for the first time we present long-term regression analysis and the correlation between air pollutants and mixing height at Capital region in India. Pollutants such as particulate matter, nitrogen oxides, sulfur oxides etc. are harmful to human health. Study of pollutant variation and its relationship with mixing height is of importance not only for environmental protection but also for the public at large. The aim of this study was to statistically analysed and modelled the relationship between mixing height (MH) and air pollutants such as SO<sub>2</sub>, NO<sub>2</sub>, and PM<sub>10</sub> for the capital region of India during the eight years period from 2006-2014.

## 2. DESCRIPTION OF STUDY AREA

Delhi (Latitude 28.38N, Longitude 77.10E, 235 masl) is one of the highest polluted cities of India, in the south Asian region. Delhi is situated about 1100 Km from the nearest coast on the North Arabian Sea. The area around Delhi falls in the border zone lying between the rich rain-washed Ganges plains to the east and the semi-arid tracts of Rajasthan about 160 Km to the west and south-west. The soil around Delhi is dusty [17]. It has a semi-arid climate with extreme weather conditions. During peak summers, temperature rises even beyond 45°C and in winter temperatures may fall to below 3°C. The rainy season is from July to September when the climate sometimes becomes very humid.

## 3. DATA AND METHODOLOGY

Daily average SODAR (Sonic Detection And Ranging) data for about eight years (2006-2014) for the Capital of India, Delhi is analysed to derive the mixing layer height (MH). Data of the mixing layer height over Delhi were collected from the SODAR facility installed at CPCB (Central Pollution Control Board) Delhi. The ambient air quality, long-term data used in the present study covered the period 2006 - 2014 and was obtained from the Central Pollution Control Board (CPCB). The total data set has been classified into four seasons namely winter (December-January-February); Pre-monsoon (March-April-May); Monsoon (June-July-August-September) and Post-monsoon (October-November) on the basis meteorology patterns over northern India [18].

## 4. STATISTICAL ANALYSIS

Statistical analysis is used to calculate the mean, median, mode, standard deviation, kurtosis, and skewness. Mean explains the average value. Median gives the middle values of an ordered sequence or positional average. The mode is defined as the value which occurs the maximum number of times that has the maximum frequency. Standard deviation gives the measure of "spread" or "variability" of the sample the degree of flatness or peakedness in the region about the mode of a frequency curve. Skewness describes the symmetry of data [19]. Kurtosis refers to the degree of flatness or peakedness in the region about the mode of a frequency curve. The coefficient of variation gives the relative measure of the sample [19].

## 5. REGRESSION ANALYSIS

It is a technique used for modelling and analysing the variables present in a sample. Regression analysis helps in understanding the variation in the value of the dependent variable as independent variables are varied, while the other independent variables are held fixed. Regression line of Y (dependent variable) on X (independent variable) is defined as



$$Y = b_{yx}X + C \quad (1)$$

[19] where C is a constant of integration,

$$b_{yx} = r \times \frac{\sigma_y}{\sigma_x} \quad (2)$$

$r$  = Correlation Coefficient

The correlation coefficient ( $r$ ), is a measure of the strength of the linear relationship between two variables and values ranging between -1 and +1. The correlation coefficient used by [20-23] is defined as:

$$r = \frac{E(XY) - E(X)E(Y)}{\sqrt{(E(X^2) - [E(X)]^2)}\sqrt{(E(Y^2) - [E(Y)]^2)}} \quad (3)$$

$$= \frac{\text{cov}(X, Y)}{\sigma_x \sigma_y} \quad (4)$$

$\sigma_x, \sigma_y$  are the standard deviation of variables Y and X, respectively, and  $E(X), E(Y), E(XY)$  are the expected value of variables X, Y and XY, respectively.

## 6. HURST EXPONENT ( $H$ )

The Hurst Exponent ( $H$ ) is commonly used as a measure of long-term memory of time series. It relates to the autocorrelations of the time series and the rate at which they decrease as the lag between the pairs of values increases. In general,  $H$  measures the relative tendency of the time series either to regress strongly to the mean or to cluster in a direction.  $H$  ranges between 0 and 1 and a value of 0.5 indicates a true random walk (a Brownian time series), suggesting that there is no correlation between any element and a future element. As, the value of  $0.5 < H < 1$  indicates "persistent behaviour" or a positive autocorrelation, while a value in the range of  $0 < H < 0.5$  points out "anti-persistent behaviour" or a negative autocorrelation [22].  $H$  is defined as follows:

$$H = \left| \frac{a-1}{2} \right| \quad (5)$$

whereas  $a$  is the slope value from the linear regression analysis.

## 7. FRACTAL DIMENSION ( $F$ )

The Fractal Dimension ( $F$ ) analysis gives an indication of how completely a fractal appears to fill space, as one zooms down to finer and finer scales. The  $F$  is related to  $H$  via the formula:

$$F = 2 - H \quad (6)$$

$F$  analysis is well suited to analyse the variability of a given time series. If  $F$  is 1.5, there is no correlation among amplitude changes consistent of two successive time intervals. Thus, no trend in amplitude can be distinguished from the time series and, therefore, the process is unpredictable. However, as  $F$  decreases to 1, the process becomes more and more predictable, and it shows "persistence", while for values between 1.5 and two the process exhibits "anti-persistence". Specifically, a decrease in the amplitude of the process is more likely to lead to an increase in the future; hence, the predictability again increases [22-23].

## 8. PREDICTABILITY INDEX ( $PI$ )

The Predictability Index ( $PI$ ) describes the behaviour (predictable or unpredictable) of time series. And is defined as follows [20]:

$$PI = 2|F - 1.5| \quad (7)$$

If  $PI$  is close to zero, then the corresponding process approximates the usual Brownian motion. If  $PI$  is nearly one, the process is very predictable.

## 9. RESULTS AND DISCUSSION

### Temporal Variation of MH, SO<sub>2</sub>, NO<sub>2</sub> and PM<sub>10</sub>

The daily average Variation of MH, SO<sub>2</sub>, NO<sub>2</sub> and PM<sub>10</sub> over Delhi are presented in Fig. 1.

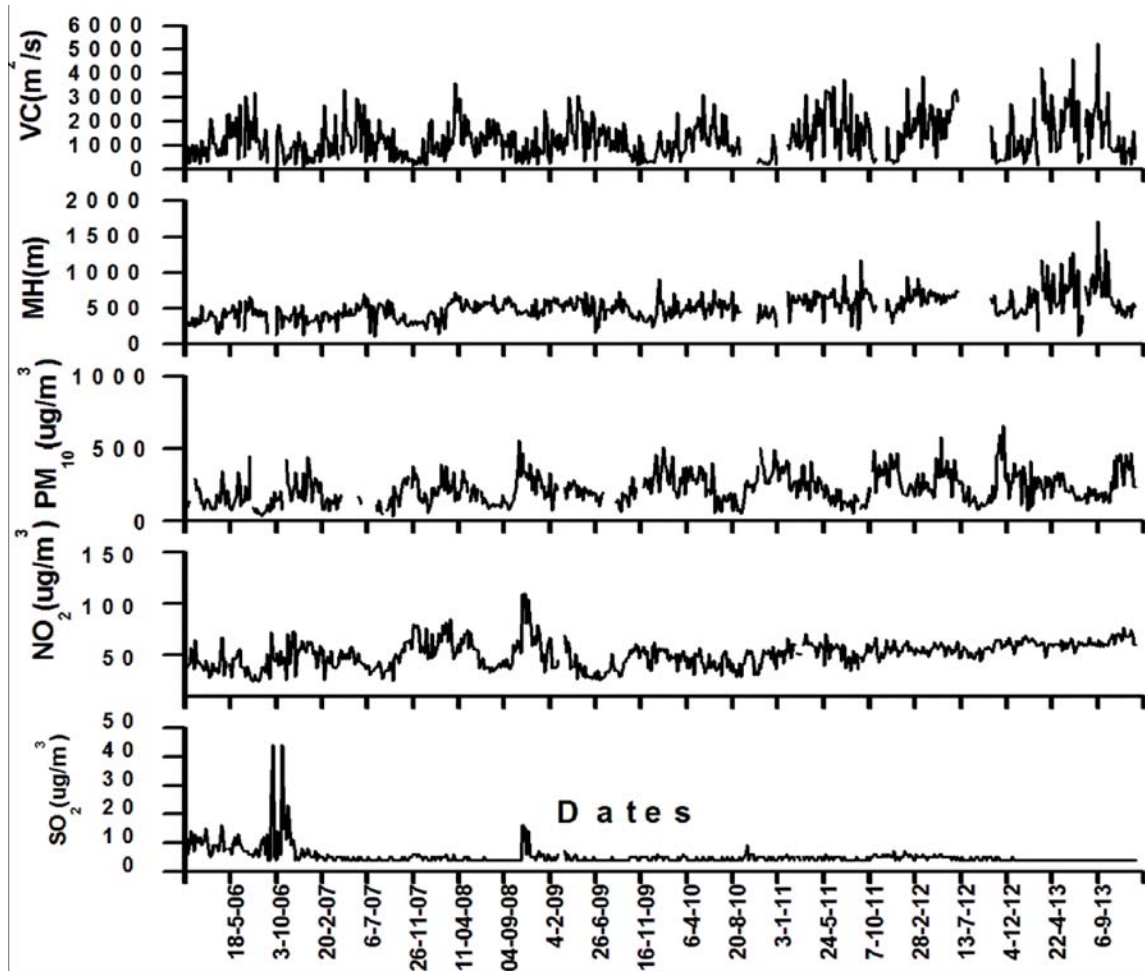


Fig. 1 Daily variation mixing height (MH) and air pollutants (SO<sub>2</sub>, NO<sub>2</sub> and PM<sub>10</sub>) over Delhi during the period from Jan 2006 - Feb 2014.

The average concentrations of air pollutants SO<sub>2</sub>, NO<sub>2</sub> and PM<sub>10</sub> during the study period were  $5 \pm 2.3 \mu \text{gm}^{-3}$ ,  $52 \pm 13 \mu \text{gm}^{-3}$  and  $221 \pm 104 \mu \text{gm}^{-3}$  respectively. The minimum and maximum concentration of SO<sub>2</sub> was  $4 \mu \text{gm}^{-3}$  and  $23 \mu \text{gm}^{-3}$  and for NO<sub>2</sub> was  $24 \mu \text{gm}^{-3}$  and  $110 \mu \text{gm}^{-3}$  and for PM<sub>10</sub>  $35.6 \mu \text{gm}^{-3}$  and  $651.3 \mu \text{gm}^{-3}$  respectively. From this study, it has been observed in the mean concentration of SO<sub>2</sub> decreased whereas NO<sub>2</sub> increased but under the National Ambient Air Quality Standards (NAAQS) prescribed limits. On the other hand, particulate matters (PM<sub>10</sub>) exceed the values  $100 \mu \text{g}/\text{m}^3$  of NAAQS over Delhi. Nowadays increasing PM concentration over Delhi areas is the subject of concern. With the rapid urbanisation and corresponding increase in the traffic and energy consumption, there has been growing evidence that ambient concentration levels of PM<sub>10</sub> high in Delhi [24]. The major source of PM<sub>10</sub>, are referred as windblown dust, secondary aerosol, coal combustion, traffic exhausts and biomass burning, *etc.* [3]. The mixing heights are in the range of 115-1717 m with a mean depth of about  $520 \pm 186$  m over the period about eight years (2006-2014).

10. CORRELATION BETWEEN AIR POLLUTANTS AND MIXING HEIGHT

The Correlation coefficient between different pairs of MH and air pollutants is represented in Table 1.

Table -1 Correlations

	Mixing Height (MH)	Ventilation Coefficient (VC)
SO <sub>2</sub> Pearson Correlation	-0.248**	-0.156**
Sig. (2-tailed)	0.000	0.000
N	565	565
NO <sub>2</sub> Pearson Correlation	0.106*	-0.066
Sig. (2-tailed)	0.011	0.117
N	565	565
PM <sub>10</sub> Pearson Correlation	-0.084	-0.219**
Sig. (2-tailed)	0.055	0.000
N	524	524

\*\* . Correlation is significant at the 0.01 level (2-tailed).

\* . Correlation is significant at the 0.05 level (2-tailed).

It has been observed that MH is negatively correlated with SO<sub>2</sub> and PM<sub>10</sub> whereas MH is positively correlated with NO<sub>2</sub>. Positive correlation represents persistent behaviour with the variables. The positive value of the correlation coefficient indicates that as one value increases other tend to increase and the negative value of the correlation coefficient indicates that as one value increases other tend to decrease.

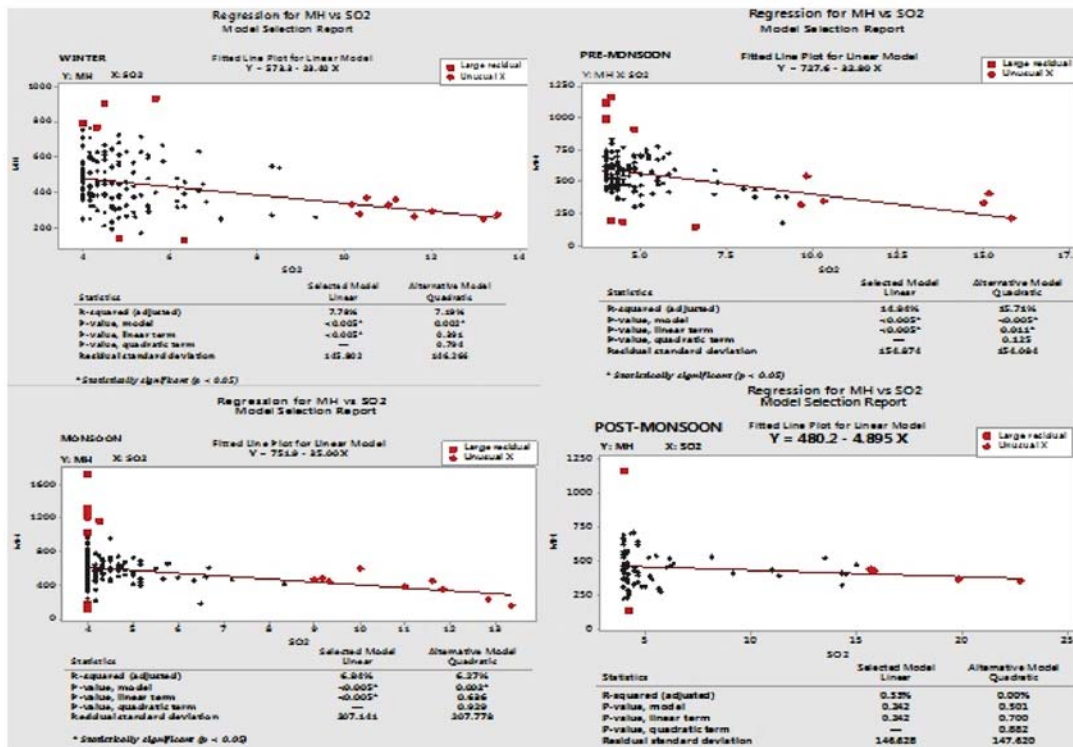


Fig. 2(a) to (d) Regression for mixing height (MH) and air pollutant SO<sub>2</sub>, over Delhi in India.

Fig. 2 shows the scatter plots of mixing height (MH) against that of air pollutants (SO<sub>2</sub>, NO<sub>2</sub>, and PM<sub>10</sub>) concentration during different seasons.

The Figs. 2(a, d, j & g) indicates that SO<sub>2</sub> and MH are negatively related to one another with a linear relationship during all seasons, *i.e.*, winter, pre-monsoon, monsoon and post-monsoon. The R- squared value (for both quadratic and linear model), p-value, *etc.* have been given in the table below the scatter plot for each season. For winter, pre-monsoon and monsoon season clearly negative and statistically significant relations have been observed while during post-monsoon statistically significant neutral to negative trend have been found. The linear regression model for the daily data gave the following equation for all four seasons between SO<sub>2</sub> and MH:

$$MH = 573.3 - 23.40 (SO_2) \quad (\text{Winter}) \quad (8)$$

$$MH = 727.6 - 32.80 (SO_2) \quad (\text{Pre-monsoon}) \quad (9)$$

$$MH = 751.9 - 35.00 (SO_2) \quad (\text{Monsoon}) \quad (10)$$

$$MH = 480.2 - 4.895 (SO_2) \quad (\text{Post-monsoon}) \quad (11)$$

The above equations reveal that the SO<sub>2</sub> concentration decreases with increasing mixing height concentration. Equation (8) shows that the line intersects MH axis at 573.3 with a slope of -23.40 (SO<sub>2</sub>) that is on the SO<sub>2</sub> = 0, MH is 573.3 m and for each increase in a SO<sub>2</sub> concentration, the MH decreases on the average by 23.40 m during winter. Similarly, during pre-monsoon, monsoon and post-monsoon for each season increase in SO<sub>2</sub>, the MH decreases on the average by 32.80 m, 35.00 m and 4.895 m respectively.

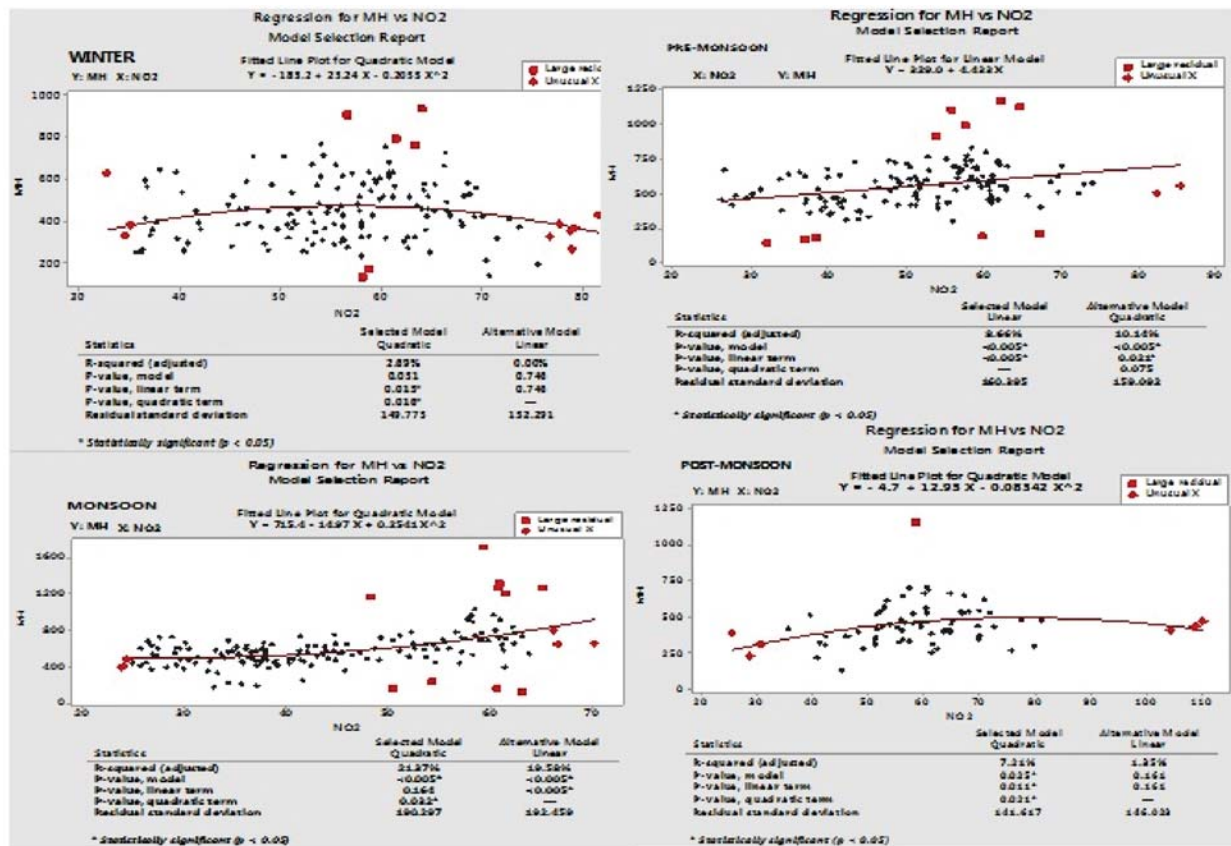


Fig. 2(e) to (h) Regression for mixing height (MH) and air pollutant NO<sub>2</sub>, over Delhi in India.

The Fig. 2 (b, e, h & k) represents the linear or quadratic relations between NO<sub>2</sub> and MH in all seasons. During winter, monsoon and post-monsoon season, significant non-linear quadratic relations have been found between NO<sub>2</sub> and MH. However, in pre-monsoon and monsoon season statistically significant positive linear relation has been observed between NO<sub>2</sub> and MH. The equations for the linear or quadratic model are expressed as:

$$MH = -183.2 + 23.24 (NO_2) - 0.2055 (NO_2)^2 \quad (\text{Winter}) \quad (12)$$

$$MH = 329.0 + 4.433 (NO_2) \quad (\text{Pre-monsoon}) \quad (13)$$

$$MH = 715.4 - 14.97 (NO_2) + 0.2541 (NO_2)^2 \quad (\text{Monsoon}) \quad (14)$$

$$MH = -4.7 + 12.93 (NO_2) - 0.08342 (NO_2)^2 \quad (\text{Post-Monsoon}) \quad (15)$$

In equation (12) during winter and post-monsoon seasons, the coefficient on NO<sub>2</sub> is positive, and the coefficient on NO<sub>2</sub><sup>2</sup> is negative, that suggests that NO<sub>2</sub> has a positive effect on MH until a turning point is reached. Beyond that value, NO<sub>2</sub> has a negative impact on MH. However, during monsoon season opposite behaviour has been observed that the coefficient on NO<sub>2</sub> is negative and the coefficient on NO<sub>2</sub><sup>2</sup> are positive means NO<sub>2</sub> has a negative effect on MH till a turning point is reached. Afterward NO<sub>2</sub> has a positive impact on MH.

Soni *et al.*, [25] also reported that during winters the mixing height level and wind speed is low at the same time the wood, waste and coal burning increases [26]. Also the concentration of SO<sub>4</sub> and NH<sub>4</sub> increases in winters due to the transport of pollutants from thermal power plants as a result of prevailing north westerlies. Secondary aerosols like SO<sub>4</sub><sup>2-</sup> and NO<sub>3</sub><sup>-</sup> released by the anthropogenic sources (SO<sub>2</sub> and NO<sub>2</sub>) during daytime and NO<sub>2</sub> react with O<sub>3</sub> to form the nitrate radical (NO<sub>3</sub>), which is a strong oxidant and plays an important role in NOx polluted areas at night [27]. The residence time of NOx in the lower troposphere is short. In the absence of sunlight, NO<sub>2</sub> has a longer lifetime in the atmosphere, which explains that the NO<sub>2</sub> columns are on average higher during wintertime.

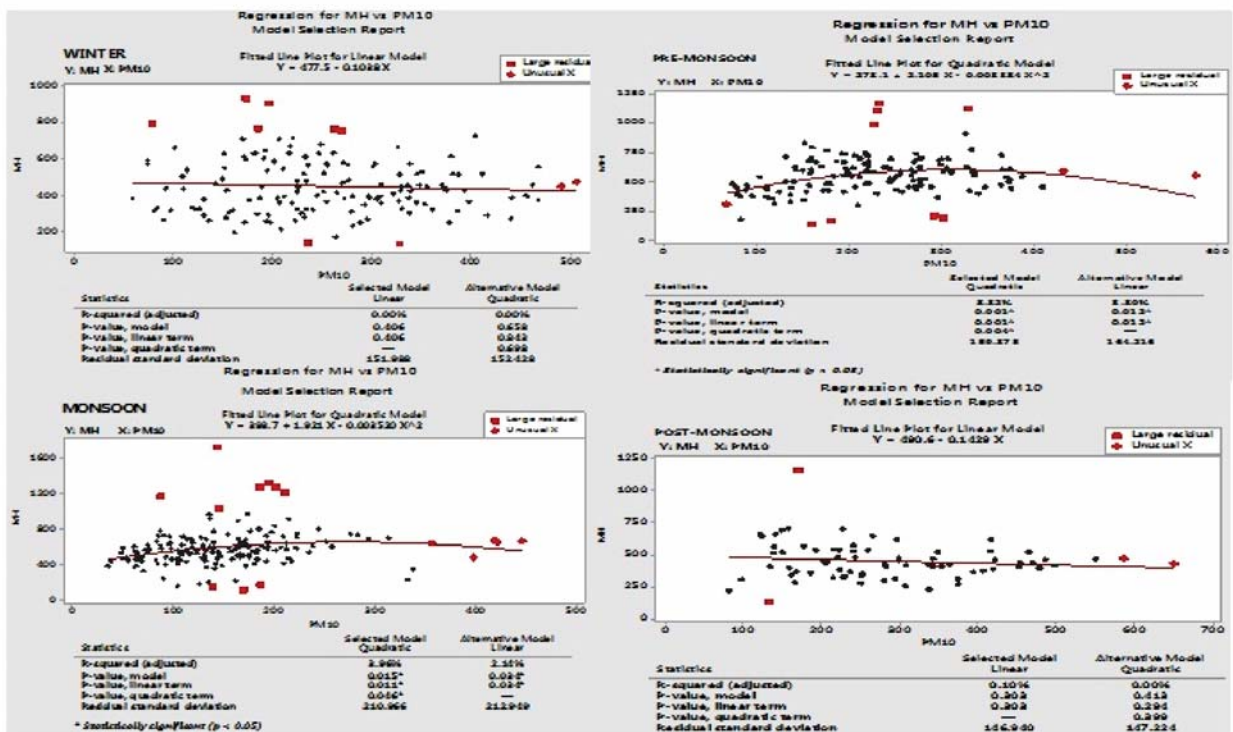


Fig. 2 (i) to (l) Regression for mixing height (MH) and air pollutants PM<sub>10</sub> over Delhi in India.

The Figs. 2(c, f, i & l) denotes the linear or quadratic relations between PM<sub>10</sub> and MH in different seasons. It is clear from figures that during winter statistically significant almost constant and in post-monsoon neutral to negative linear relation have been observed while in monsoon and pre-monsoon season statistically significant quadratic relation has been found. Ding, [28] also reported that the concentration of PM10 is decreased with higher boundary layer height. All the equations for a linear or quadratic model between PM<sub>10</sub> and MH are given below.

$$MH = 477.5 - 0.1038 (PM_{10}) \quad \text{(Winter)} \quad (16)$$

$$MH = 278.1 + 2.105 (PM_{10}) - 0.00338 (PM_{10})^2 \quad \text{(Pre-monsoon)} \quad (17)$$

$$MH = 393.7 + 1.921 (PM_{10}) - 0.0035 (PM_{10})^2 \quad \text{(Monsoon)} \quad (18)$$

$$MH = 490.6 - 0.1429 (PM_{10}) \quad \text{(Post-Monsoon)} \quad (19)$$

Equation (20) represents the final regression model equation among the all air pollutants (SO<sub>2</sub>, NO<sub>2</sub>, PM<sub>10</sub>) and equation (21) shows the final model for all air pollutants and mixing height from the whole period daily average data.

$$PM_{10} = 52.5 - 2.74 (SO_2) + 3.519 (NO_2) \quad (20)$$

It is clear from Equation (20) that concentration of PM<sub>10</sub> is predicted to increase 3.519µg/m<sup>3</sup> when the NO<sub>2</sub> concentration goes up by one, decrease by 2.74µg/m<sup>3</sup> when SO<sub>2</sub> concentration goes up by one and is predicted to be 52.5µg/m<sup>3</sup> when both NO<sub>2</sub> and SO<sub>2</sub> are zero. The concentration of the PM<sub>10</sub> is increased due to the increase of secondary inorganic aerosols [26].

$$MH = 515.7 - 48.6(SO_2) + 0.175(PM_{10}) + 5.95(NO_2) + 0.766(SO_2)^2 + 0.054(SO_2) * (PM_{10}) - 0.0146 + (PM_{10})*(NO_2) \quad (21)$$

$$MH = 676.1 - 33.54 (SO_2) + 0.5674 (SO_2)^2 \quad (22)$$

$$MH = 220.7 + 10.32 (NO_2) - 0.08215 (NO_2)^2 \quad (23)$$

$$MH = 484.2 + 0.4870 (PM_{10}) - 0.001201 (PM_{10})^2 \quad (24)$$

It is clear from equations (20) that incremental impact of NO<sub>2</sub> is higher than SO<sub>2</sub> in PM<sub>10</sub>. Similarly, final model equation (21) represents the higher incremental impact of SO<sub>2</sub> than NO<sub>2</sub> and PM<sub>10</sub> on MH. SO<sub>2</sub> is a major pollutant from industrial emissions whereas NOx are the major pollutants emitted by vehicular or mobile sources.

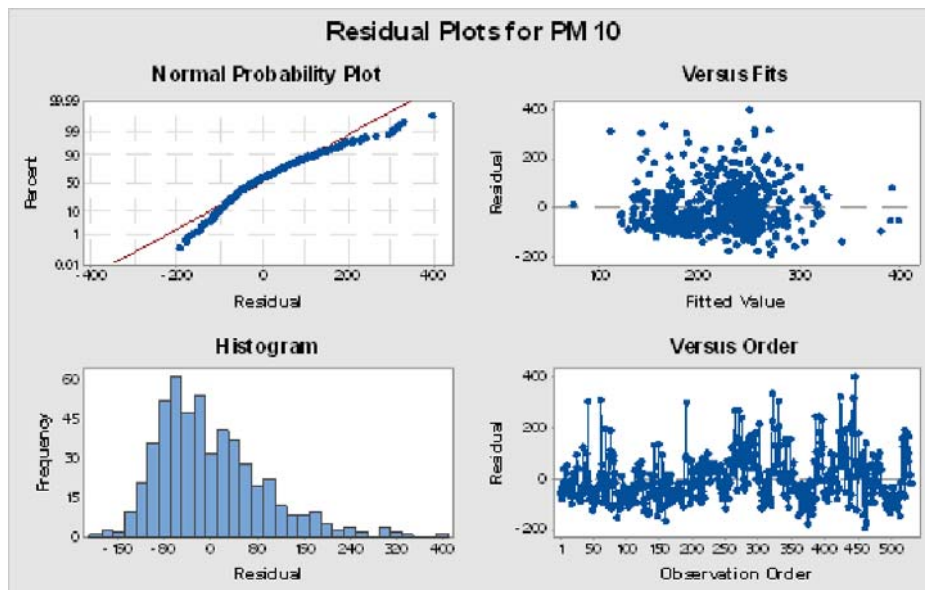


Fig. 3(a)

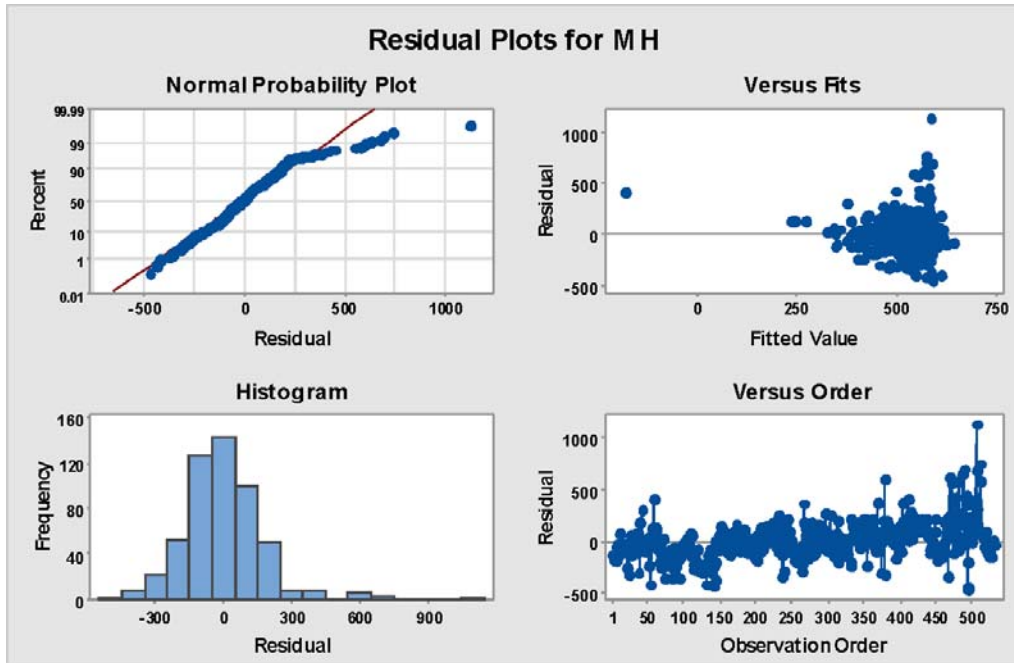


Fig. 3(b)

Fig. 3 (a) and (b) Residual plot for PM<sub>10</sub> and Mixing Height.

Fig. 3(a) and 3(b) represents the residual plots for MH and PM<sub>10</sub>. The graph on the top left checks the assumption of normality of error terms. In this case, it is observed that the most of the points are clustered around red line indication that the error terms are approximately normal. Thus our assumption of normality is valid. The graph on the top right plot the error terms against the fitted values. There are approximately half of them are above, and half are below the zero line indicating that our assumption of error terms having mean zero is valid. The bottom left graph again re-emphasizes the normality assumption. Though, our sample size is 533. The bottom right graph is also important in this case because data is a time series and order of the data is important. A clear cyclic pattern indicates that error terms are dependent on the time variable. The equation (21) to (24) shows the final regression model for the total and each air pollutants separately.

### 11. STATISTICAL ANALYSIS

Table 2, depicts the statistical analysis of mixing height and air pollutants. Statistical analysis of each parameters MH, SO<sub>2</sub>, NO<sub>2</sub> and PM<sub>10</sub> have been discussed here.

**Table 2.** Descriptive Statistics

Parameters	Mean	Median	Mode	Std. Dev.	Skewness	Kurtosis	Slope	R <sup>2</sup>	H	D	PI
MH(m)	515.44	501.92	250a	183.0	1.302	5.177	0.51	0.5	0.75	1.25	0.5
SO <sub>2</sub> (µg/m <sup>3</sup> )	5.28	4.00	4	3.25	7.064	69.976	-0.006	-0.36	1.0	1.0	1
NO <sub>2</sub> (µg/m <sup>3</sup> )	51.26	53.00	61	12.88	0.420	1.425	0.025	0.35	0.99	1.01	0.98
PM <sub>10</sub> (µg/m <sup>3</sup> )	220.75	206.00	273	105.1	0.724	0.335	0.17	0.29	0.91	1.09	0.82

a -Multiple modes exist. The smallest value is shown.

H - Hurst Exponent, D - Fractal Dimension, PI - Predictability Index

Mean, median and mode values are different; thus, the MH, SO<sub>2</sub>, NO<sub>2</sub> and PM<sub>10</sub> curve does not follow normal behaviour. Standard deviation value is high for all four parameters thus the data values are not close to each other. Skewness value is approximate 0 for NO<sub>2</sub> and PM<sub>10</sub> thus, the curve is symmetrical and platykurtic however the skewness value is 1.302, and 7.064 respectively for MH, SO<sub>2</sub>, thus the curve is not symmetrical and platykurtic.

Furthermore, the statistical parameters H, D, and PI are also summarised in Table 1. It is shown that all the values of H are nearly ranged 0.5<H<1 indicates "persistent behaviour" or a positive autocorrelation, for all parameters, which indicates a true random walk (Brownian time series). Similarly, the value of D is equal or more than 1.0 Thus, the process becomes more and more predictable, and it shows "persistence" and the value of PI is also nearly one for SO<sub>2</sub>, NO<sub>2</sub>, and PM<sub>10</sub>, meaning that the process is very predictable. The graphical representation of statistical parameters of MH, SO<sub>2</sub>, NO<sub>2</sub> and PM<sub>10</sub> are represented in Fig. 4.

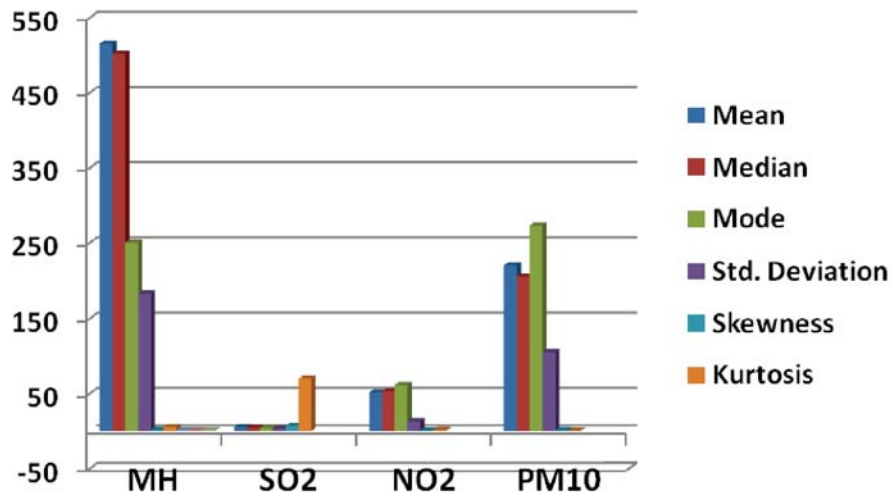


Fig. 4 Graphical representation of statistical analysis of mixing height (MH) and air pollutants (SO<sub>2</sub>, NO<sub>2</sub> and PM<sub>10</sub>) over Delhi in India.

## 12. CONCLUSION

The mechanisms involved in mixing height and air pollutants are complex and time dependent. Various factors affect the air quality level, including physical characteristics of the site, environment, meteorological parameters, diurnal and seasonal effects, ventilation system, etc. The relationships between MH and air pollutants (SO<sub>2</sub>, NO<sub>2</sub>, and PM<sub>10</sub>) are highly nonlinear and some factors are highly correlated with others.

The multiple regression equations among the air mentioned above pollutants and MH have been established separately for each air pollutants and combined for all air pollutants to predict the value of MH regarding the air pollutants. Additional, we have found out the correlation between air pollutants and MH and used these results to decrease the number of dependent variables from two to one and predict any one of the parameters regarding only one (dependent) parameter. It was found that an inverse relationship exists between MH and SO<sub>2</sub> data during all seasons, and positive relationship found between MH and NO<sub>2</sub> during winter, post-monsoon and pre-monsoon season. The almost neutral relation has been found between PM<sub>10</sub> and MH. SO<sub>2</sub> is a major pollutant from industrial emissions whereas NO<sub>x</sub> is the major pollutants emitted by vehicular or mobile sources. Therefore, the industrial emissions are predominantly responsible for the decrease in mixing height. It can be concluded that an important part of the variance of the observed SO<sub>2</sub>, NO<sub>2</sub> and PM<sub>10</sub> concentrations is caused by the MH *i.e.* that the influence of MH upon these air pollutant concentrations is significant.



**13. REFERENCES**

- [1] P. Seibert, F. Beyrich, S.-E. Gryning, S. Joffre, A. Rasmussen and P. Tercier, 2000. Review and intercomparison of operational methods for the determination of the mixing height, *Atmos. Environ.*, **34**(7), 1001-1027, DOI: 10.1016/S1352-2310(99)00349-0.
- [2] S. Roy, P. Gupta and T.N. Singh, 2012. Studies on Meteorological Parameters and Mixing Height in Gold Mining Area. *Resources and Environment*. **2**(5), 228-239; DOI: 10.5923/j.re.20120205.06.
- [3] S. Tiwari, A.K. Srivastava, D.S. Bisht, T. Bano, S. Singh, S. Behura, M.K. Srivastava, D.M. Chate and B. Padmanabhamurty, 2009. Black Carbon and Chemical Characteristics of PM10 and PM2.5 at an Urban Site of North India. *J. Atmos. Chem.* **62**, 193-209.
- [4] F. Halek, M. Keyanpour, A. Pirmoradi and A. Kavousi, 2010. Estimation of Urban Suspended Particulate Air Pollution Concentration. *Int. J. Environ. Res.*, **4**(1), 161-168, ISSN: 1735-6865, 161.
- [5] A.K. Gupta, R.S. Patil and S.K. Gupta, 2004. A statistical analysis of particulate data sets for Jawaharlal Nehru port and surrounding harbour region in India. *Environmental monitoring and assessment*, **95**, 295-309.
- [6] P. Goyal and Sidhartha, 2003. Present scenario of air quality in Delhi: a case study of CNG implementation. *Atmos. Environ.* **37**, 5423-5431.
- [7] V. Kathuria, 2004. The impact of CNG on vehicular pollution in Delhi: a note. *Transportation Research Part D-Transport and Environ.* **9**(5), 409-417.
- [8] R. Khaiwal, Wauters Eric., K. Tyagi Sushil, M. Suman and R. van Grieken, 2006. Assessment of air quality after the implementation of Compressed Natural Gas (CNG) as fuel in public transport in Delhi, India. *Environmental Monitoring and Assessment* **115**, 405-417.
- [9] K. Ravindra, E. Wauters, S.K. Tyagi, S. Mor and R. Van Grieken, 2006. Assessment of air quality after the implementation of compressed natural gas (CNG) as fuel in public transport in Delhi, India. *Environ. mont. And assess.*, **115**(1-3), 405-41.
- [10] V.P. Aneja, A. Agarwal, P.A. Roelle, S.B. Phillips, Q. Tong and N. Watkins, *et al.*, 2001. Measurements and analysis of criteria pollutants in New Delhi, India. *Environ. Modell. And Software* **27**(1), 35-42.
- [11] K. Schäfer, S. Emeis, H. Hoffmann and C. Jahn, 2006. Influence of mixing layer height upon air pollution in urban and sub-urban areas", *Meteorol. Z.*, **15**, 647-658.
- [12] S. Emeis, C. Münkel, S. Vogt, W. Müller and K. Schäfer, 2004. Determination of mixing-layer height. *Atmospheric Environment*, **38**, 273-286.
- [13] S. Emeis and K. Schäfer, 2006. Remote sensing methods to investigate boundary-layer structures relevant to air pollution in cities. *Bound-Lay.Meteorol.*, **121**, 377-385.
- [14] V.D. Assimakopoulos and C.G. Helmis, 2003. Sodar mixing height estimates and air pollution characteristics over a Mediterranean big city. *Environmental Technology*, **24**(10), 1191-1199.
- [15] K.H. Ashrafi, M. Shafie-Pour and H. Kamala, 2009. Estimating Temporal and Seasonal Variation of Ventilation Coefficients. *Int. J. Environ. Res.*, **3**(4), 637-644, ISSN: 1735-6865 637.
- [16] M. Kumar, A. Kumar, C. Mallik, N.C. Mahanti and A.M. Shekh, 2011. Daytime boundary layer behaviour over the eastern region (per-humid climate) and western regions (semi-arid climate) of India: a case study *Meteorol Atmos Phys*, **111**, 55-64; DOI 10.1007/s00703-010-0116-6.
- [17] L.T. Khemani, M.S. Naik, G.A. Momin, R. Kumar, R.N. Chatterjee, G. Singh and B.V.R. Murty, 1985. Trace elements in the atmospheric aerosols at Delhi, north India. *Journal of Atmospheric Chemistry*. **2**, 273-285.
- [18] S. Ramachandran and S. Kedia, 2012. Radiative effects of aerosols over Indo-Gangetic plain: environmental (urban vs. rural) and seasonal variations. *Environ. Sci. Pollut. Res.* **19**, 2159e2171.
- [19] I. Chenini and S. Khemiri, 2009. Evaluation of ground water quality using multiple linear regression and structural equation modelling. *Int. J. Environ. Sci. Technol.*, **6**(3), 509-519.

- [20] G. Rangarajan, 1997. A climate predictability index and its applications. *Geophys Res Lett*, **24**(10), 1239-1242.
- [21] G. Rangarajan and M. Ding, 2000. Integrated approach to the assessment of long range correlation in time series data. *Phys. Rev. E.*, **61**(5), 4991-5001.
- [22] G. Rangarajan and D.A. Sant, 2004. Fractal dimensional analysis of Indian climatic dynamics. *Chaos, Solitons Fractals* **19**, 285-291.
- [23] K.S. Parmar and R. Bhardwaj, 2013. Water quality index and fractal dimension analysis of water parameters. *Int. J. Environ. Sci. Tech.*, **10**(1), 151-164.
- [24] P.K. Gupta, K. Singh, C.K. Dixit, N. Singh, C. Sharma, S. Sahai, A.K. Jha, D.P. Singh, M.K. Tiwari and S.C. Garg, 2007. Spatial Distribution in Aerosol Mass and Size Characteristics between Delhi and Hyderabad during Land Campaign in February 2004. *Indian J. Radio Space Phys.* **36**, 576-581.
- [25] K. Soni, S. Singh, T. Bano, R.S. Tanwar, S. Nath and B.C. Arya, 2010. Variations in single scattering albedo and Angstrom absorption exponent during different seasons at Delhi, India. *Atmos. Environ.* **44**, 4355-4363
- [26] P.S. Khillare, S. Balachandran and AB.R. Meena, 2004. Spatial and temporal variation of heavy metals in an atmospheric aerosol of Delhi. *Environmental Monitoring and Assessment.* **90**, 1-21.
- [27] P. Wayne (Ed), 1991. The nitrate radical: physics, chemistry, and the atmosphere, *Atmos. Environ.* **25**, 1-203.
- [28] J. Ding, 2013. The impact of HARMONIE high-resolution meteorological forecasts on the air quality simulations of LOTOS-EUROS. Royal Netherlands Meteorological Institute, Ministry of Infrastructure and the Environment.

# Evaluation of disc and shell horns sound quality characteristics

Tapan. K. Mahanta and B. Venkatesham\*

*Department of Mechanical and Aerospace Engineering*

*Indian Institute of Technology Hyderabad, Kandi, Telangana 502285, India*

*\*e-mail: venkatesham@iith.ac.in*

[Received: 20-02-2017; Revised: 26-05-2017; Accepted: 29-05-2017]

## ABSTRACT

The present paper discusses a methodology, for studying characteristics influencing an automotive horn's sound quality, based on objective analysis and subjective (jury) tests. For this, twenty two horn sound samples are considered. Psychoacoustics parameters (such as loudness, sharpness, roughness, fluctuation strength and tonality) and index of relative sensory pleasantness are calculated for recorded sound samples in objective analysis. Two types of subjective tests which are relevant test (RT) and Semantic differential test (SDT) are developed. These tests are conducted with participation of thirty subjects, aged between 20-40 years with normal hearing. A selection chart is proposed based on subjective test data to select an appropriate horn which has relevance and pleasantness. A correlation study based on principal component analysis is done between objective analysis data and subjective test data. A transformation matrix is calculated from subject ratings and objective metrics profile. The expected performance in subject rating is predicted using transformation matrix and psychoacoustic parameters.

## 1. INTRODUCTION

Most of the working products create a specific sound and a distinctive signature on human perception. Few sounds are generated for warning purposes. For example, an alarm, ambulance siren, factory siren, police vehicle siren and a vehicle horn, *etc.* A vehicle horn is one of the major noise contributors in urban noise pollution. In developing countries, people tend to use vehicle's horn most frequently (honking) while driving. It is impulsive in nature and creates annoyance to listeners. The major reasons for honking could be traffic indiscipline, lacking infrastructure, genuine warning signal, habitual, *etc.* Domestic passenger vehicles like motor cycles and cars use disc and shell horns. Most of the automotive manufacturers are interested to create uniqueness to their vehicle horn sound which also should be congenial to listeners with proper warning. This factor motivates the current study of pleasantness evaluation of both disc and shell horns in a car.

Disc horn, works on the principle of sound generation due to mechanical vibrations of the metal disc (diaphragm). Shell horn works on the principle of air column oscillation, inside the channel. Lemaitre *et al.* [1]-[2] studied extensively on sound quality of car horns. They discussed about the perceived quality of car horn sounds within a psycho-acoustical frame work. Jennings *et al.* [3] described different tools and techniques to understand automotive sound quality and subjective perception. Sound quality study includes subjective

(jury) test, and objective analysis. The purpose of subjective test is to collect humans' perception about sound. Development of an appropriate subjective test method depends on the problem description. Objective analysis is used to calculate Sound Quality (SQ) metrics like loudness, sharpness, fluctuation of strength (FS), roughness and tonality, *etc.*, based on empirical equations Zwicker *et al.*[4]. The purpose of current study is to investigate whether there is a correlation between the subjects' rating and objective psychoacoustic parameters of automotive horn sound. Next, an attempt is made to predict jury's response based on objective analysis data by using principal component analysis. Bowen *et al.*[6] discussed the use of "Sensory profile" (SP's) to make a correspondence between the component and structural decisions made by product engineers, and the perceptual reactions of a user to the product sound. They found SP's for various models of washing machines and vacuum cleaners using principal component analysis. Bowen *et al.*[7] discussed principal component analysis (PCA) and conversion of a large number of SQ metrics into few orthogonal (principal) components or factors. These components are composed of a weighted sum of the (standardized) original metrics. By using these principal components, they predicted user reactions to sounds from a particular type of product. Kang *et al.*[8] developed a quality index for shell horn using the "spectrum decay" (SD) slope. They developed SD slope from spectrum analysis of the interior sounds produced by car horns. They performed objective evaluation method for the perceived quality of a car horn sound based on psychoacoustic metrics and subjective test.

Section 2 of this paper describes the correlation methodology for both subjective and objective evaluations. Before correlation, the objective analysis data is processed using PCA. Section 3 explain details recording the horn sound samples. Section 4 and 5 describe procedures of subjective test conducted and objective psychoacoustic parameter evaluation. Section 6 describes in what manner PCA was applied to objective data. Section 7 details the results and discussions.

## 2. METHODOLOGY

Fig. 1 shows the methodology followed to correlate subjective and objective data of an automotive horn sound. The initial step is to record the horn sound samples by using data acquisition system (DAQ) (Squadriga II) and binaural head set (BHS-II). Consequent steps are subjective and objective evaluation. Later, PCA is used to reduce the dimensionality of the objective data set and extract the principal factors. Final step is to correlate the subjective test with the objective analysis results. Subjective evaluation process is time consuming and costly. By using the proposed method, a design engineer can predict a subjective rating through the psychoacoustic metrics. It minimizes the number of subjective tests during the product development.

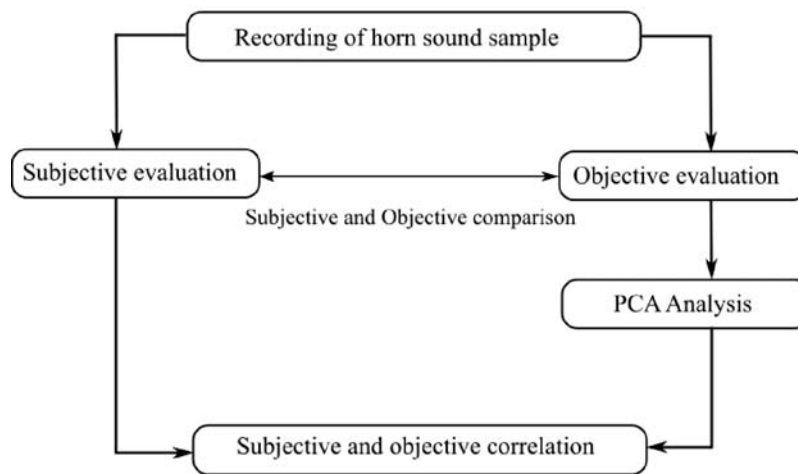


Fig.1. Methodology for subjective and objective correlation.

### 3. RECORDING OF THE SOUND SAMPLE

An experimental test setup is developed for recording horn sounds. Sound recording is carried out in an open space. Continuous honking samples are recorded for one second at a distance of one meter from the horn's front direction. Fig. 2 shows the line diagram of automotive horn sound recording test setup. It consists of horn, horn relay, 12V battery source, Squadriga II, binaural head set (BHS II) and a display unit. Sound is recorded using BHS II and Squadriga II with sampling frequency at 44.1 kHz. A total of twenty two horns from five manufacturers are considered for measurements in which eighteen are disc type and four are shell type.

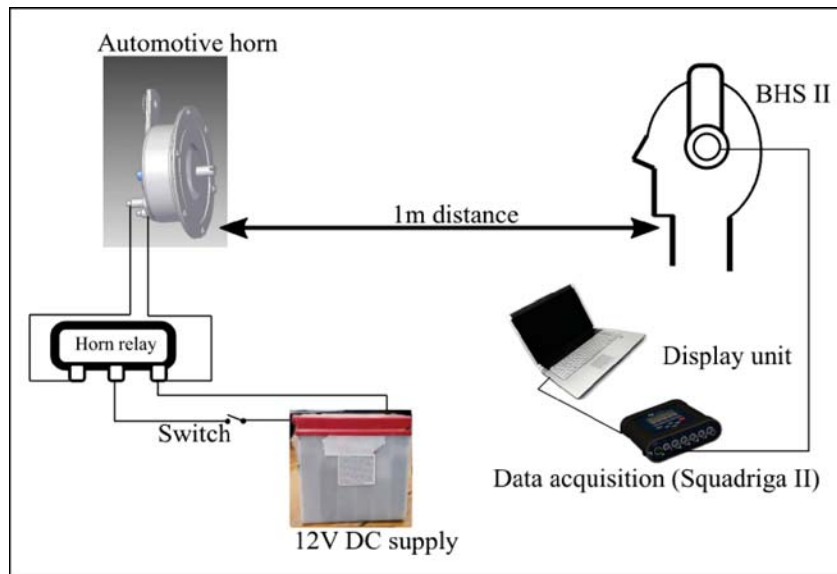


Fig. 2. Automotive horn sound recording test setup using binaural head set.

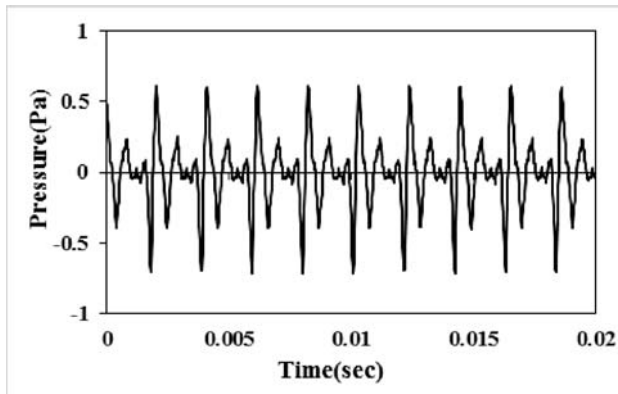
Binaural recording and playback are done using BHS II head set. This head set has two 1/4 " ICP microphones, and it has independent direction (ID) equalization while recording and field dependent equalization for playback. The operating temperature range of headset is  $-10^{\circ}\text{C}$  to  $60^{\circ}\text{C}$ . Maximum sound pressure level while recording is 130dB with total harmonic distortion less than one percent. Three sound samples were recorded for each horn and variation between the measurements are less than 1dB. Background noise levels during the measurements are 45-50dB, which is very low with respect to measured signal sound pressure levels. Total SPL of all the recorded horn sample will be in the range of 95dB to 113dB. So, the influence of background noise on measured signal is insignificant.

Table 1 shows the notation followed for different horns used in the test and their fundamental frequency. Where "M" stands for manufacturer, DH for disc horn and SH for shell horn. Two discs and two shell horns from manufacturer 1, six-disc horns and two shell horns from manufacturer 2, Similarly, six, one and three-disc horns from manufacturer 3, 4 and 5, respectively are taken.

All the twenty two horn sound samples are recorded. A typical wave form and frequency spectrum of a shell horn and disc horn are shown in Figs. 3 and 4, respectively. The fundamental frequency is at 485 Hz for shell horn. The SPL peak frequency in shell horn occurs at 1455 Hz and at third harmonic. Dominant sound pressure contribution lies in the frequency range of 500-2500 Hz for shell horn. The fundamental frequency is at 366 Hz for disc horn. The SPL peak frequency in disc horn occurs at 3348 Hz and at ninth harmonic. Dominant sound pressure contribution lies in the frequency range of 3000-4000 Hz for disc horn.

**TABLE 1.** Horn notation followed in the test and their fundamental frequency.

Horn notation	Horn Type	Fundamental Frequency (Hz)	Horn notation	Horn Type	Fundamental Frequency (Hz)
M1DH1	Disc	366	M2SH2	Disc	485
M1DH2	Disc	434	M3DH1	Disc	366
M1SH1	Shell	416	M3DH2	Disc	412
M1SH2	Shell	494	M3DH3	Disc	355
M2DH1	Disc	355	M3DH4	Disc	416
M2DH2	Disc	419	M3DH5	Disc	366
M2DH3	Disc	366	M3DH6	Disc	419
M2DH4	Disc	431	M4DH1	Disc	377
M2DH5	Disc	333	M5DH1	Disc	355
M2DH6	Disc	421	M5DH2	Disc	431
M2SH1	Shell	400	M5DH3	Disc	362



**Fig. 3(a).** Acoustics pressure time wave form of M2SH2 horn (0-0.02 Sec).

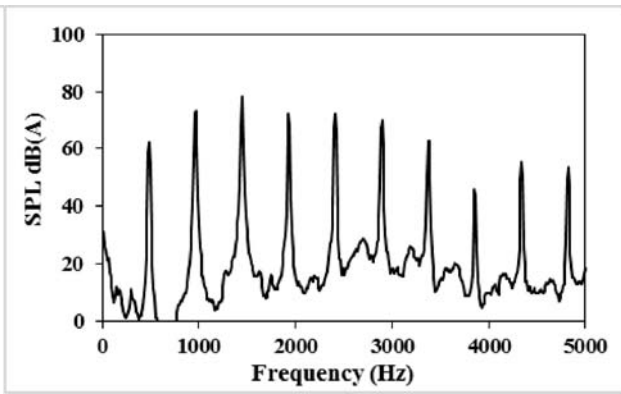


**Fig. 3(b).** Sound pressure levels spectrum of shell horn (M2SH2) (0-5000 Hz).

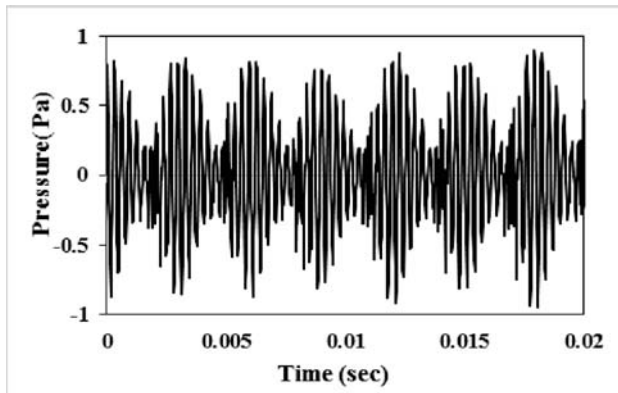


**Fig. 4(a).** Acoustics pressure time wave form of M3DH5 horn (0-0.02 Sec).

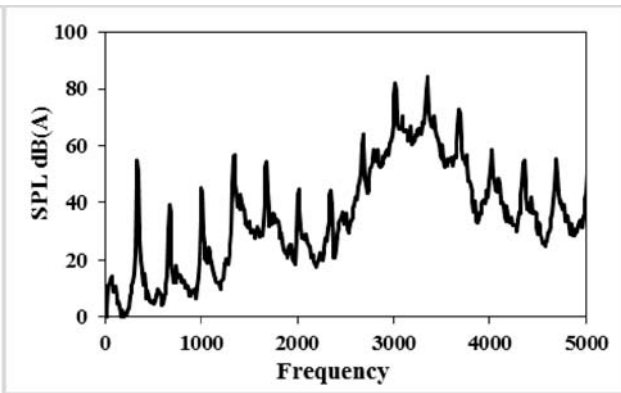


**Fig. 4(b).** Sound pressure level spectrum of disc horn (M3DH5)(0-5000 Hz).

It is observed from Figures 3(b) and 4(b) that sound pressure level, peak frequencies and dominant frequency range for shell horns are lower when compared to the disc horns. Also, it's observed that disc horns have sharp sound quality characteristics when compared to shell horn, and leads to inferior pleasantness feeling. This might be one of the reasons why subjects prefer shell horns.

#### 4. SUBJECTIVE TEST PROCEDURE

All the horn sounds are recorded for a duration for one second as shown in Figs. 3(a) and 4(a). The recorded sound waves are listened by thirty subjects (age ranged from 20 to 40 years). Hearing ability of all the subjects is normal. Otto *et al.*[9] provided details of jury evaluation methods for automotive applications. Two types of evaluation tests are selected as part of evaluation method based on current problem's objective. They are (i) Relevant Test (RT), (ii) Semantic Differential Test (SDT). The purpose of relevant test is to identify the sound of a significant horn model, which people can recognize as an automotive horn, especially car horn. These results are strongly depended on subject's knowledge and experience. Twenty two horn sound samples are played via head phones (Sennheiser HD600) in a quiet room for relevant test. The subjects are free to choose any one sound sample, listen to it for one second and provide their response, to determine if it's an automotive car horn sound or not.

Semantic differential test (SDT) consists bi-polar variables with seven verbal interval scales. Each bi-polar variable may have a relation to another variable. A bi-polar pair is simply an adjective and its antonym. The adjectives generally consist the attributes of sound. Twenty two horn sound samples are considered for SDT test. Subjects can listen to each sample as many times as possible and provide their response on a seven-point verbal scale with bi-polar adjective variables. This test helps in identifying sound quality characteristics. Questions and response scales for the two tests are given in Appendix A. Customized software is developed with a simple graphical user interface (GUI). The customized SQ software could play sound sample files and also record the subject's response in two modules with proper instructions for each module. Sound samples are loaded in "\*.wav" format.

#### 5. OBJECTIVE PSYCHOACOUSTIC PARAMETER EVALUATION

In this study, psychoacoustic metrics such as loudness, roughness, sharpness, fluctuation strength and tonality are used to calculate relative sensory pleasantness index according to Zwicker model Zwicker *et al.* [4]. It can be written as

$$\frac{P}{P_0} = e^{-\left(\frac{0.7R}{R_0}\right)} e^{-\left(\frac{1.08S}{S_0}\right)} \left\{ 1.24 e^{-\left(\frac{2.43T}{T_0}\right)} \right\} e^{-\left(\frac{0.023N}{N_0}\right)^2} \quad (1)$$

where,  $\frac{N}{N_0}$  is a loudness ratio;  $\frac{S}{S_0}$  is a sharpness ratio;  $\frac{T}{T_0}$  is a tonality ratio, and  $\frac{R}{R_0}$  is a roughness ratio.

#### 6. PRINCIPAL COMPONENT ANALYSIS

Principal component analysis can transform the original set of variables into a smaller set which are linear combination. The transformation of data set happens in such a way that, primary principal component (PC) has the maximum variance among other components. Very few principal components are sufficient to explain the majority of the total variance. PCA compresses size of the data set by preserving important information. Objective parameter of horn samples are standardized (mean zero and standard deviation one) preliminary to principal component analysis. This step is needed as the each of the metrics has complete different units of measurement. Metric profile is a matrix which is formed by applying principal component analysis while retaining only four principal components.

Two set of data are created from twenty two horn sound samples. First and second data set (validation) consist of fourteen and eight horn sound sample, respectively. PCA is applied to first data set. From this analysis, four dominant factors (PC1, PC2, PC3 and PC4) are sufficient to explain the majority of total variance.  $[A]_{p \times q}$  Matrix is formed by retaining four PCs. where  $p, q$  are number of sound samples, number of principal

component retained.  $[B]_{p \times 1}$  Matrix is subjective pleasantness obtained for fourteen sound sample. By using Eq. (2), a linear transformation vector  $\{x\}$  is calculated from "first data set" information.

$$[A]\{x\} = [B] \quad (2)$$

$\{x\}$  is the transformation vector of size  $(q \times 1)$ . Eq. (2) has fourteen linear equations and four unknowns, so it's over determined problem. Vector  $\{x\}$  can be solved as a pseudo-inverse problem by using singular value decomposition method. The calculated transformation vector  $\{x\}$  obtained from "first data set" can be used to predict subject (jury) response by using Eq. (3).

$$[A]\{x\} = [B] \quad (3)$$

Where,  $[A]_{p \times q}$  matrix is formed by four PCs for second data set.  $[B]_{p \times 1}$  Predicted mathematically. Subjective (jury) response of second data set (eight) is compared to mathematically (as per Eq. 3) predicted subjective response. Fig. 5 shows the process of PCA being applied, transformation vector  $\{x\}$  calculation and procedure to predict subjective response mathematically.

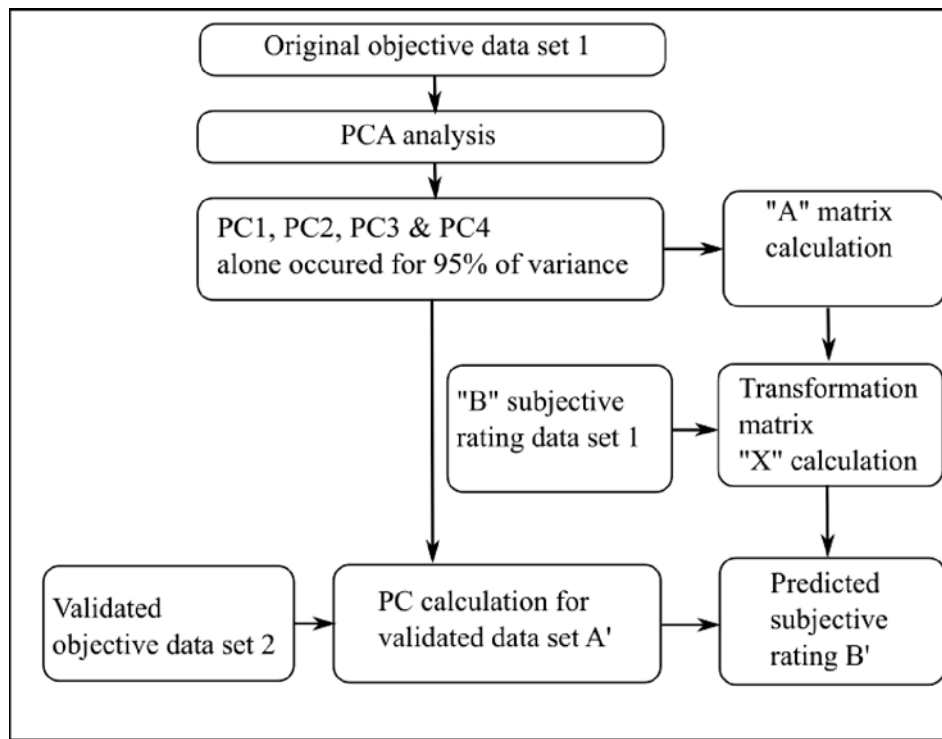


Fig.5. PCA validation flow chart of data set 1 and data set 2.

## 7. RESULTS AND DISCUSSIONS

### 7.1. RT Results

The number of subject responses in RT test is normalized by the total number of subjects. The same is expressed in percentage. Fig. 6 shows a normalized percentage of relevance for all test sound samples. Most of the subjects recognized disc horns as a car horn sound when compared to shell horns, as the same are being used in many car models thus making it more familiar to people. Hence, it has an influence in the jury rating.



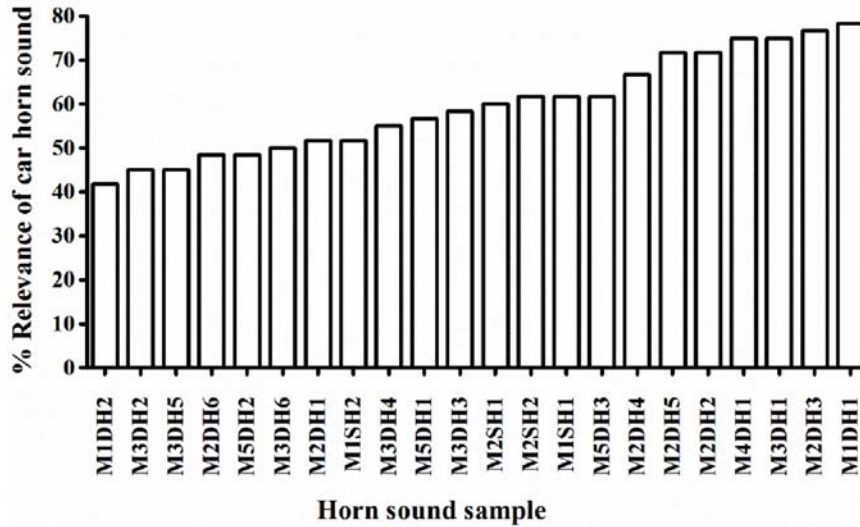


Fig. 6. Results of relevant percentage of different car horn sounds based on RT test.

7.2. SDT Results

The subjective responses in SDT test for different sound samples are normalized to minimize the data variation of subject ratings using Eq. (4)

$$N_{ij} = \frac{X_{ij} - \mu_j}{\sigma_j} \tag{4}$$

Where,  $N_{ij}$  is normalized value of respective sound samples,  $X_{ij}$  is rating value of the  $i^{th}$  subject to the  $j^{th}$  sound sample,  $\mu_j$  is mean value of  $j^{th}$  sound sample and  $\sigma_j$  is standard deviation of  $j^{th}$  sound sample.

Fig. 7 shows the comparison of disc and shell horn normalized results for seven bi-polar variables in the box-plot. It is observed from the mean value comparison that shell horn is louder and pleasant when

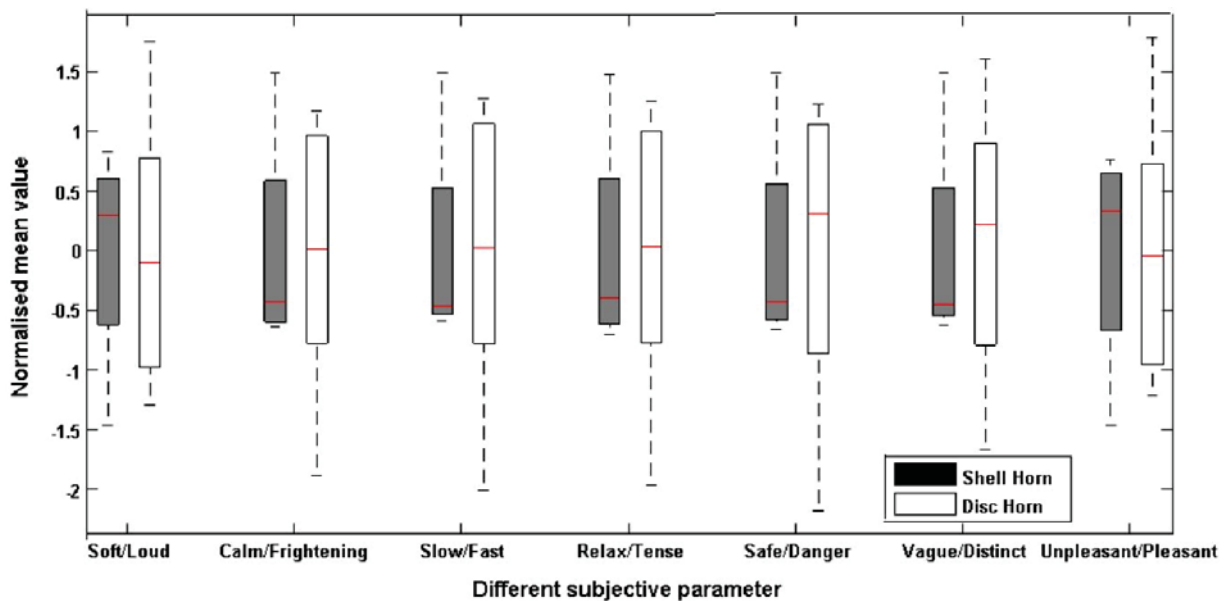


Fig. 7. Comparison of disc and shell horn SDT results in normalized form for each bipolar variable.

compared to disc horn. If the normalized mean values is negative and it can be interpreted as first variable is dominant. Based on the mean value comparison, shell horns have sound characteristics like calm, slow, relax, safe and vague when compared to disc horns.

The psycho-acoustics metrics (objective parameters) and indices calculation methodology is adopted for estimating objective parameters in the current manuscript as described by Zwicker *et al.* [4] and Venkatesham *et al.*[15]-[16].

Fig. 8 shows the box-plot of objective parameters comparison for both shell and disc horns. It's observed that sharpness, roughness and tonality's normalized mean values of shell horn are low when compared to disc horn. However, loudness of shell horn is more when compared to disc horn and similar observations were made in subjective test.

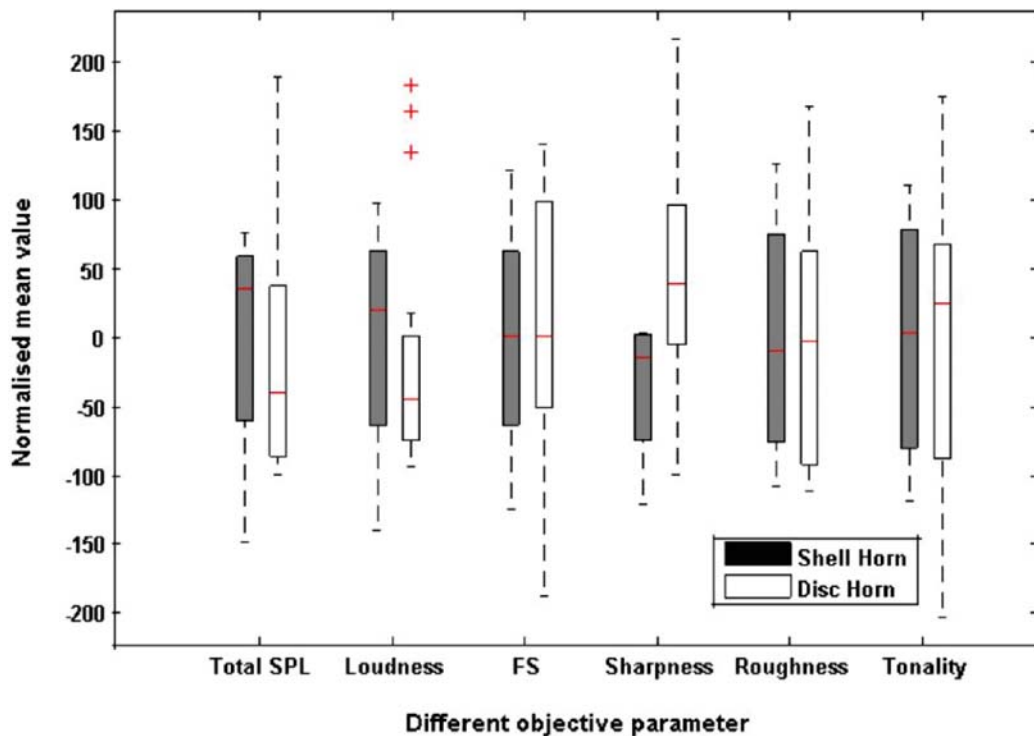


Fig. 8. Comparison of normalized objective parameters for Shell and Disc horn.

Sound pressure level data has a smaller range variation and most of the horns are designed to meet the legislation requirement on SPL. However, there is a wider distribution on objective parameters. Fluctuation strength and roughness values are similar in nature for both disc and shell horns. It's observed that there is higher loudness, lower sharpness and lower tonality mean value for shell horns when compared to disc horns.

Considering M2DH3 horn sound as reference (due to its wide usage) relative sensory pleasantness index is calculated for all horn sound samples. However, this procedure is not restricted for a particular model of the horn as a reference and can be repeated with other horns. If the relative sensory pleasantness index value is higher than reference value (0.19) then it's considered as pleasant sound otherwise unpleasant. Fig. 9 shows the pleasantness index for objective test results. It's observed that shell horns, (M1SH1, M2SH1, M1SH2, and M2SH2) are more pleasant when compared to disc horns. Also, it's observed that disc horns have sharp sound quality characteristics when compared to shell horn which leads to inferior pleasantness feeling. This might be one of the reasons why subjects prefer shell horns.

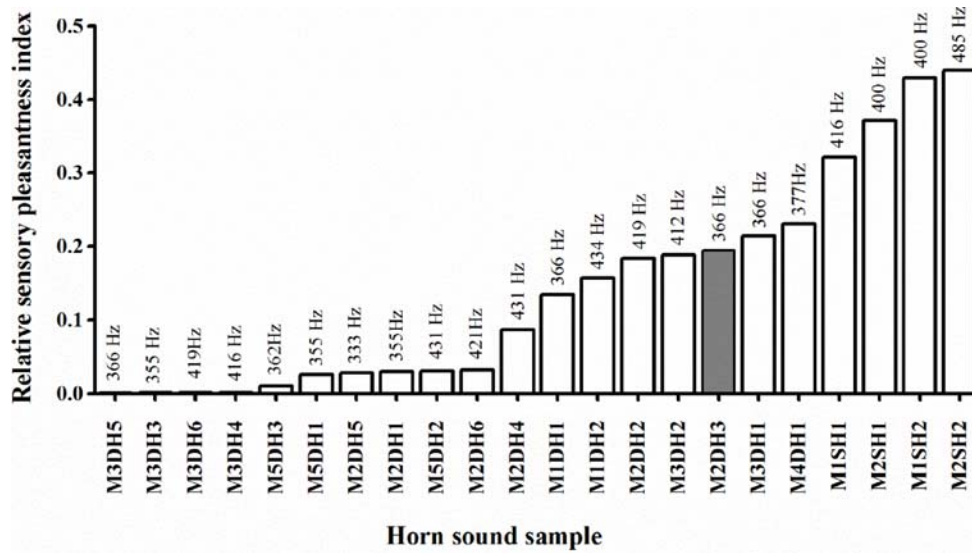


Fig. 9. Comparison of different horns relative sensory pleasantness index with reference to disc horn(M2DH3).

These results are useful to identify the extreme pleasant or unpleasant horn sound samples with respect to reference sound. The samples which are on extreme left and right of the reference sound sample as shown in Fig. 9 are considered as "most unpleasant" and "most pleasant", respectively. Similarly, sound samples which are near to the reference sample are considered as "less pleasant" and "more pleasant" sounds, respectively.

Fig. 10 shows the comparison of normalized pleasantness mean value of the objective and subjective results for disc and shell horns. It's observed that shell horns are more pleasant when compared to disc

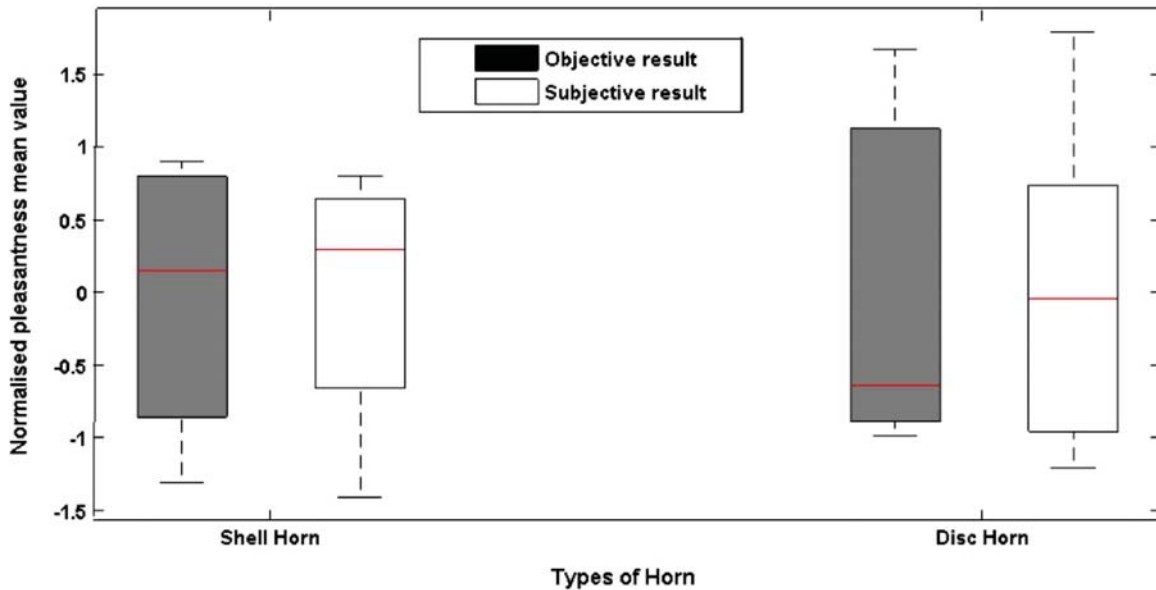


Fig. 10. Normalized pleasantness values comparison of subjective and objective results for Disc and Shell horn.

**Table 2.** Summary of pleasantness data results in subjective and objective data analysis

Horn sample	Subjective test data	Objective data analysis	Horn sample	Subjective test data	Objective data analysis	Horn sample	Subjective test data	Objective data analysis
M1SH1	Pleasant	Pleasant	M5DH3	Unpleasant	Unpleasant	M2DH1	Unpleasant	Unpleasant
M1SH2	Pleasant	Pleasant	M5DH1	Unpleasant	Unpleasant	M2SH1	Pleasant	Pleasant
M3DH1	Unpleasant	Pleasant	M5DH2	Unpleasant	Unpleasant	M2SH2	Pleasant	Pleasant
M3DH2	Unpleasant	Pleasant	M2DH5	Pleasant	Unpleasant	M4DH1	Pleasant	Pleasant
M3DH3	Unpleasant	Unpleasant	M2DH6	Pleasant	Unpleasant	M1DH1	Pleasant	Unpleasant
M3DH4	Unpleasant	Unpleasant	M2DH2	Pleasant	Unpleasant	M1DH2	Pleasant	Unpleasant
M3DH5	Unpleasant	Unpleasant	M2DH3	Pleasant	Unpleasant			
M3DH6	Unpleasant	Unpleasant	M2DH4	Pleasant	Unpleasant			

horns. There is a wider range of variation in sound quality parameters for disc horn as shown in Fig. 8. Table 2 shows the summary of the pleasantness data result for both subjective and objective tests.

It's observed that sound sample pleasantness prediction based on the objective parameters exactly matches with subjective response for "most unpleasant" and "most pleasant" group. However, there is uncertainty in the prediction for "less pleasant" and "more pleasant" group. Subjective results for pleasantness are sensitive to type of instrumentation, subject's knowledge and cognitive effects Jennings *et al.*[3]. Subjective test data of RT and SDT tests are arranged in a chart form as shown in Fig. 11. This chart can be used to select an appropriate horn from a given test horn data base. Shell horns have a higher pleasantness index, and disc horns have a good percentage of recognition as a car horn sound. Designer can fix the limits for percentage.

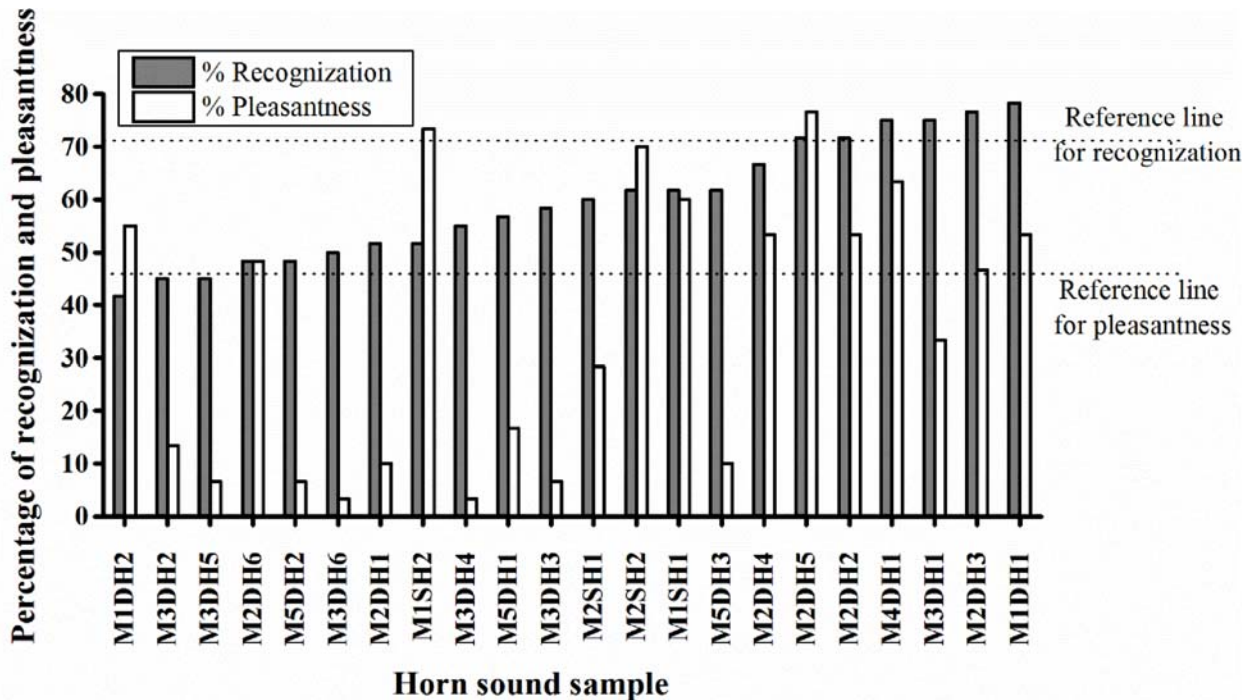


Fig. 11. Horn selection chart based on RT and SDT test.

### 7.3. PCA Results

Fig. 12 shows correlation result of actual subjective rating and predicted subjective rating for the second data set and their regression curve by following the method explained in Fig. 5. The calculated value is 0.82, which shows that there is good correlation between the subjective mathematically predicted results and subjective (jury) results. The proposed transformation approach based on PCA analysis helps to minimize the number of jury tests repetition and guides to estimate the subjective response at design stage. This identical transformation vector can be used for predicting subject's response to the sounds of another product in this equivalent class.

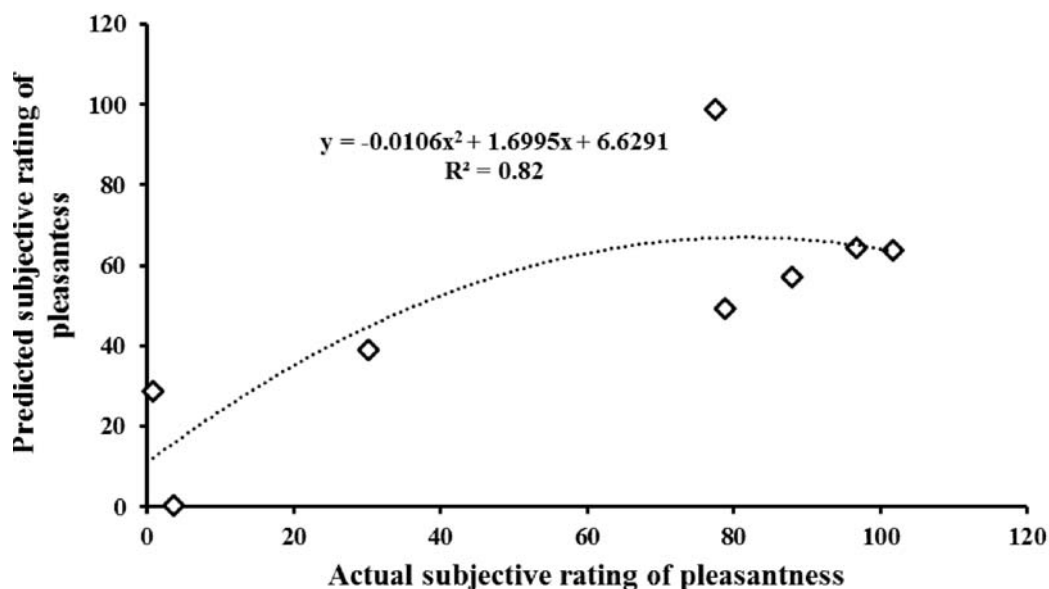


Fig. 12. Comparison of actual and predicted jury rating of pleasantness based on PCA approach.

## 8. CONCLUSIONS

The present manuscript discusses the evaluation of sound quality characteristics of automotive horn based on subject response and psychoacoustic objective parameters. Relevant test (RT) has been developed to capture the recognition as a car horn sound. Horn sound characteristics are captured in SDT test using seven bipolar variables on a verbal scale. The preferred characteristics for pleasant sound based on SD test are soft, calm, relax and slow. Horn selection chart based on existing subjective test data is developed for appropriate horn selection. It is observed from the chart that shell horns are more pleasant and preferred choice than disc type horns. Similar observations are obtained based on objective pleasantness evaluations. Shell horns have lower sharpness value as compared to disc horns. A correlation between a set of objective psychoacoustics parameters and subject's response for horn sound has been established using Principal Component Analysis. Metrics profile of horn sound is calculated based on the limited number of principal components. A transformation matrix is developed between subjective and objective test data. The proposed method results are verified. It will be useful to assess the jury's response for new horn sounds at design stage based on its objective test data.

## 9. ACKNOWLEDGMENTS

We would like to thank Department of Science and Technology, Government of India for financial support to conduct current investigation and Indian Institute of Technology Hyderabad for providing the required resources.

## 10. REFERENCES

- [1] G. Lemaitre, P. Susini, S. Winsberg, S. McAdams and B. Letinturier, 2007. The sound quality of car horns: a psychoacoustical study of timbre, *Actaacustica united with Acustica*, **93**(3), 457-468.
- [2] G. Lemaitre, P. Susini, S. Winsberg, S. McAdams and B. Letinturier, 2009. The sound quality of car horns: Designing new representative sounds, *Actaacustica united with Acustica*, **95**(2), 356-372.
- [3] P. Jennings, G. Dunne, R. Williams and S. Giudice, 2010. Tools and techniques for understanding the fundamentals of automotive sound quality, Proceedings of the Institution of Mechanical Engineers, Part D: *Journal of Automobile Engineering*, **224**(10), 1263-1278.
- [4] H. Fastl and E. Zwicker, 2007. Psychoacoustics: Facts and models, *Springer Science and Business Media* **22**.
- [5] M. Bodden, 1997. Instrumentation for sound quality evaluation, *Acta Acustica united with Acustica*, **83**(5), 775-783.
- [6] D.L. Bowen and R.H. Lyon. Mapping perceptual attributes of sound to product design choices. *Noise Control Engineering Journal*, **51**(4), 271-279.
- [7] D.L. Bowen, 2008. Correlating sound quality metrics and jury ratings. *Sound and Vibration*, **42**(9), 12.
- [8] H.S. Kang, T. Shin, D.C. Park and S.K. Lee, 2015. Quality index of dual shell horns of passenger cars based on a spectrum decay slope. *International Journal of Automotive Technology*, **16**(6), 929.
- [9] N. Otto, S. Amman, C. Eaton and S. Lake, 1999. Guidelines for jury evaluations of automotive sounds (No. 1999-01-1822). *SAE Technical Paper*.
- [10] W.H. Cho, J.G. Ih, S. H. Shin and J.W. Kim, 2011. Quality evaluation of car window motors using sound quality metrics. *International Journal of Automotive Technology*, **12**(3), 443-450.
- [11] R.P. Leite, S. Paul and S.N. Gerges, 2009. A sound quality-based investigation of the HVAC system noise of an automobile model. *Applied Acoustics*, **70**(4), (2009) 636-645.
- [12] M. S.Khan and C. Dickson, 2012. Evaluation of sound quality of wheel loaders using a human subject for binaural recording. *Noise Control Engineering Journal*, **50**(4), 117-126.
- [13] M.F. Guillén, 2007. The soundscape experience. In *19<sup>th</sup> International Congress on Acoustics*.
- [14] R.H. Lyon, 2003. Product sound quality-From perception to design. *Sound and vibration*, **37**(3), 18-23.
- [15] B. Venkatesham, N. Pradeep, Goutham and J. Kim, 2012. Preliminary study on automotive horn sound quality. *National Symposium on Acoustics, India*.
- [16] T.K. MahaNta and B. Venkatesham, 2014. Correlation of objective and subjective data of automotive horn. *National Symposium on Acoustics, India*.
- [17] T.K. MahaNta, B. Venkatesham and B. Karri, 2015. Statistical processing of subjective test data for sound quality evaluation of automotive horn. *National Symposium on Acoustics, India*.
- [18] MATLAB User Manual.

## APPENDIX A: Subjective test questionnaire

### A.1 RT Test Instructions

Dear participant,

A sample of horn sounds are presented to you. You have to answer the question with your response of "yes" or "no" in relevant test. The sounds are played only once. The next sound clip will be ready for play after entering your input.

#### Note:

We are interested on your spontaneous opinion. There is no right or wrong answer.

Can you identify it as a car horn sound? (Yes/No)

### A.2 SDT Test Instructions

Dear participant,

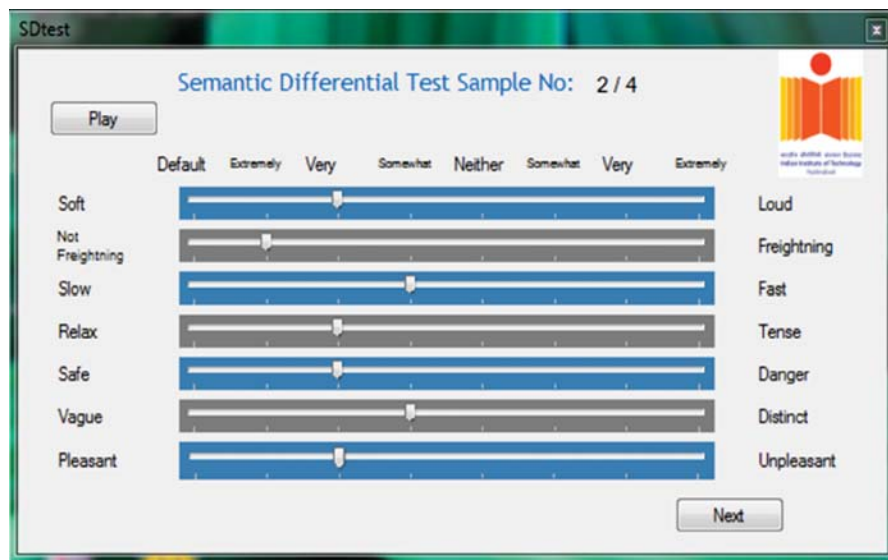
A sample of horn sounds are presented to you. You have to provide inputs for seven attributes on a verbal scale. A bipolar pair is formed for each attribute with an adjective and its antonym. Your response for each bipolar pair can be recorded by dragging a slider. The sound sample can be played as many times as you want. The next sound sample will be ready for play after entering your inputs.

#### Example:

For a soft/ loud bipolar pair, a sound can be evaluated as extremely, very or somewhat soft or extremely, very or somewhat loud based on how you perceive that sound. If you do not think that the sound is either soft or loud, the part of the scale labeled neither should be marked. The same procedure is repeated for other bipolar pairs.

Which category does this sound fall in?

(Soft/Loud, Calm/Frightening, Slow/Fast, Relax/Tense, Safe/Danger, Vague/Distinct, Pleasant/Unpleasant)



(Snap shot of SDT test)

## INFORMATION FOR AUTHORS

### ARTICLES

The Journal of Acoustical Society of India (JASI) is a refereed publication published quarterly by the Acoustical Society of India (ASI). JASI includes refereed articles, technical notes, letters-to-the-editor, book review and announcements of general interest to readers.

Articles may be theoretical or experimental in nature. But those which combine theoretical and experimental approaches to solve acoustics problems are particularly welcome. Technical notes, letters-to-the-editor and announcements may also be submitted. Articles must not have been published previously in other engineering or scientific journals. Articles in the following are particularly encouraged: applied acoustics, acoustical materials, active noise & vibration control, bioacoustics, communication acoustics including speech, computational acoustics, electro-acoustics and audio engineering, environmental acoustics, musical acoustics, non-linear acoustics, noise, physical acoustics, physiological and psychological acoustics, quieter technologies, room and building acoustics, structural acoustics and vibration, ultrasonics, underwater acoustics.

Authors whose articles are accepted for publication must transfer copyright of their articles to the ASI. This transfer involves publication only and does not in any way alter the author's traditional right regarding his/her articles.

### PREPARATION OF MANUSCRIPTS

All manuscripts are refereed by at least two referees and are reviewed by the Publication Committee (all editors) before acceptance. Manuscripts of articles and technical notes should be submitted for review electronically to the Chief Editor by e-mail or by express mail on a disc. JASI maintains a high standard in the reviewing process and only accept papers of high quality. On acceptance, revised articles of all authors should be submitted to the Chief Editor by e-mail or by express mail.

Text of the manuscript should be double-spaced on A4 size paper, subdivided by main headings-typed in upper and lower case flush centre, with one line of space above and below and sub-headings within a section-typed in upper and lower case understood, flush left, followed by a period. Sub-sub headings should be italic. Articles should be written so that readers in different fields of acoustics can understand them easily. Manuscripts are only published if not normally exceeding twenty double-spaced text pages. If figures and illustrations are included then normally they should be restricted to no more than twelve-fifteen.

The first page of manuscripts should include on separate lines, the title of article, the names, of authors, affiliations and mailing addresses of authors in upper and lower case. Do not include the author's title, position or degrees. Give an adequate post office address including pin or other postal code and the name of the city. An abstract of not more than 200 words should be included with each article. References should be numbered consecutively throughout the article with the number appearing as a superscript at the end of the sentence unless such placement causes ambiguity. The references should be grouped together, double spaced at the end of the article on a separate page. Footnotes are discouraged. Abbreviations and special terms must be defined if used.

### EQUATIONS

Mathematical expressions should be typewritten as completely as possible. Equation should be numbered consecutively throughout the body of the article at the right hand margin in parentheses. Use letters and numbers for any equations in an appendix: Appendix A: (A1, A2), etc. Equation numbers in the running text should be enclosed in parentheses, i.e., Eq. (1), Eqs. (1a) and (2a). Figures should be referred to as Fig. 1, Fig. 2, etc. Reference to table is in full: Table 1, Table 2, etc. Metric units should be used: the preferred from of metric unit is the System International (SI).

### REFERENCES

The order and style of information differs slightly between periodical and book references and between published and unpublished references, depending on the available publication entries. A few examples are shown below.

#### *Periodicals:*

- [1] S.R. Pride and M.W. Haartsen, 1996. Electro seismic wave properties, *J. Acoust. Soc. Am.*, **100** (3), 1301-1315.
- [2] S.-H. Kim and I. Lee, 1996. Aeroelastic analysis of a flexible airfoil with free play non-linearity, *J. Sound Vib.*, **193** (4), 823-846.

#### *Books:*

- [1] E.S. Skudrzyk, 1968. *Simple and Complex Vibratory Systems*, the Pennsylvania State University Press, London.
- [2] E.H. Dowell, 1975. *Aeroelasticity of plates and shells*, Nordhoff, Leyden.

#### *Others:*

- [1] J.N. Yang and A. Akbarpour, 1987. Technical Report NCEER-87-0007, Instantaneous Optimal Control Law For Tall Buildings Under Seismic Excitations.

### SUBMISSIONS

All materials from authors should be submitted in electronic form to the JASI Chief Editor: B. Chakraborty, CSIR - National Institute of Oceanography, Dona Paula, Goa-403 004, Tel: +91.832.2450.318, Fax: +91.832.2450.602, (e-mail: bishwajit@nio.org) For the item to be published in a given issue of a journal, the manuscript must reach the Chief Editor at least twelve week before the publication date.

### SUBMISSION OF ACCEPTED MANUSCRIPT

On acceptance, revised articles should be submitted in electronic form to the JASI Chief Editor (bishwajit@nio.org)



ISSN 0973-3302

# THE JOURNAL OF ACOUSTICAL SOCIETY OF INDIA

Volume 44

Number 3

July 2017



A Quarterly Publication of the ASI  
<http://www.acousticsindia.org>



# The Journal of Acoustical Society of India

The Refereed Journal of the Acoustical Society of India (JASI)

**CHIEF EDITOR:**

**B. Chakraborty**

CSIR-National Institute of Oceanography

Dona Paula,

Goa-403 004

Tel: +91.832.2450.318

Fax: +91.832.2450.602

E-mail: bishwajit@nio.org

**ASSOCIATE SCIENTIFIC EDITOR:**

**A R Mohanty**

Mechanical Engg. Department

Indian Institute of Technology

Kharagpur-721302, India

Tel. : +91-3222-282944

E-mail : amohantyemech.iitkgp.ernet.in

**Editorial Office:**

**MANAGING EDITOR**

**Mahavir Singh**

**ASSISTANT EDITORS:**

**Yudhisther Kumar**

**Devraj Singh**

**Kirti Soni**

ASI Secretariat,

C/o Acoustics, Ultrasonics & Vibration

Section CSIR-National Physical Laboratory

Dr. KS Krishnan Road

New Delhi 110 012

Tel: +91.11. 4560.8317

Fax: +91.11.4560.9310

E-mail: asisecretariat.india@gmail.com

The **Journal of Acoustical Society of India** is a refereed journal of the Acoustical Society of India (ASI). The ASI is a non-profit national society founded in 31st July, 1971. The primary objective of the society is to advance the science of acoustics by creating an organization that is responsive to the needs of scientists and engineers concerned with acoustics problems all around the world.

Manuscripts of articles, technical notes and letter to the editor should be submitted to the Chief Editor. Copies of articles on specific topics listed above should also be submitted to the respective Associate Scientific Editor. Manuscripts are refereed by at least two referees and are reviewed by Publication Committee (all editors) before acceptance. On acceptance, revised articles with the text and figures scanned as separate files on a diskette should be submitted to the Editor by express mail. Manuscripts of articles must be prepared in strict accordance with the author instructions.

All information concerning subscription, new books, journals, conferences, etc. should be submitted to Chief Editor:

*B. Chakraborty, CSIR - National Institute of Oceanography, Dona Paula, Goa-403 004,  
Tel: +91.832.2450.318, Fax: +91.832.2450.602, e-mail: bishwajit@nio.org*

Annual subscription price including mail postage is Rs. 2500/= for institutions, companies and libraries and Rs. 2500/= for individuals who are not ASI members. The Journal of Acoustical Society of India will be sent to ASI members free of any extra charge. Requests for specimen copies and claims for missing issues as well as address changes should be sent to the Editorial Office:

*ASI Secretariat, C/o Acoustics, Ultrasonics & Vibration Section, CSIR-National Physical Laboratory, Dr. KS Krishnan Road,  
New Delhi 110 012, Tel: +91.11.4560.8317, Fax: +91.11.4560.9310, e-mail: asisecretariat.india@gmail.com*

The journal and all articles and illustrations published herein are protected by copyright. No part of this journal may be translated, reproduced, stored in a retrieval system, or transmitted, in any form or by any means, electronic, mechanical, photocopying, microfilming, recording or otherwise, without written permission of the publisher.

Copyright © 2017, Acoustical Society of India

ISSN 0973-3302

Printed at Alpha Printers, WZ-35/C, Naraina, Near Ring Road, New Delhi-110028 Tel.: 9810804196. JASI is sent to ASI members free of charge.

**B. CHAKRABORTY**

Chief Editor

**MAHAVIR SINGH**

Managing Editor

**A R MOHANTY**

Associate Scientific Editor

**Yudhishter Kumar Yadav**

**Devraj Singh**

**Kirti Soni**

Assistant Editors

## EDITORIAL BOARD

**M L Munjal**

IISc Bangalore, India

**S Narayanan**

IIT Chennai, India

**V R SINGH**

PDM EI New Delhi-NCR, India

**R J M Craik**

HWU Edinburg, UK

**Trevor R T Nightingale**

NRC Ottawa, Canada

**N Tandon**

IIT Delhi, India

**J H Rindel**

Odeon A/S, Denmark

**E S R Rajagopal**

IISc Bangalore, India

**G V Anand**

IISc Bangalore, India

**S S Agrawal**

KIIT Gurgaon, India

**Yukio Kagawa**

NU Chiba, Japan

**D D Ebenezer**

NPOL Kochi, India

**Sonoko Kuwano**

OU Osaka, Japan

**Mahavir Singh**

CSIR-NPL, New Delhi, India

**A R Mohanty**

IIT Kharagpur, India

**Manell E Zakharia**

ENSAM Paris, France

**Arun Kumar**

IIT Delhi, India

**Ajesh K. Abraham**

IISH Mysore, India

**S V Ranganayakulu**

GNI Hyderabad, India



# The Journal of Acoustical Society of India

A quarterly publication of the Acoustical Society of India

Volume 44, Number 3, July 2017

## ARTICLES

### Qualification tests on spacecraft and launch vehicle subsystems for acoustic environment

*S. Murugan, K. Velmurugan, D. Padmini, S.M. Rekha and K.N. Arun Kumar* ..... 125

### Vibration and acoustic testing of spacecraft

*M.N.M. Patnaik and S. Shankar Narayan* ..... 132

### A novel hybrid passive study on reduction of aircraft cabin-floorboard vibro-acoustic interaction

*N. Chandra, B. Balakrishnan and S. Raja* ..... 141

### Influence of acoustic reflection on measurement locations in a large reverberation chamber

*S. Murugan* ..... 152

### Novel experimental set-up for characterization of acoustic source

*N. Mallikarjun Naik, M. Rajesh, P. AtchutaRamayya, P. Anil Kumar and D. Venugopal* ..... 160

### Vibro-acoustic response of composite payload fairings subjected to acoustic excitation

*P. Geena George, S. R. Arun Raj, P. R. Murali and R. Neetha* ..... 166

### Investigation of acoustic characteristics during the liquid engine starting transient phase through scale model test

*Iyer Saisanthosh, Jopaul K Ignatius, S. Sankaran and R. Ajithkumar* ..... 172

## INFORMATION

Information for Authors

Inside back cover



## FOREWORD

Acoustics related problems are one of the major concerns in aerospace industries that are required to be addressed efficiently to have a trouble free journey of rockets, spacecraft, missiles and aircraft. The noise generated by the launch vehicles during lift off and in the atmospheric flight can affect the performance of the spacecraft and launch vehicle subsystems is one such example. Similarly the aircraft noise is required to be suppressed to have a pleasant environment inside the cabin.

This special edition dedicated to Acoustic testing on Aerospace Structures contributed by experienced scientific engineers at various Indian national aerospace centers has revealed the insight information about the noise and vibration aspects of aerospace structures.

The article titled *Qualification tests on spacecraft and launch vehicle subsystems for acoustic environment* contributed by *S. Murugan, K. Velmurugan, Padmini.D, Rekha S.M, K.N. Arun Kumar* outlines the acoustic testing of space bound structures. The importance of such tests and various methods that are followed worldwide are outlined. The article also covers broadly the reverberant acoustic test of spacecraft and launch vehicle subsystems that are required to be qualified for the acoustic environment during their take-off and transonic flight. The sub systems of reverberant acoustic test facility and noise generation techniques are briefed. The delicacy in the test procedure with respect to the exposure time of test article during acoustic simulation is well emphasised.

The article authored by *M.N.M Patnaik and S. Shankar Narayan* on *vibration and acoustic testing of spacecraft* emphasises the need aspects of the dynamic testing of spacecraft and its sensitive subsystems. The article describes various dynamic testing methods performed in qualifying the spacecraft for the severe dynamic loads. Authors highlighted the advantages of the in-house developed force measurement device (FMD) that measures the dynamic base forces and the moments of the spacecraft under test in all three directions. Also the article outlined the in-house developed test data analysis software DYNTEST that reduces the results processing time significantly. Authors presented the simulation and characterisation of micro vibration of spacecraft that experiences during orbit manoeuvre. Authors focused on a novel technique that by pass the conventional vibration test for similar spacecraft structures is adopted by performing modal shaker test in the reverberation chamber. Authors have also briefed about alternate procedure for performing the shock test with modal hammer in order to reduce the cost and risk associated with conventional shock test.

Technical article on *A novel hybrid passive study on reduction of aircraft cabin-floorboard vibro-acoustic interaction* authored by *N. Chandra N. Chandra\*, B. Balakrishnan and S. Raja* describes an innovative technique adopted in controlling the cabin noise of an aircraft. Authors presented the experimental studies conducted on a typical segment of an aircraft fuselage, simulating noise spectrum below the floor board. Experimental results show the reduction of noise in the cabin with the help of constrained layer damping (CLD) patches and further reduction is observed with the introduction of melamine foam over the CLD. Authors also performed the numerical simulation in finding the structural and acoustic modes and verified the same with experimental methods. The noise reduction obtained by these simulations of CLD patches are discussed.

Article on *Influence of acoustic reflection on measurement locations in a large reverberation chamber* contributed by *S. Murugan*, contains valuable information about the sound reflection behaviour in an enclosed chamber near rigid walls. The findings in this article will largely benefit the reverberant acoustic test engineers especially on the diffusivity of reverberant field with reference to the wall reflections. This article explains the variation of sound pressure field near the surfaces, edges and corners of a large enclosure. Extensive experimental studies were performed by the author and matched well with the theoretical predictions. Measurement locations of microphones used for acoustic testing on launch vehicle interstages and spacecraft can be arrived efficiently from these studies to ensure accurate sound pressure level measurements around a test article.

The article titled *Novel Experimental Set-up for Characterization of Acoustic Source* contributed by *N. Mallikarjun Naik, M. Rajesh, P. AtchutaRamayya, P. Anil Kumar, D. Venugapoal* brought out the characterisation technique of a special purpose high intensity wide band noise generator. The electromagnetic mechanism involved in this typical noise source are well described and the conversion of this electromagnetic force into the acceleration of the moving coil is estimated experimentally for calibration and validation.

The article on *Vibro-acoustic response of composite payload fairings subjected to acoustic excitation* authored by P. Geena George, S. R. Arun Raj, P. R. Murali, R. Neetha presents the sound transmission across the payload fairing (also called heat shield) of a launch vehicle that affects the satellite housed inside. Authors highlighted the causes of this high intensity acoustic loads that can damage the critical components of the satellites and the launch vehicle sub systems. This article also brought out the difference in the acoustic signature of two different shapes of payload fairing. Flight measured data are presented for straight nose cone and ogive shaped payload fairing configurations. Results indicate the reduction of internal acoustic field in the ogive shaped payload fairing as it reduced the external acoustic level due to aero dynamic noise.

The article titled *Investigation of acoustic characteristics during the liquid engine starting transient phase through scale model test* authored by Iyer Saisanthosh, Jopaul K Ignatius, S.Sankaran and R. Ajithkumar reports the acoustic characteristics of the supersonic nozzle of a rocket liquid engine. Authors presented the experimental studies performed to investigate the acoustic pressure distribution along the inner wall of the nozzle due to the shock induced flow separation. Water injection technique that was deployed to understand the effect on the flow separation mechanism is highlighted. This article presented the surface flow visualisation studies through nozzle along with acoustic and vibration measurements for better understanding of the severe pressure oscillation that causes the vibration. The article concluded with valuable understanding on how the water injection influences the separation phenomenon thus suppressing the broadband shock associated noise.

As I conclude this overview, I would like to thank Dr. Biswajit Chakraborty, Chief Editor of JASI for his valuable support throughout the preparation of this special issue. My sincere gratitude to Mr. S. Murugan, for sparing his valuable time and for all the inputs in ensuring the quality of the selected articles.

**Dr. Ranjan Moodithaya**

*Guest Editor*

Chief Scientist & Head (Rtd), Acoustic Test Facility,  
National Aerospace Laboratories, Bangalore - 560 032, India

# Qualification tests on spacecraft and launch vehicle subsystems for acoustic environment

S. Murugan, K. Velmurugan, D. Padmini, S.M. Rekha and K.N. Arun Kumar  
Acoustic Test Facility, CSIR-National Aerospace Laboratories, Bangalore 560037  
e-mail: murugan@nal.res.in

(Received : 05.07.2017; Revised : 18.07.2017; Accepted : 02.08.2017)

## ABSTRACT

Acoustic tests are performed on spacecraft and launch vehicle sub systems to qualify them for the acoustic environment that they encounter during flight. The importance of acoustic testing is described in this article. Various methods of simulating the acoustic environment is highlighted. Reverberant acoustic tests are generally performed on large sized test articles. The salient features of the reverberation chamber and its various components are presented. The test procedures and required data analysis are detailed.

## 1. INTRODUCTION

Satellites are launched by powerful rockets with an escape velocity of 12 km/s, imposing severe dynamic loads on their subsystems and payloads. Travel through the atmospheric layer is a critical stage in the life of the spacecraft and onboard rocket systems. They experience such noise fields until they cross the atmospheric layer of about 100 kilometers thick. However, during the flight, major part of the dynamic loads experienced by the launch vehicle and spacecraft structure are from acoustic sources, essentially due to launch vehicle generated noise at lift-off and aerodynamic noise caused by turbulence due to flow separation and local protuberances (ref. Fig.1). It is therefore essential to test all spacecraft and launch vehicle subsystems for such acoustic environment, for their mechanical effects, under simulated conditions on ground mainly in a reverberant acoustic chamber. The acoustic loads simulated are similar to those experienced by the vehicle in flight and this helps in qualifying the structure in order to ensure safe operation.

## 2. SIMULATION TECHNIQUES OF ACOUSTIC ENVIRONMENT

Acoustic environment can be simulated using progressive wave tubes, standing wave tubes, direct field or reverberant acoustic facility. These simulation techniques have their own merits and de-merits. Reverberant acoustic test facility is widely used for qualification of spacecraft and launch vehicle subsystems generating a uniformly distributed diffused acoustic field around the specimen. A description of each technique is provided in brief below.

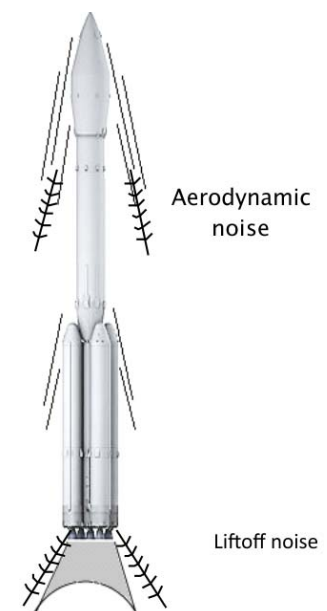


Fig. 1 Noise sources of launch vehicle during liftoff and transition flight

### 2.1 Progressive Wave Tube (PWT).

In a progressive wave tube, sound waves travel along a duct of uniform cross section from an acoustic source, which is coupled to one end. The other end of the duct is terminated with acoustic insulation in order to prevent reflection of the propagating sound waves. The specimen test section inside the duct, will experience the desired intensity of acoustic energy (ref. Fig 2). These facilities are suitable for testing panels and scaled down models of launch vehicles. Progressive wave testing is suitable for simulation of some degree of spatial variation of acoustic field along the length of the duct. The limitation for this method is the un-controlled spectrum simulation and large harmonic distortions at higher intensity.

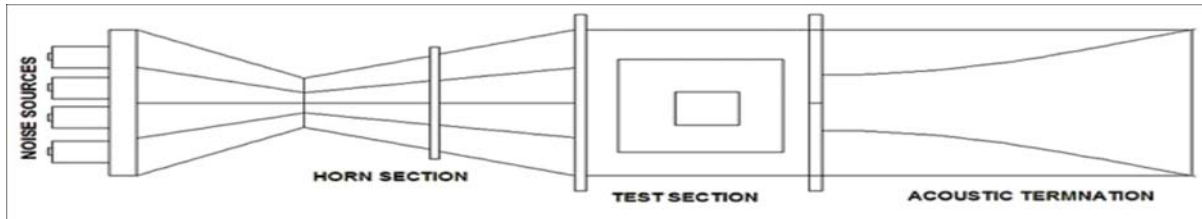


Fig. 2 Progressive Wave Tube acoustic testing

### 2.2 Standing Wave Tube (SWT).

In a standing wave tube, acoustic source is coupled to one end and the other end is terminated with hard reflecting surface such that standing waves are established in the tube (ref. Fig 3). These standing waves are characterized by the existence of pressure nodes and anti-nodes that are fixed in space. Thus the standing wave tube facility is capable of generating high level of sound with discrete frequency. These facilities are useful in evaluation and diagnostics of post-test failure of sub systems.

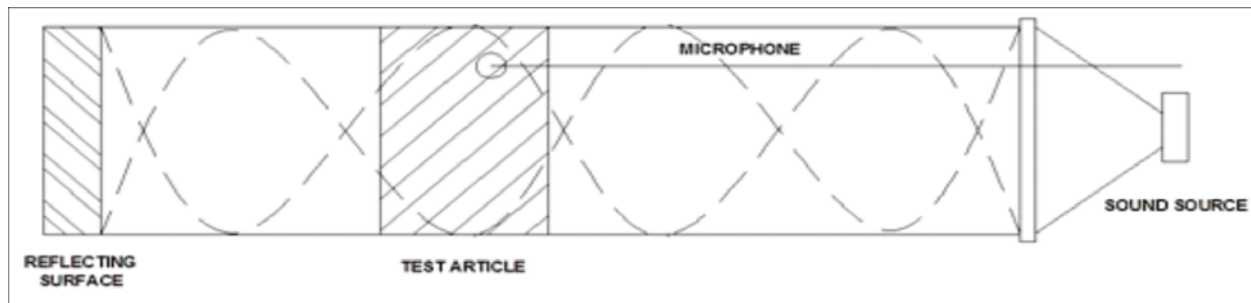


Fig. 3 Standing Wave Tube acoustic testing

### 2.3 Direct Field Acoustic Testing (DFAT).

Direct field acoustic testing is a method of exposing a test article to high intensity acoustic levels using an array of acoustic sources, typically loud speakers in a circular form (ref. Fig 4). The acoustic energy reflected from the test article is absorbed in the surrounding volume. By controlling the spectrum of excitation of individual sources, some degree of spectrum control and its spatial variation can be simulated. It has a number of logistical advantages in terms of using a simple loud speaker system. However, direct radiation requires greater acoustic power than reverberation chambers to achieve the same required acoustic level, which is a limitation.

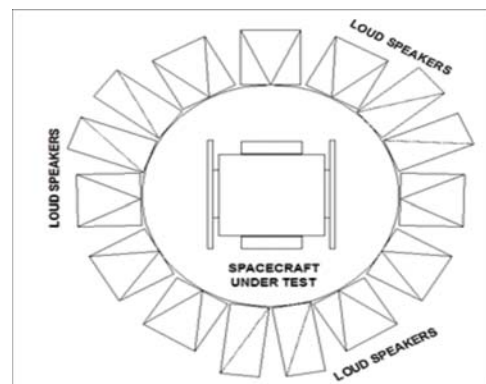


Fig. 4 Direct field acoustic testing



## 2.4 Reverberant acoustic test facility (RATF).

Reverberation chambers are made of hard reflecting walls to ensure a diffused sound field with broad band characteristics. Noise sources which are coupled to the chamber through horns are supplied with air or nitrogen gas and modulated by an electro-magnetic or hydraulic servo mechanism. RATF (Ref. Fig. 5) is widely popular because of the possibility of simulating closely, acoustic levels that are encountered by the spacecraft and launch vehicle subsystems during flight. The time average of mean square sound pressure level is more or less same everywhere in the reverberation chamber in such facilities.

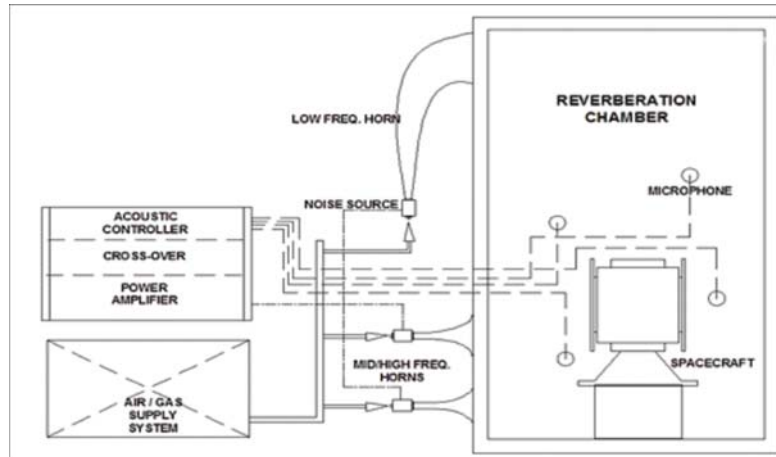


Fig. 5 Reverberant acoustic testing

### 2.4.1 Reverberant Acoustic Testing

The purpose of acoustic testing is to simulate the actual launch environment to the degree required to produce the same effects that the test article would experience in service. These tests conform to US MIL Standard 810G. The purpose of testing falls broadly under the following categories:

- Search for weak elements in the subsystems with respect to acoustic fatigue.
- Qualification test to demonstrate the spacecraft and launch vehicle subsystems performance in meeting design goals.
- Acceptance test to uncover workmanship nature of defects.
- Measure the vibration response on various subsystems to define test level specification for vibration tests on them

### 2.4.2 Acoustic spectrum

Spacecraft or launch vehicle sub systems are tested in a reverberation chamber by simulating the acoustic spectrum that is defined by two parameters namely; frequency and sound pressure level. These input acoustic loads are derived from aerodynamic model testing in a wind tunnel and further refined from the data collected from previous launches. A typical spectrum of launch vehicle and spacecraft is shown in Fig. 6. Frequency components are wide band in nature, hence they are grouped in octave or one third octave bands. In general, they are specified from 31.5 to 8000 Hz octave bands. Overall sound pressure level (OASPL) is the logarithmic average of all the octave bands level. The shape of acoustic spectrum in terms of amplitude vary with launch vehicles.

### 2.4.3 Reverberation chamber

The geometry and sizing of the reverberation chamber is done in such a way that it provides the best acoustic mode distribution in the lowest frequency of interest. The larger the volume, the more uniform

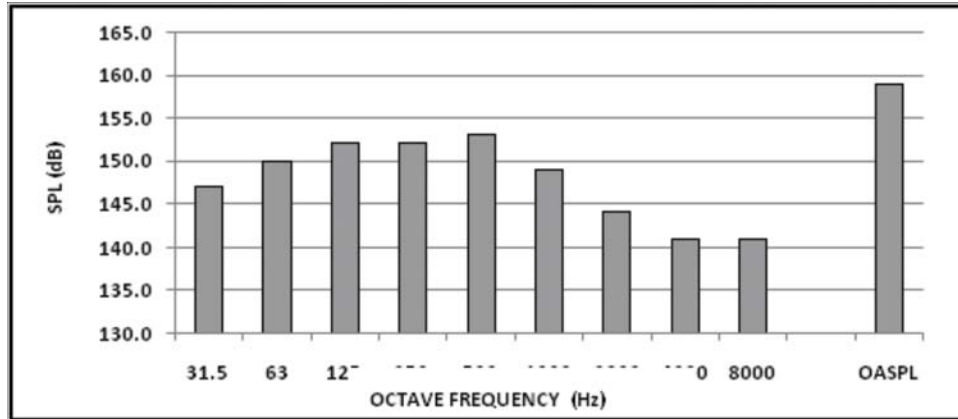


Fig. 6 Typical acoustic spectrum of a launch vehicle subsystem

the spatial distribution of energy will be at low frequencies. Chambers are made of steel reinforced concrete with wall thickness varying from 200 to 500 mm. Wall thickness is determined with regard to the capability to withstand internal dynamic acoustic pressure as well as providing the necessary acoustic attenuation to prevent noise pollution in surrounding buildings. Internal surfaces of the chamber are treated to optimally cover all porous openings thereby minimizing sound absorption. Hard epoxy paints are used on the chamber surfaces to improve reflective characteristics. A door made of steel reinforced concrete similar to the walls facilitates entry of the test specimen to the chamber. Once the test specimen is positioned in the chamber, proper sealing arrangement between the wall and the door ensures minimum leakage of sound through these gaps to adjacent areas. The chamber has openings with a metallic interface ring for mounting of horns. An exhaust duct for air or gas to escape during from the chamber during operation is provided.

#### 2.4.4 Noise sources and horns

Powerful noise sources are required to simulate the launch vehicle noise environment in a reverberation chamber. High intensity noise sources convert gas/pneumatic energy into acoustic energy by means of a modulation process. A typical noise source is illustrated in Fig. 7. A permanent magnet and voice coil arrangement oscillate the moving armature over the fixed armature when the electrically shaped signals are provided. Air or gas passing through the slots in the armatures create a differential pressure across the slots and hence sound is produced. The frequency and amplitude of the sound thus generated is proportional to the frequency of oscillation and displacement of the moving armature respectively.

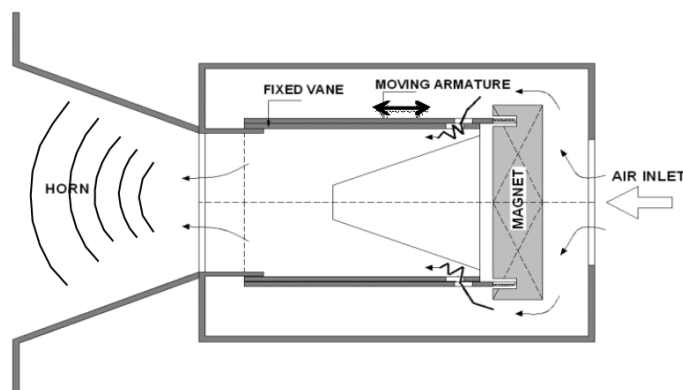


Fig. 7 High intensity noise generator based on air stream modulation

Horns are used to couple the high impedance acoustic source to the low impedance chamber, thus improving the efficiency of sound transmission. Lower cut off frequency of the horns determines the frequency above which sound can be transmitted through them effectively. Hence multiple noise sources are connected through different cut off frequency horns to cover the wide band acoustic spectrum specified for testing aerospace structures in a reverberation chamber

#### 2.4.5 Air or gas supply system

Air or gas with regulated pressure is required to generate the noise through the modulation process. Air is generally used in most of the acoustic test facilities. Air compressor delivers compressed air into a huge storage tank which feed the noise sources through pressure and flow control valves. Spacecraft testing facilities prefer gaseous nitrogen for the noise sources in order to provide a clean and inert environment required for spacecraft and subsystems. A gaseous nitrogen plant consists of a liquid nitrogen storage tank, feeding vaporizers which convert the liquid nitrogen into gaseous nitrogen and supply it to the noise sources at ambient temperature through control valves. Alternatively, hot water bath system is used for liquid to gas conversion.

#### 2.4.6 Test specimen mounting

Test specimen are generally mounted on a trolley in the assembly area and moved into the reverberation chamber. Low weight subsystems like spacecraft solar panels are provided with a bungee cord suspension in the test chamber. As a general thumb rule, the volume of the specimen shall be within 10 percent of the volume of chamber in order to avoid influence on the diffusivity of the sound field.

#### 2.4.7 Instrumentation

##### 2.4.7.1 Microphones

Microphones are positioned around the test specimen to monitor and control the acoustic levels as per the specified spectrum. The actual number of microphone measurements required to ensure proper measurement of the sound field in the reverberation chamber is determined based on the test specimen size and the standard deviation of the sound field measured by using a large number of microphones around the test specimen. Microphones are mainly of two types namely; free field and pressure field microphones. Free field microphones are designed to compensate for the effect of the microphone itself in the field where the sound waves are free to expand outwards forever from the source. Pressure field microphones are designed to respond in a uniform manner to any signal arriving on its measuring surface from any angle. Therefore, Pressure field microphones are ideally suitable for diffused field measurement in a reverberation chamber.

Microphones work on the principle of variation of electrical energy when the diaphragm of the microphone responds mechanically to the acoustic pressure being sensed. Condenser type microphones (ref. Fig. 8) use a capacitor to convert acoustical energy into electrical energy. A capacitor has two plates with a voltage between them. One of these plates is made of very light material and acts as the diaphragm. The diaphragm vibrates when struck by sound waves, changing the distance between the two plates and therefore changing the capacitance. A voltage is required across the capacitor for this to work. The microphones used for acoustic testing are capable of measuring sound pressure level up to 170 decibels. The average size of the microphone diaphragm is  $\frac{1}{4}$  of an inch.

##### 2.4.7.2 Accelerometers

Number of accelerometers are mounted at various sensitive locations of the test specimen to measure vibration response

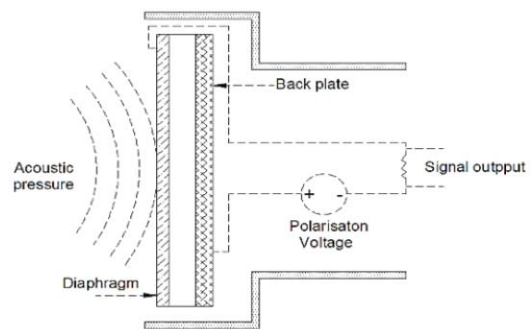


Fig. 8 Condenser microphone

during an acoustic test. Structural response data is analysed to determine if individual subsystems are capable of withstanding the acoustic loads they are subjected to and their responses are within the design values in terms of vibration levels and frequencies. The acceleration response data is also useful for deriving the input load spectra for vibration tests on spacecraft and launch vehicle subsystems using a vibration shaker.

Accelerometers are the most commonly used sensors for measuring vibration. The basic working principle of such a device is presented in Fig. 9. It consists of a moving mass on a spring and dashpot, attached to a moving solid base. The acceleration of the moving solid base results in a differential movement 'x' between the mass 'M' and the solid base.

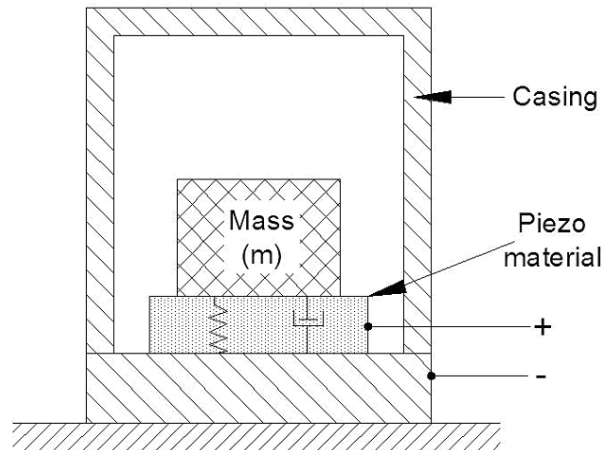


Fig. 9 Piezo electric accelerometer

This relative displacement 'x' can be measured in different ways, using piezoelectric material, either in longitudinal or shear mode. In such configurations, the strain applied to the piezoelectric material is proportional to the relative displacement between the mass and the base thus converting mechanical motion into an electrical signal.

#### 2.4.8 Noise generation and testing

After positioning microphones around the specimen and instrumentation of accelerometers on the structure, acoustic test is performed by generating the specified noise spectrum in the chamber. Noise generators are controlled by an automatic control system that regulates the modulator drive signal by comparing the microphone feedback signal with the set spectrum. Modern acoustic controllers are capable of controlling the overall spectrum with a tolerance of  $\pm 1$  dB. Acoustic tests are classified as flight acceptance tests and qualification tests. In flight acceptance tests, the acoustic levels required to be simulated will be similar to actual flight levels experienced by the spacecraft. Qualification test is performed to validate the design loads of the structure and hence test acoustic levels will be 3 dB higher than flight acceptance levels. Qualification tests are normally performed on developmental pro-type structures whereas flight acceptance tests are performed on actual flight hardware.

In both cases, the simulation is performed in three stages namely; low, mid and full level tests. Low level will be -6 dB of full level test to ensure all instrumentation as well as set parameters are functioning normally. Mid-level test will be -3 dB, followed by full level test. In general, duration of each low and mid-level test will be 30 seconds. Full level test for flight acceptance and qualification tests are 60 and 120 seconds respectively. A repetition of the low level test called signature test will be conducted after the full level test to ensure the repeatability of specimen response indicating that the specimen has not undergone any permanent deformation/failure for the maximum acoustic load.

#### 2.4.9 Data acquisition and analysis

The microphone and accelerometer signals acquired during acoustic testing are analysed using a digital signal analyser. Microphone signals contain data over a wide frequency bandwidth ranging from 20 to 12000 Hz, hence they require high sampling rates of at least 30000 samples per second. The sum average of individual microphone signals is the acoustic spectrum which is required to be generated in the test chamber.

Vibration response data analysis is analysed up to 2000 Hz generally, hence the sampling rate required is 7000 samples per second. Power spectral density with overall g-rms is evaluated. Transfer function is obtained by computing the ratio of power spectral density of vibration response in  $g^2/Hz$  to the input acoustic pressure in  $Pa^2/Hz$ . Transfer function, as a health parameter indicates the linearity of structural response to the applied acoustic load at various test levels.

#### 2.4.10 Post acoustic test checks

After completion of an acoustic test, the test specimen is subjected to critical structural inspection as well as functional tests of subsystems. In the case of spacecraft, physical inspection of solar cells on each solar panel, deployment test of solar panels and antenna, feed horn alignment, etc. are some of the important post acoustic tests to be performed to ensure perfect performance. In case of launch vehicles/subsystems, physical inspection of all structural elements, torques of fasteners, radiography inspection of CFRP elements, bonding homogeneity of insulation material, etc. are carried out.

### 3. ACOUSTIC TEST FACILITIES WORLDWIDE

Growing size of spacecraft and launch vehicles demand large size test facilities worldwide. Payload fairing otherwise called as heat shield of a launch vehicle housing the spacecraft is the largest specimen to be tested in a reverberation chamber. Presently the largest chamber in use for testing inter planetary mission space programme stages is about 2900 cubic meter in volume. This requires a large number of noise sources with over all acoustic power up to 4000 KW. Very few manufacturers worldwide can provide such high intensity acoustic sources to cater to the above requirements.

### 4. SUMMARY

Acoustic tests play a very vital role in qualifying space bound structures for the noise environment encountered during lift off and atmospheric flight. This is one of the mandatory dynamic tests that spacecraft and launch vehicle subsystems undergo during the developmental stages and also as pre-flight acceptance. Over testing as well as under-testing of the specimen in terms of the required acoustic spectrum equally impacts the purpose of acoustic testing. Repetition of acoustic tests on space bound structures can affect the performance in several ways as acoustic fatigue is of serious concern on the mechanical design of space structures. Hence in order to accomplish completely successful tests, operation and maintenance of these facilities require excellent skillsets and training as test durations are extremely limited with zero margin of error.

### 5. REFERENCES

- [1] C.V.R. Reddy and M.S. Prabhu, 1993, Spacecraft and acoustics, *J. Spacecraft of technology*, **3**(1), 1-21
- [2] S. Balakrishna *et al.*, 1988, "Design, Construction and evaluation of ISRO-NAL Acoustic Test Facility", 39<sup>th</sup> Congress of the International Astronautical Federation, Bangalore, India, pp. 6-7.

# Vibration and acoustic testing of spacecraft

**M.N.M. Patnaik and S. Shankar Narayan**  
*Structures Group, ISRO Satellite Centre, Bangalore*  
*e-mail address: patnaik@isac.gov.in*

(Received: 17.08.2017; Accepted: 23.08.2017)

## ABSTRACT

Present day spacecraft structural designs are changing considerably with new mission requirements and with a philosophy of faster, better and cheaper realisation mode. Further with advancement in computational methods and experience gained, the structural design is highly optimised. In this scenario, spacecraft dynamic testing is emphasised to be more efficient, accurate and with time reduction. All these call for improvisations in conventional spacecraft dynamic test methodology with the aid of new technologies. Improvements to spacecraft dynamic tests like force limited vibration testing, dynamic characterization of on orbit micro vibrations, hammer tap method for shock characteristic derivation etc. are incorporated into the ISRO spacecraft dynamic testing. These improvisations have contributed tremendously to achieve an efficient and reliable spacecraft dynamic testing in line with the new organizational requirements.

## 1. INTRODUCTION

Spacecraft are subjected to variety of dynamic environment which include quasi static, vibration and acoustic loads during launch, pyrotechnic shocks generated by separation / deployment mechanisms, on orbit jitter and sometimes planetary landing loads. These loads include low frequency sinusoidal, random, acoustic and shock loads. These dynamic loads are critical for the design of spacecraft and need test validations. Design for on-orbit jitter reduction is critical for the spacecraft with high resolution cameras and sensitive optical payloads. Spacecraft dynamic load specifications depend on the launch vehicle, satellite configuration and mission events. Spacecraft design validation and its ability to withstand the dynamic loads are demonstrated by dynamic testing. In case of spacecraft with sensitive optical payloads, the on orbit jitter caused due to the operation of rotating elements like reaction wheels, gimbal mechanisms, cryo coolers etc., severely affect the payload performance. It is required to reduce / have spectral knowledge of the on board micro vibrations for optimizing the payload performance. This calls for spacecraft micro vibration measurements on ground, involving the specialized test setup and instrumentation.

In the early days of space program, it was a common practice to build a qualification model of the spacecraft which was dedicated for the testing. In the current scenario to build faster, better and cost effective spacecraft, there is only one 'proto-flight' model which is subjected to all ground testing and then it is launched. Further with maturity in design and technical experience, the structural design margins are reduced and there is increased emphasis on analyses and less on the test. All these point to increase the efficiency of dynamic testing. This paper details the various dynamic tests performed on ISRO spacecraft program with thrust on new dynamic testing techniques adopted.

## 2. SPACECRAFT VIBRATION TESTS

Spacecraft is subjected to low frequency transients / sinusoidal vibrations during various flight events. These loads are specified as accelerations at the base of the spacecraft. Typical sine vibration specification of PSLV along longitudinal axis is shown in Table 1.

**Table1:** PSLV sine vibration specification

Frequency (Hz)	Amplitude
5 - 11.5	4.5 mm
11.5 - 38	1.2 g
38 - 60	1.2 g - 0.5g
60 -100	0.5g

For the test, spacecraft is mounted on an electro-dynamic shaker using a suitably designed fixture. The spacecraft is subjected to specified sine sweep test along all three axes. Fig. 1 shows a typical lateral axis sine vibration test setup for a geostationary satellite. In traditional vibration test of spacecraft, due to high impedance of the test fixture, the test article is unduly subjected to very high responses at its resonance, which otherwise are unlikely during actual flight. This necessitates the limiting of the shaker drive force to the values based on the dynamic coupled load analysis (DCLA) results of the spacecraft and the launch vehicle mathematical models. Fig. 2 shows a typical spacecraft longitudinal test input spectrum. The notching at 65 and 82 Hz correspond to the fundamental resonance frequencies of the spacecraft.



Fig. 1. Lateral axis sine vibration test setup

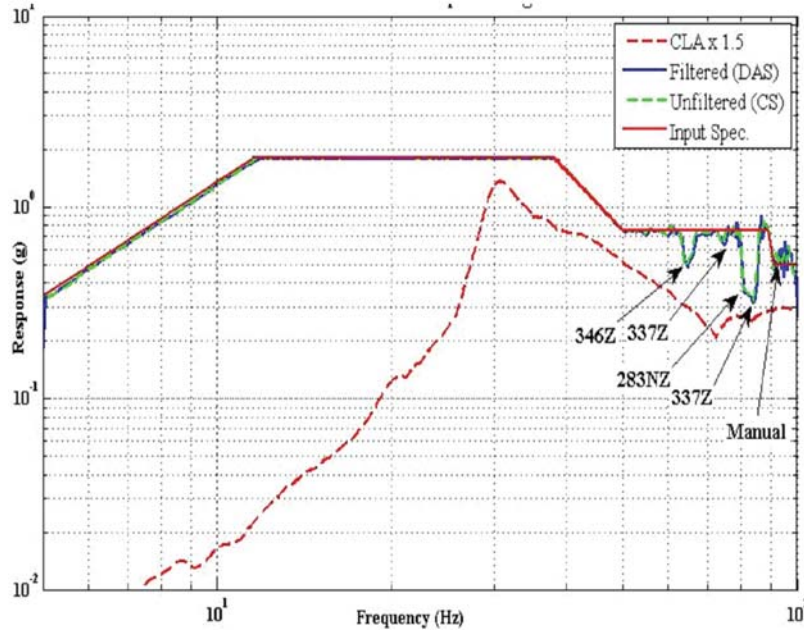


Fig. 2. typical spacecraft test input spectrum

Conventionally, the dynamic base force at resonance are estimated indirectly from the shaker armature current and interface strain calibration method, which in some cases cause under testing or over testing of the spacecraft. With the advent of tri axial force sensors, a force measurement device (FMD) is developed [1] which incorporate these gauges and can measure the dynamic base forces and the moments in all three directions. Fig. 3 shows the FMD and Fig. 4 depicts the use of FMD during vibration test.

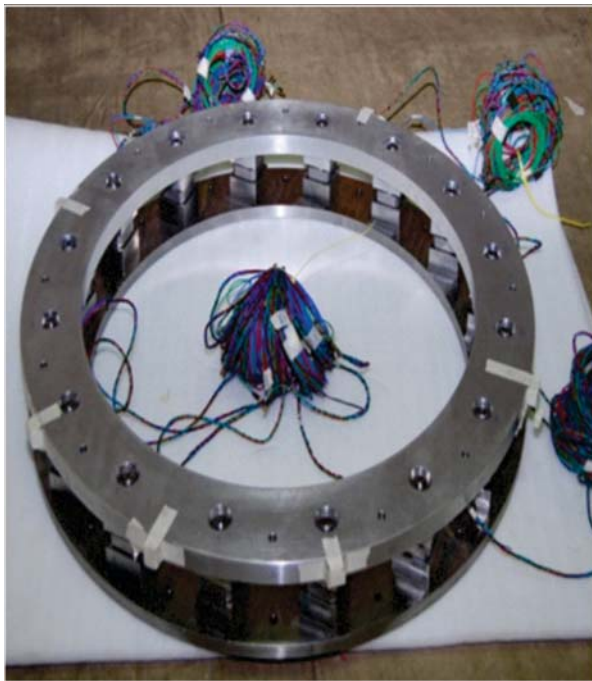


Fig. 3. force measurement device



Fig. 4. Vibration test with FMD



The FMD application envisages force limited vibration (FLV) testing of spacecraft [2], which ensures optimal vibration test. The use of FMD is highly advantageous for vibration testing of spacecraft with unsymmetrical structure, with large lateral CG offset and estimation of modal effective mass from the measured base forces and moments.

Vibration testing of spacecraft involves measurement of responses at important locations on the spacecraft. A typical spacecraft vibration test has 250 acceleration sensors. The test measured data is analysed to derive the spacecraft dynamic characteristics and the test input notching estimation. The full level test input is arrived by encompassing the requirement of CLA and design limits of subsystems. Performing these analyses on large channel data is cumbersome and prone to human errors. A customized test data analyses software "DYNTTEST" is build in-house to handle large test data, process, analyse and necessary test computations. Features like notching prediction, selection of peak acceleration responses, dynamic characteristics estimation and signature test comparisons are built into the DYNTTEST. Fig. 5 shows a snapshot of DYNTTEST front panel. The test data processing by DYNTTEST has tremendously reduced the data analysis duration, which aided in reduction of test campaign duration and enhanced the test computational reliability

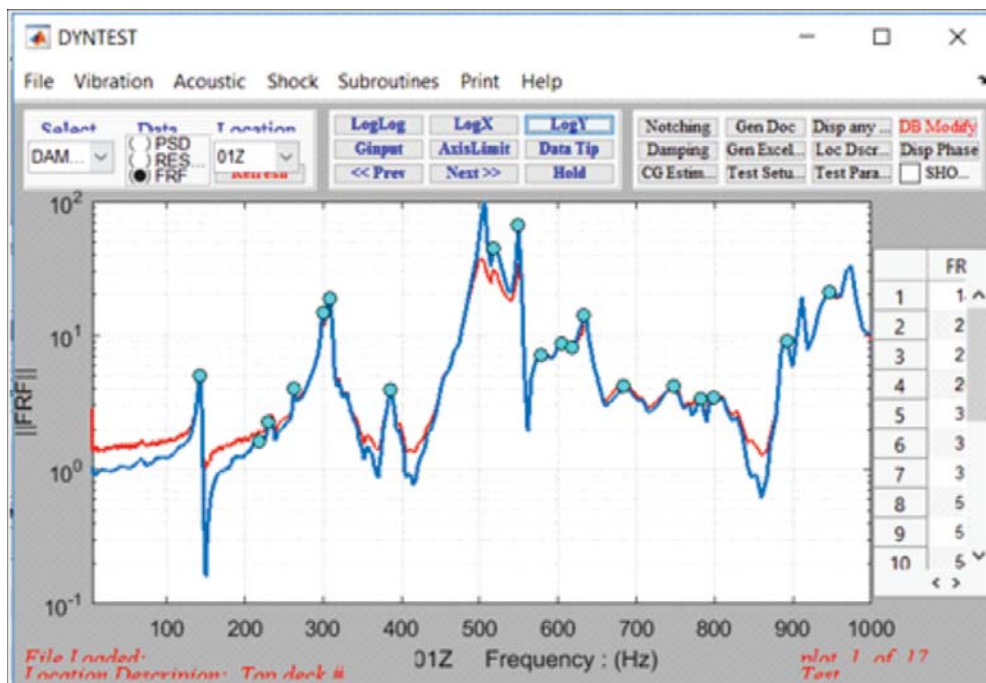


Fig. 5. Snapshot of DYNTTEST

## 2.1 Spacecraft micro vibration measurement

On orbit spacecraft micro vibrations generated by the operation of various moving elements on board like reaction wheels, cryo cooler pumps, gimbal mechanisms etc., affect the performance of the high sensitive optical payloads [3]. Efforts are pursued to attenuate these micro vibrations by design and by introducing isolation schemes. However, the knowledge of spectral variation of on-board disturbance is essential for optimal performance of the payload. The micro vibration measurement tests are conducted on flight model spacecraft. The vibration levels are measured at the payload critical elements during the operation of reaction wheels and other moving elements, simulating the on orbit operational profile. The test setup includes simulation of zero 'g' condition of spacecraft by low frequency suspension. Fig. 6 shows the test setup for micro vibration measurements. The measured data is analysed for identification of operating condition of each moving element that are critical for payload performance.



Fig. 6. Micro vibration measurement test setup

## 2.2 Spacecraft acoustic test

At the time of lift-off and during the atmospheric flight, the spacecraft experiences high intensity acoustic loads which are transmitted through the heat shield or flaring. The acoustic specifications of PSLV for spacecraft are given in Table 2.

**Table 2:** PSLV acoustic specification

Octave band center freq.(Hz)	SPL (dB)
31.5	124
63	126.5
125	130
250	136
500	140
1000	135
2000	128
4000	125
8000	122
OASPL	143

The acoustic testing of spacecraft is done in ISRO reverberation chamber. The diffuse field environment is generated by electro-pneumatic transducers. Fig. 7 shows spacecraft acoustic test setup in reverberation chamber (RC). Gaseous nitrogen is used for the acoustic field generation and the acoustic spectrum around the spacecraft in the RC is through automatic control system. The acoustic loads are critical for large appendages like solar panels, reflectors *etc.* Majority of the spacecraft structural members are made of honeycomb sandwich panels and the electronic packages are mounted on them. The dynamic acoustic loads acting on these panels in turn cause random vibration excitation of the packages. The measured vibration response will reveal the structural integrity of the spacecraft. The acoustic test also ensures the workmanship quality of the spacecraft assemblies

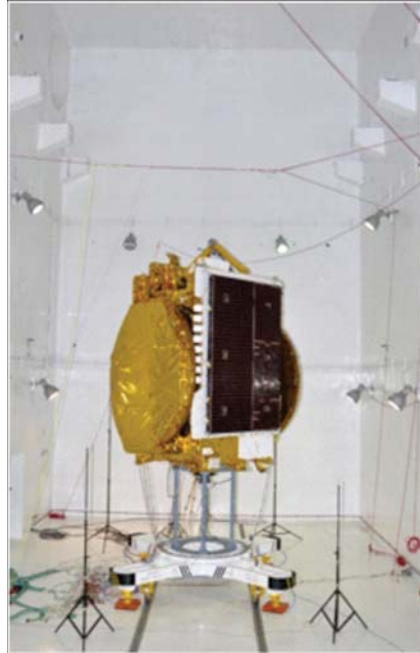


Fig. 7. Spacecraft acoustic test setup

In recent missions with identical spacecraft like in IRNSS series, which are realized in a short schedule and where the spacecraft test camp duration was cut down, a new methodology of vibration and acoustic testing has been adopted. In this methodology, the conventional shaker dynamic characterization tests are skipped and a common test setup in RC for modal test and acoustic test was envisaged [4]. Fig. 8 shows the test setup for combined acoustic and modal test on a spacecraft and Table 3 compares the test mode frequency with the conventional shaker based test values.



Fig. 8. spacecraft modal test setup in RC

**Table 3: spacecraft mode comparison**

Mode Description	Frequency (Hz)	
	Modal survey test	Shaker test
Dolly flexing mode-lateral	11.3,11.9	.....
Lateral bending along Z axis	23.43	25.5
Lateral bending along Y axis	24.03	25.8
Solar panel modes	57.3,66,71	57.1,67,70
CCR bracket mode	62,66	65.8
TTC antenna mode	61	61
Longitudinal mode (X)	---	70.6,77.3
LAM mode	39,40	39.0,39.1

### 2.3 Shock test

Shock loads are induced during the flight events such as separation of rocket stages, heat shield separation and ejection of spacecraft. Also the appendage deployment mechanism which employ pyrocutters do generate local high shock levels. Most of the shocks are generated by the pyrocutting and is of high frequency content. The spacecraft shock specification by PSLV is 1500 g upto 5000 Hz. Shock tests are generally conducted on spacecraft (flight or structural model) which require simulation of actual pyrocutting event. Fig. 9 shows the clamp band release shock test setup. Spacecraft shock test is expensive and involves participation of different agencies. In some cases, a shock characterisation test is carried out, in which possible highest shock level are applied and the corresponding shock transfer functions along the spacecraft are obtained. These transfer functions are extrapolated to estimate the shock levels at various zones on the spacecraft.

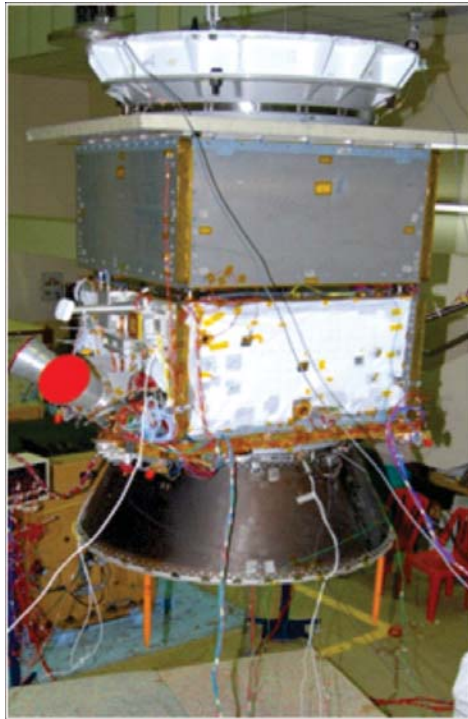


Fig. 9. spacecraft clamp band release shock test setup

Alternately, a simplified "hammer tap test" method is developed at ISAC [5], wherein the shock characteristics can be experimentally obtained with reasonable accuracy upto 2000 Hz without using a pyrocutter. A low level high frequency shocks are generated by the hammer tap at the spacecraft interface. This method simulates the pyrocutting shock and the shock characteristics can be obtained at an early stage of the spacecraft assembly without the requirement of a separate test setup. Fig. 10 shows comparison plots of shock transfer function at a location on spacecraft obtained from the hammer tap test and the conventional shock test.

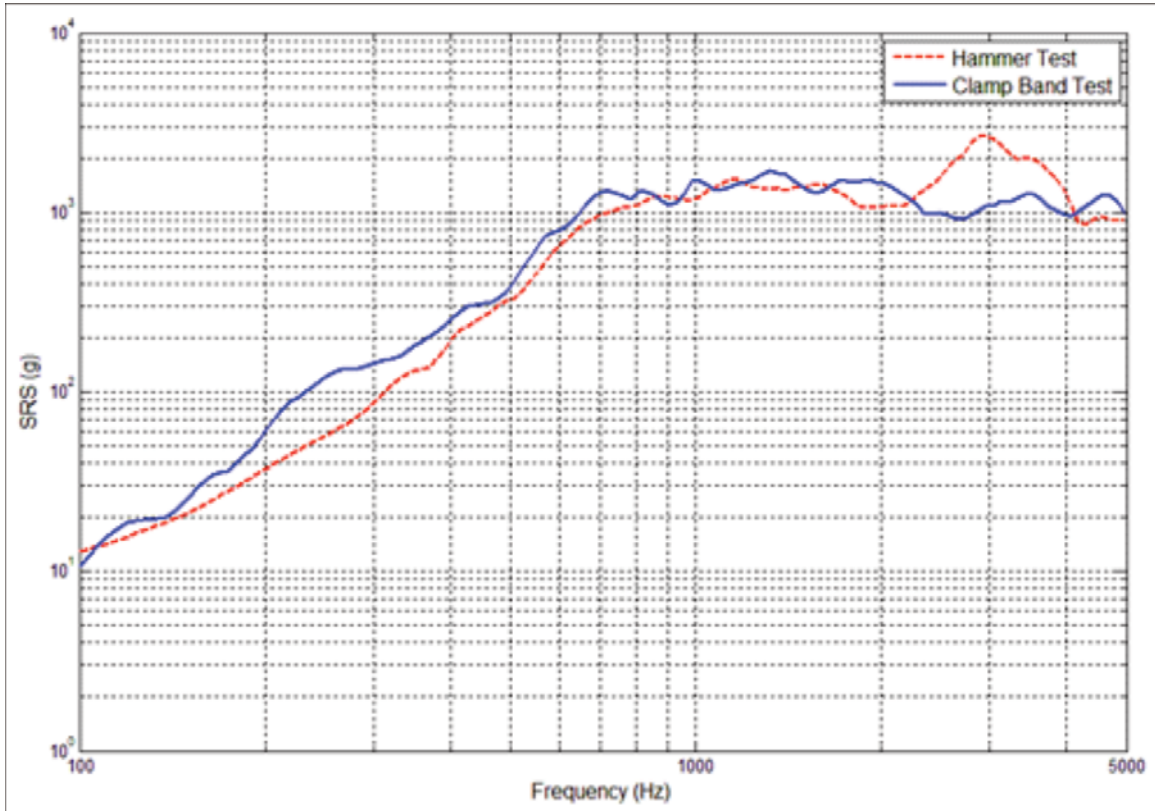


Fig. 10. Shock responses plots from CBRT and hammer test

### 3. CONCLUSION

The present day challenge is to make the spacecraft dynamic testing more efficient, so that testing will survive the requirement of faster, better spacecraft realization philosophy. Without testing, the risk of flight failures is too high. Improvements to the spacecraft dynamic test methods in terms of efficiency, accuracy and time reduction are being constantly pursued with the help of expertise and technological advancements.

### 4. REFERENCES

- [1] Sameer Deshpande, M.N.M. Patnaik, S. Shankar Narayan and Vaibhav Mittal, 2014. "Force Measurement Device (FMD) for spacecraft vibration test", *Journal of spacecraft technology*.
- [2] T.D. Scharon, 1997. "Force limited vibration testing monograph", NASA Reference publication, RP-1403.
- [3] Jean-Michel LE DIGOU, 1998. "Micro-vibration measurements on SPOT 4, Results of the micromedy experiment", proceedings European conference on spacecraft structure, material and mechanical testing, Braunschweig, Germany.

- [4] Sameer Deshpande, M.N.M. Patnaik and S. Shanakar Narayan, 2014. "Modal survey test on flight spacecraft in conjunction with acoustic qualification", *National seminar on Aerospace structures and Technologies*.
- [5] M.N.M. Patnaik, S. Shankar Narayan, Vaibhav Mittal and Sameer Deshpande, 2015. "Comparison of shock characteristics by clampband release and hammer tap test on spacecraft", *Journal of spacecraft technology*.

# A novel hybrid passive study on reduction of aircraft cabin-floorboard vibro-acoustic interaction

N. Chandra\*, B. Balakrishnan and S. Raja  
CSIR-National Aerospace Laboratories, Bangalore 560017  
\*e-mail: nchandra@nal.res.in

(Received: 18.07.2017; Accepted: 03.08.2017)

## ABSTRACT

Cabin noise control has gained a great deal of interest in the design of modern aircraft. A large component of low frequency noise in aircraft is attributed to the dynamic interaction of structural members with fluid medium. A few vibration modes of flexible panels of an aircraft couple significantly with fuselage cavity modes and radiate the noise efficiently. This paper describes an experimental/numerical methodology to identify the vibro-acoustic interaction of aircraft cabin with floorboard panels and a novel approach for the reduction of structure borne interior noise using constrained layer damping (CLD) patches and melamine foam. A typical segment of fuselage with floorboard was fabricated with radial and longitudinal stiffeners and the experiment was conducted by coupling it to a receiving cavity. The free-free boundary condition was simulated by placing the fuselage on partially inflated tubes and the soft sponge at the interface. Modal test was conducted on the fuselage to identify the structural modes. Cavity modes of the cabin were identified by acoustic modal test using calibrated acoustic source and an array of microphones. Both structural and acoustic modes were compared with a numerical simulation. Strongly coupled vibro-acoustic modes were then identified by comparing structural and acoustic modes. The interaction of the floorboard with the fuselage (receiving cavity) was studied by placing the source at the bottom cavity (source cavity) and by comparing the sound pressure levels between the source and the receiving cavity. A typical low frequency spectrum of noise from 0 to 250 Hz was simulated and fed through the acoustic source. The noise inside the cabin was reduced by reducing the vibration of strongly coupled panel modes using optimally placed CLD patches. The layout of CLD patches was logically chosen by identifying the hot spots of the panels using modal test results. The higher segment of simulated low frequency noise was further efficiently reduced by planting a layer of 10 mm melamine foam all around the fuselage inner surface. An overall level of 7 dB reduction was achieved by using few CLD patches and a thin melamine coating.

## 1. INTRODUCTION

The signature of noise spectra in an aircraft is a combination of structure-borne, air-borne and engine noise. The structure-borne noise is low frequency in nature and originates from the vibration of flexible parts of the fuselage. The air-borne noise is high frequency in nature and originates from the interaction of fluid medium with the structure. Numerous researchers have investigated various noise reduction approaches. The methods considered include structural modifications, passive damping and active vibration/noise control. Most of the conventional passive techniques as detailed in [1] [2] and [3] such as added mass,

damping, stiffness and system modification through redesign have proved unsatisfactory in many applications for several reasons. These methods imply a significant mass increase, do not work well at low frequencies and it is difficult to predict their effect except in some simple cases. The active methods are Active Vibration Control (AVC), Active Noise Control (ANC) and a recent approach which is proven efficient and adopts smart technology is Active Structural Acoustic Control (ASAC). In ANC [4] [5] and [6] several secondary sources are used to attenuate the radiated noise field but the effect is very local. Active Vibration Control (AVC) studied by several authors like [7] [8] and [9] emphasizes the reduction of the structural vibration disturbance but does not guarantee that the associated noise radiation will be reduced. ASAC approach as embodied in the research of Fuller and his co-workers [10] and [11], is to use control inputs applied directly to the structure in order to reduce or change the vibration distribution with the object of reducing the overall sound radiation.

Passive damping treatments are widely used in engineering applications in order to reduce vibration and noise radiation [12,13]. Constrained Layer Damping (CLD) is a treatment to control the vibration of a structure by bonding a layer of damping material between the structure's surface and an additional elastic layer (that is, the constraining layer), whose relative stiffness is greater than that of the damping material, so that energy is dissipated through cyclic deformation of the damping material, primarily in shear. Plenty of research has been done in the field of passive measures to reduce the noise emission, for instance Hendriks [14], Hekma Wierda [15], Roozen [16] and Huang [17]. Some examples of passive measures are sound absorbing materials like glasswool and foam, reflecting wall panels and passive constraining layer damping (PCLD) treatments. Polydamp Hydrophobic Melamine Foam [PHM] provides excellent acoustical absorption and thermal conductivity and meets the most stringent FAR 23 and 25 flame, smoke and toxicity requirements, including FAR 25.856 radiant panel testing and all other vehicle standards is considered in this paper as a potential candidate combined with the CLD patches. This hybrid approach provides a greater level of noise reduction compared to classical passive methods.

## 2. EXPERIMENTAL SETUP

### 2.1 Test article

The test specimen was fabricated with 1.5 mm thick aircraft quality aluminum with a length of three meters and a radius of one meter. It was made with radial and longitudinal stiffeners representing a half portion of a typical turboprop aircraft. The bottom flat portion of the specimen was a representation of a floor board. Both ends of the specimen were covered with semi-circular plywood board of 12.5 mm thickness. The three-dimensional view of the specimen is shown in Figure 1-a.

### 2.2 Support system and receiving cavity

The specimen was supported on four tubes inflated to half of their normal pressure rating to simulate the free-free boundary condition. A representative of the cabin is realized through a receiving chamber and the

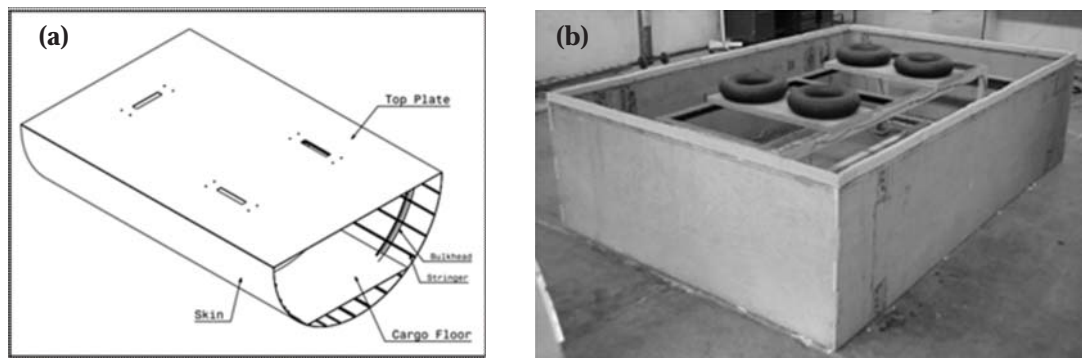


Fig. 1. (a) segmented fuselage section (b) support system and receiving cavity



supporting structure, inflated tubes and the wooden box is shown in Figure 1-b. Four tubes were kept on a rigid steel frame having a height of 750 mm. In order to study the vibro-acoustic interaction between the two acoustic cavities the bottom cavity was fabricated with 25 mm thick plywood boards. The interfacing edges between the two cavities were filled with soft sponge. The size of the bottom cavity was 3 meters in length, 2 meters in width and 0.75 meters in height.

### 3. FINITE ELEMENT ANALYSIS PROCEDURE

Finite element modelling of the fluid (interior cavity) and the fuselage (structure) was carried out using HYPERMESH. The aluminum fuselage was modelled using shell elements available in NASTRAN® (CQUAD4). Aluminum fuselage consists of skin, bulkhead, stringers, floor board and luggage board. The fluid has been numerically modelled using solid elements available in NASTRAN® (CHEXA and CPENTA). Fluid grid points were defined on GRID bulk data entry by specifying a value of -1 in field 7. The MAT1 entry defines the material property entry for structure and the MAT10 entry defines bulk modulus and mass density properties for fluid in NASTRAN®. The finite element model is shown in Figure 2. The properties of the structure and the fluid are given in Table 1. Normal mode analysis was carried out for fluid and structure. Separately to find the natural frequencies and mode shapes. The fluid degrees of freedom are not constrained.

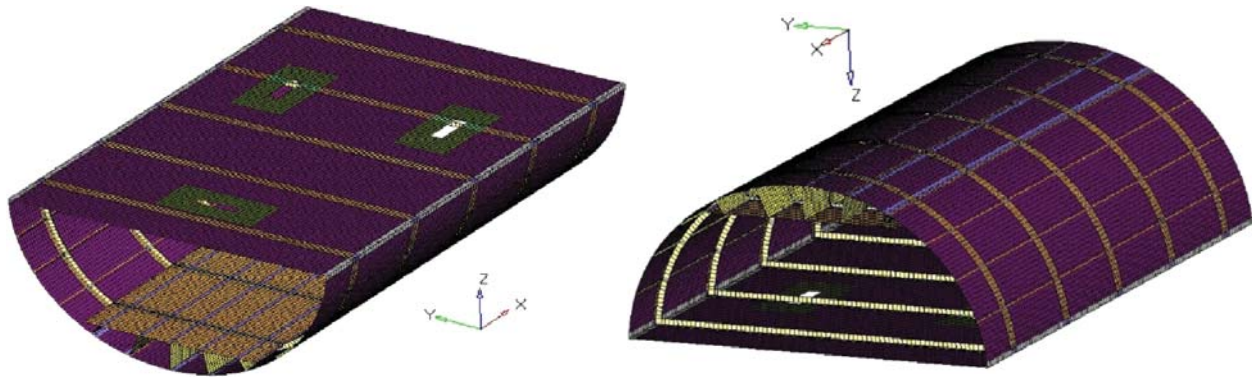


Fig. 2. Finite element model of segmented half fuselage

### 4. EXPERIMENTAL METHODOLOGY

#### 4.1 Modal Testing

The objective of conducting modal test is to identify the modal parameters experimentally. The modal parameters are natural frequencies, modal damping and mode shapes. Single input multi output (SIMO) technique was adopted as modal test methodology. LMS SCADAS III multi-channel data acquisition system

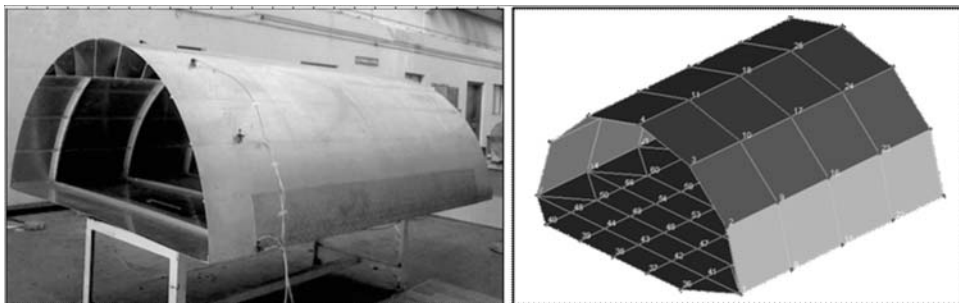


Fig. 3. Modal test setup and response locations

was used as hardware and Test.Lab software was used for data acquisition and analysis. Seven numbers of tri-axial accelerometers were used for response measurement on the cylindrical surface. The fuselage was divided into seven stations and sensors were moved accordingly to each station for data collection. Ten numbers of uniaxial accelerometers were mounted on the bottom panels in Z direction. A total of 86 response locations were identified for acceleration measurement. The input force was given through instrumented impulse hammer. The modal test setup and the response locations are shown in Figure 3. A frequency band of 0-256 Hz with spectral lines of 512 was used. An exponential window for response and a rectangular window for force were set. The data was measured in the form of Frequency Response Function (FRF) for each location. A sum FRF was then computed from all the FRFs and modal parameters were estimated by Polymax® based curve fitting technique with a model order of 64.

**Table 1. Properties of the structure and the fluid**

Properties of structure			Properties of fluid		
Young's Modulus	$72 \times 10^9$	Pa	Speed of sound	343	m/s
Poisson's Ratio	0.33	--	Bulk Modulus	0.14	MPa
Mass Density	2800	Kg/m <sup>3</sup>	Mass Density	1.25	Kg/m <sup>3</sup>

**4.2 Vibro-acoustic characterization**

**4.2.1 Measurement of vibro-acoustic modes:**

PROSIG P2080 dynamic data acquisition system with 16 channels of ADCs and 4 channels of DACs was used for acoustic data measurement. Acquisition V4 software for test configuration and data acquisition and DATS signal processing software for data processing was used. 12 numbers of pre-polarized condenser microphones were used for acoustic response measurement as shown in Figure 4. A sophisticated LMS low-mid frequency volume acceleration sound source was used as acoustic source. The source is capable of high noise levels up to 96 dB (at a distance 1m from source) with frequency bandwidth of 10-800 Hz with an inbuilt calibrated volume acceleration sensor for measuring the source strength directly. DYNACORD S900 standard precision power amplifier was used to drive the signals to the sound source. In this study the source was kept in the bottom cavity and excited with a burst random signal of 0-250 Hz bandwidth. The drive point was kept at microphone location M7. The response of volume acceleration sensor is measured as excitation input in m<sup>3</sup>/(m/s<sup>2</sup>) similar to force transducer in structural modal testing. The microphones were assigned a spatial direction.

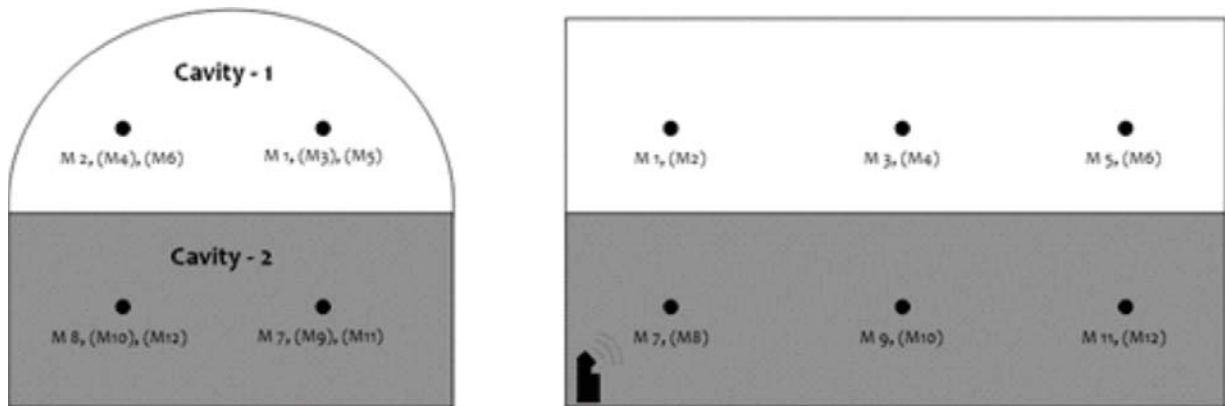


**Fig. 4. Microphones and acoustic source locations**

### 4.3 Sound transmission loss characterization

It is important to understand the noise transmission characteristics of the two cavities before attempting to control. With this focus in mind, the acoustic source was kept in one cavity and the noise transmitted to the other cavity is quantified. This study was conducted by locating the sources in cavity-1 and cavity-2 successively. The simulated aircraft noise spectrum was fed to the noise source through a power amplifier. The response of the microphones was acquired in time domain for approximately 60 seconds. These signals were then processed in Prosig DATS signal processing software. The RMS harmonic level is estimated from the time response. The human ear response matches with the A weighting scale and it is the industry standard. A weighting was applied in frequency domain to the RMS harmonic spectrum. 1/3<sup>rd</sup> octave analysis was carried out for the A weighted spectrum. All the microphones were calibrated before the measurement using a hand held calibrator.

### 4.4 Noise control studies

The control of noise inside the bottom half fuselage is envisaged through passive technique using constrained layer damping and melamine foam. In this study aircraft quality CLD strip of 3M trade mark was used. The CLD strips were cut into two different sizes of 100 × 100 mm and 200 × 100 mm and were optimally placed based on the results of modal test. The hot spots of all the panel modes were overlaid and strips were placed at the extreme region of hot spot where the modal strain energy is more.

## 5. RESULTS & DISCUSSIONS

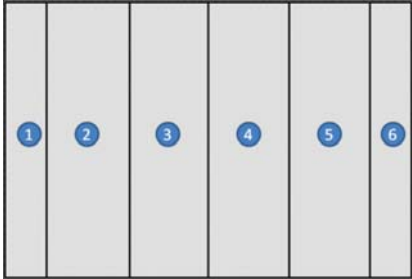
### 5.1 Structural and acoustic modes

Structural and acoustic modal analysis were carried out using finite element analysis, to understand the structural and cavity dynamic characteristics. The analysis provided the baseline data for experimental setup in terms of frequency range and nature of modes. The modes obtained through experiment are categorized into three groups; rigid body modes, global elastic modes and the panel modes. A comparison between experimental frequencies and analytical frequencies is made and a good comparison has been found. The structural frequency and damping value of each mode are tabulated in Table 2. The measured acoustic modes of both the cavities are tabulated in Table 3. A total of 18 modes are identified in the low frequency segment from 0-250 Hz

**Table 2. Structural modes**

Mode Number	Exp.	Frequency (HZ) FEM	Description
<b>Rigid Body Modes</b>			
1	1.83	--	Roll
2	2.65	--	Pitch
3	4.26	--	Translation - Z
<b>Global Elastic Modes</b>			
4	5.18	--	Breathing in lateral direction
5	12.24	13.99	Breathing in vertical direction
6	16.80	15.08	Breathing with roll
7	24.76	22.06	Entire bottom panel bending with shell rotation
8	30.84	31.69	Entire bottom panel bending with shell pitching
9	46.63	45.58	Twist

Panel Modes			
10	65.65	65.98	Panels 1, 5 & 6
11	73.02	73.32	Panel 2
12	79.84	78.93	Panel 1
13	105.19	106.12	Panels 3 & 4
14	113.79	113.55	Panel 6
15	124.80	124.57	Panel 3
16	130.73	--	Panel 1 & 2
17	140.89	--	Panel 2 & 4
18	215.77	215.79	Center of panel 3 & 4
19	231.27	230.76	Panels 2, 3 & 4



The diagram shows six vertical panels arranged in a row, labeled 1 through 6 from left to right. Each panel is represented by a grey vertical bar with its corresponding number inside a blue circle.

**5.2 Identification of coupled modes**

It is observed that the rigid body and global elastic modes fall within 0-50 Hz bandwidth and does not couple with acoustic modes. It is also appealing to note that the sound field with less than 50 Hz is less audible to human ears (The threshold of hearing is 20 Hz!). It then shows that most of the panel modes contribute to the interaction of fluid-structure and generates structure borne noise. A close observation was made between the cavity modes and the panel modes and a list of strongly coupled modes and the corresponding modeshapes are given in Table 4 & Figure 5, respectively.

**5.3 Sound transmission loss without any treatment**

The low frequency spectrum of typical turboprop aircraft noise signature was simulated using signal generation tool of DATS signal processing software. The low frequency component up to 800 Hz generally contains several harmonics over a random signal. The harmonics correspond to the BPF of the propeller with 20-30 dB above random and the random part corresponds to the flow induced and other components of noise. In the present study, a several Gaussian random signals of different band width and amplitude within 0-800 Hz were generated and combined to form hill shape base random signal. Three harmonic signals of 90, 180 and 270 Hz were generated and superimposed. The base random and superimposed harmonic signals are combined to get the final spectrum. OASPL was measured at each microphone location in both the cavities and the amount of sound level reduction is tabulated in table 5. Up to 12 dB reduction in OASPL is noticed without any control treatment.

**Table 3. Acoustic modes**

Cavity 1										
Mode No	1	2	3	4	5	6	7	8	9	10
Frequency (Hz)	44.6	49.28	63.41	73.47	77.29	87.81	95.27	105.29	112.88	123.40
Mode No	11	12	13	14	15	16	17	18		
Frequency (Hz)	128.22	150.07	159.12	179.58	184.0	201.33	216.15	233.27		
Cavity 2										
Mode No	1	2	3	4	5	6	7	8	9	10
Frequency (Hz)	45.36	49.47	63.61	73.83	77.36	87.98	96.97	106.72	115.70	122.38
Mode No	11	12	13	14	15	16	17	18		
Frequency (Hz)	132.46	150.76	157.79	180.69	188.17	199.65	216.94	233.38		

**Table 4. Vibro-acoustic modes**

Coupled Frequency (Hz)											
Mode No	1	2	3	4	5	6	7	8	9	10	11
Panel	46.63	65.65	73.02	79.84	105.19	113.79	124.80	130.73	140.89	215.77	231.27
Cavity 1	44.60	63.41	73.47	77.29	105.29	112.88	123.40	128.22	150.07	216.15	233.31
Cavity 2	45.36	63.61	73.83	77.36	106.72	115.70	122.38	132.46	150.76	216.94	233.38

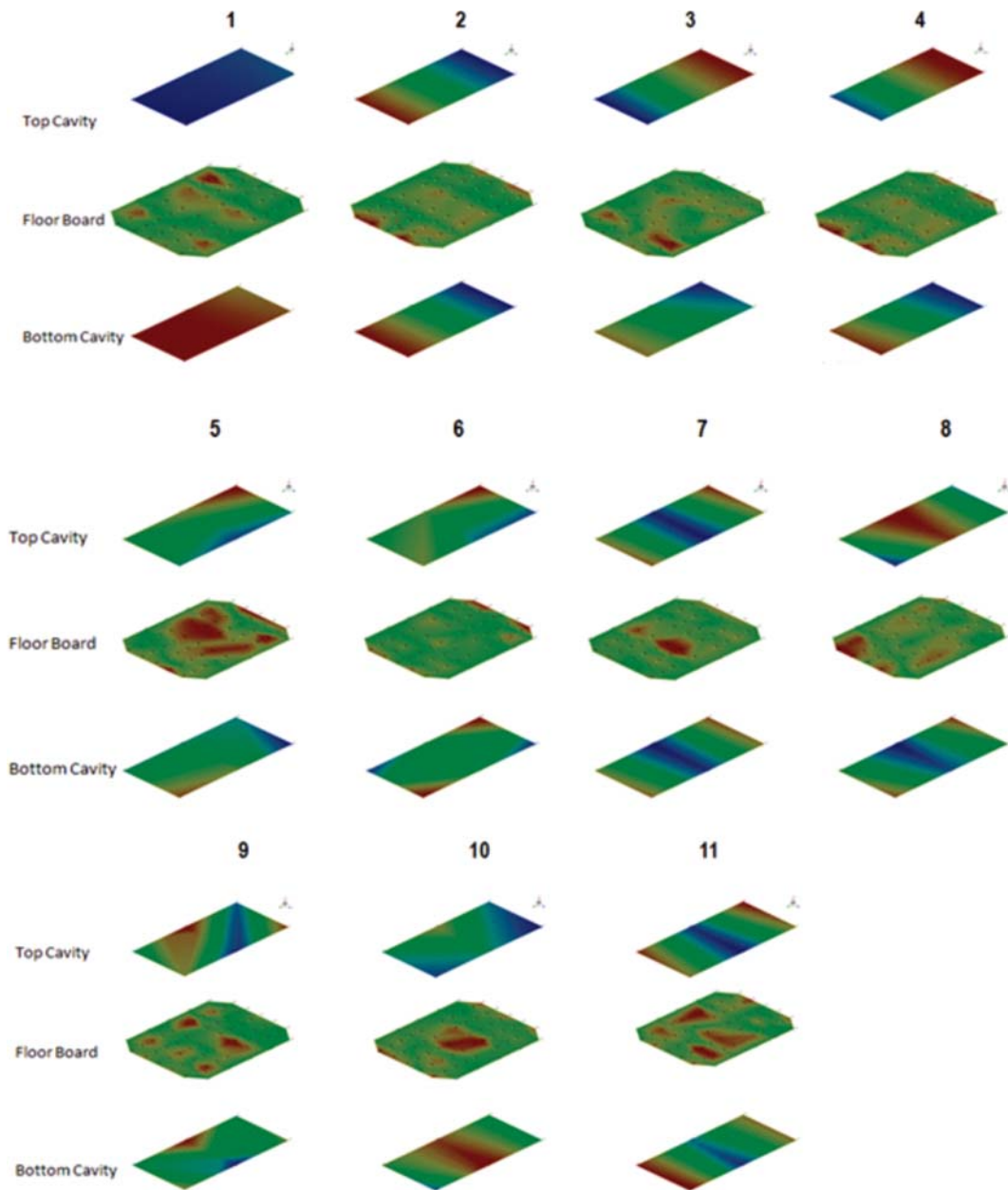


Fig. 5. Mode shapes of vibro-acoustically coupled modes

**Table 5. Sound reduction without any control**

OASPL (dBA), 0-250 Hz				
Cavity 2		Cavity 1		Reduction
Mic No	OASPL	Mic No	OASPL	OASPL
7	89.10	1	79.60	9.50
8	86.50	2	76.10	10.40
9	87.70	3	79.60	8.10
10	88.10	4	79.10	9.00
11	85.5	5	77.80	7.70
12	88.50	6	79.80	8.70

**5.4 Vibro-acoustic control using constrained layer damping**

The reduction of vibration levels of strongly coupled panel modes with the fuselage modes using patches of CLDs is presented in this study. In this study aircraft quality CLD strip of 3M trade mark was used. The CLD strips were cut into two different sizes of 100 × 100 mm and 200 × 100 mm and were optimally placed based on the results of modal test. The hot spots of all the panel modes were overlaid and strips were placed at the extreme region of hot spot where the modal strain energy is more. The schematic of the CLD placement on the floor board panel is shown in Figure 6. The CLD patches were placed only on the floor board panel since the panel modes are well coupled with cavity modes. The 1/3<sup>rd</sup> octave spectrums of SPL are given in Figure 7. The SPL intensity plot is shown in Figure 8. A spatial average of all the six microphones in each cavity is considered as a metric to measure the noise reduction. A 4.58 dB reduction was observed through optimal placement of CLD patches.

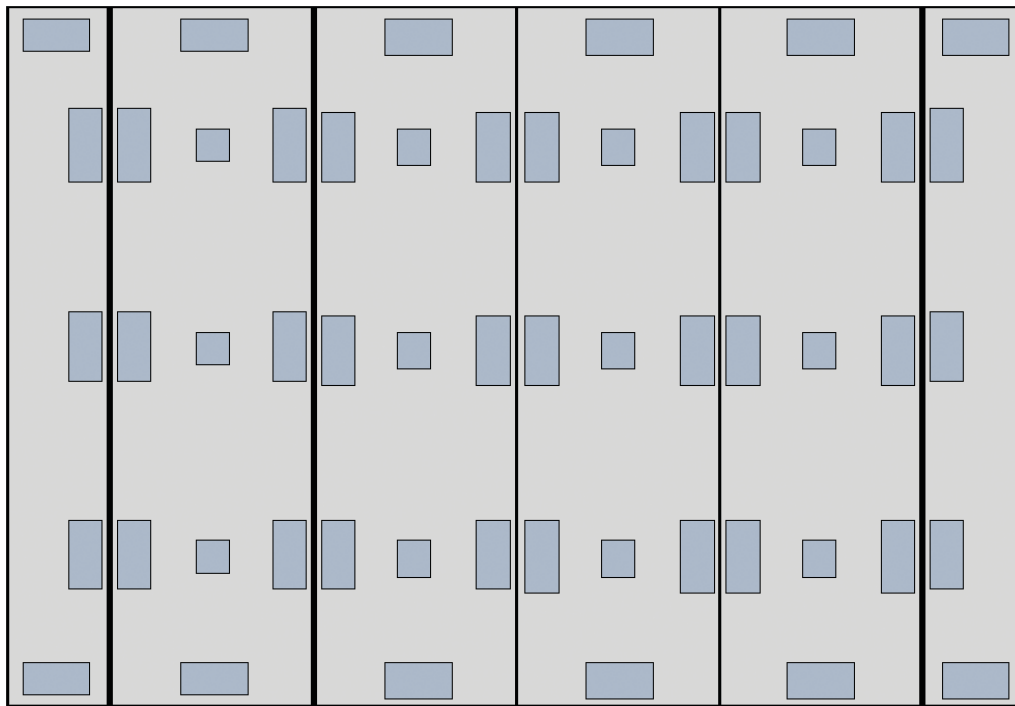


Fig. 6. Optimal placement of CLD patches on floor board panels

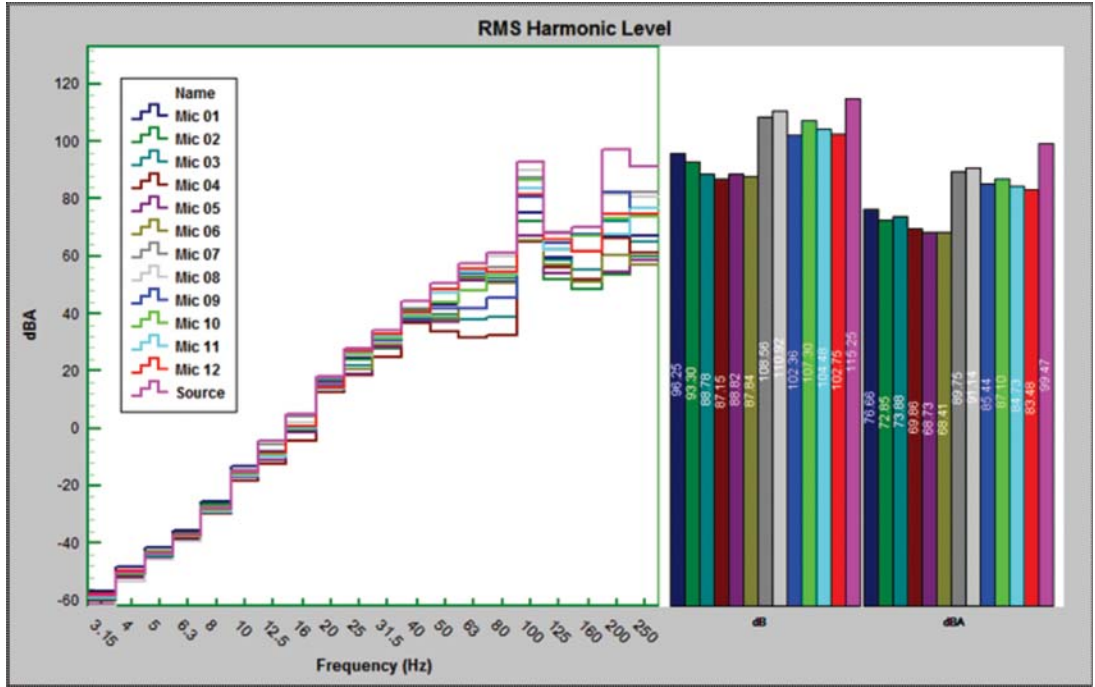


Fig. 7. 1/3<sup>rd</sup> octave spectrum and OASPL with CLD

### 5.5 Vibro-acoustic control using hybrid CLD and Melamine foam concept

Polydamp Hydrophobic Melamine Foam [PHM] is an ideal lightweight acoustical and thermal insulation product for aircraft, aerospace, transportation, marine, medical, power generation and architectural applications where resistance to water penetration and retention, low flame propagation and minimal smoke generation are requirements. In this study, melamine foam of thickness 10 mm was installed all around inside the fuselage. The melamine foam integration inside the fuselage is shown in Figure 9. An additional reduction of 2.35 dB was observed through 10 mm melamine foam. In total, CLD+ melamine foam contributed for a reduction of 6.93 dB. The SPLs for CLD + Melamine foam case is shown in Figure 10.

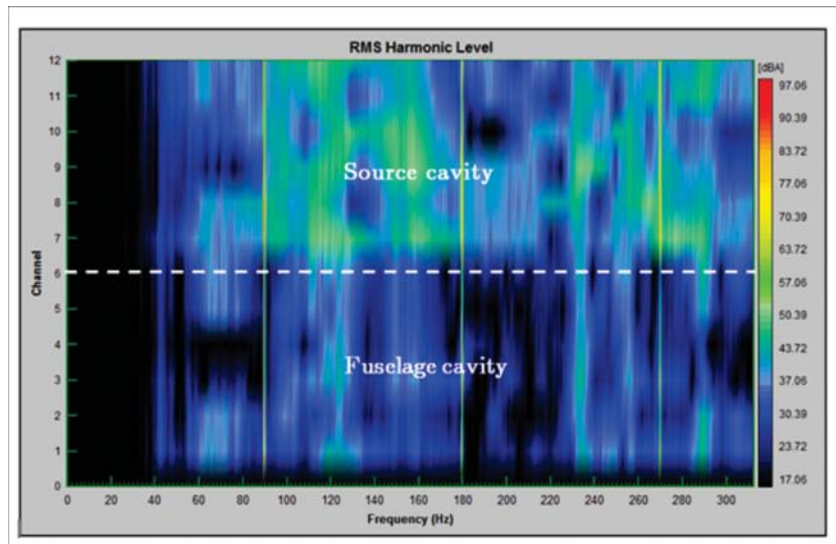


Fig. 8. SPL intensity plot with CLD patches



Fig. 9. Melamine foam installed segmented fuselage

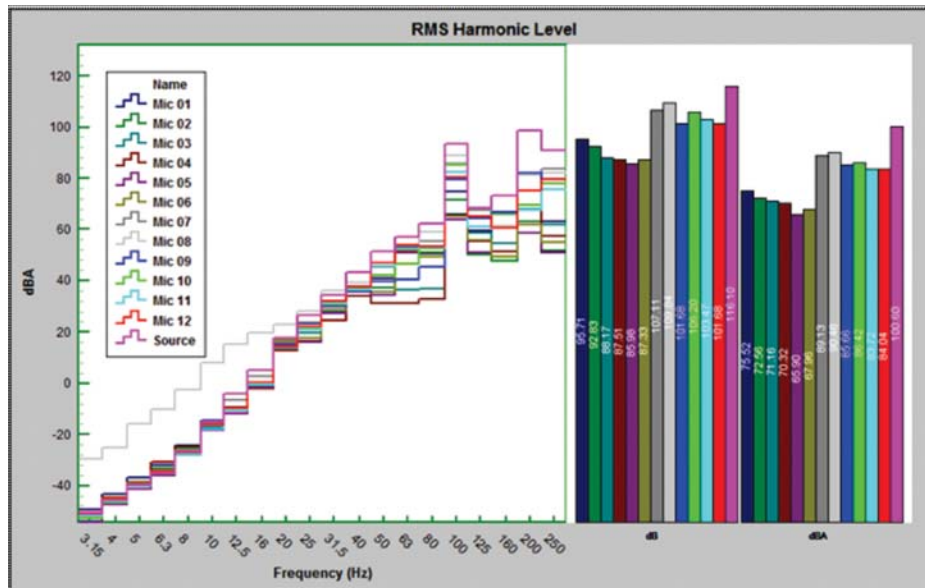


Fig. 10. 1/3<sup>rd</sup> octave spectrum and OASPL with CLD and melamine foam

## 6. CONCLUSIONS

Vibro-acoustic characterization and noise control study was conducted on a 3 meters long half fuselage model to understand the interaction of floorboard vibration. Vibro-acoustic characteristics of the fuselage structure have been experimentally evaluated. A detailed study of strongly coupled structural modes with fluid modes was carried out. This study revealed that most of the panel modes interact strongly with the fluid modes. Based on these results, an attempt was made to control the noise through vibration control using constrained layer damping strips. The low frequency part of turboprop aircraft was simulated and generated through calibrated acoustic source. The damping strips were optimally placed based on the modal test results on the floor board panels and the noise was generated in the bottom cavity. A spatially averaged 4.58 dBA reduction was observed in the fuselage cavity with CLD. Subsequently, 10 mm thick melamine foam was put on the complete inside surface of the fuselage walls in addition to CLD on the floorboard panels. A spatial average of 6.93dB reduction was achieved with CLD and foam.



## 7. ACKNOWLEDGEMENTS

The authors would like to greatly acknowledge the scientists of Impact and Structural Crashworthiness Group for providing the fuselage. The technical support provided by the staff of Dynamics and Adaptive Structures Group is greatly acknowledged. The authors are indebted to the Director of National Aerospace Laboratories and Head, STTD for supporting the above work under the NCAD project.

## 8. REFERENCES

- [1] L.L. Beranek, 1993. Acoustics, American Institute of Physics, Inc.
- [2] L.E. Kinsler, A.R. Frey and A.B. Coppens, J.V., 1982. *Sanders Fundamentals of Acoustics*, third edition, John Wiley & Sons, Inc.
- [3] L.L. Beranek, 1988. Noise and Vibration Control, Institute of Noise Control Engineering.
- [4] P. Lueg, 1936. U S Patent No. 2043416. Process of silencing sound oscillations.
- [5] J.E. Efwocs Williams, 1984. *Anti-Sound*, Proceedings of royal Society of London A35, 63-88.
- [6] P.A. Nelson and S.J. Elliot, 1992. *Active Control of Sound*, Academic Press, London.
- [7] C.R. Fuller, S.J. Elliott and P.A. Nelson, 1996. *Active Control of Vibration*. London: Academic Press, Inc.,
- [8] C.H. Hansen and S.D. Snyder, 1997. *Active Control of Noise and Vibration*, London: E & FN SPON,
- [9] A. Preumont, 1997. *Vibration control of active structures: An introduction*, Netherlands, Kluwer Academic Publishers.
- [10] C.R. Fuller, 1985. Experiments on reduction of aircraft interior noise using active control of fuselage vibration, *J. Acoust. Soc. Am.*, **78**(S1), S79.
- [11] C.R. Fuller, 1988. Analysis of active control of sound radiation from elastic plate by force inputs, *Proceedings of inter noise '88*, Avignon, **2**, 1061-1064.
- [12] A.D. Nashif, D.I.G. Jones and J.P. Henderson, 1985. *Vibration Damping*, John Wiley & Sons.
- [13] C.T. Sun and Y.P. Lu, 1995. *Vibration Damping of Structural Elements*, Prentice Hall PTR, Englewood Cliffs, New Jersey,
- [14] A.C. Hendriks, 2004. *Passieve demping van mechanische systemen*, MSc thesis, TU/e and Philips,
- [15] S.C. Huang, D.J. Inman and E.M. Austin, 1996. Some design considerations for active and passive constrained layer damping treatments. *Smart Mater. Struct.*, **5**, 301-313.
- [16] N.B. Roozen, 1998. *Visco-elastic constraining layers applied to the QBC covers of a MRI system*. Philips.
- [17] J.E. Hekma Wierda, 1997. *Vibration control by means of constraining layers*, MSc thesis.

# Influence of acoustic reflection on measurement locations in a large reverberation chamber

**S. Murugan**

*Acoustic Test Facility, National Aerospace Laboratories, Neelakantan Wind Tunnel Center  
Campus, Bangalore 560 037, India,  
e-mail: murugan@nal.res.in*

(Received: 19.07.2017; Revised: 27.07.2017; Accepted: 02.08.2017)

## ABSTRACT

High intensity acoustic testing is performed on the spacecraft and launch vehicle subsystems in large reverberation chambers. Acoustic measurements of such tests are influenced by the reflection of sound waves from the rigid walls of the chamber. It is therefore important to understand the reflection characteristics of the sound wave to arrive at the optimum positioning of microphones near the chamber walls for acoustic measurements. This paper deals with the sound pressure level (SPL) at various distances from different reflecting planes in comparison with diffused or non-reflecting locations and experimentally verifies the theoretical calculations. This paper also highlights the SPL measurement locations in a reverberation chamber defined by various standards.

## 1. INTRODUCTION

Spacecraft and launch vehicle subsystems are tested in a reverberation chamber as part of their acoustic environment qualification. The uniform diffused acoustic load around the test specimen is affected by the chamber wall reflections. It is important to study the characteristics of this unavoidable interference to arrive at the minimum distance from the walls for positioning the microphones in a reverberant chamber. For testing of launch vehicle subsystems, MIL Standard 1504C (1994) and NASA handbook 7005 (2001), specify the location of the microphone as one half the distance from the test article to the nearest chamber wall, but not closer than 0.5 meters. For general purpose acoustic characterization of noise sources, the standard ISO- 3741 (2010) specifies the microphone location at a minimum of 1-meter distance from any of the surfaces of the room. According to the standard ISO - 3743-2 (1994), no microphone position shall be closer to the surface of the room than a quarter wavelength of the sound corresponding to the lowest octave band in which measurements are made. It has been observed that for the two lower octave bands of 31.5 Hz and 63 Hz, the reflected sound waves significantly affect the measurement when the microphone is positioned at a distance of around 1-meter from the reflecting surface. Earlier, Waterhouse (1958) applied the Rayleigh's formula to estimate the relative power output of a simple source as a function of position near one-, two- and three plane reflectors. This paper applies the Rayleigh's formulas to theoretically arrive at the variation of sound pressure level due to reflection from the surface, edge (a wall and floor) and corner (two adjacent walls and floor) of a reverberation chamber. The sound pressure level is measured within the central ten percent volume of the chamber for a diffused field and at specific distances from the surfaces in a reflected field. The difference in SPL between the diffused and reflecting field is found closely matching with the theoretical calculation

## 2. THEORETICAL CALCULATION OF SPL VARIATION DUE TO SURFACE, EDGE AND CORNER REFLECTIONS

According to Lamb (1931) the sound reflected by the surface is considered to emanate from one or more image sources. In one-plane or surface reflection, the acoustic output of one image source combines with that of the object source and results in variation of power output  $W$  with respect to the free field power output,  $W_f$ . The acoustic image sources of one-plane, two-plane or edge and three-plane or corner reflections are shown in Fig. 1. The variation of power output for surface reflection is given by Waterhouse (1958) :

$$W/W_f = 1 + j_0(x') \quad (1)$$

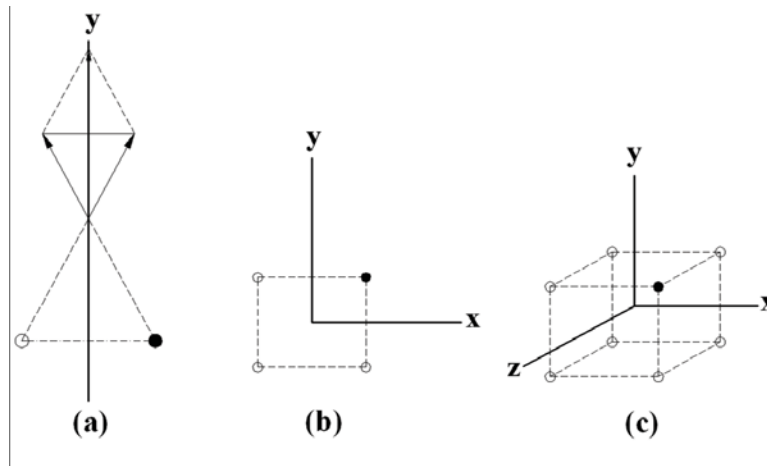


Fig. 1. Acoustic images at (a) surface, (b) edge and (c) corner reflections. (Courtesy: Waterhouse, R.V.)

Where,  $j_0(x')$  is the spherical Bessel function.

$$j_0(x') = (\sin x') / (x') \text{ and } x = 4\pi x / \lambda.$$

Here 'x' is the distance of the object source from the reflecting plane. Same expression is used in this paper to compute the variation in the SPL,  $\Delta\text{dB}$ . Fig. 2 shows  $\Delta\text{dB}$  for typical values of 'x' in terms of wavelength.

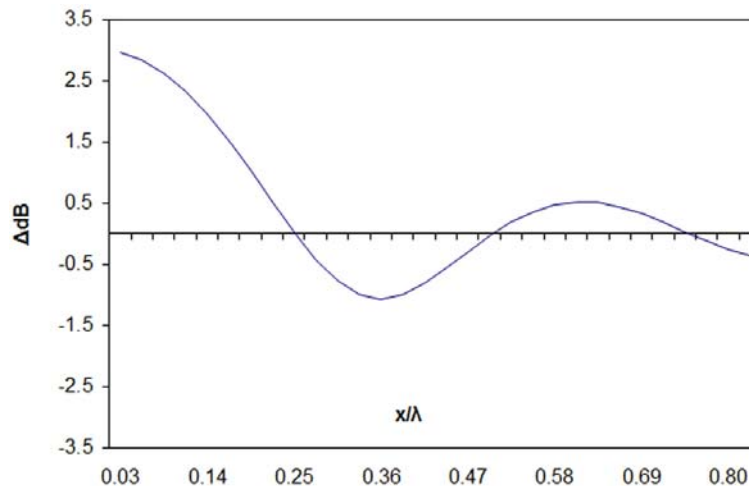


Fig. 2. Theoretical calculation of sound pressure level variation,  $\Delta\text{dB}$  for typical 'x' values from reflecting surface (one-plane).

Similarly, for edge reflections,  $\Delta\text{dB}$  is computed using

$$W/W_f = 1 + j_0(x') + j_0(y') + j_0(\rho') \tag{2}$$

Where  $y' = 4\pi y/\lambda$ ;

$\rho' = 4\pi\rho/\lambda$ ;

$\rho = (x^2 + y^2)^{1/2}$

For corner reflection,  $\Delta\text{dB}$  is computed using

$$W/W_f = 1 + j_0(x') + j_0(y') + j_0(z') + j_0(\rho1') + j_0(\rho2') + j_0(\rho3') + j_0(r') \tag{3}$$

Where  $z' = 4\pi z/\lambda$ ;

$\rho1' = 2k(x^2 + y^2)^{1/2}/\lambda$ , etc., and

$r' = 2k(x^2 + y^2 + z^2)^{1/2}$

Using the above expressions,  $\Delta\text{dB}$  for typical ' $\rho$ ' and ' $r$ ' values for edge and corner reflections are computed in terms of wavelength and plotted as shown in Figs. 3 and 4 respectively.

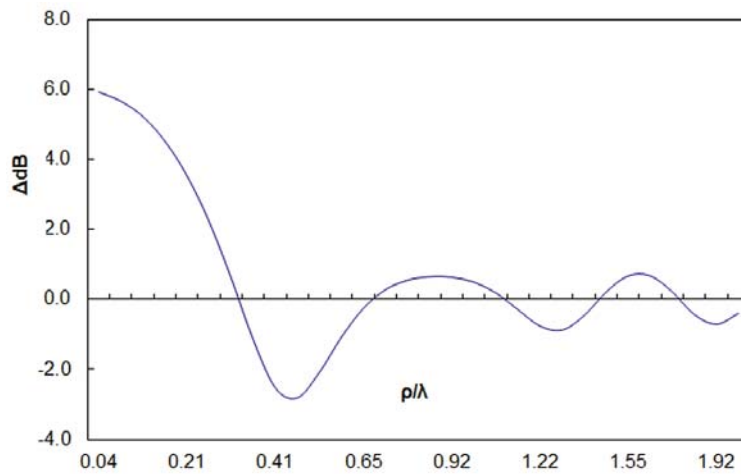


Fig. 3. Theoretical calculation of sound pressure level variation,  $\Delta\text{dB}$  for typical ' $\rho$ ' values from reflecting edge (two-plane).

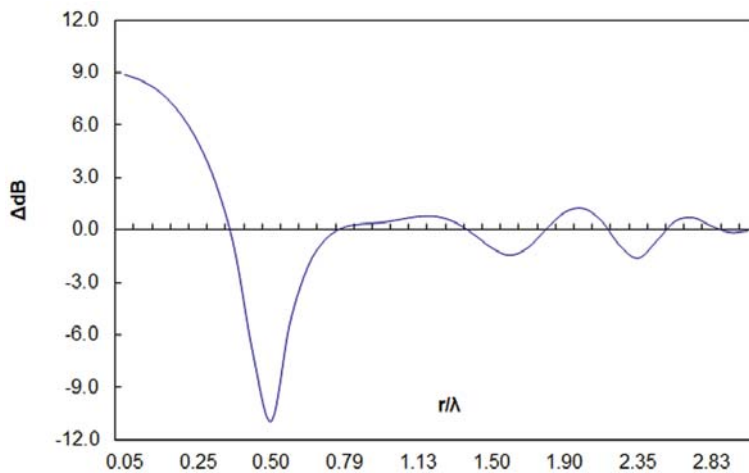


Fig. 4. Theoretical calculation of sound pressure level variation,  $\Delta\text{dB}$  for typical ' $r$ ' values from reflecting corner (three-plane).

### 3 EXPERIMENTAL STUDIES

Measurements were conducted in a reverberation chamber of Volume 1100 cubic meters and size 8.2 (L) x 10.3 (B) x 13.0 (H) meter. Four microphones were positioned in the central ten percent volume of the chamber. The sound field in this volume is considered as diffused without the influence of wall reflections as given by Balakrishna et.al. (1988). The SPL in this volume is within a deviation of +/- 1 dB. The average SPL of the four microphones is used as the reference SPL value for the diffused field. For surface reflection studies, microphones were positioned at a distance 'x' = 0.30, 0.65, 1.2 and 2.0 meters from the wall such that no edge or corner reflection influences the measurement. Figure 5 shows the location of microphones from the surface of a wall. Various acoustic spectra with the overall sound pressure level in the range of 122 to 155 dB were simulated using high intensity acoustic sources mounted on one side of the wall. At 'x' = 0.30 meters,  $\Delta dB$  in octave bands for various acoustic spectra simulation is calculated and averaged as  $\Delta dB_{av}$ . Similarly,  $\Delta dB_{av}$  is calculated for 'x' = 0.65, 1.2 and 2.0 meters. Figure 8 shows the comparison of experimental and theoretical values of  $\Delta dB_{av}$  in terms of wavelength. Similarly, for edge reflection studies, microphones were placed at  $\rho = 0.90$  ( $x = y = 0.64$ ), 1.90 ( $x = y = 1.34$ ) and 2.80 ( $x = y = 1.98$ ) meters from the edge of chamber walls as shown in fig. 6. Figure 7 shows the microphone locations for corner reflection studies. The microphones were placed at  $r = 1.10$  ( $x = y = z = 0.65$ ), 2.30 ( $x = y = z = 1.35$ ) and 3.45 ( $x = y = z = 1.98$ ) meters from the corner of chamber walls as shown in fig. 7.

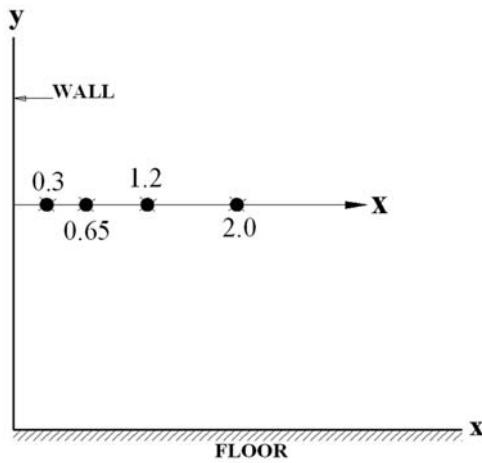


Fig. 5. Microphone locations from a reflecting wall surface (one-plane)

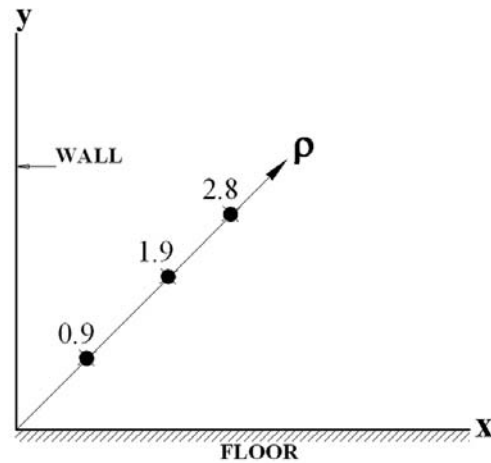


Fig. 6. Microphone locations from a reflecting edge (two-plane).

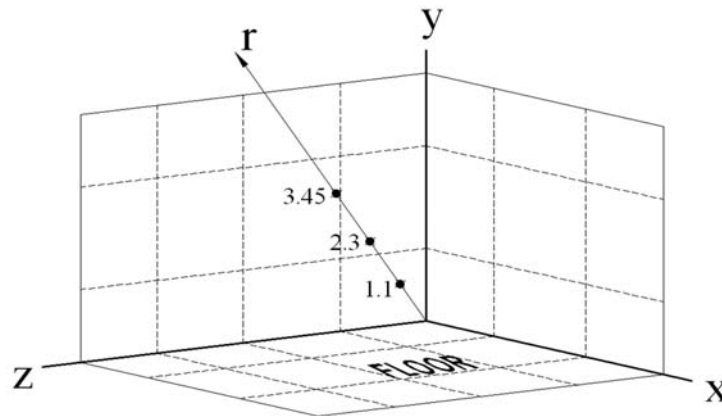


Fig. 7. Microphone locations from a reflecting corner (three-plane)

$z = 2.0$ ) meters from the corner of the chamber. The  $\Delta dB_{av}$  in comparison with diffused field microphones for the above locations for edge and corner reflections are plotted along with theoretical calculations as shown in Figs. 9 and 10 respectively.

#### 4 RESULTS AND DISCUSSION

The SPL variation with respect to the microphone location in terms of wavelength from reflecting planes are calculated theoretically and plotted along with the experimental results as shown in Figs. 8, 9 and 10. Experimental results are in agreement with theoretical calculations. From the experimental data, SPL variation with reference to the diffused field microphones in terms of octave band frequencies is plotted for surface, edge and corner reflection as shown in Figs. 11, 12 and 13 respectively.

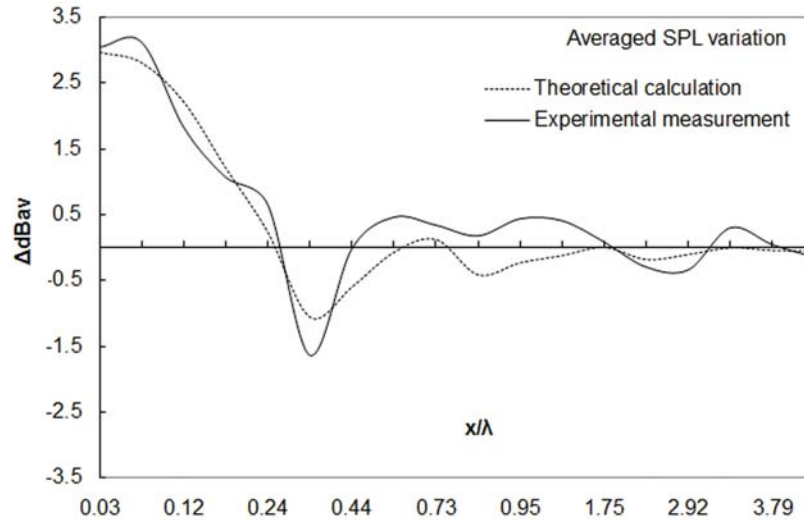


Fig. 8. Averaged SPL variations at discrete distances in terms of wavelength from a reflecting wall surface: Comparison of experimental measurements with theoretical calculation.

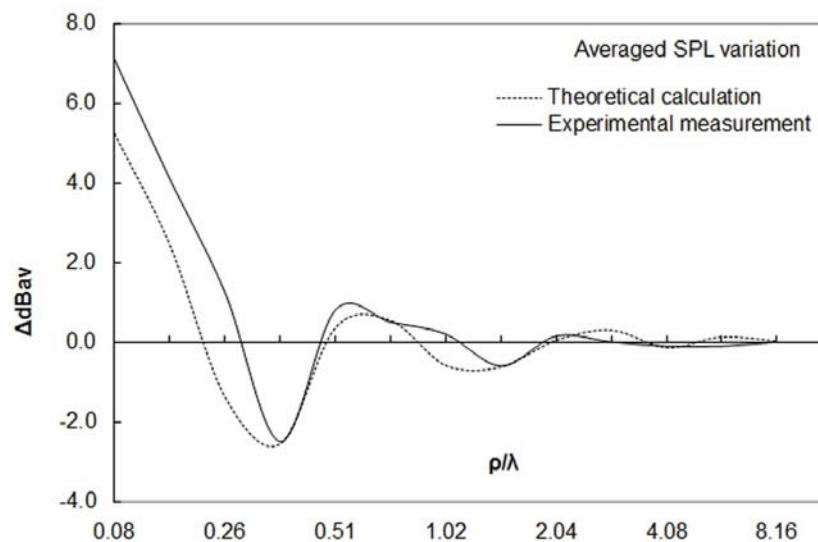


Fig. 9. Averaged SPL variations at discrete distances in terms of wavelength from a reflecting edge: Comparison of experimental measurements with theoretical calculation.

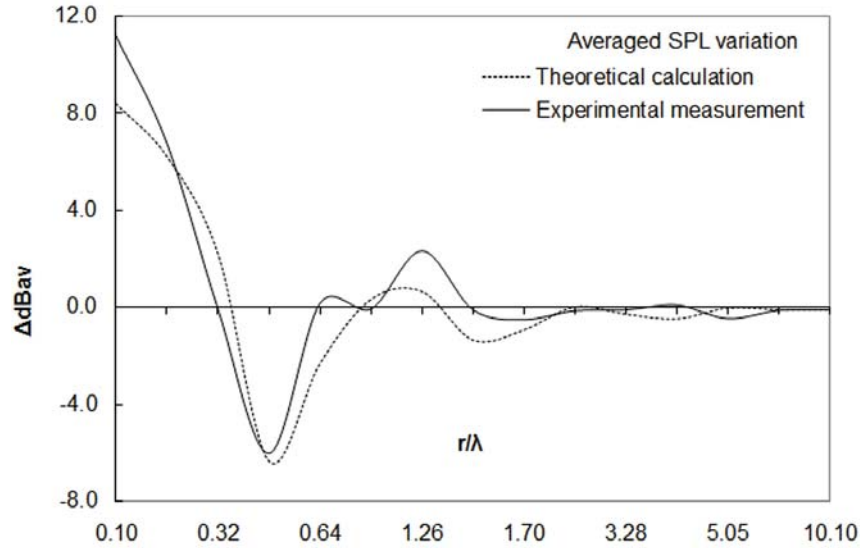


Fig. 10. Averaged SPL variations at discrete distances in terms of wavelength from a reflecting corner: Comparison of experimental measurements with theoretical calculation.

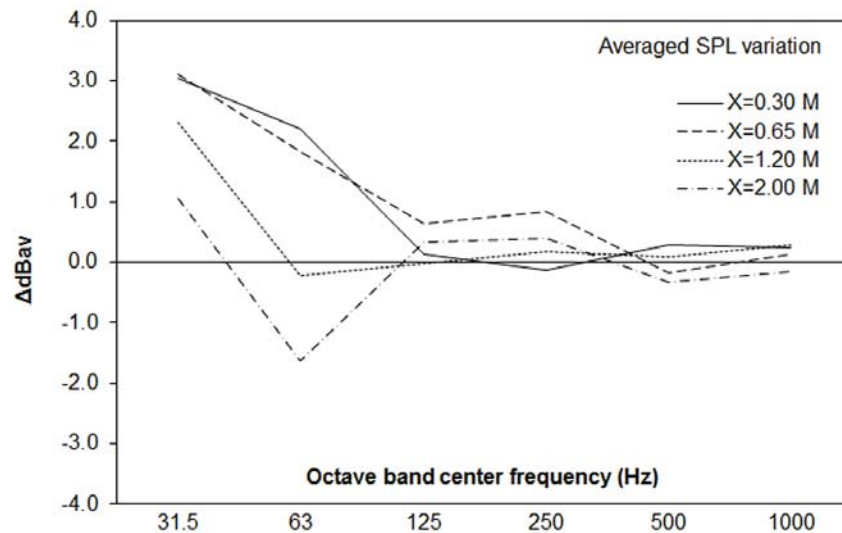


Fig. 11. Averaged SPL variations in octave band frequencies at discrete locations of microphone from a wall surface.

#### 4.1 Surface reflection:

For surface reflection, as shown in Fig. 11, an increase in SPL with reference to the diffused field microphones of the order of 2 to 3 dB is observed in 31.5 Hz octave bands for distances up to 1.2 meters from the wall. No SPL variation is observed in other bands for the same distances. At 2.0-meter distance, SPL is 2 dB less than the diffused field of 63 Hz octave band. According to Waterhouse (1958) this reduction in SPL level is due to the destructive interference of the sound waves occurring in the region  $0.36\lambda$  to  $0.78\lambda$  for all reflecting planes. This was observed in theoretical estimation curves as shown in Figs. 2, 3 and 4. In this case, the reduction is observed at  $0.37\lambda$  as shown in Fig. 8.

#### 4.2 Edge reflection:

In the case of edge reflection, as seen in Fig. 12, an increase in SPL up to 7 dB in 31.5 Hz octave band is observed at a distance of  $\rho = 0.9$  meters. Whereas, in 63 Hz band, SPL is 2.8 dB lower than the diffused field due to the interference of the sound wave at a distance  $\rho = 1.9$  meters, *i.e.*, is  $0.35\lambda$ .

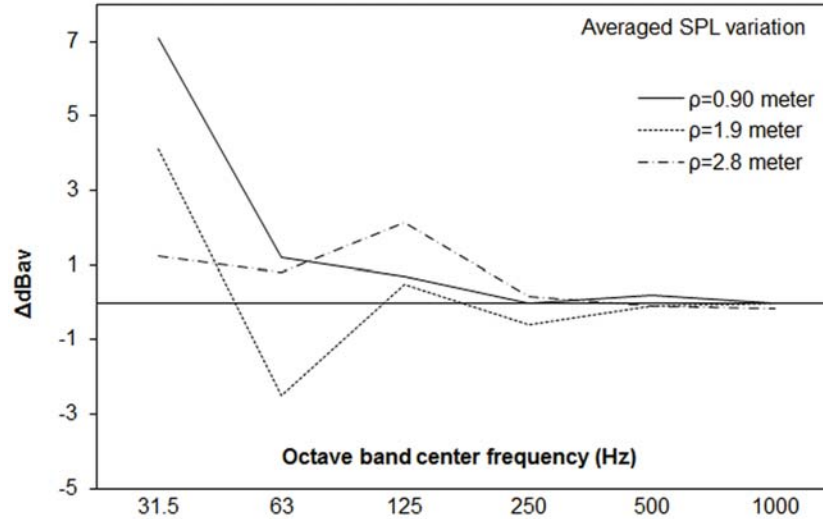


Fig. 12. Averaged SPL variation in octave band frequencies at discrete locations of microphone from an edge.

#### 4.3 Corner reflection

For corner reflection measurements, as shown in Fig. 13, an increase in SPL of up to 11 dB is observed in 31.5 Hz octave band at a distance of  $r = 1.10$  meters and reduction in the SPL of about 6 dB in 63 Hz octave band at a distance of  $r = 2.3$  meters. The reduction in 63 Hz band is due to destructive interference which occurs at a distance of about half a wavelength from the corner. Similar reduction in 125 Hz band is also observed at a distance of  $r = 1.10$  meters which is half a wavelength distance.

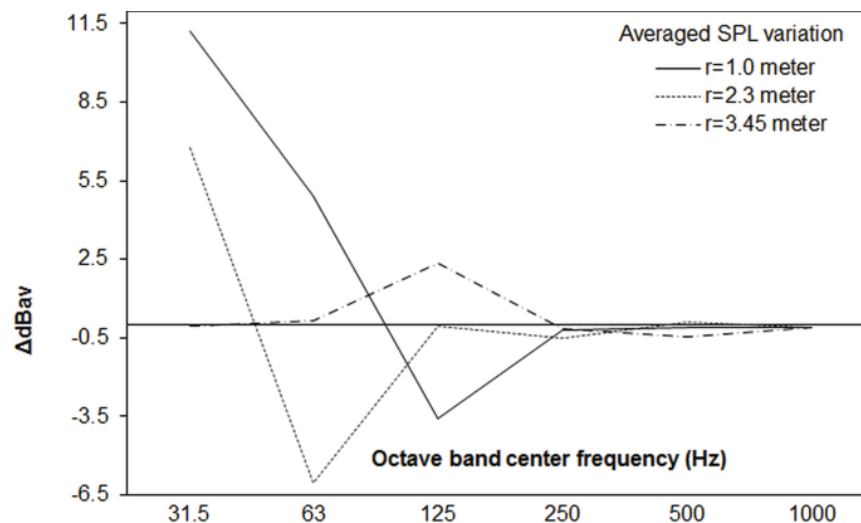


Fig.13. Averaged SPL variation in octave band frequencies at discrete locations of microphone from a chamber corner.



## 5 CONCLUSIONS

The close match of experimental measurements with theoretical calculations of the SPL will help in predicting the variation of SPL with reference to the diffused field at various distances from the reflecting planes of a reverberation chamber. Increase in SPL is observed at 31.5 and 63 Hz octave bands up to a distance of 1.2 meters from the respective surfaces. Substantial decrease in SPL is observed at approximately 2.0 meters from the corner of the chamber in the 63 and 125 Hz frequency bands. Hence microphones are required to be located beyond 1.2 meters from the surface or edge and 2 meters from the corner of a reverberation chamber in order to avoid influence of reflections on the measurement. Practical studies confirm that the microphones can be placed at a minimum of 0.5 meters from the test article surface unless the test article is hard in nature.

## 6 ACKNOWLEDGMENTS

I sincerely thank the Acoustic Test Facility team at National Aerospace Laboratories, Bengaluru, India, for the help and assistance provided for the experimental study.

## 7 REFERENCES

- [1] S. Balakrishna, *et al.*, 1988. "Design, Construction and evaluation of ISRO-NAL Acoustic Test Facility", 39<sup>th</sup> Congress of the International Astronautical Federation, Bangalore, India, pp. 6-7.
- [2] ISO 3743 - 2, 1994. "Acoustics - Determination of sound power level and sound energy levels of noise source using sound pressure - Engineering methods for small, movable sources in reverberant fields", p. 7.
- [3] ISO 3741, 2010. "Acoustics - Determination of sound power level and sound energy levels of noise source using sound pressure - Precision methods for reverberation test", p. 13.
- [4] H. Lamb, 1931. "Dynamical Theory of Sound (Edward Arnold and Company, London), second edition", pp. 229-233.
- [5] MIL-STD-1540C, 1994. "Military Standard Test Requirements for launch upper-stage and space vehicles", p. 39.
- [6] NASA Handbook -7005, 2001. "Dynamic Environmental Criteria, NASA", p. 228.
- [7] R.V. Waterhouse, 1958. "Output of a sound source in a reverberation chamber and other reflecting environments", *The journal of the acoustical society of America*, **30**(1), 4-13.

# Novel experimental set-up for characterization of acoustic source

N. Mallikarjun Naik\*, M. Rajesh, P. AtchutaRamayya,  
P. Anil Kumar and D. Venugapoal

*Environmental Test Facility (ENTEST), Research Centre Imarat (RCI), DRDO, Hyderabad, India*

*\*e-mail: mallikarjun.rcilab.in*

(Received: 03.08.2017; Accepted: 09.08.2017)

## ABSTRACT

Noise is unwanted sound. Noise generating mechanisms can be obtained by vibrating a surface, and modulating high pressure jets. High pressure jets can be a very significant source of noise. During lift-off of missiles and launch vehicles, the high speed turbulent flow mixed with ambient atmosphere results in significant noise generation which will be greater than 160dB. The noise so generated is reflected back on the airframe, which will hamper electronics within. Hence, there is always a necessity to simulate the same noise (Diffuse field) within the laboratory before clearing the item for flight. Generally, this noise is simulated in a reverberant chamber to which, acoustic sources are coupled with the help of horns. To generate significant noise, noise sources are required to modulate (fluctuate) the compressed air by varying the flow passage area or operating at high pressure ratios so as to simulate required overall sound pressure level of the shaped spectrum. Acoustic modulators, valves, high pressure jets are the examples of such noise sources. Modulation of the air gap can be done with the help of electrodynamics or electrohydraulic mechanisms. Electrodynamic principle requires a voice coil and permanent magnet in order to give required fluctuating forces for varying flow passage area. Heat generation of the voice coil during the operation increases with increase in input current. This paper deals with a novel experimental set-up for evaluation of complete characteristics of the air modulator without giving higher input current. This was established by considering the response of the fluctuating member and then forming a mathematical relationship under the assumption of a linear system. This technique ascertains the compliance of mechanical parameters such as stiffness, dimensional clearance etc., with specifications. This paper also deals with the eliminating the electrical excitation by mechanical force (Exciter) to get the desired acceleration to simulate higher current ratings. It is also a time saving method for integrating the actual hardware to the realistic application.

## 1. INTRODUCTION

Airstream modulation is one of the oldest and most common method of generating acoustic energy. All animals generate sound by this method, and it can be found in wind noises of the tree, factory whistles and sirens. In each case there is a source of flow and some elements designed to alter the flow in varying manner [1], [2], [3]. For example, two knife edges may be vibrated towards each other so that at maximum amplitude they exactly touch and lead to a maximum separation. The drawback of this mechanism is that there is chance of collision of the two blades with each other and tight closure of the flow is not possible.

If the two knife edges are slightly displaced in their planes of movement so that they may overlap each other with which reasonably tight closure and opening of the flow will be established without interference between the blades. The use of such blades, which can be operated in parallel require higher amount of air and result in the generation of higher acoustic pressure than that possible with a single set of opposing blades.

The motion of armature slots (modulation slots), in turn comes from the voice coil actuation. The stator will be constrained and armature will be moving under the influence of the electro-mechanical force. The modulation of the slots breaks the airstream into puffs of air similar to sirens. These puffs are then transferred into pressure pulses inside the throat of acoustic horn.

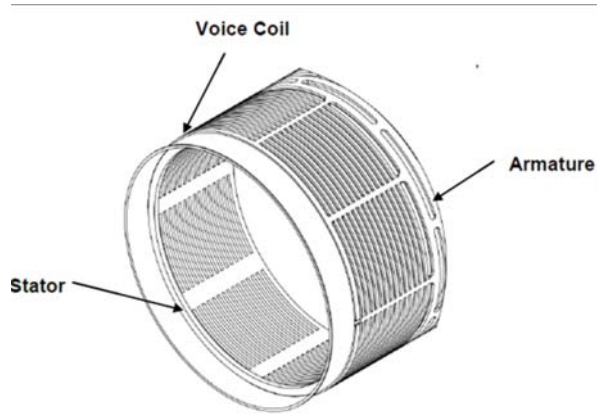


Fig. 1. Acoustic source (Stator slots are stationary and armature slots are required to move and voice coil winding not shown)

Voice coil actuation systems are direct drive, limited motion, that use a permanent magnetic field and coil winding (conductor) to produce a force proportional to the current applied to coil. This actuation system is used for high acceleration, high frequency applications.

The electromechanical conversion of the voice coil actuator is governed by Lorentz Force Principle. The law of physics states that if current carrying conductor is placed in a magnetic field, a force will act upon on it. The magnitude of the force is determined by

$$F = kBiLN \tag{1}$$

where,  $k$ =Constant,  $B$ =Magnetic flux density,  $i$ =Current,  $L$ =Length of the conductor and  $N$ =No. of turns

Here, the direction of force generated is a function of the direction of the current and magnetic field vectors. Specifically, it is a cross product of two vectors. If the direction of the current is reversed, then the direction of force on the conductor will also be reversed. The stator and armature are mounted in such a way that the first positive force to close flow fully and negative force to open the flow fully. Hence the stator and armature slots should be partially closed.

If the magnetic field and the length of a conductor are constants, then the generated force is directly proportional to input current.

Fig. 2 also illustrated that a conductor moving through a magnetic field will have a voltage induced across the conductor. The magnetic voltage,  $E$ , is determined by

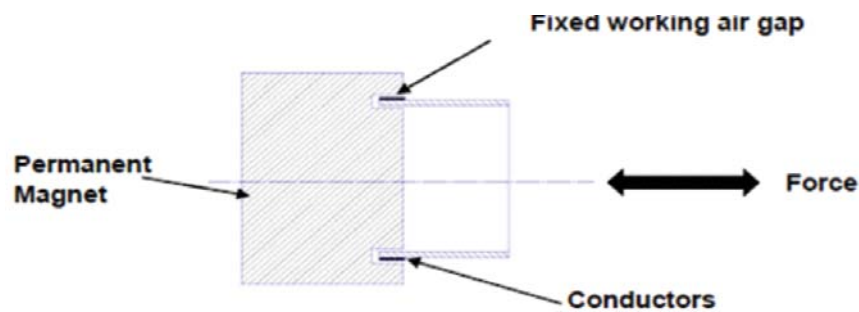


Fig. 2. Lorentz Force Principle

$$E = k B v L N \tag{2}$$

where, E = Magnetic voltage, B= Magnetic flux density, v = velocity of the conductor, L = Length of the conductors, N = No. of turns

Eq. (1) and Eq. (2) can be restated as follows: A device that contains a permanent magnetic field and coil winding moving in the field will produce a force proportional to input current [carried in the coil] and voltage proportional to velocity of the coil.

## 2. EXPERIMENTAL SET-UP

Experimental set-up devised for evaluation of characteristics of acoustic source is shown in Fig. 3.

Signal generator or function generator is used to generate a (periodic function) sinusoidal input in analog domain and it is generally used in designing, testing, troubleshooting and repairing of electronic and electroacoustic devices. Function generator generates a mathematical function for evaluation of the system. Generated signal is fed to amplifier so as to increase the amplitude of the signal. The amount of the amplification provided by the amplifier is measured by its gain. Voice coil current is measured with ammeter connected before the modulator as shown in Fig. 3.

As per the experimental set-up, the magnetic field and length of the conductors are constants, the generated force is proportional to the input current which is measured by the ammeter.

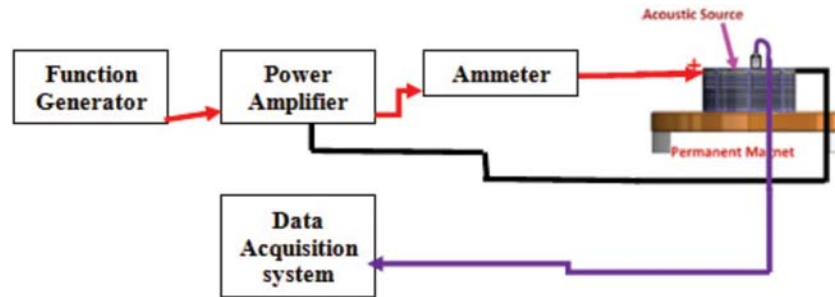


Fig. 3. Experimental set-up with input current as excitation

## 3. EXPERIMENTAL PROCEDURE

The prime aim of the work is to measure the acceleration response of the vibrating body for increments of current in steps 0.5, 1.0, 1.5, 2.0, 2.5 Amp and to form a mathematical relationship between the input current and acceleration. In this particular set-up, the drive current was set to the maximum of 2.5 Amp to avoid over heating of the voice coil. In order to operate the voice coil more than 2.5 amp, there should be sufficient cooling to dissipate the heat loads, which is a complicated set-up to establish on the working table.

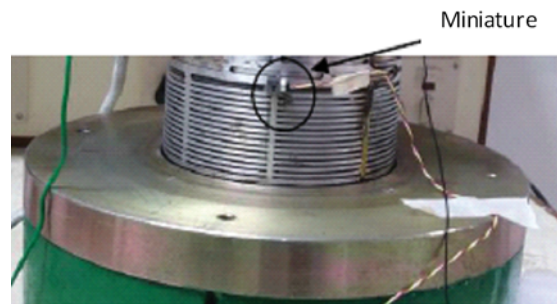


Fig. 4. Accelerometer mounting location

Tri-axial, light weight (1.0 gram) miniature, ceramic shear ICP accelerometer is used to measure the acceleration of the vibrating body under different input currents as shown in Fig. 4. This accelerometer signal is fed to the data acquisition system for storage and data analysis.

#### 4. ANALYSIS AND RESULTS

Input drive current to the air modulator can be represented by

$$i = A \sin(2 * \pi * f * t) \tag{3}$$

where,  $A$  is the amplitude of the current,  $f$  is the frequency of the excitation (i.e.,) 100Hz,  $t$  is time.

Vibrating characteristics of the cylindrical shell for different input currents has been captured by varying the amplifier gain, keeping excitation input current pattern constant.

A sample of time domain acceleration signal is shown in Fig. 5, which was captured during 1-amp excitation of input current.

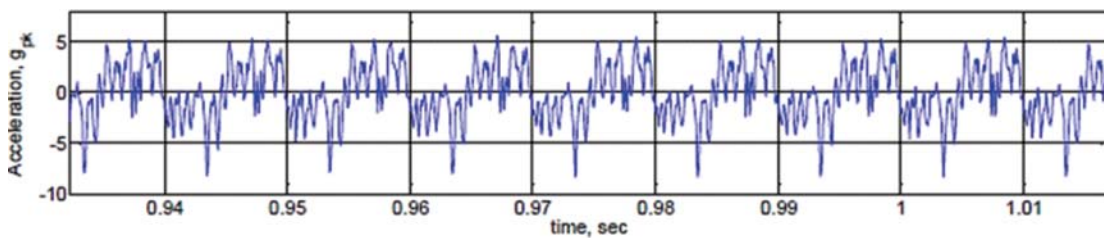


Fig. 5. Typical acceleration time history for 1.0 amp.

This acceleration time history data is converted into frequency domain by Fourier transformation [4]. It is evident from Fig. 6 that the maximum acceleration amplitude is present and rest of the frequencies are multiple harmonics of it.

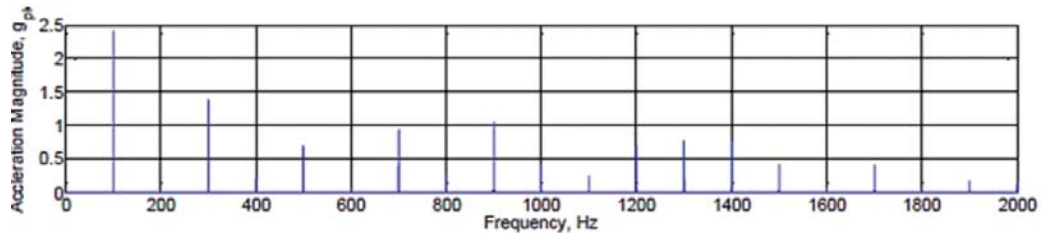


Fig. 6. Frequency domain of Fig. 5.

Similarly frequency domain acceleration magnitude is compared for all current inputs as shown in Fig. 7 and same is summarized in Table 1.

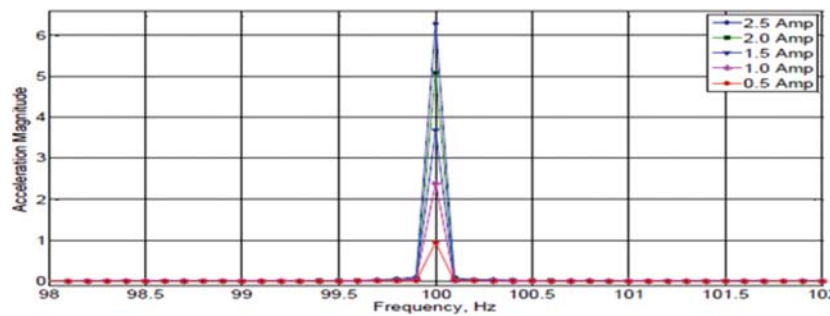


Fig. 7. Comparison of acceleration amplitude gpk as a function of input currents.

**Table 1. Comparison of gpk as a function input current at 100Hz**

Sl. No	Input Current (amp)	gpk	Sl. No	Input Current (amp)	gpk
1	0.0	0.0008 (instrumentation floor noise)	4	1.5	3.672
2	0.5	0.943	5	2.0	5.079
3	1.0	2.408	6	2.5	6.292

A curve has been fitted to the above mentioned data and same is shown in Fig. 8. Further this has been represented in mathematical form is given by

$$g_{pk} = P_1x + P_2 \tag{4}$$

Where,  $P_1 = 2.579$ ,  $P_2 = -0.1580$

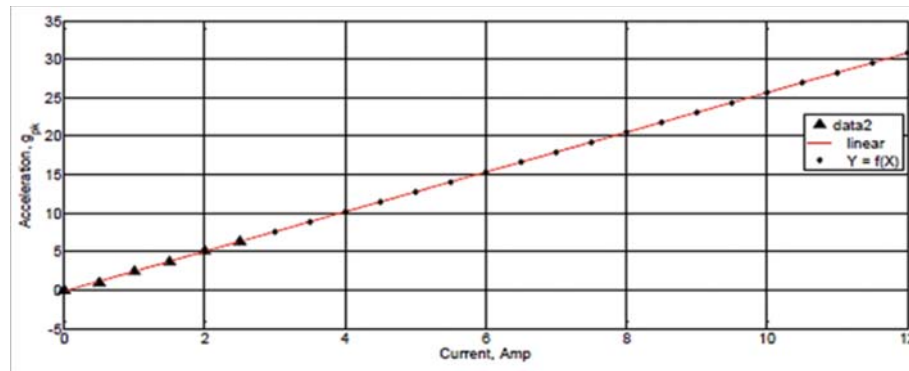


Fig. 8. Curve fit of experimental values with linear approximation

Acceleration response at 10 amps is observed to be 25.63 gpk. From the above, displacement of the slot is calculated as follows:

$$x = \frac{g_{pk}}{(2 * \pi * f)^2} * 9.81$$

$$x = \frac{25.63}{(2 * \pi * 100)^2} * 9.81 = 0.637 \text{ mm}$$

## 5. CONCLUSIONS

Higher input currents larger than 3.0 amps without forced external cooling can damage the voice coil, at the same time one need to know the characteristics of the modulator at different input currents to close and open the slot by 100%. This has been attempted using an experimental set-up for initial 6 data points, without exceeding 2.5 amp, which has resulted in a mathematical model, using which one can estimate the displacement of the slot mathematically. Knowing the acceleration response of the vibrating body, one can also excite the structure mechanically using an exciter to get such an acceleration and see if the slots are opening as per the requirement.

This set-up is extremely useful for evaluating the modulator performance before it is installed in a reverberation chamber/suitable applications.

## 6. ACKNOWLEDGEMENT

The authors would like to thank Director RCI for according permission to publish this work.

## 7. REFERENCES

- [1] G.M. Lillely, 1958. "On the Noise from Air Jets", British ARC, 20376.
- [2] M.J. Lighthill, 1954. "On sound generated aerodynamically-2, Turbulence as a source of sound", Proc. Roy. Soc. A222.
- [3] M.L. Munjal. 'Noise and Vibration Control', IISc lecture Notes Series.
- [4] Kihong Shin and Joseph K. Hammond, "Fundamentals of signal processing for sound and vibration engineers", John Wiley & Sons, Ltd.

# Vibro-acoustic response of composite payload fairings subjected to acoustic excitation

P. Geena George, S. R. Arun Raj, P. R. Murali and R. Neetha

*Structural Dynamics Response and Stability Analysis Division, Structural Engineering Entity,  
Vikram Sarabhai Space Centre, ISRO, Thiruvananthapuram, Kerala-695022  
e-mail: geena\_george@vsc.gov.in*

(Received: 17.07.2017; Accepted: 26.07.2017)

## ABSTRACT

Launch vehicle payload fairings are subjected to acoustic excitations during launch and atmospheric regime of flight. At lift-off these excitations result from the propulsion system generated noise field surrounding the vehicle and in transonic and supersonic portions of the flight, aerodynamically generated acoustic field is incident on the vehicle. The high levels inside the fairing can excite and damage lightweight structures of the spacecraft, such as solar panels. The acoustic transmission problem is augmented by the development of more powerful engines and by use of larger fairings built with lightweight composite materials aiming at reducing fairing weight, maximizing payload capability and reducing costs. To reduce the severity of internal acoustic field, acoustic protection systems are used in payload fairings. Ogive payload fairings reduce the external aero acoustic levels. The vibration response and sound transmission loss characteristics of composite payload fairings with acoustic protection systems for straight nose cone and ogive nose cone payload fairings were determined through acoustic test and are presented in this paper. The flight acoustic measurements made on these payload fairings are also presented in this paper.

## 1. INTRODUCTION

Composites structures have started replacing several Aluminum structures in aerospace industry because of their higher strength and stiffness, larger payload envelope, lighter weight and better fabrication benefits. These advantages, however, are accompanied by poor sound transmission loss characteristics of composite structures. Severe noise levels occurring during launch may damage fragile payload inside the payload fairing (PLF). Therefore, the need arises to mitigate the noise transmission through composite payload fairing structure and provide an acceptable environment for the payload. The lift off acoustic noise external to the fairing is reduced by the use of water injection techniques and launch duct covers. The external aero dynamic noise is reduced by the use of ogive payload fairings. Ogive fairings provide more payload room, are easier to produce, and smooth the airflow to limit sound and vibration, making the ride more comfortable.

The vibration response and sound transmission loss characteristics of composite payload fairings with straight nose cone [1] and ogive nose cone were determined through acoustic test and are presented in this paper. The acoustic tests were conducted in a reverberation chamber of size 8 m × 10 m × 13 m. The test results were used to generate spacecraft acoustic test specification, vibration test specification for components



mounted on the payload fairing. The data of flight internal and external acoustic measurements for both the fairings are also studied and presented in this paper .

## 2. COMPOSITE PAYLOAD FAIRINGS

The composite payload fairing was developed to meet the payload envelope requirement of 4000 kg class spacecraft's. The payload fairings are bulbous in configuration and consists of a cylindrical portion, boat tail and nosecone portion. The payload fairing with straight nose cone is shown in Fig. 1a and that with Ogive nose cone is shown in Fig. 1b. They are made of CFRP sandwich construction with high strength Carbon epoxy face sheets and Aluminum alloy honeycomb core. Acoustic tests were conducted on the payload fairings in order to obtain the sound transmission loss characteristics of the payload fairing with acoustic protection systems and the vibration responses. The external acoustic test levels were determined from scale model staticfiring and wind tunnel tests.



Fig. 1a. Composite Payload Fairing with straight nose cone in Reverberation chamber

Fig. 1b. Composite Payload Fairing with Ogive nose cone in Reverberation chamber

The acoustic field in the reverberation chamber and the acoustic field inside the PLF were monitored using microphones.

The external acoustic field simulated in the reverberation chamber and the acoustic field inside the payload fairing cylindrical region for the payload fairing with straight nose cone and ogive nose cone along with acoustic protection system during acoustic test in the reverberation chamber are shown in Fig.2.

It is seen that the attenuation characteristics of both the payload fairing are similar. The inner field is marginally lower for the straight nose cone PLF in the low frequencies.

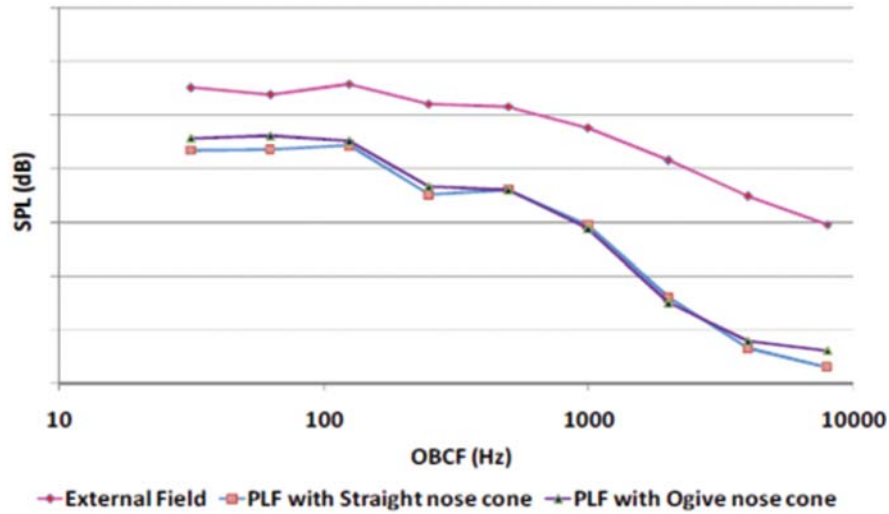


Fig. 2. Comparison of acoustic field inside the payload fairing during acoustic test

Vibration response was measured on the PLF skin, interface rings, isolated decks, input to the vent valve, pyro elements, umbilical shutter, umbilical mounting ring and input to PLA bracket. The comparison of vibration responses on the cylinder skin of the payload fairings are shown in Fig. 3. It can be seen that the overall vibration response on the cylinder skin for both the PLFs are similar

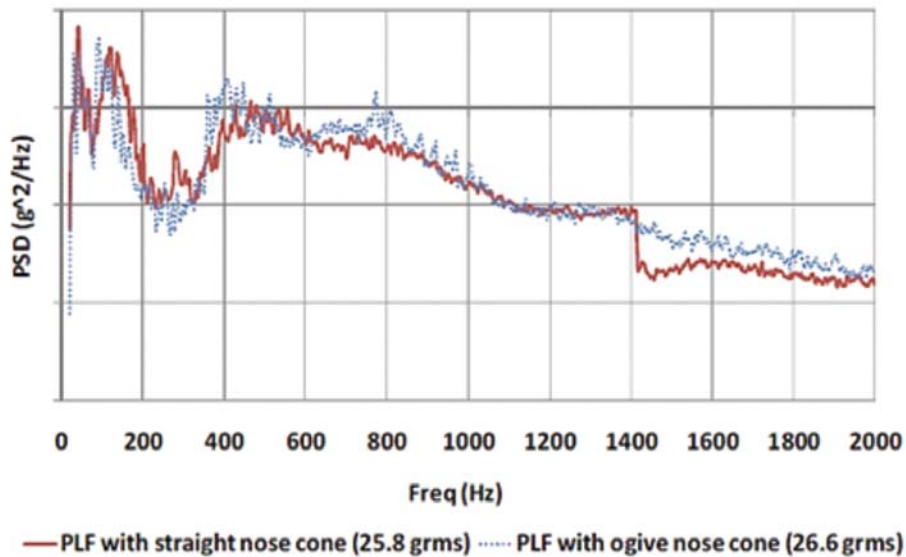


Fig. 3. Vibration response on PLF cylinder skin

### 3. GENERATION OF SPACECRAFT TEST SPECIFICATION

The sound attenuation characteristics obtained from the acoustic test and earlier flight experience are used to generate the spacecraft specification for Ogive payload fairing. Attenuation obtained from acoustic test and flight expected attenuation derived from earlier flight data are considered. To have a conservative estimate on internal acoustic field minimum of these attenuation is used for generating the acoustic test specification for the spacecraft. Thus arrived acoustic test specification for spacecraft is shown in Fig. 4.

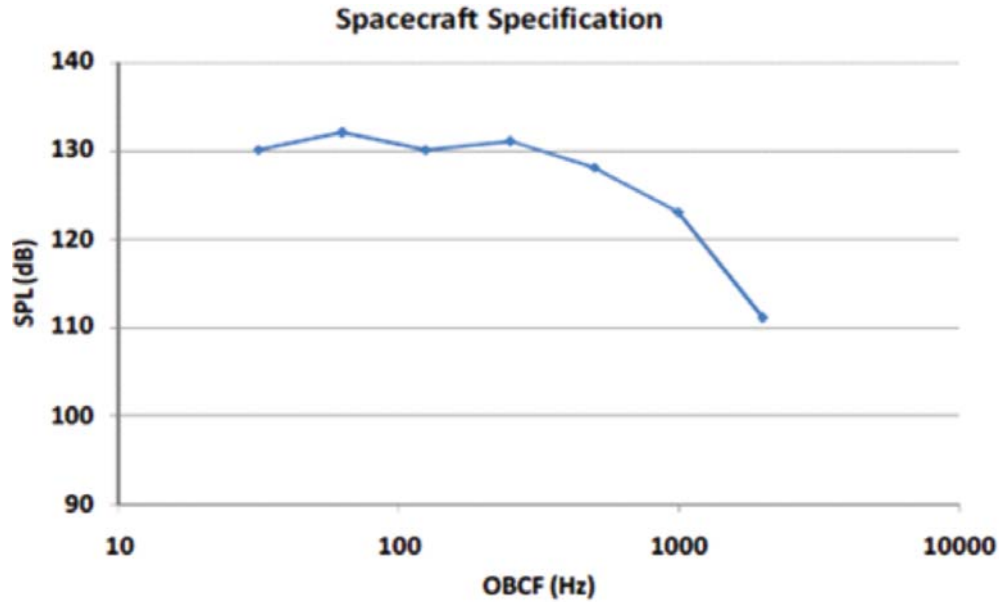


Fig. 4. Spacecraft Acoustic Test Specification

#### 4. COMPARISON OF FLIGHT DATA ON PAYLOAD FAIRING

The payload fairings were instrumented with microphones to obtain the external and internal acoustic field during flight. The comparison of the external acoustic field for the straight nose cone and ogive nose cone payload fairings in the cylinder region for the lift off environment is given in Fig. 5a and that during the aerodynamic regime is given in Fig. 5b.

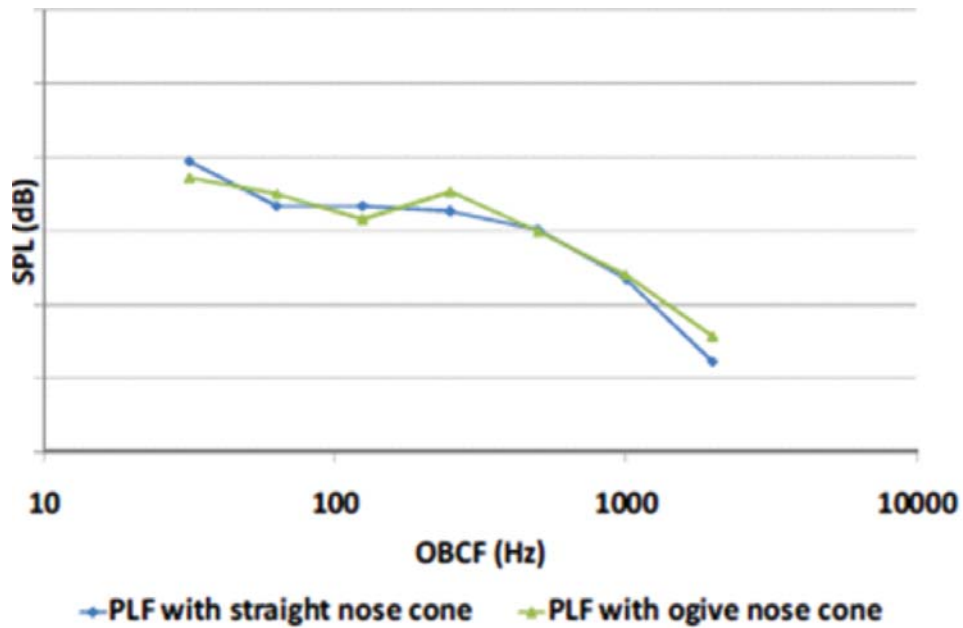


Fig. 5a. Comparison of acoustic field on the payload fairing during lift off

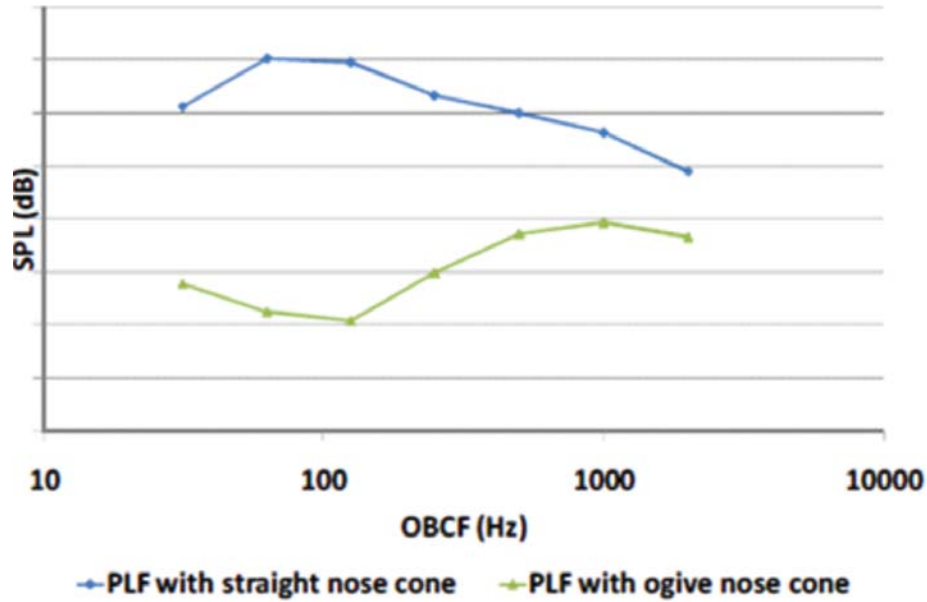


Fig. 5b. Comparison of acoustic field on the payload fairing during aerodynamic regime  
 It is seen that during the aerodynamic regime there is large reduction in the external acoustic field for PLF with Ogive nose cone.

The comparison of the internal acoustic field in the cylinder region for the straight nose cone and ogive nose cone payload fairings for the lift off environment is given in Fig. 6a and that during the aerodynamic regime is given in Fig. 6b.

It is seen that during the aerodynamic regime there is large reduction in the internal acoustic field for PLF with Ogive nose cone. The flight measured PLF internal acoustic field was within the spacecraft acoustic test specification.

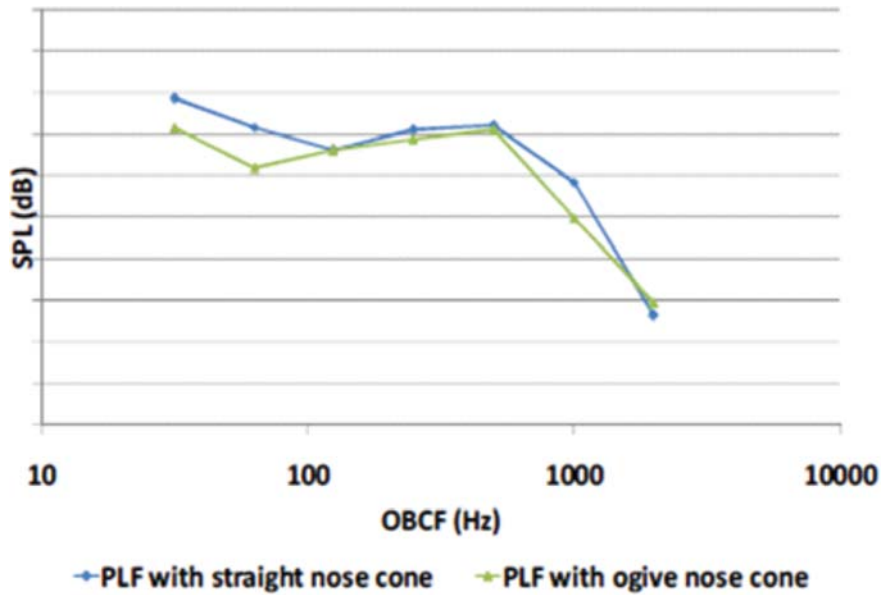


Fig. 6a. Comparison of acoustic field inside the payload fairing during lift off

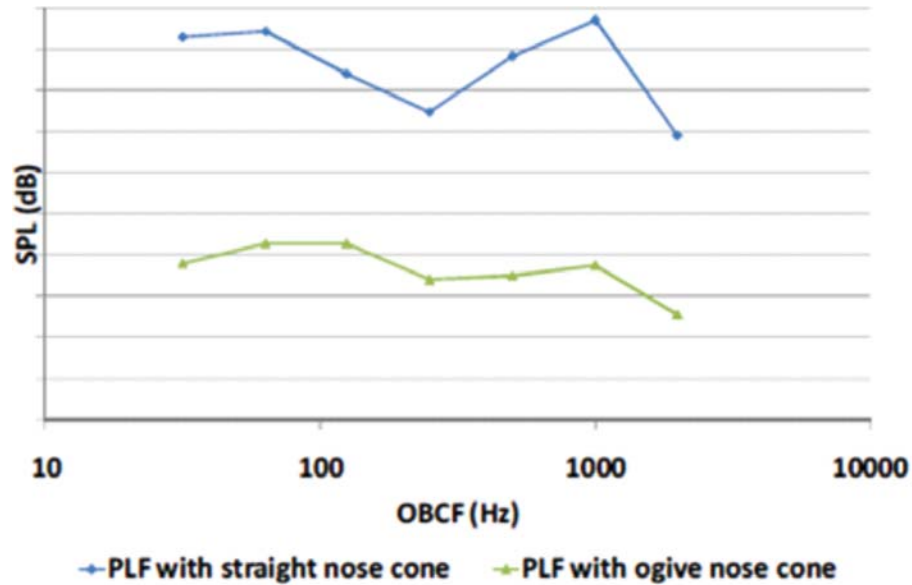


Fig. 6b. Comparison of acoustic field inside the payload fairing during aerodynamic regime.

## 5. CONCLUSION

The field inside the payload fairing and the vibration response on the cylinder skin of the payload fairing obtained from acoustic tests conducted on composite payload fairings with straight nose cone and ogive nose cone in reverberation chamber are studied. The attenuation characteristics of both the payload fairing are similar. The sound attenuation characteristics obtained from the acoustic test and previous flight experience are used to generate the spacecraft specification for Ogive payload fairing. During the aerodynamic regime there is a large reduction in the external and internal acoustic field for PLF with Ogive nose cone. The flight measured PLF internal acoustic field for ogive PLF was within the spacecraft acoustic test specification both at lift off and aerodynamic regime of flight

## 6. ACKNOWLEDGEMENT

The authors would like to thank project team for providing an opportunity to study the payload fairings. The support of NAL, ATF during the acoustic test programmers described is gratefully acknowledged. The authors would also like to thank Deputy Director (Structures Entity), VSSC and Group Director, Structural Dynamics and Modeling Group for their encouragement and kind permission to publish this paper.

## 7. REFERENCES

- [1] P. Geena George, P. R. Murali, R. Neetha, P. Balachandran and S. Anamaya Pillai, "Vibration Response and Sound Transmission Loss Characteristics of Composite Payload Fairings", ISAMPE National Conference on Composites INCCOM-13.

# Investigation of acoustic characteristics during the liquid engine starting transient phase through scale model test

Iyer Saisanthosh<sup>1</sup>, Jopaul K Ignatius<sup>2</sup>, S. Sankaran<sup>2</sup> and R. Ajithkumar<sup>1</sup>

<sup>1</sup>*Department of Mechanical Engineering, Amrita School of Engineering (Amritapuri),  
Amrita Vishwa Vidyapeetham, India.*

<sup>2</sup>*Aero Acoustic Test Facility (AATF), Sathish Dhawan Space Center,  
SHAR, ISRO, Sriharikota, India.*

[Received: 20-02-2017; Revised: 26-05-2017; Accepted: 29-05-2017]

## ABSTRACT

Supersonic nozzle flow in a liquid rocket engine with a high degree of overexpansion especially during the slow transient is susceptible to flow separation owing to the existence of adverse pressure gradient at off design conditions and the resultant internal shocks would lead to the shock induced flow separation. This would result in oscillatory pressure distribution along the inner wall of the nozzle divergent contour, thus generating a dynamically varying side loads. In the study presented here, subscale cold flow tests were conducted to investigate the influence of nozzle flow parameters on the separation phenomenon and its corresponding influence on the acoustic characteristics at various locations upstream and downstream of the nozzle exit plane. A toroidal water injection scheme was envisaged at the exit plane of the nozzle during the transient periods (quasi steady state with discretely varying stagnation pressure) to understand its effect on the flow separation mechanism. Surface flow visualization studies in conjunction with acoustic and vibration measurements along the nozzle divergent and also outside the nozzle exit plane were carried out to obtain a closer insight into the problem. Separation lengths were calculated semi-empirically using various separation criteria available in the open literature and comparisons were made with the experimental results. Water injection was found to influence significantly, the separation phenomenon as well as the position of the shock in the divergent contour, resulting in a benign flow and acoustic behaviour.

## 1. INTRODUCTION

High performance and upper stage nozzles have a higher area ratio, which leads to highly over expanded condition during lift-off. This makes the nozzle prone to the problem of flow separation due to insufficient stagnation pressures. The problem is further compounded in case of liquid rocket engines, which have got a relatively long ignition transient of the order of 4-6 seconds. Hence, the separation of the flow is inevitable due to the adverse pressure gradient and the separation point seems to advance along the nozzle divergent, as the stagnation pressure increases with time. During this period of separation, violent pressure oscillations are expected and result in severe vibration when coupled with natural frequency of the structure would lead to resonance and nozzle failure. Many studies have been carried out in this regard, analysing the influence of flow separation in nozzle performance during off design conditions. Several experimental studies involving subscale as well as full scale models were carried out [1-6]. These studies were

supplemented with numerical simulation [7-9]. Two prominent separation patterns were observed in the nozzle namely, Free Shock Separation (FSS) and Restricted Shock Separation (RSS).

In FSS, the flow detaches itself from the nozzle wall and flows as a free jet. A recirculation region is formed behind the separation region entraining ambient air. The wall pressure characteristics can be predicted by the shockwave boundary layer interaction theory [2 & 3]. Sunley and Ferriman [4] have studied separation in the conical nozzles of 150 half angle and observed that in the wall pressure measurement, the lowest pressure observed is not the separation pressure, but it is the pressure at the point where the separation is initiated slightly upstream of the separation point. Romine *et al.* [10] did an analytical study of the separation point, deriving relation for the same based on the normal shock solution and the triple point solution. They observed that the experimentally produced data matches with the triple point solution obtained by the pressure and flow balance. This leads to the conclusion that the triple point plays a very important role in the flow separation. Nave and Coffey [11] observed high magnitude of side load during the transition from FSS structure to the RSS structure. The pressure downstream of the separation point has shown an unsteady behaviour with strong oscillations attaining values above the ambient pressure hinting at flow reattachment. RSS is a phenomenon, wherein, the flow separates and then reattaches to the nozzle wall at discrete locations [1, 2 & 3]. Frey *et al.* [6] studied the RSS separation pattern and found that the exit pressure of the nozzle flow greatly influences the shock induced separation pattern in thrust optimized contours. Shams *et al.* [7] numerically simulated the flow separation phenomenon due to shocks, and they found a large stabilized recirculation zone (a stabilized trapped vortex [8]) behind the cap shock pattern which was first observed numerically and confirmed experimentally by Chen *et al.* [8]. They further observed that the vortex size increases with the increasing nozzle pressure ratio [8]. A transition from the cap shock pattern to the Mach disk pattern was observed when the normal shock crosses the point of intersection of the internal shock and the nozzle axis. In spite of the extensive study undertaken, the influence of water injection on the separation phenomenon are to be studied in detail and that forms the motivation and objective of the present work. This phenomenon is very critical especially for the space faring community, where the larger liquid stages are employed during advanced propulsion systems lift-off and nozzle protection system adopting water injection is to be enabled at launch pads to mitigate this problem.

## 2. EXPERIMENTAL SETUP AND INSTRUMENTATION

The experimental setup was designed for the sub-scale cold flow simulation to visualize the shock induced separation phenomenon observed during the starting transients of liquid propellant engines. The present study was conducted without and with water injection using a toroid provided at the nozzle exit plane.

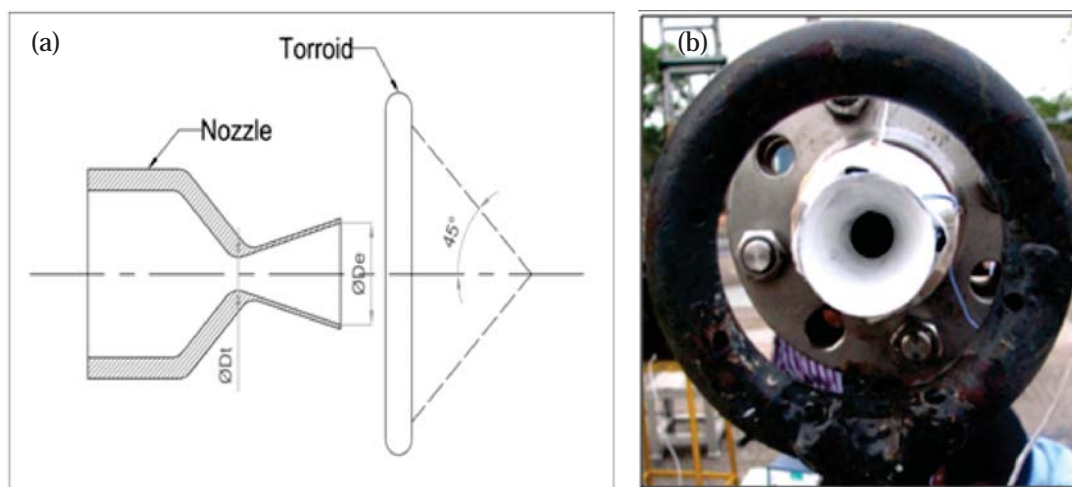


Fig. 1. Experimental Setup (a) Schematic of the experimental setup, (b) Photographic view of the test setup.

Highly pressurized Nitrogen modules were used to conduct the cold flow tests which would give the required steady stagnation pressures for each test case. The ignition transient phase of the liquid rocket engine is simulated in a quasi-steady manner by discretely varying the stagnation pressure and the experimental setup is shown in Fig. 1.

The test article is a conical C-D nozzle with a half angle of  $15^\circ$ , having throat diameter ( $D_t$ ) of 13.3 mm and an exit diameter ( $D_e$ ) of 34.8 mm conforming to an area ratio of 6.8. The nozzle was designed for a fully expanded exit jet Mach number of 3.5 with a pressure ratio of 77.1. The Table 1 gives the nozzle simulation parameters for the cold flow tests conducted. The toroidal water injection scheme was provided with an internal diameter of 80 mm corresponding to 2.3 times the nozzle exit diameter. It has got 8 orifices distributed along its circumference with equal spacing for fluid injection having an injection angle of  $45^\circ$  with respect to the nozzle axis. The injection pressure and mass flow rate of water is kept constant as 3 bar and 4 kg/s respectively, which is designed for the fully expanded condition of the selected nozzle. However, it is to be noted that the mass flow rate ratio (MFR) of primary (core flow) to the secondary water injection is found to vary with respect to the stagnation pressure variation with time.

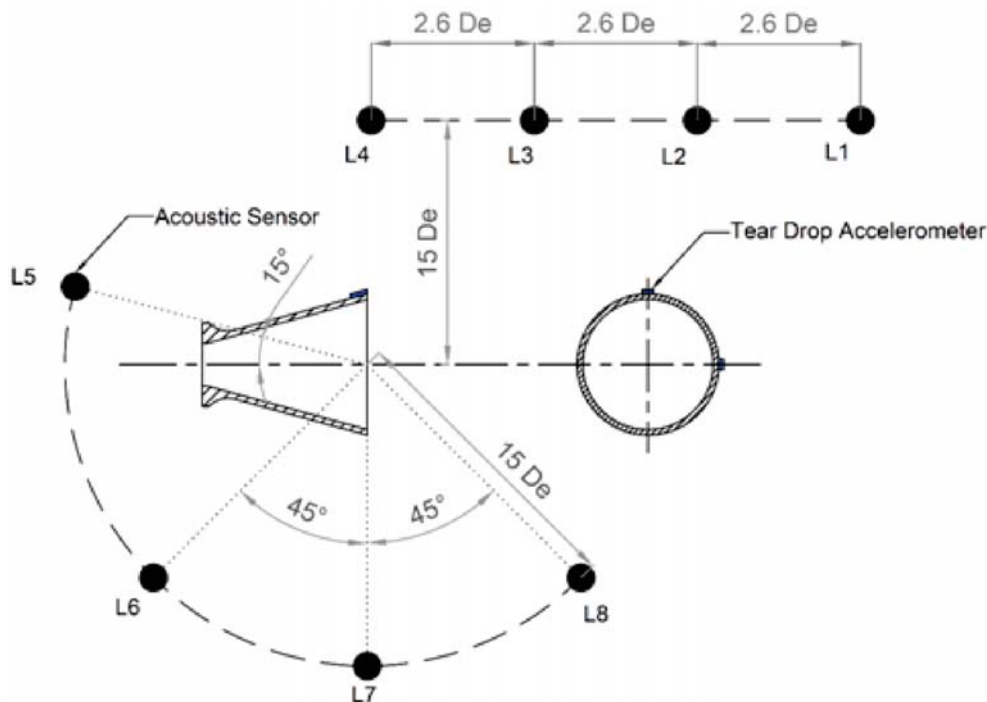


Fig. 2. Acoustic and Vibration measurement scheme.

The acoustic measurement scheme is presented in Fig. 2. The acoustic sensors were of  $\frac{1}{4}$ " B&K pressure field type and also PCB make with at least 70 kHz frequency response with an amplitude of 172 dB maximum with an accuracy of  $\pm 1.5$  dB. These acoustic sensors were placed outside the nozzle exit plane with 4 acoustic sensors were kept in a linear array of  $2.6 D_e$  apart axially and  $15 D_e$  laterally. Another set of 4 acoustic sensors were mounted in an arc formation, having a radius of  $15 D_e$  as shown in figure with different angles. The acoustic sensors were oriented in a horizontal plane passing through the central axis of the nozzle exit plane. In addition, two tear drop accelerometers have been placed in orthogonal planes, which were used to measure the vibration amplitude of the nozzle under study during transient period. The measurement scheme is depicted in Fig. 2. The acquired data was analysed and the spectrum plots are presented with a frequency resolution of 25 Hz for the vibro-acoustic analysis along with OASPL (dB).



**Table 1.** Nozzle simulation parameters (1 : 32.76)

Thermo-Physical Properties	
Exit diameter	34.8 mm
Throat diameter	13.3 mm
Area ratio	6.8
Mass flow rate	1.2 kg/s
Chamber pressure	37.1 bar
Exit Mach number	3.5
Ratio of specific heats ( $\gamma$ )	1.4

### 3. RESULTS AND DISCUSSIONS

#### 3.1 Flow visualization and Variation of Separation Length

Visualization was done using Surface flow visualization technique. A coating of titanium dioxide mixed in olive oil was applied to the inner surface of the nozzle divergent contour. The applied coating responds to the surface shear imposed by the moving fluid and displays the streak line pattern. Fig. 3 (a) & (b) shows the streak line pattern observed during the testing. From the visualization, it's seen that water injection causes a shift in the separation line, moving it towards the nozzle throat. The unsteady separation evident by the non-homogenous separation line is seen becoming steadier for increasing chamber pressures. Reduced separation length due to water injection indicates the movement of the shock that induces separation towards the nozzle throat. For a constant chamber pressure, the shock position inside the nozzle is influenced by the back pressure, indicating water injection in the downstream region is influencing the static pressure in the nozzle exit plane. Recirculation patterns are observed in the separated region of the flow. For increasing chamber pressure, the separation line moves towards the exit. It is due to the shock being pushed outward, towards the exit for increasing values of driving pressures. As the chamber pressure increased, the unsteady asymmetric separation line became more and more steady and axis-symmetric due to the water injection. From the preliminary observations it's clear that the water injection is stabilizing the internal shock inside the divergent contour, by influencing the back pressure, that is leading to a reduction in the separation plane tilt.



(i) Without water injection

(ii) With water injection

Fig. 3(a). Surface flow visualization for 5 bar stagnation chamber pressure without water injection and with water injection



(i) Without water injection (ii) With water injection

Fig. 3(b). Surface flow visualization for 25 bar stagnation chamber pressure without water injection and with water injection

The separation criteria found in the open literature were used to estimate the separation length from the nozzle throat plane [12]. The experimental results were found to be in good agreement with the empirically calculated ones. Fig 4 compares the separation length obtained empirically with the experimental results. Summerfield's criterion provided the best approximation for all the simulated cases. Separation length calculated using other criteria were found to have a very less margin of error in the lower stagnation chamber pressure values, with the magnitude of error increasing with an increase in-stagnation chamber pressure. From Fig. 5, it's seen that water injection is pushing the separation line towards the throat of the nozzle. This can be correlated with the visualization patterns presented in Fig. 3. For lower chamber pressure values, the difference isn't large. But as the stagnation chamber pressure is increased, the difference in the separation length observed, with and without water injection, is increasing. Separation phenomenon is highly dependent of the ambient pressure and the position of the shock inside the nozzle. The water injection scheme employed was found to influence the position of shock that induces separation inside the divergent portion.

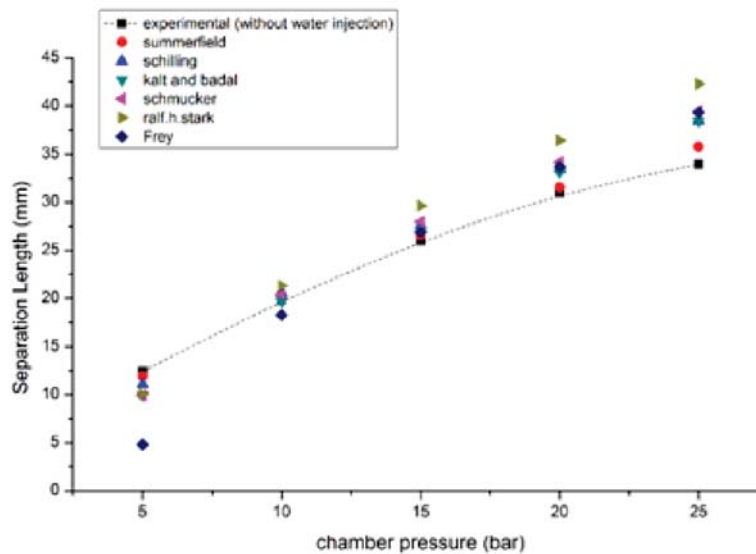


Fig. 4. Comparison between semi-empirically calculated and experimentally observed separation length

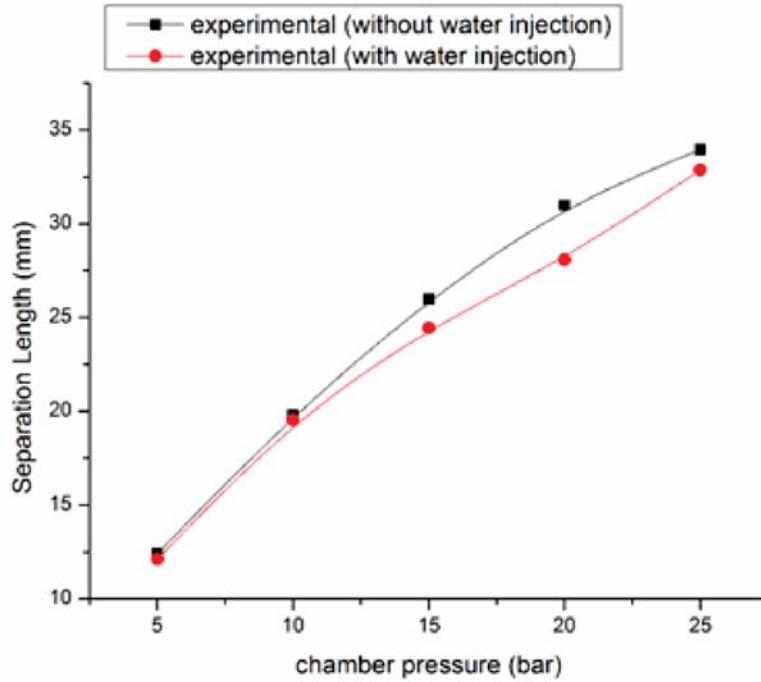


Fig 5 : Comparison between separation lengths with and without water injection.

### 3.2 Aero elastic coupling

An average reduction of 5 dB is observed in sound levels at all the sensor locations due to water injection as depicted by the Overall Sound Pressure Level (OASPL) plots in Fig. 6. As the stagnation chamber pressure

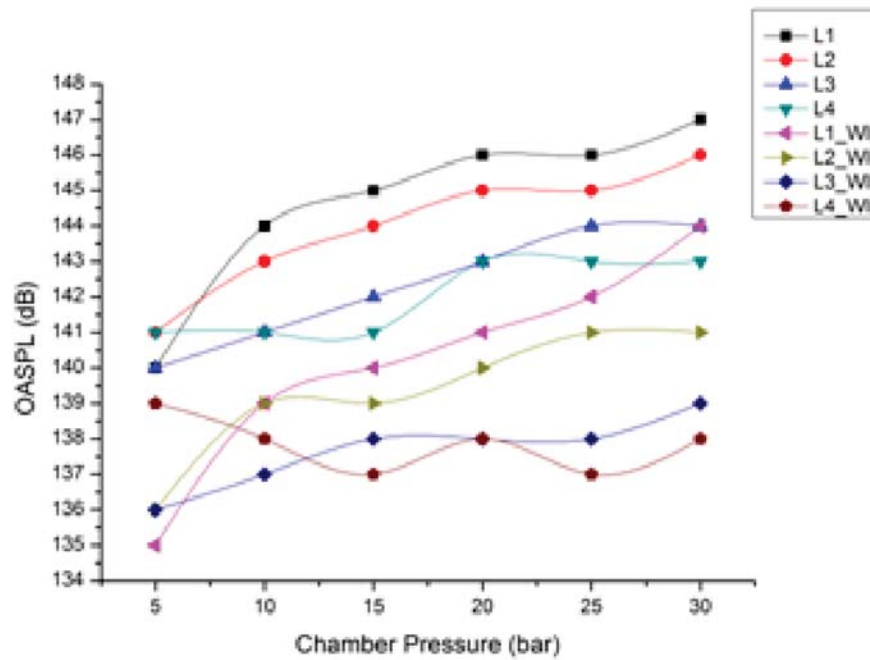


Fig 6 : Overall sound pressure levels (OASPL) at different locations downstream.

increased, the measured sound levels by each sensor also increased suggesting the movement of shock towards the nozzle exit plane which is also evident from the visualization pattern seen in Fig. 3. One of the major aspects of the liquid engine rocket nozzle is the coupling between the acoustic feedback loop phenomena and the vibration resonance modes of the nozzle. The acoustic modes generated due to the shock induced flow separation inside the nozzle and associated shock oscillation trigger the nozzle vibration. Once the acoustic and vibration mode frequencies are very close, it will be aiding one another and the sound pressure and vibration magnitudes will be significantly amplified. Corresponding to the nozzle vibration mode, the nozzle pressure mode also will be developed inside the nozzle wall.

In order to separate out the natural frequencies of the test setup and CD nozzle from the vibration modes during the cold flow test, simple tap tests are carried out. The result is shown in Fig. 7. The frequencies corresponding to full test setup with the mounting of the CD nozzle is given in the Fig. 7. Also the mode frequencies of the CD nozzle alone without integrating to the test setup are also given in Fig. 7.

Now coming to the cold flow acoustic and vibration measurements, Fig. 8 shows both sound and acceleration PSD. L4 microphone and top accelerometer is considered for the analysis. From Fig. 8, the first acoustic mode is occurring at 1100 Hz. The feedback loop frequency of 1100 Hz is the strongest tone inducing significant vibration of the nozzle mounting setup as seen from the vibration spectra. The second acoustic mode is not invoking corresponding vibration. The third acoustic mode and nozzle second mode frequencies are very close and the coupling effect is taking place. But the most significant coupling effect is seen at 4400

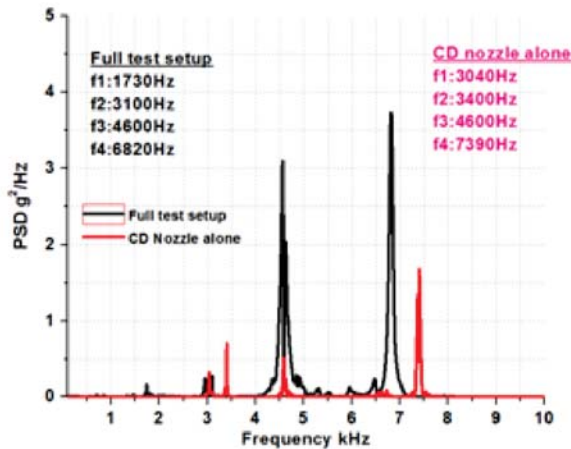


Fig. 7. Spectra from tap test of the test setup and CD nozzle stagnation chamber pressure at L4 and nozzle top accelerometer

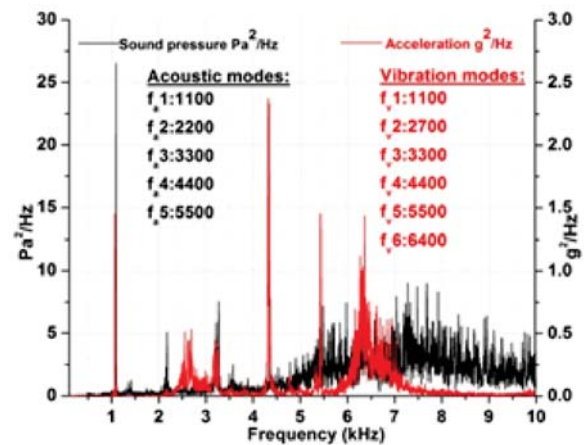


Fig. 8. Acoustics and vibration mode comparison at 20 bar

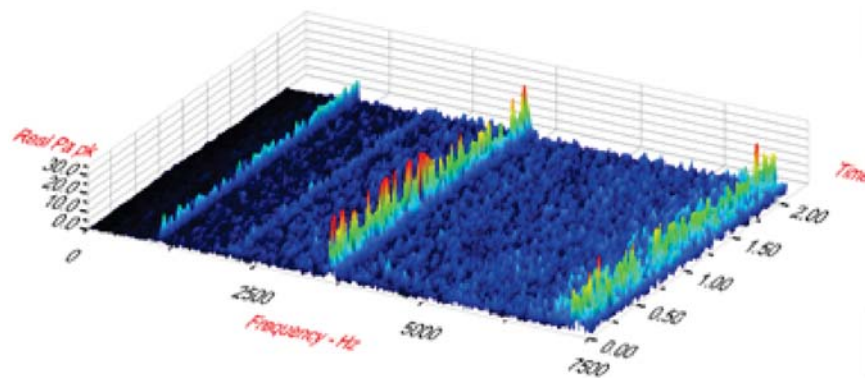


Fig. 9. Acoustic modes observed for 20bar stagnation pressure at L4 microphone.

Hz with peak acoustic and vibration amplitudes. Here both acoustic and vibration modes are aiding each other causing a constructive interference. The typical spectra with shock induced tones are evident in all the sound spectra. The same case is considered with the time frequency trace in Figures 9, 10 and 11.

In Fig. 9 the time frequency trace of the L4 microphone is shown. The consistent presence of the acoustics modes confirms the feedback loop phenomena occurring during the nozzle transient. The corresponding nozzle vibration is also given in the time frequency plot in Fig. 10. The acoustics induced modes and nozzle modes are also observed consistently in the time line in Fig. 10. Further to compare the time frequency plots of sound and vibration, the plots are represented in spectrogram mode as shown in Fig. 11. In Fig. 11 both sound and vibration frequency traces is directly compared. The aero elastic coupling at 3300 Hz and 4400 Hz is evident in the time line of the spectrogram in Fig. 11.

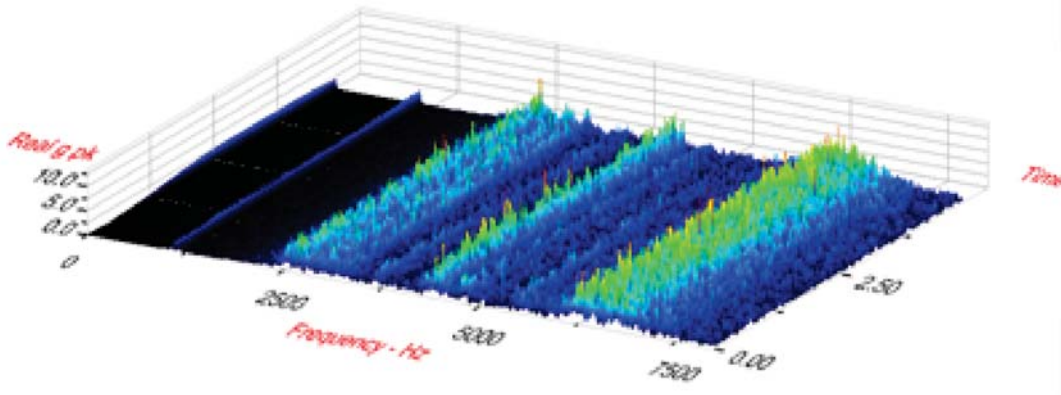


Fig. 10. Vibration modes of the test setup with nozzle measured at the top of the nozzle for 20bar stagnation pressure

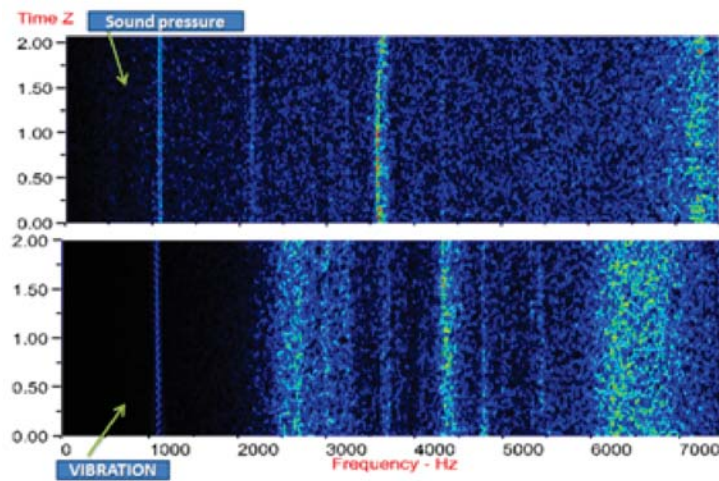


Fig. 11. Comparison of sound and vibration spectrogram for the nozzle at 20bar stagnation pressure.

Now coming to the effect of water injection, referring to Fig. 12, the present injection method is not suppressing the tones significantly. However, it is highly effective in suppressing the broadband shock noise and high frequency fines scale mixing noise. In fact, significant acoustic suppression is visible beyond 2kHz for all the stagnation pressures in the range of 5-30bar as shown in Figures 12(a)-(g). The present study clearly indicates that water injection is highly effective in suppressing the shock induced broadband

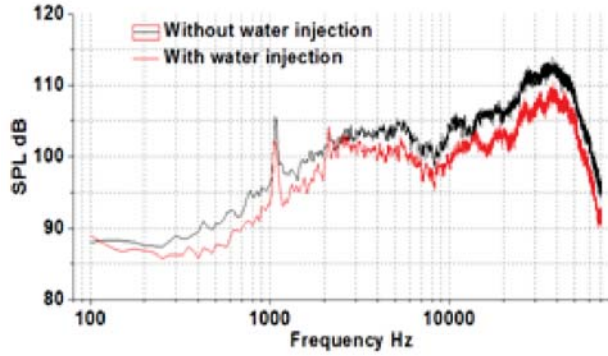


Fig. 12(a). Sound spectra for 5 bar stagnation chamber pressure

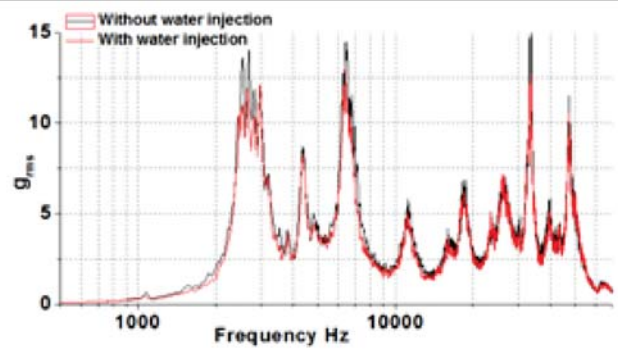


Fig. 12(b). Vibration spectra for 5 bar stagnation chamber pressure

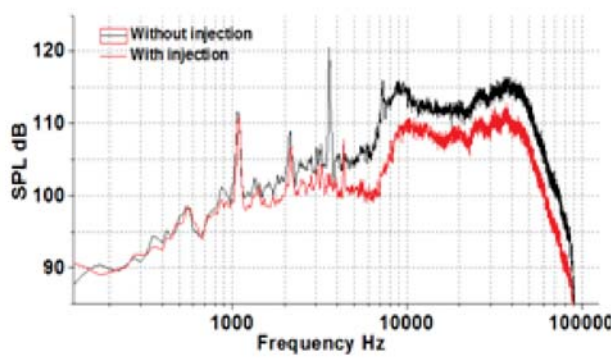


Fig. 12(c). Sound spectra for 15 bar stagnation chamber pressure

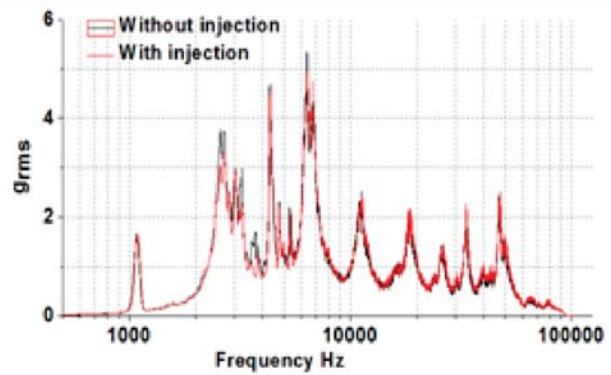


Fig. 12(d). Vibration spectra for 15 bar stagnation chamber pressure

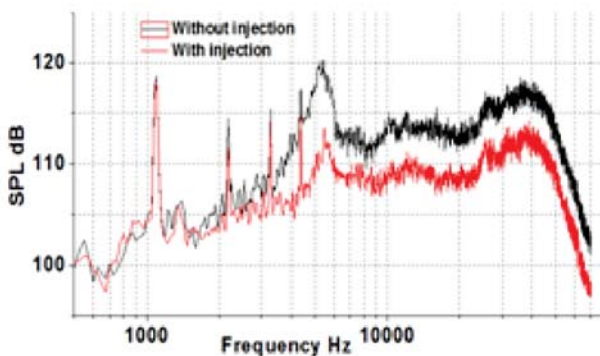


Fig. 12(e). Sound spectra for 25 bar stagnation chamber pressure

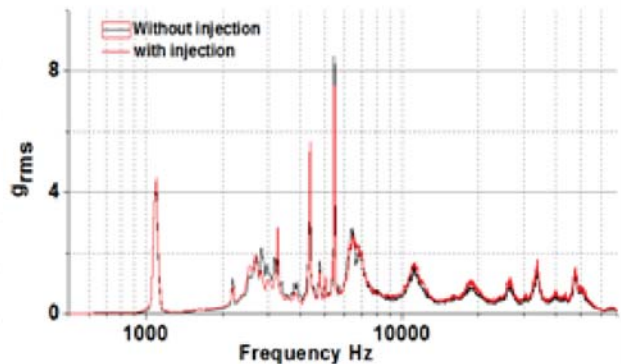


Fig. 12(f). Vibration spectra for 25 bar stagnation chamber pressure

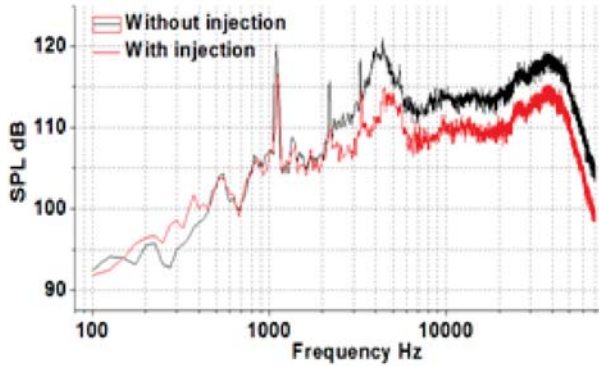


Fig. 12(g). Sound spectra for 30 bar stagnation chamber pressure

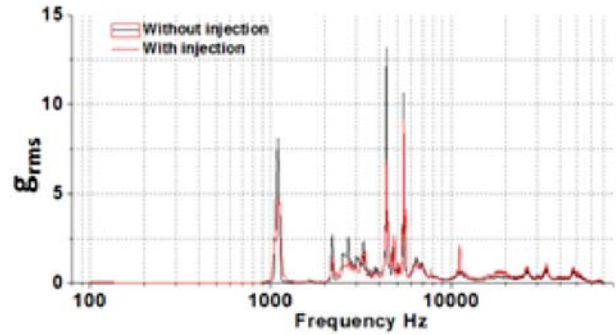


Fig. 12(h). Vibration spectra for 30 bar stagnation chamber pressure

Fig. 12. Sound spectra at L4 and vibration at top location for varying stagnation pressures.

acoustics. The inability to suppress the tone as evident from Fig. 12 is indicating the fact that the water injection outside the nozzle is not influencing the feedback loop. The dynamics of shock induced flow separation and corresponding acoustic tones are less influenced by the current water injection scheme. Hence it is required to investigate further injection scheme which will affect these tones. The vibration amplitude is also less affected by the water injection. The water injection should reduce vibration induced by the acoustic modes. Further investigations should aim for significant suppression of the tones and corresponding nozzle vibration. Hence it may be noted that water jets aiming at the gas jet from the nozzle exit is sufficient enough to suppress the shock induced broad band shock noise. However, the nozzle vibration is less effected by the water injection. Hence in future, further atomization of water jet at the nozzle exit has to be considered and try to dampen down the shock dynamics inside the CD nozzle by the entrained water droplets.

#### 4. CONCLUSION

Water injection was found to influence the position of separation line inside the divergent contour, implying an influence over the position of shock that induces separation inside the divergent contour. Visualization shows a reduction in the tilt of the separation plane for higher stagnation pressure cases. Acoustic modes observed due to shock induced flow separation was found to trigger Nozzle vibration. Significantly strong aero elastic coupling effect was seen at 4400 Hz due to the constructive interference of acoustic and vibration modes. The Mass Flow Ratio (MFR) and the employed injection scheme play a key role in tone suppression. The injection scheme employed for the present study proved highly effective in suppressing the Broadband Shock Associated Noise (BBSN). Significant suppression was observed beyond the 2kHz range, but the inability of the employed scheme to suppress the noise associated with flow separation necessitates the need for further investigation in the domain of suppression schemes envisaged specifically for flow separated nozzles.

#### 5. ACKNOWLEDGEMENT

Authors express their sincere gratitude towards SDSC SHAR, ISRO, and Sriharikota top management for their constant support and encouragement in conducting R&D studies.

#### 6. REFERENCES

- [1] Jan O'stlund, Tomas Damgaard and Manuel Frey, 2004. Side-Load Phenomena in Highly Over Expanded Rocket Nozzles, *Journal of Propulsion and Power*, **20**(4).

- [2] Jan Ostlund, 2004. Supersonic flow separation with application to rocket engine nozzles, Technical Report from Royal Institute of Technology, Department of Mechanics, Sweden.
- [3] Jan Ostlund, 2002. Flow processes in rocket engine nozzles with focus on flow separation and side-loads, PhD thesis, Report from Royal Institute of Technology, Department of Mechanics, Sweden
- [4] H.L.G. Sunley and V.N. Ferriman, 1964. Jet separation in conical nozzles, *Journal of the Royal Aeronautical Society*, **68**.
- [5] C. Genin, R. Stark, O. Haidn, K. Quering and M. Frey, 2013. Experimental and numerical study of dual bell nozzle flow, *Progress in Flight Physics*, **5**, 363-376.
- [6] Manuel Frey and Gerald Hagemann, 2000. Restricted Shock Separation in Rocket Nozzles, *Journal of Propulsion and Power* **16**. A. Shams, S. Girard and P. Comte, 2012. Numerical simulation of shock-induced separated flows in over expanded rocket nozzles, *Progress in Flight Physics*, **3**, 169-190.
- [7] C.L. Chen, S.R. Chakravarthy and C.M. Hung, 1994. Numerical investigation of separated nozzle flows. *AIAA J.* **32**, 1836-1843.
- [8] W. Kwan and R. Stark, 2002. Flow separation phenomena in subscale rocket nozzles, Proceedings of 38<sup>th</sup> AIAA/ASME/SAE/ASEE Joint Propulsion Conference & Exhibit, Indianapolis, Indiana.
- [9] G.L. Romine, 1998, Nozzle flow separation, *AIAA Journal*, **36**(9) 1618-1625.
- [10] L.H. Nave and G.A. Coffey, 1973. Sea-level side loads in high-area-ratio rocket engines. 9<sup>th</sup> Propulsion Conference.
- [11] Ralf H Stark, 2005. Flow separation in nozzles, A Simple Criterion, 41<sup>st</sup> AIAA/ASME/SAE/ASEE Joint Propulsion Conference & Exhibit.



## INFORMATION FOR AUTHORS

### ARTICLES

The Journal of Acoustical Society of India (JASI) is a refereed publication published quarterly by the Acoustical Society of India (ASI). JASI includes refereed articles, technical notes, letters-to-the-editor, book review and announcements of general interest to readers.

Articles may be theoretical or experimental in nature. But those which combine theoretical and experimental approaches to solve acoustics problems are particularly welcome. Technical notes, letters-to-the-editor and announcements may also be submitted. Articles must not have been published previously in other engineering or scientific journals. Articles in the following are particularly encouraged: applied acoustics, acoustical materials, active noise & vibration control, bioacoustics, communication acoustics including speech, computational acoustics, electro-acoustics and audio engineering, environmental acoustics, musical acoustics, non-linear acoustics, noise, physical acoustics, physiological and psychological acoustics, quieter technologies, room and building acoustics, structural acoustics and vibration, ultrasonics, underwater acoustics.

Authors whose articles are accepted for publication must transfer copyright of their articles to the ASI. This transfer involves publication only and does not in any way alter the author's traditional right regarding his/her articles.

### PREPARATION OF MANUSCRIPTS

All manuscripts are refereed by at least two referees and are reviewed by the Publication Committee (all editors) before acceptance. Manuscripts of articles and technical notes should be submitted for review electronically to the Chief Editor by e-mail or by express mail on a disc. JASI maintains a high standard in the reviewing process and only accept papers of high quality. On acceptance, revised articles of all authors should be submitted to the Chief Editor by e-mail or by express mail.

Text of the manuscript should be double-spaced on A4 size paper, subdivided by main headings-typed in upper and lower case flush centre, with one line of space above and below and sub-headings within a section-typed in upper and lower case understood, flush left, followed by a period. Sub-sub headings should be italic. Articles should be written so that readers in different fields of acoustics can understand them easily. Manuscripts are only published if not normally exceeding twenty double-spaced text pages. If figures and illustrations are included then normally they should be restricted to no more than twelve-fifteen.

The first page of manuscripts should include on separate lines, the title of article, the names, of authors, affiliations and mailing addresses of authors in upper and lower case. Do not include the author's title, position or degrees. Give an adequate post office address including pin or other postal code and the name of the city. An abstract of not more than 200 words should be included with each article. References should be numbered consecutively throughout the article with the number appearing as a superscript at the end of the sentence unless such placement causes ambiguity. The references should be grouped together, double spaced at the end of the article on a separate page. Footnotes are discouraged. Abbreviations and special terms must be defined if used.

### EQUATIONS

Mathematical expressions should be typewritten as completely as possible. Equation should be numbered consecutively throughout the body of the article at the right hand margin in parentheses. Use letters and numbers for any equations in an appendix: Appendix A: (A1, A2), etc. Equation numbers in the running text should be enclosed in parentheses, i.e., Eq. (1), Eqs. (1a) and (2a). Figures should be referred to as Fig. 1, Fig. 2, etc. Reference to table is in full: Table 1, Table 2, etc. Metric units should be used: the preferred from of metric unit is the System International (SI).

### REFERENCES

The order and style of information differs slightly between periodical and book references and between published and unpublished references, depending on the available publication entries. A few examples are shown below.

#### *Periodicals:*

- [1] S.R. Pride and M.W. Haartsen, 1996. Electro seismic wave properties, *J. Acoust. Soc. Am.*, **100** (3), 1301-1315.
- [2] S.-H. Kim and I. Lee, 1996. Aeroelastic analysis of a flexible airfoil with free play non-linearity, *J. Sound Vib.*, **193** (4), 823-846.

#### *Books:*

- [1] E.S. Skudrzyk, 1968. *Simple and Complex Vibratory Systems*, the Pennsylvania State University Press, London.
- [2] E.H. Dowell, 1975. *Aeroelasticity of plates and shells*, Nordhoff, Leyden.

#### *Others:*

- [1] J.N. Yang and A. Akbarpour, 1987. Technical Report NCEER-87-0007, Instantaneous Optimal Control Law For Tall Buildings Under Seismic Excitations.

### SUMMISSIONS

All materials from authors should be submitted in electronic form to the JASI Chief Editor: B. Chakraborty, CSIR - National Institute of Oceanography, Dona Paula, Goa-403 004, Tel: +91.832.2450.318, Fax: +91.832.2450.602, (e-mail: bishwajit@nio.org) For the item to be published in a given issue of a journal, the manuscript must reach the Chief Editor at least twelve week before the publication date.

### SUMMISSION OF ACCEPTED MANUSCRIPT

On acceptance, revised articles should be submitted in electronic form to the JASI Chief Editor (bishwajit@nio.org)